University of the Witwatersrand

School of Chemical and Metallurgical Engineering

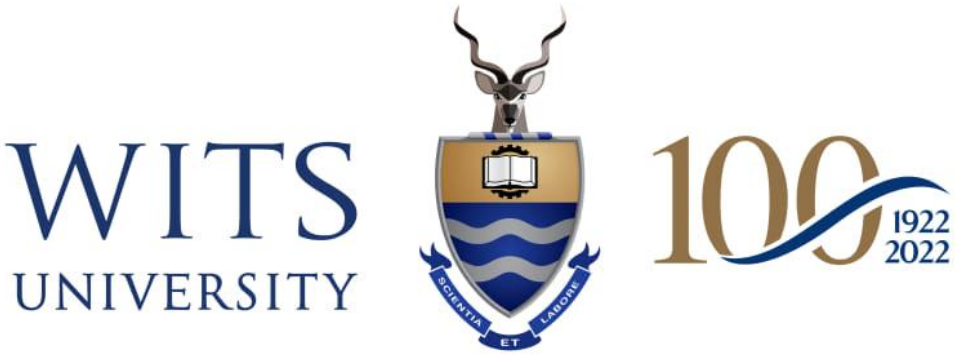

Zaynab Adam Cader

(1408757)

Influence of Cr/C Ratio on Cooling Curve Characteristics, Microstructure, Mechanical Properties, and Corrosion Performance of High-Chrome Cast Iron.

A dissertation submitted to the Faculty of Engineering and the Built Environment in fulfilment of the requirements for the degree of *Master of Science* in Metallurgical Engineering

Supervisors: Prof Josias W van der Merwe

: Prof Michael O Bodunrin

: Dr Desmond E Klenam

July 2025

Declaration

I, Zaynab Adam Cader, hereby declare that this master's dissertation is my own original work. The dissertation is submitted for the award of Master of Science in Metallurgical Engineering in the School of Chemical and Metallurgical Engineering, University of the Witwatersrand, Johannesburg, South Africa. This work has not been submitted for any other degree at any other University.

Abstract

High-chromium cast irons (HCCIs) are widely used in industries requiring superior wear and corrosion resistance, such as mining, petrochemical, and milling operations. The performance of these alloys is primarily dictated by their Cr/C ratio, which influences carbide formation, size, shape, and distribution within the microstructure. Despite extensive research on HCCIs, knowledge gaps remain regarding the combined effects of the Cr/C ratio and heat treatment on microstructure evolution, mechanical properties, wear resistance, and corrosion behaviour. This study investigates the influence of the Cr/C ratio and heat treatment on the microstructural characteristics of Cr24 HCCIs, with a focus on their hardness, toughness, wear resistance, and corrosion performance. Three different compositions were cast with varying C content and subjected to microstructural analysis using scanning electron microscopy (SEM), energy-dispersive X-ray spectroscopy (EDS), and X-ray diffraction (XRD). Hardness testing was performed using Vickers and Brinell methods, while wear behaviour was evaluated through pin-on-disc tribometer tests. Corrosion resistance was assessed using potentiodynamic polarisation testing in acidic (0.5M H_2SO_4), neutral chloride (3.5wt.% NaCl), and alkaline (0.5M NaOH) solutions. The findings reveal that a higher Cr/C ratio produces a finer, more uniformly distributed carbide network, while a lower Cr/C ratio results in larger, more interconnected carbides. Hardness and wear resistance increased with higher carbide volume, but excessive carbide coarsening led to higher wear rates due to three-body abrasion. Heat treatment improved fracture toughness but did not significantly enhance wear or corrosion resistance, as expected. The treatment, designed for Cr28 alloys, led to excessive secondary carbide precipitation, which depleted matrix chromium, reducing passive film stability and increasing corrosion susceptibility in aggressive environments. In corrosion testing, chloride and acidic solutions attacked carbide-matrix interfaces, accelerating localised corrosion, whereas alkaline environments led to selective carbide dissolution. A homogeneous carbide distribution improved corrosion resistance by supporting a stable passive film, while large, interconnected carbides promoted material degradation. The study confirms that optimising the Cr/C ratio, carbide morphology, and heat treatment parameters is essential to achieve the best balance between hardness, wear resistance, toughness, and corrosion resistance. These findings provide valuable insights into microstructural tailoring strategies for improving the durability of HCCIs in industrial applications.

Dedications

In the name of Allah, the Most Gracious, the Most Merciful.

This work is dedicated firstly to God, my Creator and Maker. The owner of the knowledge to be disseminated through this dissertation and any other derivatives. All that I do is for His pleasure and worship.

To my family and brothers. Their unwavering support and prayers throughout my whole journey until the end.

My late supervisor, Prof. Josias van der Merwe, for the opportunity he granted me to pursue this MSc as well as enhance my skills in microstructural analysis through the operation of the CHMT SEM.

To my supervisor, Prof. Michael Bodunrin, and his family, who have been unwavering pillars of support throughout the journey.

To myself, for proving to myself that I am capable.

All of you are the reason I did not quit despite the challenges faced in the duration of this MSc.

Acknowledgements

To Allah, my creator, the owner of the heavens and earth, the owner of all the knowledge in existence. All praises and glory belong to You. Everything flows from you and to you. Despite the hardships faced, you pulled me through and granted me strength repeatedly. You were there when no one was. I was never alone; you were always with me. It was you who comforted me and dried my tears when no one was there to. I asked you, and you responded. You lived up to your promise. Ya Al-Qareeb, Ya Al-Mujib, you are The Absolute truth.

My late supervisor, Prof. J. W. van der Merwe, I know you would be proud of the work I have done. To my supervisor, Prof. Michael Bodunrin, thank you for the constant guidance throughout, from my undergraduate research till the completion of my MSc. The candid reviews and comments are exactly what I required for this work to come together. Thank you for pushing me beyond my comfort zone and helping me down to the analysis of the contents of this work. Words can never express how grateful I am. To my 2nd supervisor, Dr. Desmond Klenam, thank you for the technical guidance and the valuable lessons that you provided through the Thursday group meetings. My writing would have not been up to standard without your guidance.

To the staff of Richard Ward, Donald Mohale, Vhonani Munyangane, Letta Ntuli, and Collen. I appreciate all the efforts that went into assisting me with acquiring the necessary results for this work. Without your assistance, this work would have been incomplete. A heartfelt gratitude to the staff of the Metallurgical Engineering School at the University of Johannesburg, Brayner Nelwalani and Nompumelelo; your efforts are the entire reason why this work was successful to begin with. Thank you for extending grace and providing the necessary space and equipment that were pivotal to the entirety of this work.

A special thank you to AESA-RISE for the funding that went into the research and work done in this dissertation.

I would like to extend my heartfelt thanks to the colleagues and staff of the Next Frontiers in Advanced Materials Lab (NFAML) for their unwavering support, expert guidance, and collaborative spirit throughout this research journey. Your dedication and encouragement have been instrumental in every stage of my work. As the first official graduate of NFAML, I am proud to carry forward the lab's legacy of innovation and excellence. Thank you for fostering an environment where ideas flourish and breakthroughs become possible.

To my friends Takunda Maunganidze, Nicola Rundora, Olufemi Bamisaye, Iyanu Williams, and Smarte Anekwe. Thank you for your support, advice, and assistance during the course of this MSc. A special thank you to Dr. Olufemi Bamisaye for spending sleepless nights assisting with experiments and reviewing my work and for fighting with me to ensure this work is up to standard. Words can never truly appreciate the sacrifices you volunteered to ensure my success. I am truly grateful for you.

Finally, thank you to Adam Cader's family and my mother, father, and brothers Rashid and Fareed Adam Cader. Thank you for holding my hand throughout and strengthening me whenever I lost strength and for your constant prayers and wishes for my success. May Allah repay you back manyfold.

To everyone else who assisted even in the smallest way who I might not have mentioned, thank you so much. May Allah return many folds

Research Contributions

This work in this dissertation contributed to the following Journal Articles:

- Nelwalani, B. N., van der Merwe, J., Munyangane, V., Cader, Z. A., Rampaku, T., & Klenam, D. (2024). On the influence of compositional variations in high chrome cast iron: an assessment of microstructure and mechanical behaviour. *Manufacturing Review*, *11*, 1–12
- Cader, Z. A., Bamisaye, O. S., Klenam, D., Bodunrin, M. O., & Nelwalani, B. N. (n.d.). Optimizing Hardness, Toughness, and Wear in High-Chromium Cast Irons Through Cr/C Ratio-Dependent Microstructure Design. ***In Review***.
- Cader, Z. A., Bamisaye, O. S., Klenam, D., Bodunrin, M. O., & Omole, S. O. (n.d). Understanding Microstructural Effects of Corrosion Behaviour of Cr24 in Nuetral,Acidic and Alkaline Solutions. ***In Review.***

Table of Contents

List of Figures

List of Tables

Chapter 1: Introduction

1.1 Background

In the mining, mineral processing, and petrochemical industries, equipment components are routinely exposed to highly aggressive environments characterised by abrasive wear, impact loading, and corrosive chemical exposure. These harsh service conditions often lead to premature equipment failure, resulting in increased maintenance costs, operational downtime, and associated safety risks (Yang & Li, 2012). High-chromium white cast irons (HCCIs) are commonly employed in such applications due to their excellent hardness, wear resistance, and cost-effectiveness (Ngqase & Pan, 2020). The performance of these alloys is strongly influenced by their microstructural characteristics, particularly the type, size, and distribution of hard chromium carbides embedded within the matrix. Among the key compositional factors affecting the microstructure is the chromium-to-carbon (Cr/C) ratio, which plays a critical role in determining the nature and morphology of carbides formed during solidification and subsequent heat treatment (Guo et al., 2021). Despite the significance of this ratio, its combined effect on microstructure and resulting mechanical properties remains insufficiently understood, particularly in relation to the specific environmental demands encountered in local industrial sectors. This study therefore aims to investigate the influence of the Cr/C ratio on the microstructural evolution and mechanical performance of HCCIs, with the objective of optimising alloy compositions for improved reliability under the typical service conditions experienced in South African industry.

High chromium white cast irons are a specialised type of cast iron containing chromium as the primary alloying element. The typical composition ranges from 11-30 wt.% Cr, 1.8-6 wt.% C, and up to 5 wt.% Mo, along with trace amounts of copper, nickel, manganese, silicon, and vanadium (Ortega-Cubillos et al., 2015). The HCCIs are an important class of wear-resistant materials used in industries like mining, mineral processing, cement manufacturing, and pulp and paper industries, where stable performance in harsh environments is crucial (Ngqase & Pan, 2020). These cast irons can exhibit hypoeutectic, eutectic, or hypereutectic compositions depending on their carbon content. Hypoeutectic compositions with a typical carbon range of 1.8 wt.%-3.6 wt.% are often preferred for standard foundry applications due to their favourable properties, as they typically have a more controlled solidification process that results in a desirable microstructure balancing hardness, toughness, and wear resistance

(Guitar et al., 2018). The mechanical properties of high chrome white cast irons are influenced by several factors, including the Cr/C ratio, solidification rate, and the presence of alloying elements like Mo, Mn, Cu, and Ni (Yang et al., 2014). Adjusting these parameters allows tailoring the characteristics of the material for specific applications. Additionally, other carbide-forming elements can be added to the alloy to target desired properties.

The as-cast microstructure of HCCI typically consists of a network of eutectic hard M_7C_3 or $M_{23}C_6$ carbides within an austenitic matrix developed through a non-equilibrium process of solidification due to solute enrichment between dendrites, which deviates from equilibrium composition (Pellizzari, 2010; Sánchez-Cruz et al., 2020). High chromium cast irons can exhibit hypoeutectic, eutectic, or hypereutectic compositions depending on their carbon content. Hypoeutectic compositions are often preferred for standard foundry applications due to their favourable properties (Yang & Lei, 2012). The chemical composition and cooling rate determine the type of alloy and final microstructure. Cooling curves are used to trace the transformation of the material as it solidifies, while the phase diagram of the material shows us the different types of microstructures and phase transformations at the different cooling stages. This analysis is essential in understanding how processing conditions interact with composition, particularly the Cr/C ratio, to influence carbide nucleation and growth. Solidification of hypoeutectic HCCIs begins with the formation of primary austenite dendrites as the melt cools down from the liquidus temperature (Lora & Diószegi, 2012; Diószegi et al., 2015). As the temperature decreases further, the remaining liquid undergoes eutectic transformation, forming a mixture of austenite and chromium-rich M_7C_3 carbides. This two-phase structure is critical for achieving the desired balance of mechanical properties in the final casting (Yang & Lei, 2012). Proper control of the cooling rate and alloy composition during the solidification process is crucial to refine the microstructure and optimise the performance characteristics of the cast iron.

High chrome cast iron is primarily subjected to abrasive wear, but it can also experience erosive and impact wear, depending on the application. The high wear resistance of HCCIs primarily arises from the formation of hard chromium carbides of type M_7C_3 in the microstructure, which significantly increases their ability to withstand abrasive and erosive wear (Cui et al., 2016). The typical M_7C_3 carbides in HCCI have an extremely high hardness range of 1500-1800 HV, which contributes to the overall hardness along with the reasonably hard austenitic matrix (Fraś et al., 2015; Guitar et al., 2018). The presence of these carbides

in the austenite matrix creates a composite-like material where the carbides act as a barrier to wear, which functionally prevents the matrix from being easily abraded. The wear resistance of HCCIs is influenced by the volume fraction, size, and distribution of the carbides. A greater carbide volume increases the overall wear resistance of the alloy (Guo et al., 2021). Additionally, finer carbides are more effective at resisting wear, as they distribute the hard phase more evenly in the matrix. This effectively leads to a more consistent wear pattern, preventing the initiation and propagation of cracks (Fraś et al., 2015). Coarse carbides, while hard, can create stress concentrations that may lead to premature failure of the material under certain conditions (Gadhikar et al., 2014). The wear characteristics of the alloy may also be manipulated by applying additional heat treatment procedures. The hardness and toughness of the alloy can be altered through processes such as quenching and tempering, which ultimately impacts the material's resistance to wear (Guitar et al., 2018).

The primary objectives of heat treatment in HCCIs are to improve hardness, wear resistance, and toughness, which are essential for their performance in their respective demanding applications (Chen et al., 2022). Austenisation, which is often accomplished by heating the material to destabilising temperatures (950°C to 1050°C), is the first step in the heat treatment process (Herring, 2007; Clarke, 2014). Tempering is then carried out at subcritical or low temperatures of about 250°C to 750°C (Ma et al., 2012; Xu et al., 2014). Steel and other similar materials can have their mechanical qualities improved by this process. The material is quickly cooled during quenching, usually generating a martensitic structure that makes the material harder but also more brittle. To counteract this, tempering is used to increase toughness and ductility and decrease brittleness, all of which are essential for achieving the required qualities for a variety of applications (Shveikin et al., 2022; Alagheband & Ghanbari, 2024). Tempering is essential for producing the best mechanical qualities appropriate for a range of industrial applications by lowering brittleness while increasing toughness and ductility. Hardness significantly decreases when the tempering temperature rises above 550°C, which is an important consideration for HCCIs for particular uses. Thus, improving the mechanical qualities required for high-performance applications is dependent on the heat treatment procedure of HCCIs, with considerations of the tempering temperatures.

High chrome cast irons are used in a variety of industries, as previously mentioned, which all introduce a different set of variables that affect the way the material behaves in various ways. This introduces a complexity when it comes to knowing exactly how to customise the material

for the respective uses. The Cr/C ratio influences the microstructure of the material, which ultimately affects the way the material will behave in these environments. This means that multiple types of HCCIs need to be developed to suit the different environments, such as acidic, basic, and alkaline, and to wear environments that require certain levels of hardness and toughness qualities. This research is aimed at studying the effects of the Cr/C content on the microstructure of hypoeutectic HCCIs and how the microstructure influences the mechanical properties such as the hardness, toughness, wear, and corrosion. The goal of this study is to examine how the properties of the material impact the mechanical properties of the finished material by varying its composition. Additionally, this study will investigate how a developed heat treatment technique may improve the final hardness, fracture toughness, wear resistance, and corrosion resistance of the material. The heat treatment is included as a secondary step, mainly to enhance the properties already seen in the as-cast condition; however, the primary focus will be on the optimisation of the Cr/C ratio to suit conditions they are popularly subjected to in local industry.

1.2 Problem Statement

High-chromium cast irons (HCCIs) are widely used in industries requiring high hardness, wear resistance, and corrosion resistance, such as mining, milling, petrochemical processing, and marine environments (Abd El-Aziz et al., 2015). These properties are largely determined by the microstructure, which consists of a matrix phase reinforced by hard carbides such as M_3C, M_7C_3, $M_{23}C_6$, and M_3C_2, each forming based on the chemical composition and processing conditions (Bedolla-Jacuinde et al., 2005). The Cr/C ratio is a critical factor in this, as it governs carbide formation, shape, size, and dispersion within the matrix, which in turn dictates hardness, wear performance, and corrosion resistance. Despite extensive research on HCCIs, the mechanism by which the Cr/C ratio influences microstructural evolution and, consequently, material performance remains inadequately understood. A deeper understanding of this mechanism is essential for optimising alloy design, ensuring that the Cr/C ratio is tailored to achieve the best combination of hardness, wear resistance, and corrosion protection from a microstructural perspective.

The Cr/C ratio directly affects carbide type, morphology, and distribution, leading to significant variations in mechanical and environmental durability. A lower Cr/C ratio increases carbide volume, which enhances hardness and wear resistance, but also leads to coarser, interconnected carbides, making the material more brittle and prone to fracture (Guo et al., 2021). Conversely, a higher Cr/C ratio results in fewer but finer carbides, improving toughness but lowering wear

resistance (Wang et al., 2018). The shape and size of carbides also play a key role; for example, elongated, rod-like carbides enhance wear resistance but increase brittleness, whereas finer, evenly dispersed carbides improve the balance between strength and ductility (Wang et al., 2018). Additionally, the microstructure influences corrosion behaviour, where higher carbide fractions reduce the reactive surface area, improving passive film stability, but larger, interconnected carbides can act as localised corrosion sites, accelerating degradation in aggressive environments (Gong et al., 2023). Understanding how the Cr/C ratio controls these microstructural features and their effects on material performance is crucial for optimising HCCIs for industrial use.

Despite this, existing research often isolates the effects of Cr and C individually, rather than considering their combined influence through the Cr/C ratio. Additionally, the interaction between the Cr/C ratio and cooling rate during solidification is not well understood, even though solidification kinetics play a crucial role in determining carbide morphology, size, and segregation patterns (Panichkin et al., 2023). Faster cooling typically refines carbides, improving toughness, while slower cooling allows carbides to coarsen, increasing brittleness (Panichkin et al., 2023). However, how the combined effects of the Cr/C ratio and cooling conditions shape the final microstructure and mechanical properties remains unclear, limiting the ability to predict and optimise alloy behaviour in real-world applications. Heat treatment further complicates this relationship by modifying carbide morphology, often promoting secondary carbide precipitation that can deplete chromium from the matrix, affecting passivation and corrosion resistance (Zhang et al., 2022). The lack of a clear understanding of how the Cr/C ratio, cooling rates, and heat treatment collectively influence carbide formation and stability presents a major challenge in optimising HCCI processing and alloy design.

In South Africa, HCCIs are widely used in mining, processing, and marine industries, where components such as mill liners, crusher hammers, slurry pump impellers, and valves must withstand abrasive wear, high-impact forces, and corrosive conditions (Singh, 2016). The industry requires alloys that can perform well under acidic, alkaline, and chloride-rich conditions while maintaining structural integrity. However, poor microstructural control due to improper Cr/C ratio selection often leads to premature material failure, resulting in high maintenance costs, equipment breakdowns, and productivity losses. To enhance reliability, durability, and service life, ultimately decreasing downtime frequency, duration, and cost, it is essential to develop an alloy design strategy that optimises the Cr/C ratio based on its microstructural effects. Despite the critical role of HCCIs in these environments, their

performance is frequently compromised due to an inadequate understanding of how the Cr/C ratio affects microstructural evolution, leading to the failures experienced in service. Existing research often isolates the roles of chromium and carbon, rather than addressing their combined influence on carbide formation, a key factor controlling carbide morphology, type, size, and shape, which in turn governs corrosion resistance and mechanical properties under varying processing conditions. This lack of clarity limits the ability to design alloys that meet the durability and performance demands of South African industries. By understanding how the Cr/C ratio influences carbide morphology and distribution and how this translates into mechanical and corrosion behaviour, industries can tailor HCCI compositions for specific applications, improving material performance and operational efficiency.

This research primarily aims to investigate how variations in the Cr/C ratio influence the microstructural evolution, hardness, wear behaviour, and corrosion resistance of hypoeutectic HCCIs in the as-cast condition. The study focuses on understanding how the Cr/C ratio governs the formation, size, shape, and distribution of carbides within the matrix and how these microstructural features affect the performance of the alloy. In addition, selected heat treatments are applied to evaluate whether further improvements in mechanical and corrosion properties can be achieved. The findings will contribute to the optimisation of alloy composition, cooling conditions, and heat treatment parameters, ensuring that HCCIs achieve the best possible balance of hardness, wear resistance, and corrosion resistance for industrial applications.

1.3 Research Questions

1. How does the Cr/C ratio affect the microstructure of HCCIs?
2. How does the Cr/C ratio affect the hardness and fracture toughness of HCCIs?
3. How does the resulting microstructure affect the wear resistance of HCCIs?
4. How does the resulting microstructure affect the corrosion resistance of the HCCIs?

1.4 Aims and Objectives

The aim of the research is to study the influence of Cr/C ratio on the microstructural, mechanical, wear, and corrosion properties of hypoeutectic HCCIs.

The objectives are:

1. To determine the effects of Cr/C ratio on the solidification behaviour and resulting microstructural constituents of hypoeutectic HCCIs, using computational analysis of cooling curves and experimental characterisation through scanning electron

microscopy (SEM) with energy dispersive spectroscopy (EDS) and x-ray diffraction (XRD).

2. To evaluate the influence of Cr/C ratio on the hardness and fracture toughness of hypoeutectic HCCIs, using standard mechanical testing methods such as Vickers and Brinell hardness testing and Charpy impact testing.
3. To assess how Cr/C ratio-induced microstructural variations affect the wear of hypoeutectic HCCIs by conducting pin-on-disc wear tests.
4. To assess how the Cr/C ratio-induced microstructural variations affect the corrosion performance of hypoeutectic HCCIs by conducting electrochemical corrosion testing under simulated South African industrial conditions.

1.5 Research Motivation

The South African national economy is largely reliant on its mining and manufacturing as critical contributors. The country is amongst the largest contributors of minerals such as gold, platinum, and iron ore in the world (Mulaba-Bafubiandi & Singh, 2018; Usman et al., 2019; Esau et al., 2023). High chrome cast irons are used in areas that require materials with high abrasion resistance and highly corrosive areas because of their reputable hardness and desirable corrosion resistance. High chrome cast irons are also relatively affordable for a wide variety of uses, rendering them pivotal in the construction of the earth mining, petrochemical, and milling industries. The optimisation of the alloys is thus critical to ensure that the equipment in these applications can withstand harsh environments for longer periods without the need for frequent repairs and additional maintenance costs.

In mining, these environments typically simulate abrasive slurries with quartz particles in low-pH mine water containing sulphates (SO_4^{2-}), chlorides (Cl^-), and elevated temperatures, while in petrochemical applications, equipment is exposed to chloride-rich solutions saturated with carbon dioxide (CO_2) and hydrogen sulphide (H_2S) gases at high temperatures and low pH, replicating sour service conditions in refineries and chemical plants (Mutileni et al., 2023). Additionally, highly alkaline environments such as those found in gold tailings neutralised with lime ($Ca(OH)_2$) or caustic cleaning operations using sodium hydroxide (NaOH) in petrochemical refineries are also prevalent, exposing materials to pH levels above 12 and creating aggressive corrosion conditions that demand equally robust alloy performance (Mutimutema et al., 2022). Given this wide range of corrosive and abrasive conditions, the performance of high chrome cast irons (HCCIs) must be carefully matched to the specific environments in which they are applied. However, in addition to corrosion, equipment in these

sectors is also subject to extreme mechanical demands such as impact and abrasive wear, which further complicates material selection and highlights the need for tailored alloy solutions.

The difficulty with HCCIs is that they are sought for great abrasion and wear resistance, yet there is little customisation for each of the various settings in which they are used. Because HCCIs are used in a variety of industries, each with its own set of conditions and elements that influence the mechanism of failures in the material, tailoring is critical to the optimisation of alloy utilisation. This can be achieved by applying minor modifications in the composition of the alloys, resulting in enormous differences that can be customised for the diverse situations. The mechanical properties of the alloy are directly related to the microstructure, particularly the type and distribution of carbides as well as the properties of the matrix. There is a need to understand how the composition affects each of the properties of the alloy, particularly the microstructure, and how its features affect the final material's integrity. Studying how the Cr/C ratio would be the first step towards optimising the alloy to suit the local mining conditions in South Africa.

Additionally, components in mining and mineral processing are subjected to high levels of impact loads and abrasive wear. While fracture toughness affects the capacity of HCCIs to endure mechanical shocks without cracking, hardness is a crucial factor in the ability of HCCI resistance to wear. The optimal Cr/C ratio can improve mechanical properties such as hardness and impact toughness. For instance, a combination of 2.7 wt.% C and 18 wt.% Cr, followed by specific heat treatments, results in high hardness of 62 HRC and good impact toughness of 8.2 J/cm², as demonstrated by Gong et al. (2017). In addition, Liu et al. (2025) report that the optimal Cr/C ratios, which are in the range of 8 to 11, provide the best abrasion resistance in high chromium white cast iron. This is especially important in deep-level mining activities in South Africa, where components are exposed to abrasive and impact conditions. By lowering maintenance expenses and downtime, optimising the Cr/C ratio for both attributes can increase operational effectiveness. Furthermore, the enhanced wear and corrosion resistance of optimised hypoeutectic HCCIs is essential for industries like petrochemicals, where machinery is subjected to both high temperatures and chemically harsh media.

Furthermore, in South Africa, in the petrochemical industries, where companies like SASOL and other refineries play an important role in the energy and chemical processing industry, the reliability and durability of processing equipment are crucial factors to the efficiency of the plants. Equipment in these harsh environments is prone to failure by wear and corrosion, which

leads to frequent downtime, safety issues, and environmental hazards. Guo et al. (2021) and Yang & Li (2012) emphasise on how the wear resistance of high chrome cast iron is directly affected by the Cr/C ratio. Higher carbon content generally increases wear resistance due to the formation of more and larger carbides, which are harder and more wear-resistant; however, excessive carbon can lead to brittleness and reduced impact toughness (Guo et al., 2021). By finding the critical Cr/C ratio, enabling the best hypoeutectic HCCIs characteristic of the custom wear and corrosion properties to the local environment pH and experienced chemical reactions, this would significantly increase the performance of the equipment and service life.

Despite the widespread use of hypoeutectic HCCIs in these demanding environments, limited studies have focused on the specific influence of the Cr/C ratio on microstructural development and performance, particularly in hypoeutectic compositions used in local applications. Much of the existing literature investigates the roles of chromium and carbon independently, without fully examining how their combined ratio affects carbide formation, morphology, and phase distribution. Although several studies have explored the influence of Cr/C ratio on phase stability and mechanical properties (Bedolla-Jacuinde et al., 2005; Ortega-Cubillos et al., 2015; Stachowiak et al., 2015; Abdel-Aziz et al., 2017), and others have studied the effect of cooling rates on carbide distribution (Zhang et al., 2018; Sasaguri et al., 2019; Goto et al., 2023; Panichkin et al., 2023), few have integrated these factors into a unified framework. Furthermore, most studies either focus on the as-cast condition or evaluate heat treatment effects in isolation, without considering how the solidification microstructure, shaped by the Cr/C ratio, interacts with subsequent thermal processing (Ai et al., 2011; Karantzalis et al., 2009; Zhang et al., 2022). This research is therefore motivated by the need to address this practical and academic gap. By investigating how controlled variations in the Cr/C ratio influence solidification behaviour, microstructural evolution, and resulting mechanical and corrosion properties of hypoeutectic HCCIs, this study seeks to provide a clearer understanding of alloy performance under real-world South African service conditions. The findings aim to inform the design of tailored HCCI compositions that enhance equipment performance, extend service life, and reduce operational downtime, ultimately supporting improved efficiency and reliability in critical industrial applications.

1.6 Structure of Dissertation

Chapter 1: Introduction. An introduction to the topic, a statement about the gaps in the current literature, a problem statement, and a list of specific research objectives that, if met, will enable a contribution to this field of knowledge are all included in Chapter 1.

Chapter 2: Literature Review. This chapter contains a detailed summary of the previous work that has been done on HCCIs. This includes summarised published work by Bedolla-Jacuinde et al. (2005); Karantzalis et al. (2009); Wiengmoon et al. (2011); and Ngqase & Pan (2020) on popularly studied domains of HCCIs. The literature review is an extensive review on the effect of composition on the mechanical properties of HCCIs, such as corrosion, wear, and hardness.

Chapter 3: Materials and Methods. In this chapter, the details of the computational and experimental approaches employed in this work are presented. A discussion of the many testing methods, analytical methods, testing standards, and equipment needed to accomplish each goal is also included in this section.

Chapter 4: The effects of Cr/C ratio on the microstructural properties of hypoeutectic HCCIs. In this section of the dissertation, objective one, "Determine the effects of Cr/C ratio on the microstructural properties of HCCIs," is addressed through computational analysis, including ThermoCalc and analysis of the cooling curve characteristics on the solidification behaviour of the resulting microstructure and presentation of results acquired from experiments and an extensive analysis of the acquired results from microstructural analyses.

Chapter 5: The effects of Cr/C ratio on the hardness and fracture toughness of hypoeutectic HCCIs. The third objective of the work requires discussion on how the Cr/C ratio affects the hardness and fracture toughness properties of HCCIs. The analysis and discussion are presented in detail in this chapter, informed by the impact testing and hardness experimental work done.

Chapter 6: The influence of microstructural constituents on the wear properties of hypoeutectic HCCIs. The results and discussion in this chapter will provide a detailed explanation of how the microstructure influences the wear and corrosion properties of HCCIs through analysis of the results acquired during the wear and corrosion experiments performed.

Chapter 7: The influence of microstructural constituents on the corrosion properties of hypoeutectic HCCIs. The results and discussion in this chapter will provide a detailed explanation of how the microstructure influences the corrosion properties of HCCIs. This will be done through analysis of the results acquired during corrosion experiments performed.

Chapter 8: Conclusions and recommendations. This chapter summarises the main ideas of the work done with respect to previous work done by other researchers, providing a summative conclusion to the detailed discussions from the dissertation. Furthermore, recommendations on future work to be done on HCCIs are also done here.

Chapter 2: Literature Review

2.1 Introduction

This paper provides a comprehensive review of the process in the manufacturing of high chromium cast iron. Of particular note is the vital role of the ratio of Cr/C, the cooling curve of solidification, and the resultant impact on mechanical properties, particularly wear resistance, hardness, toughness, and corrosion performance. HCCIs are normally applied in various industry applications such as mining, petroleum, or grinding because of their dominant wear-resistant characteristics and resistance to corrosion. The optimisation of the Cr/C ratio in the alloys influences the formation of carbides and the existence of an austenitic matrix, which largely governs the final microstructure and hence the overall performance of the material.

The composition of alloying elements plays a key role in influencing the cooling curve, ultimately affecting phase nucleation and growth during casting. Since different cooling rates lead to distinct microstructural features, the distribution and morphology of hard carbides vary accordingly. These variations directly impact the mechanical properties of high-chromium cast irons (HCCIs), which, in turn, determine their suitability for specific applications. Chapter 2 is structured to provide a thorough exploration of these aspects, beginning in Section 2.2 with a discussion on the composition and industrial relevance of HCCIs. This section offers background information and establishes motivation for the study. Section 2.3 follows with an overview of the microstructure, particularly emphasising the role of carbides in the mechanical performance of the alloy. The significance of solidification cooling curves and their role in understanding phase transformations during casting is explored in Section 2.4. In Section 2.5, the effects of the Cr/C ratio on microstructure are examined, while also addressing the combined influence of chromium and carbon. Thermodynamic and kinetic theories related to phase formation are covered in Section 2.6. Moving forward, Sections 2.7 and 2.8 discuss mechanical properties, including methods of evaluation and the impact of heat treatment on HCCIs. To bridge the knowledge gaps, Section 2.9 outlines areas requiring further research, setting the stage for the present study. Lastly, Section 2.10 wraps up the chapter with a summary of key findings.

2.2 High Chrome Cast Iron (HCCI): Composition and Industrial Relevance

High-chrome cast iron (HCCI) has a unique chemical composition that grants it great resistance to wear and corrosion under severe use or exposure conditions. Hypoeutectic HCCIs are a type of cast iron with a typical composition of between 11 and 30 wt.% Cr and between 1.8 and 3.6

wt.% C. It may contain minor additions of other elements, significant being molybdenum, manganese, silicon, and trace vanadium (Bedolla-Jacuinde et al., 2005; Ngqase & Pan, 2020; Sudhakar et al., 2022). This particular composition of the elements initiates the formation of numerous complex carbides during solidification, which impacts heavily on the overall mechanical properties of the alloy. The proper addition of alloying elements is crucial for the proper application of the material to support them against failure and wear and for corrosion resistance. At the same time, it is necessary that the alloy be adjusted so that it can meet the needs of diverse industrial applications in terms of toughness and hardness.

The chemical composition of the HCCI is very carefully engineered to give chromium the master role over all alloying elements. In addition to chromium and carbon, molybdenum contributes to improvements in carbide phase stability and corrosion resistance (Scandian et al., 2009; Du et al., 2024). These elements interact favourably during solidification to allow easy formation of hard chromium-rich carbides within the austenite matrix. The resulting microstructure is beneficial for applications necessitating wear resistance and corrosive environments. Therefore, it lends importance to the setting of precise control on the chemical composition, since minor variations may affect the phase stability and carbide morphology greatly. This microstructural control translates directly into performance under harsh conditions, which explains the wide adoption of HCCI across various South African industries.

High-chromium cast irons in South Africa are widely utilised in industries such as mining, petrochemical, and milling due to their exceptional performance in harsh operational conditions (Tang et al., 2011; Goto et al., 2023; Panichkin et al., 2023). In such demanding environments, materials must possess the ability to endure extreme mechanical and chemical stresses. Conventional steel, when exposed to abrasive particles and high loads, erodes rapidly (Islam et al., 2015). In contrast, HCCI, with its robust chemical composition and superior microstructural properties, provides a more durable solution for such applications.

In the petrochemical industry, HCCI is extensively used in critical infrastructure components such as valves and piping, which are exposed to aggressive chemically reactive media. The high chromium content of HCCI enables the rapid formation of a protective oxide layer, ensuring metastable passivation that enhances resistance to internal temperature fluctuations and prevents rapid degradation (Tang et al., 2009; Akinribide et al., 2022; Goto et al., 2023). This dual capability of withstanding both mechanical and chemical challenges makes HCCI a crucial material for applications requiring reliability and durability. Consequently, its use in the

petrochemical sector highlights its adaptability across various environmental conditions. The advantage of HCCIs is their diverse applicability in different environments beyond just chemical resistance. The wear and impact performance of HCCIs also play a major role in heavy-duty operations.

Another key application of HCCI is in milling operations, where wear resistance and impact toughness are critical. Milling components manufactured from HCCI experience continuous mechanical stress and abrasive wear, necessitating superior frictional properties, hardness, and ductility (Guitar, Nayak, et al., 2020; He et al., 2024; Ji et al., 2024). The fine dispersion of hard carbides within the microstructure of HCCI plays a significant role in enhancing wear resistance (Chung et al., 2013). This microstructural advantage extends the service life of milling components, reducing maintenance requirements, minimising unscheduled shutdowns, and ultimately improving operational productivity.

The superior durability of HCCI in extreme environments further demonstrates its exceptional performance across a range of industries. Jain et al. (2021), Trepczyńska-Łent et al. (2021), and Zhao et al. (2024) report that this alloy is particularly well-suited for settings where materials must endure high temperatures, corrosive atmospheres, and severe abrasive wear. The extended lifespan of HCCI components and the reduction in the need for frequent replacements contribute to significant cost savings. From a financial perspective, this makes HCCI a viable investment for industries requiring robust, long-lasting materials that support seamless operational efficiency.

HCCI also enhances operational reliability in extreme working conditions, from exposure to corrosive gases to heavy mechanical loads. Equipment manufactured from HCCI is less likely to fail under harsh conditions, thereby reducing the risk of catastrophic breakdowns, improving safety, and avoiding costly downtime (Yang & Li, 2012; Guo et al., 2021). The unique chemical composition of the alloy offers superior protection against surface degradation and prolonged exposure to aggressive environmental factors (Wu et al., 2025). This reliability is particularly vital in industries where continuous operation is necessary, and interruptions result in substantial financial losses and safety hazards. Furthermore, HCCI can be processed and altered through various techniques, including casting, heat treatment, and surface modification through compositional manipulation, to enhance its properties for specific industrial applications. The ability to tailor the microstructure of HCCIs through controlled cooling rates and heat treatment allows for the optimisation of the carbide morphology, striking a balance

between hardness and toughness (Abdel-Aziz et al., 2017; Guitar et al., 2020). This processing versatility ensures that HCCI can be adapted to meet the stringent demands of diverse industrial environments. In addition to its technical benefits, HCCI is a sustainable material due to its longevity and low maintenance requirements, which significantly reduces the need for frequent replacements (Goto et al., 2023; Panichkin, Kenzhegulov, et al., 2023). This contributes to lower raw material consumption, energy usage, and waste generation, aligning with environmental sustainability goals. Moreover, the recyclability of cast iron further enhances its environmental viability, making it a responsible choice for industries committed to resource efficiency and long-term sustainability (Mitterpach et al., 2017; Monteleone et al., 2024).

In conclusion, the unique chemical composition of HCCI, characterised by high chromium, carbon, and other key alloying elements, underpins its outstanding performance in highly demanding South African industrial applications. The resulting microstructure provides excellent wear resistance, hardness, and corrosion protection. Additionally, the ability of the alloy to adapt in processing and its cost-effectiveness reinforce its importance in modern industrial applications (He et al., 2024; Ji et al., 2024). As industries continue to evolve, focusing on robust and durable materials, HCCI remains indispensable for applications that demand high wear resistance, corrosion protection, and mechanical strength, while also aligning with economic and sustainability considerations.

2.3 Microstructural Characteristics of HCCIs

The formation of an austenitic matrix interspersed with primary dendrites and eutectic mixtures containing various hard carbides in high-chromium cast iron (HCCI) is a result of its complex solidification behaviour and superior mechanical properties. The austenitic matrix has a face-centred cubic (FCC) structure, which enhances the ductility and toughness of the alloy. The dendritic morphology, in contrast, arises due to the rapid growth of primary austenite as the temperature falls below the liquidus point (Pokusová et al., 2016; Nayak et al., 2022; Salawu et al., 2022). A combination of these microstructural features is crucial in achieving an optimal balance between hardness and toughness in HCCI.

The cooling kinetics during solidification play a significant role in determining the morphology of the microstructure. Higher cooling rates promote the formation of a finer dendritic structure with a more uniform eutectic carbide distribution, whereas slower cooling rates result in coarser microstructures with potential porosity and segregation. Chen et al., (2006) and Huang et al., (2019). The kinetics of nucleation and growth during solidification influence the final size and

distribution of these microstructural features. The incomplete liquid-to-solid phase transformation leads to a eutectic reaction, producing a mixture of austenite and a hard carbide phase, which is fundamental in enhancing the wear resistance of HCCI.

Cui et al. (2016), Li et al. (2016), and Oanh & Viet (2020) discuss the types of carbides typically found in hypoeutectic HCCIs. Among the commonly occurring carbides, M_7C_3 and $M_{23}C_6$ are the most prominent, each exhibiting distinct morphologies and distributions. M_7C_3 carbides typically form irregular blocky or network-like structures within the austenitic matrix, imparting exceptional hardness and high resistance to abrasion. In contrast, $M_{23}C_6$ carbides are typically smaller, finer, and rounder in morphology and play a crucial role in enhancing wear resistance while improving toughness by aiding in crack arrest during impact loading (Xu et al., 2023). However, excessive volume of secondary carbides can have a negative effect on the toughness of the material, causing it to fracture in a brittle manner. Both carbide phases contribute significantly to the overall mechanical strength of the alloy. The carbides present in HCCI significantly contribute to its mechanical performance due to their exceptional hardness, resistance to corrosion, and wear resistance. (Yang & Li, 2012; Guo et al., 2021).

The control of these microstructural properties is primarily achieved by adjusting the chemical composition of the alloy. Elements such as molybdenum (Mo), silicon (Si), and vanadium (V) influence carbide stability and formation kinetics by segregating during solidification, thereby promoting specific carbide types (Mampuru et al., 2016; Ngqase & Pan, 2020; Liu et al., 2020). Mo encourages the formation of M_6C and $M_{23}C_6$ carbides, which enhance secondary hardening and toughness while refining the morphology of M_7C_3 carbides. Si promotes the formation of M_7C_3 carbides, increasing their volume fraction and refining their distribution, improving wear resistance but potentially reducing toughness. Vanadium, being a strong carbide former, favours the formation of MC carbides, which are extremely hard and contribute significantly to wear resistance while also refining M_7C_3 carbides to enhance toughness and crack resistance. Ni primarily stabilises the austenitic matrix, improving toughness and corrosion resistance, while Cu acts as a solid-solution strengthener, refining the microstructure and enhancing mechanical properties without significantly affecting carbide formation. The combined effects of these elements allow for precise control of the microstructure, optimising the balance between hardness, strength, and durability in industrial applications (Mampuru et al., 2016; Ngqase & Pan, 2020; Liu et al., 2020). Cooling rate continues to be a key factor in shaping the microstructure of HCCIs. Faster cooling leads to finer dendritic structures and a more homogeneous carbide distribution, improving overall mechanical properties (Panichkin et al.,

2023; Du et al., 2024). Conversely, slower cooling facilitates the formation of coarser carbides and promotes segregation, which may reduce toughness. However, subsequent heat treatments and tempering can modify these microstructural features to achieve a balance between hardness and impact resistance, refining carbide morphology and matrix characteristics.

The synergy between the austenitic matrix and carbides is crucial for the mechanical behaviour of HCCIs under stress. The hard carbides act as reinforcements within the softer matrix, effectively resisting plastic deformation and wear (Cui et al., 2016; Goto et al., 2023; Panichkin, Kenzhegulov, et al., 2023). The combination of hard and soft phases results in a structure that provides excellent resistance to abrasion while maintaining resilience against impact loading. The effectiveness of this reinforcement is largely dependent on the size, morphology, and spatial distribution of the carbides, which are in turn governed by the chemical composition and thermal history of the alloy. The inherent complexity of HCCI microstructures necessitates advanced characterisation techniques to evaluate their formation, evolution, and influence on mechanical properties. Techniques such as scanning electron microscopy (SEM) and energy-dispersive spectroscopy (EDS) enable researchers to analyse carbide morphology and matrix characteristics in detail (Bedolla-Jacuinde et al., 2005; Wiengmoon et al., 2005; Salawu et al., 2022). These analytical tools provide insights into the conditions that influence microstructural development, forming the basis for alloy design modifications aimed at improving performance in demanding applications.

In summary, the microstructure of HCCI is defined by the interplay between the austenitic matrix and various carbide phases, particularly M_7C_3 and $M_{23}C_6$. The formation of these microstructural constituents is governed by alloy composition, cooling rate, and heat treatment, all of which determine the final mechanical properties of the alloy (Boldyrev et al., 2023; Gundlach and Tartaglia, 2024). By optimising these parameters, HCCIs can be tailored for specific industrial applications, offering an exceptional balance of wear resistance, hardness, and toughness. The intricate relationship between microstructural features and the resulting mechanical characteristics remains central to the continued development and enhancement of HCCI in modern manufacturing.

2.4 Solidification and Cooling Curve Analysis of HCCIs

The solidification process of HCCI is complex, as it directly influences the final microstructure and mechanical properties of the material. According to Doğan et al. (1997) and Bedolla-Jacuinde (2001), for hypoeutectic HCCIs, the solidification process follows the below process:

The beginning of the solidification process is marked by the nucleation and development of primary austenite (γ) dendrites as the temperature falls below the liquidus point. This results from the lower carbon content of the hypoeutectic HCCIs than the eutectic composition, which first forms austenite from the melt. These dendrites keep growing as cooling proceeds, draining the surrounding liquid of chromium and carbon. Once the temperature reaches the eutectic point, the remaining liquid undergoes a eutectic transformation, solidifying into a mixture of austenite and primary and eutectic M_7C_3 carbides. This eutectic phase forms in the interdendritic regions. The final microstructure consists of a eutectic carbide network of carbides embedded in primary austenite dendrites; the solidification rate controls the distribution and form of these phases. Additionally, Chen et al. (2006) and Huang et al. (2019) report that slower cooling can lead to coarser carbide networks and enhanced segregation, while faster cooling rates refine the dendritic structure and generate finer, more uniformly dispersed carbides, hence improving mechanical characteristics. They add that higher cooling rates promote the formation of a finer dendritic structure with a more uniform eutectic carbide distribution, whereas slower cooling rates result in coarser microstructures with potential porosity and segregation. The kinetics of nucleation and growth during solidification influence the final size and distribution of these microstructural features. The incomplete liquid-to-solid phase transformation leads to a eutectic reaction, producing a mixture of austenite and a hard carbide phase, which is fundamental in enhancing the wear resistance of HCCI. When studying the microstructure under the SEM, the austenite dendrites usually show as the light phase, while the carbides show as the dark phase due to differences in their atomic number contrast (Z-contrast) and electron backscatter efficiency (Purevdorj et al., 2024). Austenite, being rich in iron (Fe) and nickel (Ni), has a higher average atomic number than carbides, which contain elements like chromium (Cr) and carbon (C). Since higher atomic number regions backscatter more electrons, they appear brighter in backscattered electron (BSE) imaging. In contrast, carbides, which have a lower overall atomic number and different electron density, scatter fewer electrons and thus appear darker in SEM images, as shown by Bedolla-Jacuinde et al., (2005) in Figure 2.1.

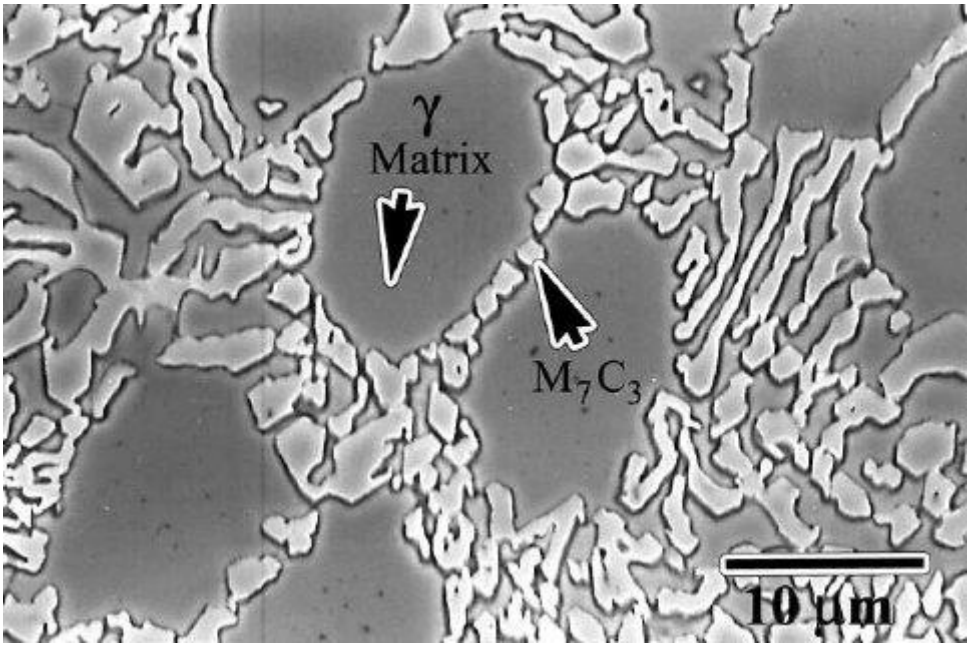

Figure 2.1: Typical SEM image contrasting on the matrix and the carbides(Bedolla-Jacuinde et al., 2005).

By analysing the cooling curve, key factors such as the onset of solidification, latent heat release, and microstructural changes over time can be understood (Yang & Li, 2012; Gong et al., 2017). The rate at which heat is removed from the melt also plays a crucial role in determining microstructural characteristics such as dendrite arm spacing and carbide distribution, both of which are essential for achieving the desired mechanical properties of HCCI (Xia et al., 2011; Zhao et al., 2013; Wan et al., 2021). The cooling rate is a significant factor in shaping the microstructure, affecting the size, morphology, and distribution of key features within the alloy. Faster cooling rates promote a higher nucleation rate while limiting dendritic arm growth, resulting in a finer dendritic network with small secondary dendrite arm spacing (Stann et al., 2021; Wan et al., 2021; Yulianto et al., 2021). This microstructural refinement enhances mechanical properties such as strength and wear resistance. Conversely, slower cooling rates allow for extended dendrite growth, leading to coarser microstructures with larger dendrite arm spacing, which can reduce the overall mechanical performance of the alloy (Xia et al., 2011; Zhao et al., 2013; Wan et al., 2021). Experimental studies confirm that secondary dendrite arm spacing is inversely proportional to the cooling rate, emphasising the need for precise thermal control during casting (Panichkin et al., 2023; Goto et al., 2023; Du et al., 2024). Additionally, the level of undercooling, where the temperature of the melt drops below the equilibrium liquidus temperature, influences the number of nucleation sites. A higher undercooling level promotes fine microstructures by increasing nucleation density, whereas a

lower undercooling level results in coarser microstructures due to slower phase growth (Kopycinski et al., 2014; Wan et al., 2021; Siekaniec et al., 2022).

Another key aspect influenced by the cooling rate is carbide formation and distribution. During solidification, solute elements such as chromium and carbon partition between the growing austenite and the remaining liquid, leading to carbide precipitation. This solute segregation determines the formation of M_7C_3 and $M_{23}C_6$ carbides, which play a significant role in the hardness and wear resistance of the alloy (Ma et al., 2006; Scandian et al., 2009; Boldyrev, 2023). Rapid cooling reduces diffusion time, promoting the formation of finely distributed carbides that improve mechanical performance, such as hardness, by hindering crack propagation. On the other hand, slower cooling allows for prolonged diffusion, resulting in the growth of coarser carbides, which can increase stress concentration points and reduce toughness (Baharudin et al., 2022; Strobl & Haubner, 2020; Yulianto et al., 2021). Proper control of the cooling rate ensures a carbide morphology that balances wear resistance with mechanical stability.

The cooling curve also provides insights into phase transformations that occur during solidification. As the alloy cools, latent heat is released at nucleation sites, slowing the cooling rate and forming thermal arrests, which appear as plateaus or inflection points in the cooling curve (Guo et al., 2021; He et al., 2024; Zhao et al., 2024). The magnitude of these thermal arrests reflects the kinetics of solid-phase transformations and microstructural evolution. A strong thermal arrest suggests a high volume fraction of primary phases, whereas rapid cooling with minimal latent heat release results in finer microstructures. The eutectic reaction, where austenite and carbide phases crystallise simultaneously, is also influenced by cooling rates. Faster cooling rates promote a fine eutectic network that enhances wear resistance and impact toughness, while slower cooling results in coarser eutectic structures that may reduce mechanical performance such as corrosion resistance. By carefully analysing the cooling curve, it is possible to control the eutectic reaction to ensure a uniform phase distribution and improve material durability through manipulation of compositions (Ma et al., 2006; Du et al., 2024; Guo et al., 2021; Panichkin et al., 2023).

Non-equilibrium solidification is another important consideration in the formation of HCCI microstructures, particularly under rapid cooling conditions where limited diffusion leads to solute segregation and the formation of metastable phases. These phases can enhance hardness and wear resistance, but they may also reduce ductility and toughness when forming continuous

networks that act as stress concentrators (Yulianto et al., 2021; Boldyrev, 2023; Gundlach and Tartaglia, 2024). The cooling curve helps identify optimal temperature ranges for controlling metastable phase formation, making it possible to design heat treatment processes that either retain or suppress these phases depending on the specific application requirements.

Beyond its role in understanding microstructural development, the cooling curve is also valuable in industrial applications where optimising cooling rates can lead to significant improvements in component consistency and mechanical performance. By refining solidification processes, manufacturers can reduce material waste and limit the need for extensive post-casting treatments. The insights gained from cooling curve analysis can also enhance simulation models for casting operations, enabling more efficient and cost-effective production methods. Advanced thermal analysis techniques, such as differential thermal analysis (DTA) and thermocouple-based monitoring, allow for real-time tracking of cooling behaviour, making it easier to predict and control microstructural evolution. These methods provide manufacturers with better control over cooling rates, allowing them to develop HCCI components with enhanced wear resistance, strength, and overall durability.

2.5 Influence of Cr/C Ratio on the Microstructural Evolution of HCCIs

The microstructural evolution of high-chrome cast iron is significantly influenced by variations in the chromium-to-carbon (Cr/C) ratio, which directly affects the formation of different phases and the distribution of carbides. Studies have shown that changes in the Cr/C ratio result in substantial modifications to the matrix composition, carbide morphology, and mechanical properties of HCCI. When the chromium content is higher than the carbon content, the matrix is more stabilised as austenite, leading to the formation of complex chromium-rich carbides. In contrast, a lower Cr/C ratio, where carbon content is relatively higher, promotes the formation of larger and more extensive carbide microstructure (Kootsookos & Gates, 2004; Guo et al., 2021). The Cr/C ratio is a key factor in balancing the volume fraction, size, shape, and distribution of carbides within the matrix, which ultimately determines the hardness, wear resistance, and toughness of the alloy (Guo et al., 2021). Achieving the optimal Cr/C ratio is critical for fine-tuning HCCI to meet the demands of abrasive and corrosive environments, ensuring a balance between strength and durability.

The interaction between chromium and carbon plays a crucial role in the nucleation and growth of carbides during solidification. When these elements are present in the right proportions, they react to form a variety of hard carbides, such as M_7C_3 and $M_{23}C_6$, which significantly improve

wear resistance. Research dating back by Inthidech & Matsubara (2008) and Wiengmoon et al., (2011)to recent studies by Lou et al. (2016), Du et al. (2024), and Liu et al., (2025) have shown that a higher Cr/C ratio results in finer carbides that are evenly distributed throughout the microstructure, reducing stress concentration sites and improving crack resistance. This effect occurs because chromium has a strong affinity for carbide formation, while carbon serves as a fundamental building block for these phases. As a result, a well-controlled Cr/C ratio promotes a fine eutectic structure, which enhances mechanical performance by improving hardness, strength, and impact resistance. The balance between Cr and C not only improves wear properties but also ensures that the matrix and carbides work together, preventing excessive brittleness.

The solidification behaviour of HCCI is also modified by changes in the Cr/C ratio, which influences the final microstructure. In alloys with a high Cr/C ratio, primary austenite forms at a higher temperature, followed by eutectic reactions that enrich the remaining liquid with carbon, leading to the formation of secondary carbides. This microstructural network enhances abrasion and impact resistance, as shown in studies by Ma et al., (2011) early on and later reinforced by Ortega-Cubillos et al., (2015) and Guo et al. (2021), and the presence of high chromium concentrations can also lead to the formation of metastable phases, which later transform into stable, hard carbides upon cooling. A higher Cr/C ratio typically results in a more uniform carbide distribution, improving structural integrity, whereas a lower Cr/C ratio often leads to coarse and uneven carbide dispersion, increasing local stress concentrations and reducing toughness. Thus, adjusting the Cr/C ratio is essential for tailoring HCCI microstructures to suit specific industrial applications.

Experimental studies have demonstrated that even small changes in the Cr/C ratio can have a significant impact on phase formation and mechanical properties. When the Cr/C ratio drops below a critical threshold, typically around 8, the microstructure becomes coarse, consisting of large carbides within a coarser austenitic matrix, which may lead to reduced wear resistance (Panichkin et al., 2023; Du et al., 2024; Liu et al., 2025). On the other hand, optimised Cr/C ratios produce finer, well-distributed carbides, which enhance mechanical strength. Finely dispersed carbides act as barriers against wear and abrasion, while the matrix retains sufficient ductility to absorb impact energy, improving overall toughness. This highlights the importance of carefully controlling the Cr/C ratio to ensure both phase stability and optimal mechanical performance. Small variations in composition can significantly affect the service life and reliability of HCCI components in harsh industrial environments.

The influence of the Cr/C ratio on carbide morphology has been extensively analysed using scanning electron microscopy (SEM) and energy dispersive spectroscopy (EDS). These techniques allow researchers to examine how variations in the Cr/C ratio affect carbide size, shape, and distribution. Studies by Pourasiabi & Gates (2022) and Liu et al. (2025) show that a higher Cr/C ratio leads to a finer carbide network with a dominating matrix, reducing the risk of stress concentration and crack initiation. Finer carbides improve hardness and wear resistance, as they restrict dislocation movement within the matrix. Conversely, a lower Cr/C ratio results in larger, coarsely distributed carbides, which act as crack initiation sites, reducing impact toughness (Yang et al., 2007; Liu et al., 2025). These findings reinforce the necessity of strict alloy composition control to ensure that the microstructural attributes of HCCI are suitable for heavy-duty applications.

The synergistic effects of chromium and carbon also influence phase stability and transformation kinetics. These elements not only determine carbide type and distribution but also affect the eutectic reaction during solidification. Research by Sasaguri et al. (2019), Oanh & Viet (2020), and Liu et al. (2025) has shown that an optimal Cr/C ratio accelerates eutectic transformation, leading to a finely intermixed microstructure of austenite and carbide phases. Faster eutectic reactions result in more uniform carbide dispersion, improving mechanical strength and minimising segregation effects. However, deviations from the optimal Cr/C ratio slow down the eutectic reaction, increasing microstructural inhomogeneity, which negatively impacts mechanical properties. These findings highlight the importance of maintaining a precise balance between Cr and C to ensure structural integrity and performance.

The Cr/C ratio also affects the response of HCCI to heat treatment processes such as quenching and tempering. Adjusting the Cr/C ratio can refine carbide networks and improve matrix properties, making the material more responsive to thermal treatments. A well-balanced Cr/C ratio during tempering promotes the precipitation of secondary carbides, which enhances toughness without compromising hardness (Ma et al., 2006; Ai et al., 2011; Tang et al., 2017). Conversely, an incorrect Cr/C ratio can lead to the formation of unwanted phases or carbide coarsening, which reduces overall mechanical performance (Tang et al., 2017; Zhang et al., 2022). Therefore, maintaining an optimal Cr/C ratio is crucial not only during solidification but also throughout post-processing treatments.

With the advancement of computational modelling, tools like Thermo-Calc are now being used to predict phase formation and carbide distribution as a function of alloy composition and

cooling rate. Recent studies by Siekaniec et al. (2022) and Sudhakar et al. (2022) have demonstrated how Thermo-Calc can model the relationship between Cr/C ratio and microstructural parameters, allowing for better alloy design and optimisation. By combining experimental data with simulation techniques, researchers can gain a deeper understanding of how chromium and carbon influence microstructural refinement, ultimately improving the wear resistance, hardness, and durability of HCCI in demanding industrial environments.

2.6 Theoretical Framework: Thermodynamic and Kinetic Principles in HCCIs

A comprehensive theoretical framework is necessary for studying HCCIs. Such a framework must cover the fundamentals of both thermodynamics and kinetics as they apply to phase transformations. In essence, processes occurring during solidification in HCCI are determined by the thermodynamics governing the phase-transforming forces, as well as by the atomic rearrangement kinetics. In this context, the state variable of grain boundary energy plays a paramount role in determining the metastability of phases under given temperature and composition conditions. Zhang et al. (2011), and later on Zhang & Yang (2018) and Ware et al. (2020) discuss that grain boundaries in high-chromium cast iron have excess free energy, which encourages grain growth and structural changes, especially during high-temperature treatments. This energy comes from the misalignment of atomic structures at the grain boundaries, making them unstable compared to the grains themselves. During solidification, this energy drives grain coarsening, where smaller grains merge into larger ones to reduce overall boundary area and energy (Flemings, 2005; Zhang et al., 2010). However, grain boundaries can become trapped in metastable states due to factors like composition segregation or the complex geometry of the microstructure. Elements such as chromium (Cr), molybdenum (Mo), and vanadium (V) can segregate at grain boundaries, altering their mobility and stabilising certain boundary structures. Additionally, the presence of carbides at grain boundaries can restrict their movement, slowing down grain growth and affecting the final microstructure. This theoretical framework explains how grain boundary energy influences the solidification kinetics of high-chromium cast iron, controlling the final grain size, carbide distribution, and mechanical properties of the alloy (Zhang et al., 2010; Zhang & Yang, 2018; Ware et al., 2020).

Classical nucleation theory describes the process of new phase formation in the matrix. This theory is also based on thermodynamics, whereby nucleation, per dictionary definition, is thought to occur when the free energy barrier to the formation of any nucleus is overcome

(Siekaniec et al., 2022; Sudhakar et al., 2022). The nucleation of primary austenite and secondary carbides in HCCI, therefore, can be promoted by undercooling, which is itself referred to as the concentration of alloying elements in the chamber, like chromium or carbon. The nucleation rate can be represented as an exponential function of the free energy barrier, where interfacial energy and temperature act as key parameters. Once nucleated, these new phases grow through atomic accretion from the matrix surroundings, a process substantially dominated by diffusion. The kinetics of this growth can be described by diffusion equations combining temperature-dependent atomic mobility. When the nucleation rate and growth rate are coupled together, they provide a clear picture of the phase transformation in HCCI and how microstructure features like dendrite arm spacing and carbide size are controlled by cooling rate and material species (Panichkin et al., 2023; Goto et al., 2023; Boldyrev, 2023).

From the perspective of the complex microstructural evolution of HCCI, diffusion plays an essential role in the transformation stage, particularly when the carbide phase is formed. The carbide phase has been the basic growth in carbon and chromium atoms diffusing into the austenitic parent phase after initial nucleation of carbon components. These diffusion-controlled growth processes in metals can be described in terms of the Fick's laws governing the movement of atomic species driven by concentration gradients (Ernst et al., 2007; Li et al., 2014; Yulianto et al., 2021). High diffusivity following extremely fast cooling is modelled in limited diffusion time and the precipitation of ultra-fine carbides; the diffusion of slower cooling conditions introduces greater atomic mobility, leading to the coarsening of the carbide precipitates (Huang et al., 2019). These diffusion-controlled mechanisms become further complicated by the interactions of additional alloying elements in the alleviation or retardation of atomic diffusion dependent on individual diffusivities or what chemically interacts with the solid matrix. (Geng et al., 2020; Liu et al., 2023). A clear understanding of these subtle but important diffusion phenomena provides a rational basis for predicting and influencing carbide size, shape, and distribution, all critical parameters that determine wear and toughness properties of HCCI.

In HCCI, the interaction between the formation of austenite and the precipitation of carbides has great significance as far as mechanical properties are concerned, as the balance between the two largely determines the mechanical properties. In other words, thermodynamic equilibriums, as prescribed by the phase diagrams, are assumed to be disturbed during fast cooling, leading to nonequilibrium phase transformations that call for a detailed description in kinetics as well as the equilibrium state. The integration of thermodynamics and appropriate

kinetic models becomes the backbone of contemporary alloy design and processing in HCCI. The "first cut" done by the phase diagram analysis (Figure 2.2) builds the centric tool in understanding Fe–Cr–C, the multimodal systems that undergird the behaviour of HCCI.

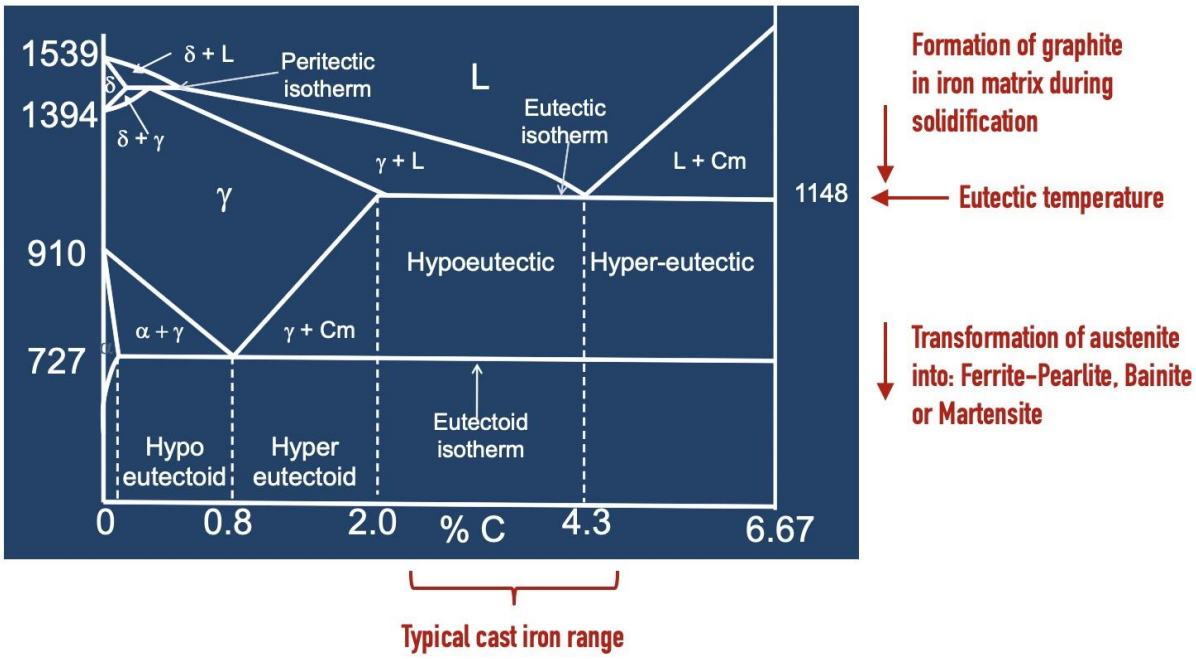

Figure 2.2: Simplified typical phase diagram (https://www.niobelcon.com/NiobelCon/niobium/niobium_in_cast_iron/).

Phase diagrams provide a representation of equilibrium phase formation as a function of temperature and composition, hence granting insights into ranges of austenite stability such as various carbide phases like M_7C_3 and $M_{23}C_6$ (Li et al., 2009; Li et al., 2021; Sudhakar et al., 2022). In the case of HCCI, the remarkably high proportion of chromium in the matrix readjusts the phase boundaries relative to those of conventional cast irons, thereby enhancing the propensity for carbide formation. A variety of software, such as ThermoCalc, is frequently employed in simulating these phase equilibria under conditions of equilibrium and non-equilibrium to forecast where the precipitation of carbides begins and the evolution of microstructure will thereafter take place with the cooling (Fan et al., 2020). In practice, one of the critical features offered through these simulations is the ability not only to validate the cooling rates observed in the laboratory but also to understand the effect on any single compositional adjustment for enhancing the metastability of phases. By comparing the results with experimental cooling curves, one could make important alloy compositions for good mechanical properties, thus bridging the gap between predictions and actual procedures.

The non-equilibrium solidification theory plays a very important role in investigating HCCI, as in real industrial casting, many times the normal equilibrium state is not reached. The kinetics of atomic diffusion are not fast enough to keep the system in equilibrium once fast cooling starts; hence, micro-segregation and metastable phase precipitation occur (Wan et al., 2005; Inden, 2007; Liu et al., 2021; Deschamps & Hutchinson, 2021). These HCCI phenomena are further enhanced by the competition between nucleation and growth during rapid cooling, promoting a fine dendritic microstructure with finely networked carbides. The concept of undercooling, that is to say, the difference between the actual temperature for the mass of the melt and that expected under equilibrium liquidus temperature, is also a crucial factor for promoting nucleation. Whenever a melting solid undergoes a higher extent of undercooling, the nucleation rate would be expected to increase proportionately (Liu et al., 2021; Lu et al., 2023), thereby ensuring that the microstructures are homogenous and fine in order to increase performance. Rapid solidification also reduces the time for atomic-liquid diffusion to take place and thus favours non-equilibrium phase distributions, which, however, come under control by manipulating processing parameters. Non-equilibrium solidification theory, therefore, describes the microstructural evolution in HCCI and stands to be beneficial for designing improved casting techniques that might enhance the steel mechanical properties by means of the fast-cooling method (Yulianto et al., 2021; Boldyrev, 2023; Gundlach & Tartaglia, 2024).

Cooling curves (Figure 2.3) turn out to be significant with regard to linking thermal history with microstructural evolution in HCCI. Essentially, the temperature-versus-time plot during the solidification process is identified by these curves, revealing the underlying transformation kinetics (Panichkin et al., 2023; Goto et al., 2023; Du et al., 2024). The shape and inflection points of the cooling curve tell tales of significant thermal events involving the onset of nucleation, latent heat, and the progress of such eutectic reactions.

The thermocouples are invaluable assets that form a digital map for all those events by being coupled to software like ThermoCalc or Nova. For instance, during a plateau on the cooling curve, there is only the release of latent heat during a phase transformation, which potentially holds the crux as to the kinetics of that transformation (Lu et al., 2023; Umantsev, 2023; Lapcikova et al., 2024).

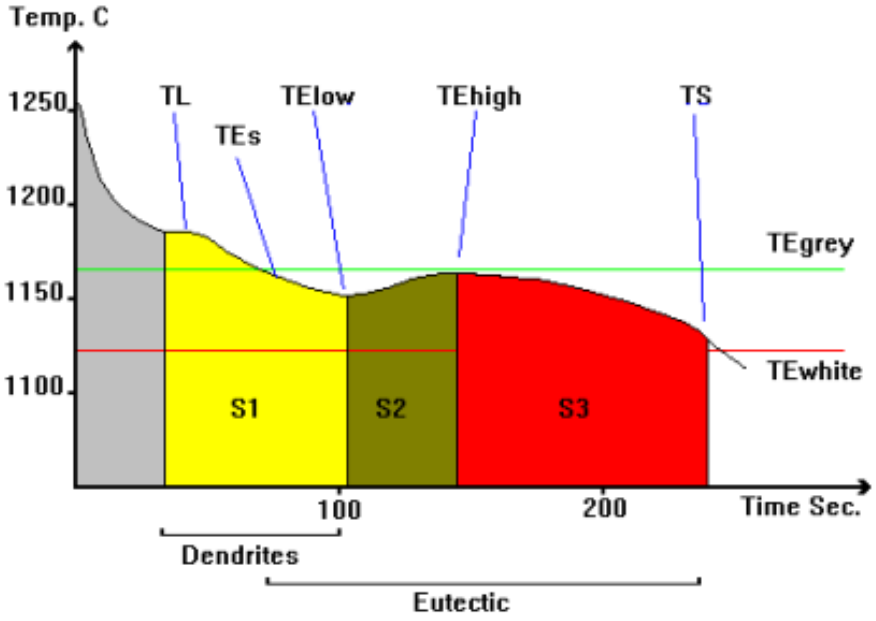

Figure 2.3: A typical cast iron solidification cooling curve.

(Rudolf. (2002)

Principally, analysing cooling curves allows inventing the cooling rate, a variable that directly influences dendrite arm spacing and carbide precipitation. A faster cooling rate, because of the increased number of nucleation sites, results in a finer microstructure, and slow cooling allows the growth of coarser features due to excessive diffusional times (Guo et al., 2016; Oanh & Viet, 2020; Guo et al., 2021). These distinctly sighted evaluations on heat transfer ease casting design and refine properties of HCCI.

Cooling curve analysis is a widely used technique for studying the solidification behaviour of cast irons, but it has several important limitations when applied to high-chromium cast irons (HCCIs). These alloys are particularly sensitive to changes in chemical composition, including minor alloying elements, which can greatly influence the solidification path and resulting microstructure. As shown by Stan et al. (2023) and Le Nué et al. (2024), even small variations in chromium and carbon content can lead to discrepancies between predicted and actual phase formations. For example, Le Nué et al. (2024) demonstrated that lowering the cooling rate after destabilisation heat treatment in hypoeutectic HCCI led to more extensive secondary carbide formation. This, in turn, depleted carbon in the austenite, raised the martensite start temperature, and lowered bulk hardness, an effect not easily detected using standard cooling curve analysis alone.

Another major limitation lies in how cooling curves interpret undercooling and eutectic reactions. The degree of undercooling during solidification, which is heavily influenced by cooling rate and mould type, affects not only the final microstructure but also defect formation such as micro-shrinkage or excessive carbide precipitation. Stan et al. (2012, 2017) discussed how undercooling below the metastable equilibrium temperature can lead to increased formation of contraction-related defects, especially in green sand moulds due to their less rigid nature and higher cooling rates. While cooling curves and their first derivatives can show general patterns for quality control, they are not sufficient for capturing the complexity of phase interactions in HCCIs, particularly under industrial conditions.

Furthermore, cooling curve analysis alone cannot reliably account for the full range of microstructural complexity present in high-Cr irons. These materials typically include a mix of primary austenite, eutectic carbides, martensite, pearlite, and secondary carbides. Because these phases can form at overlapping or similar temperature ranges and in very small volumes, cooling curve signals may miss or misrepresent them entirely. This is especially true in thin-walled castings, where higher cooling rates cause greater undercooling, promoting unexpected carbide formation or a higher fraction of pearlite. Such microstructural changes can drastically alter mechanical properties but may not be obvious from cooling curves alone.

To address these limitations, researchers increasingly rely on complementary techniques such as dilatometry, microstructural analysis (e.g., SEM and EBSD), hardness testing, and thermodynamic simulations. As noted by Prasanna Kumar et al. (2014), standard cooling curve analysis methods, along with tests like the Jominy end-quench, often fail to reflect the actual cooling conditions encountered in industrial quenching. Their development of the Reference Quench Probe allows for in-plant testing under real conditions, using specimens of the same grade and thickness as industrial components. This tool, combined with a suite of mathematical models, accurately estimates localised cooling rates, microstructure, and hardness, providing more reliable data for heat treatment design and quality assurance. Similarly, phase prediction tools such as Thermo-Calc can assist in modelling solidification and phase transformation more accurately than cooling curves alone.

This shows that while cooling curve analysis remains a useful tool for initial assessments, it lacks the resolution and flexibility needed to fully understand or predict the complex phase transformations in HCCIs. A more reliable approach combines thermal analysis with advanced

characterisation and modelling techniques to provide a complete picture of microstructure evolution and its effect on mechanical performance.

Thermodynamic models form the framework for predicting phase stability and transformation pathways in HCCI. These models are based upon calculated values of the Gibbs free energy for the different phases and offer information on the stable phase assemblage as a function of temperature and composition. Computational tools like ThermoCalc have been widely adopted in the field for simulating phase diagrams in complex systems like Fe–Cr–C (Siekaniec et al., 2022; Sudhakar et al., 2022; Du et al., 2024). Such phase diagrams provide insight into ranges of stability for austenite and carbide phases and can, in turn, provide researchers with valuable information about the influence of compositional changes on phase equilibria. For those situations where equilibrium is not established, further modulations of the thermodynamic models are necessary to include kinetic information for additional phase transformations, such as undercooling, diffusion problems, and the like. The use of thermodynamic modelling alongside kinetic modelling can actually give much better predictions of microstructural evolution during rapid solidification, which is crucially important for manufacturing processes. This approach enables alloy optimisation by way of exploiting these computational techniques for varying alloy composition and cooling rates to strike an optimal balance between wear resistance, hardness, and toughness in HCCI.

In addition to experimental techniques, computational tools such as Thermo-Calc play a crucial role in modelling and predicting phase transformations during solidification. Thermo-Calc is thermodynamic software that provides insights into equilibrium and non-equilibrium solidification behaviour by simulating phase stability, solute segregation, and carbide precipitation under different cooling conditions (Yulianto et al., 2021; Boldyrev, 2023; Gundlach and Tartaglia, 2024). The software enables researchers to model the effects of alloy composition on microstructural evolution and helps determine the formation of primary austenite, carbide phases, and eutectic transformations (Akinribide et al., 2022; He et al., 2024; Ji et al., 2024). Thermo-Calc is particularly useful for predicting the influence of cooling rate on solute redistribution, microsegregation, and carbide morphology using the Scheil-Gulliver solidification model, which provides a realistic assessment of non-equilibrium conditions (Yulianto et al., 2021; Stan et al., 2021).

Furthermore, Thermo-Calc can be combined with kinetic models to analyse phase transformation kinetics and the stability of metastable phases that form during rapid

solidification (Siekaniec et al., 2022 and Sudhakar et al., 2022). This integration allows manufacturers to optimise heat treatments and post-casting processing to refine carbide distribution, enhance wear resistance, and improve mechanical properties. By adjusting processing parameters such as the composition of the intended casts based on Thermo-Calc predictions, industries can produce HCCI components with a more refined microstructure and extended service life in harsh environments (Panichkin et al., 2023; Goto et al., 2023; Du et al., 2024).

Although Thermo-Calc is a powerful tool for predicting phase transformations, it has some limitations when applied to real-world solidification processes, especially under non-equilibrium conditions. The software is designed to calculate equilibrium phase diagrams and phase fractions, but in reality, solidification often happens under conditions where cooling is too fast for equilibrium to be maintained. The Scheil-Gulliver model, which Thermo-Calc uses to estimate non-equilibrium solidification, assumes no diffusion in the solid phase and complete mixing in the liquid, which is not always true in actual casting. It does not account for undercooling effects, dendrite growth, or metastable phase formation, all of which influence carbide distribution, phase stability, and mechanical properties. Additionally, Thermo-Calc does not fully predict microsegregation at the microscopic level, meaning its results must be combined with experimental data and other modelling techniques, such as phase-field simulations, to get a more accurate picture of how the alloy solidifies. While Thermo-Calc is valuable for alloy design, its predictions should always be verified through cooling curve analysis and microstructural observations to ensure they reflect actual casting conditions.

Overall, the cooling curve remains a powerful tool for understanding and controlling the solidification of HCCI. By analysing cooling rates, nucleation behaviour, carbide formation, and phase transformations, manufacturers and researchers can optimise the microstructure and mechanical properties of the alloy. The use of Thermo-Calc, in combination with experimental cooling curve analysis, provides a more comprehensive approach to alloy design and process optimisation. Ongoing research into solidification cooling curves and thermodynamic modelling will continue to refine casting processes, ensuring that HCCI remains a highly effective material for demanding industrial applications.

The importance of cooling curves in complement to theoretical models cannot be overstated. These curves give the real-time temperature evolution during casting and bridge the theory-experiment gap. For instance, careful analysis of these cooling curves will detail undercooling,

recalescence, and thermal arrest, all the while explicitly manifesting nucleation events and transformations (Panichkin et al., 2023; Goto et al., 2023; Du et al., 2024). The curve data and these models (thermodynamic and kinetic) can, in turn, help adjust the model parameters and refine the predictions about microstructural evolution. For example, the ThermoCalc software can be used in conjunction with cooling curve data in order to plot the phase diagrams due to the non-equilibrium state and, as a result, fast solidification that is mainly typical of industrial casting processes. The integrated approach not only validates theoretical models but also further expands its predictive capabilities so that HCCI alloys may be fabricated with microstructures that are truly optimised for specific applications (Siekaniec et al., 2022; Sudhakar et al., 2022; Du et al., 2024).

The steps taken to characterise the phase transformations and their kinetics are the right steps toward understanding the phenomenon of phase transitions during solidification. These kinetic parameters extracted from these theoretical models will certainly have direct implications on the properties and mechanical performance of HCCI. Microstructures that arise from these models are expected to add to and modify the hardness, wear resistance, and toughness of the finished alloy. For instance, a refined dendrite with a high density of fine carbides impairs dislocation mobility and cracks in the alloy, thus enhancing the overall strength and durability of any component of HCCI. It is very crucial to be able to predictably generate these properties from a combination of thermodynamic and kinetic models for alloy design, duly meeting the severe requirements imposed by industrial applications such as mining, petrochemical processing, and milling (Panichkin et al., 2023; Du et al., 2024; Gundlach and Tartaglia, 2024). These predictive models would provide scientific underpinnings to establish a relationship between cooling rate and microstructural refinement and mechanical property improvement and thus provide a theoretical baseline for graduating programs in the academy and industrial demand.

Furthermore, the theoretical framework presented in the preceding paragraphs is not only valuable in advancing our scientific knowledge of phase transformations in HCCI but could also be instrumental in guiding the development of practical thinking surrounding alloy design and process optimisation. It will be possible to tackle with greater conviction the detailed quantitative impact of yet another variable on this arena should classical thermodynamics, kinetic theories, and modern computational tools be harnessed together to properly envision and manage the composition of the alloy affected by interaction with cooling rates and microstructural evolution. Consequently, significant advancement has been made in the

processing of HCCI, and the cast parts show much improved functionality compared to the earlier wear resistance, so that toughness has become soberer because of the optimisation of cooling curves and nucleation and diffusion models, which now flex the strength of designing tailor-made for extreme industrial applications with the next generation of HCCI alloys. As demand for materials capable of performing with great reliability under severe conditions is forecasted to increase, this theoretical framework will become increasingly pivotal and will ignite new changes in alloy development and processing methods.

2.7 Mechanical Properties, Wear, and Corrosion Behaviour of HCCIs.

2.7.1 Mechanical Properties of HCCIs

Research efforts have been directed towards understanding the mechanical, tribological, and corrosion properties of HCCIs, focusing on hardness, wear resistance, and fracture toughness. The unique microstructure of HCCI, consisting of hard carbides (M_7C_3 and $M_{23}C_6$) dispersed within an austenitic or martensitic matrix, is responsible for its superior mechanical properties. Numerous studies, including those by Bedolla-Jacuinde et al. (2005), Abdel-Aziz et al. (2017); Guitar, Scheid et al. (2020) and Ngqase & Pan, (2020), have investigated the sensitivity of these properties to variations in alloy composition, carbide morphology, and distribution. Liu et al., (2025) identified an optimal Cr/C ratio range (8-11), which leads to a fine dispersion of carbides, enhancing hardness while maintaining a reasonable level of toughness. However, deviation from this range can result in coarser carbides, which negatively impact mechanical performance by increasing hardness at the expense of ductility and impact resistance. Refining microstructure to balance hardness, wear resistance, and toughness is therefore a key area of research in optimising HCCI for industrial applications.

The hardness of HCCI is primarily influenced by the volume fraction, size, and distribution of chromium-rich carbides within the austenitic matrix. Studies by dating early on by Yang et al. (2009) and reinforced in recent studies by Guitar et al. (2020) have shown that higher fractions of finely dispersed carbides increase resistance to plastic deformation, thereby enhancing hardness. However, a trade-off exists, as excessive hardness may reduce ductility. Research by Cui et al. (2016) and Du et al. (2024) has demonstrated that smaller, more uniformly distributed carbides are more effective at pinning dislocations, leading to improved mechanical performance. Studies by Abd El-Aziz et al. (2015) and Liu et al. (2025) further confirmed that HCCI alloys with an optimised Cr/C ratio exhibit greater hardness than those with lower

chromium or carbon contents. This improvement is attributed to the finer carbide network, which restricts dislocation mobility, thereby increasing resistance to localised deformation.

While hardness testing is a widely used and convenient method for evaluating the mechanical performance of HCCIs, relying on it alone can lead to misleading conclusions about the overall behaviour of the alloy, especially in complex service environments. One of the major limitations is that hardness does not always reflect true wear resistance. As shown by Camurri et al. (2021), the wear resistance of HCCI is highly influenced by the microstructure, including the shape, size, and distribution of carbides. In cases where alloys had significantly different hardness values, there was a strong correlation between hardness and wear. However, when different HCCI grades showed similar hardness, their wear resistance varied widely due to differences in carbide morphology and matrix connectivity, which hardness tests alone could not capture (Huang et al., 2008; Yu et al., 2021). This indicates that microstructure must be considered alongside hardness for a more accurate understanding of material behaviour.

Heat treatment further complicates this relationship. Different quenching and tempering processes can change the microstructure, especially the balance between martensite, austenite, and carbides, resulting in varying hardness and toughness levels. However, these changes are not always straightforward. While hardness may increase after certain treatments, it can come at the cost of reduced toughness and higher brittleness, which is critical in applications with impact or dynamic loading (Liu et al., 2008; Huang et al., 2008; Yu et al., 2021). For example, Betti & Ataiwi (2020) showed that even though hardness was reduced by sub-ambient treatments, the toughness and erosive wear resistance improved, especially in HCCI samples treated with liquid nitrogen followed by tempering. This highlights the trade-off between hardness and toughness and the need to assess both properties together.

Additionally, compositional variations, even within accepted industrial ranges, can lead to noticeable differences in hardness, microstructure, and wear performance. In the study by Nelwalani et al. (2024), slight deviations in chromium and carbon levels in HCCIs produced in jobbing foundries caused significant differences in microstructure, phase formation, and hardness, despite being within standard specifications. Using Thermo-Calc and thermal analysis software (ATAS MetStar), they showed that hardness and other properties were highly sensitive to these small changes, suggesting that chemical composition alone is not a reliable quality indicator without microstructural verification.

The lack of consistent correlation between hardness and wear resistance becomes even more problematic when performance testing is done under standard laboratory conditions. Many real-world applications of HCCI, such as in mining, cement, or petrochemical environments, involve abrasive slurries, high temperatures, or corrosive media. Hardness tests conducted in controlled lab settings do not account for these variables. Betti & Ataiwi (2020) reviewed how various environmental factors, such as pH, slurry velocity, temperature, and abrasive size, all affect HCCI wear and corrosion performance. Their work emphasised that laboratory hardness values alone are not enough to predict how a component will perform in the field.

Taken together, these findings suggest that while hardness is a useful benchmark, it should not be the only criterion used to evaluate HCCI performance. A more comprehensive approach should include microstructural analysis (using SEM or EBSD), phase prediction (via Thermo-Calc), wear testing, toughness evaluation, and environmental simulations to better capture the full performance of the alloy. This will ensure more reliable material selection and design, especially for demanding industrial applications where both wear resistance and toughness are essential. Recognising the limitations of hardness testing highlights the importance of understanding the underlying microstructure, particularly carbide morphology, which not only affects hardness but also plays a critical role in governing the response of the material to wear. As such, evaluating carbide characteristics, such as size, shape, distribution, and connectivity, is essential for accurately assessing the wear resistance of HCCI, especially in applications involving abrasion and erosion.

While hardness provides a convenient measure of surface strength, it does not capture the material's ability to resist crack initiation and propagation under stress. Therefore, to fully evaluate HCCI performance, it is essential to also consider fracture toughness, which offers a deeper understanding of the alloy’s behaviour in demanding service conditions. Fracture toughness, which represents the ability of a material to resist crack propagation, is significantly influenced by the balance between hardness and ductility in HCCIs. The type of fracture mode, whether brittle or ductile, can be determined by examining the fracture surface characteristics and deformation behaviour. Brittle fracture is characterised by a smooth, flat, and granular fracture surface with cleavage planes and river patterns, indicating rapid crack propagation with minimal plastic deformation (Guo et al., 2021). This type of fracture absorbs low energy before failure and typically occurs in hard but brittle materials like high-chromium cast irons with coarse, interconnected carbides. In contrast, ductile fracture exhibits a rough, fibrous surface with microvoids and dimples, suggesting significant plastic deformation before failure

(Wiengmoon et al., 2011). Ductile fractures occur gradually, absorbing higher energy, and are commonly observed in tougher materials where carbides are finer and more evenly distributed. By analysing the fracture morphology, one can determine the fracture mode and assess the mechanical behaviour of the material under stress. These surface characteristics can be identified as seen in Figure 2.4.

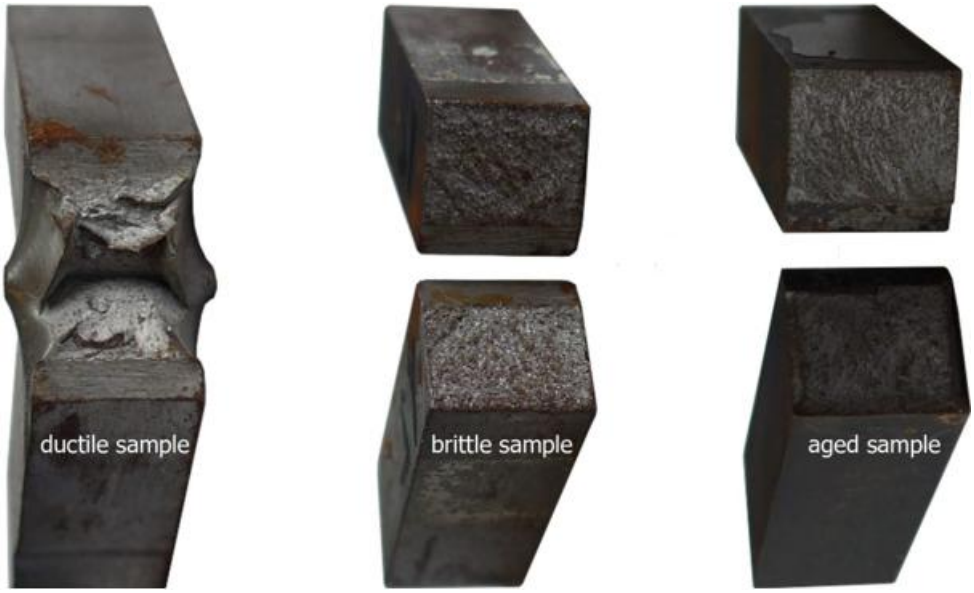

Figure 2.4: Characteristic fracture surfaces for different fracture modes after Charpy impact testing (https://www.tec-science.com/material-science/material-testing/charpy-impact-test/)

While high hardness is essential for wear resistance, excessive hardness can make the material brittle, reducing its ability to withstand impact loads. Several studies indicate that an optimal Cr/C ratio enables a balanced microstructure, ensuring both high hardness and sufficient fracture toughness. Controlling excessive hardness while preventing the formation of large, continuous carbide networks is crucial, as these networks can act as crack initiation sites, leading to brittle failure (Kootsookos & Gates, 2004; Guo et al., 2021). HCCI with a moderate Cr/C ratio has been reported to exhibit good resistance to crack propagation under impact loads, as smaller carbides disrupt crack paths, dissipating energy and improving toughness. In contrast, suboptimal Cr/C ratios can lead to excessive carbide growth, which increases hardness but reduces fracture toughness, making the material more prone to brittle failure (Yang et al., 2009; Chung et al., 2013).

To better understand the origins of these mechanical behaviours and validate the effects of Cr/C ratio on fracture toughness, detailed microstructural characterisation techniques have been employed. Microstructural characterisation techniques such as scanning electron microscopy (SEM) and energy-dispersive spectroscopy (EDS) have been employed to provide detailed

insights into the relationship between microstructure and mechanical properties. These analyses confirm that carbide distribution and morphology have a direct impact on fracture behaviour. High-resolution SEM studies by Siekaniec et al. (2022) have demonstrated that a uniform dispersion of M_7C_3 carbides enhances hardness and wear resistance, whereas coarser, irregularly spaced carbides can lead to localised stress concentrations and premature crack formation. These microstructural evaluations highlight the importance of carefully controlled alloying and processing conditions, particularly with respect to the Cr/C ratio, in optimising fracture resistance and overall performance.

Past research has demonstrated that modifying the Cr/C ratio significantly influences the mechanical properties of HCCI (Kootsookos & Gates, 2004; Ma et al., 2011; Tang et al., 2011). The advancements have also shown the same idea presented in recent studies. Both past and recent studies indicate that an initial increase in Cr/C ratio enhances hardness and wear resistance due to the formation of a dense carbide network (Yang & Li, 2012; Pourasiabi & Gates, 2022). However, excessively low Cr/C ratios can lead to the development of a coarse carbide/matrix system, which negatively impacts fracture toughness (Liu et al., 2025). For example, they found that while decreasing chromium content improves hardness, it also reduces fracture toughness, increasing the likelihood of crack propagation under dynamic loading conditions (Zheng et al., 2006; Wang et al., 2012; Zhang et al., 2022). These trends underscore the need for precise alloying control and optimised processing techniques to maintain a Cr/C ratio that ensures balanced mechanical properties in HCCI. Carefully adjusting the Cr/C ratio is essential to achieving high-performance HCCI components with enhanced wear resistance, hardness, and fracture toughness, making the alloy more suitable for high-stress industrial applications.

Furthermore, recent studies have highlighted the important role of heat treatment in improving the mechanical properties of HCCI. Heat treatments such as quenching and tempering are commonly applied after casting to further modify the microstructure and enhance the performance of the alloys (Panichkin et al., 2023; Du et al., 2024). These treatments help refine the shape and distribution of carbides and promote the formation of secondary carbides, which leads to increased wear resistance and hardness while still maintaining good toughness. For example, Sudhakar et al. (2022) showed that heat-treated HCCI samples had a more uniform carbide distribution and slightly better toughness compared to the as-cast samples. These findings show that while the Cr/C ratio and casting conditions provide the initial control over mechanical properties, heat treatment offers an additional and powerful way to further improve

the material. It not only changes the microstructure but also helps achieve the right balance between hardness, wear resistance, and toughness. This makes heat treatment especially useful for components that need to resist both wear and impact in demanding industrial environments.

2.7.2 Wear Resistance of HCCIs

Among the popular properties of HCCI, wear resistance continues to receive significant attention due to its relevance in abrasive and erosive service conditions. The presence of hard carbides plays a key role in resisting material loss under sliding and impact conditions. Studies have confirmed that Tang et al. (2011), Abd El-Aziz et al. (2015), and Guo et al. (2021) found that higher Cr/C ratios promote the formation of dense carbide networks, which effectively shield the softer matrix from excessive wear. The size and distribution of carbides are also crucial, as well-dispersed, smaller carbides create a more uniform wear pattern, reducing the risk of localised material removal. Conversely, coarser carbides or poorly distributed phases can lead to stress concentration sites, which accelerate microcracking and material degradation (Yang & Li, 2012; Wang et al., 2018; Liu et al., 2023).

High-chromium cast irons experience multiple modes of wear, as shown in Figure 2.5. These are primarily abrasive wear, adhesive wear, and erosive wear, depending on their operating conditions and microstructure (Bedolla-Jacuinde et al., 2005; Kermouche et al., 2019). Abrasive wear is the most dominant mechanism in HCCIs, occurring when hard particles or surfaces slide against the material, leading to micro-cutting, ploughing, or fragmentation of the matrix and carbides (Chung et al., 2013). This is further classified into two-body abrasive wear, where the counter surface directly interacts with the material, and three-body abrasive wear, where loose abrasive particles cause additional material removal (Filipovic et al., 2013). Adhesive wear occurs when asperities on the contacting surfaces weld together under high loads and shear off, leading to material transfer or surface damage, which is exacerbated by insufficient lubrication or severe loading conditions (Meng et al., 2019). Erosive wear results from high-velocity impact by particles, which progressively remove material through repeated deformation and fracture, often encountered in slurry pump impellers and milling components (Wiengmoon et al., 2011). The severity of these wear mechanisms depends on the carbide volume, size, shape, and distribution, as well as the Cr/C ratio, which influences the hardness and toughness of the material (Guo et al., 2021). Understanding these wear modes is crucial for optimising HCCI alloys for high-stress industrial applications where prolonged wear resistance is required.

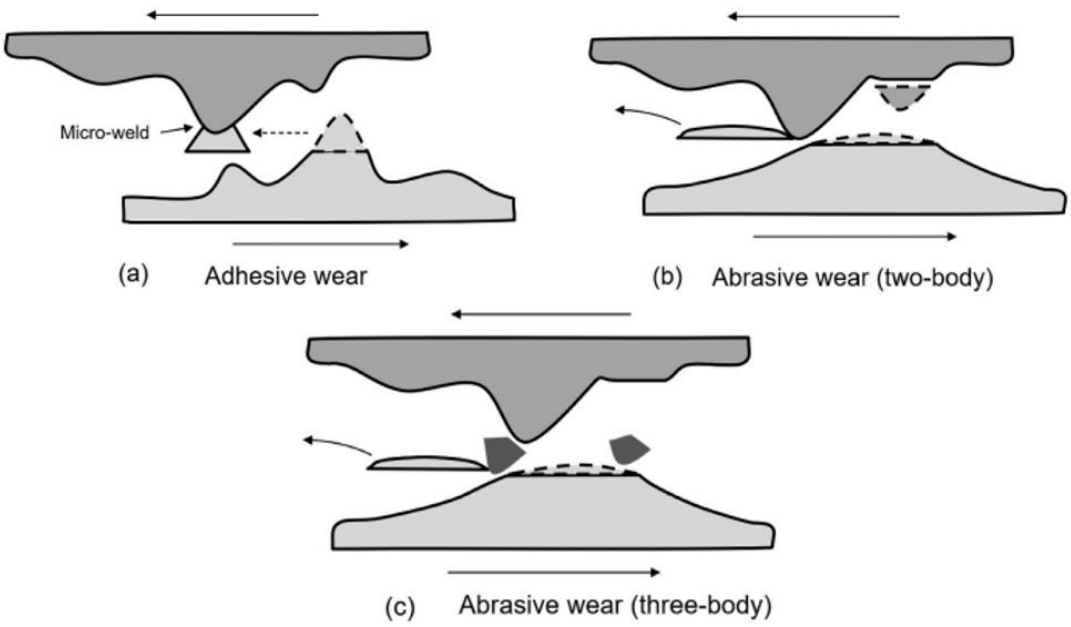

Figure 2.5: Typical wear mechanisms found in HCCIs for (a)adhesive wear, (b) abrasive wear(two-body) and (c)abrasive wear(three-body*)* (la Monaca et al., 2021).

The wear resistance of HCCI can be analysed using Archard's wear equation, which describes wear volume loss, wear coefficient, applied load, sliding distance, and the material hardness. Equation 2.1 highlights that higher hardness directly improves wear resistance, as harder material experiences lower wear volume under the same loading conditions.

$$V_w = A_w P d_{max} \qquad \text{Equation 2.1}$$

Where: V_w= wear volume (mm^3), A_w = worn surface area (mm^2), and Pd_{max}= average penetration depth (mm). The specific wear rates (SWR) of the titanium alloys were calculated using Equation 2.2 (Archard, 1953; Kiefer, 2006).

$$SWR = \frac{V_W}{F \times s} \qquad \text{Equation 2.2}$$

Where SWR = wear rate (mm^3 /Nm), F = load (N), and s = sliding distance (m). This procedure was followed for both the as-cast and heat-treated samples.

Wear in HCCI is further described by the Equal Wear Rate (EW) and Equal Pressure (EP) models, which define the wear behaviour of multiphase materials: The Equal Wear Rate (EW) Model and Equal Pressure (EP) Model describe two fundamental wear mechanisms in multiphase materials like high-chromium cast irons (HCCIs), particularly in relation to the

interaction between the matrix and carbide phases under abrasive conditions. These models define the upper and lower limits of wear resistance based on how the load is distributed between the reinforcing phase (carbides) and the matrix.

- EW Model (Equal Wear Rate): Assumes that the matrix and carbides wear at the same rate, leading to balanced material removal. This occurs when carbides are well-anchored and uniformly distributed, effectively protecting the matrix from excessive wear.
- EP Model (Equal Pressure): Assumes that the load is evenly distributed between the carbide and matrix phases, which can cause faster matrix removal and premature carbide detachment. This results in accelerated wear due to carbide pull-out, particularly if the carbides are not well integrated within the matrix.

For maximum wear resistance, it is essential to optimise the microstructure towards EW-dominant behaviour, ensuring fine carbide distribution and strong matrix support. Studies show that high Cr/C ratios, controlled solidification, and post-casting heat treatments improve wear resistance by refining carbide morphology and enhancing matrix strength (Axen & Jacobson, 1994). Optimising microstructural tailoring during casting and heat treatment can significantly enhance wear performance by refining carbide size, morphology, and distribution (Guo et al., 2016; Zhang et al., 2023). Understanding these relationships is essential for improving the resistance of HCCIs to wear-intensive environments, such as mining, cement production, and petrochemical processing.

2.7.3 Corrosion Resistance of HCCIs

While optimising the Cr/C ratio is vital for achieving desirable mechanical properties, its influence extends beyond wear and fracture behaviour, ultimately playing a critical role in determining the corrosion resistance of HCCIs, particularly in aggressive service environments. High-chromium cast irons are widely used in industries that require superior corrosion resistance, such as mining, chemical processing, and marine environments. The corrosion behaviour of HCCIs is strongly influenced by their microstructure, particularly the volume, distribution, and morphology of carbides, as well as the availability of chromium in the matrix to form a protective passive film. The corrosion resistance of these alloys varies significantly depending on the environment, including neutral chloride solutions, alkaline media, and acidic conditions. To evaluate corrosion performance, a variety of standard testing methods are applied, electrochemical techniques are widely used for more detailed analysis.

These include Open Circuit Potential (OCP) testing, which measures the natural, steady-state potential of the material in a given environment, providing insight into its corrosion tendency over time (Habib, 2015). Potentiodynamic polarisation is often used to assess passivation behaviour and corrosion current density. It indicates the thermodynamic likelihood of a material to undergo corrosion, where a more positive Ecorr value suggests a lower corrosion tendency (Tkacz et al., 2016; Aslam, 2023). Post-test surface analysis using SEM or XRD further reveals corrosion morphology and the nature of corrosion products. Together, these tests offer a comprehensive view of how microstructural features and Cr/C ratio adjustments influence corrosion resistance in HCCIs.

Chloride-containing environments, such as seawater and industrial cooling systems, are highly aggressive due to the ability of chloride ions to penetrate and destabilise passive films. The primary corrosion mechanisms in HCCIs exposed to NaCl solutions include pitting corrosion and microgalvanic corrosion, particularly at the carbide-matrix interfaces (Zhou et al., 2018). Chromium-rich M_7C_3 carbides help in passivation by reducing the number of active sites for localised attack, but uneven distribution of chromium can lead to chromium depletion in the surrounding matrix, making those areas more susceptible to corrosion (Tang et al., 2009).

The corrosion behaviour of HCCIs in chloride solutions is influenced by carbide morphology. Finer, uniformly distributed carbides enhance passivation, as they prevent large cathodic-anodic regions, thereby reducing galvanic corrosion (Yang et al., 2009). Conversely, larger, more interconnected carbides can promote corrosion by increasing the number of carbide-matrix interfaces where microgalvanic corrosion can initiate (Chang et al., 2010). Heat treatment can improve corrosion resistance by redistributing chromium more uniformly, reducing segregation at carbide-matrix interfaces, and minimising preferential attack in chloride environments (Sarac & Dikici, 2019).

In highly alkaline environments such as 0.5M NaOH, the corrosion behaviour of HCCIs is different from that observed in neutral or acidic conditions. Here, selective carbide dissolution is the dominant mechanism, as carbides corrode preferentially due to their lower self-corrosion potential compared to the metallic matrix (Clegg & McLeod, 2013). As the carbides dissolve, chromium is gradually released into the matrix, contributing to passive film formation, which enhances corrosion resistance (Liu et al., 2023). Unlike in chloride environments, this chromium release in NaOH promotes passivity rather than weakening the protective capabilities of the material. The effectiveness of passivation in NaOH depends on carbide

volume, size, and distribution. Fine and homogeneously dispersed carbides allow for steady dissolution, leading to a gradual enrichment of chromium in the matrix and the formation of a stable passive layer. Larger and more widely spaced carbides, however, can create localised areas of intense corrosion (Zhang et al., 2020). Heat treatment can influence corrosion resistance in NaOH by modifying carbide morphology. The precipitation of secondary carbides after heat treatment can deplete chromium from the matrix, reducing the amount available for passive film formation, thereby increasing corrosion rates (Moslemi et al., 2011). This behaviour marks a significant contrast to the generally beneficial effects of heat treatment in chloride environments, demonstrating that the impact of processing techniques is environment-dependent. This is further driven by the observation that if the carbide network remains homogeneous, the overall corrosion resistance can still be improved by minimising carbide-matrix interactions that promote microgalvanic corrosion (Yan et al., 2020).

In acidic environments, such as 0.5M H_2SO_4, corrosion is primarily governed by active dissolution of the metallic matrix, with localised galvanic corrosion at carbide-matrix interfaces due to the aggressive nature of sulphate ions (Lee et al., 2021). This mechanism differs substantially from the passive film protection observed in chloride and alkaline conditions, as sulphate ions continuously disrupt any protective layers. Unlike chloride or alkaline solutions, where passivation can provide protection, in sulphuric acid, the passive film is continuously disrupted, making it difficult to maintain long-term stability (Abdel-Aziz et al., 2017). Carbide morphology plays a significant role in the corrosion resistance of HCCIs in acidic solutions. Smaller and more evenly distributed carbides promote uniform corrosion, reducing the likelihood of deep localised attack (Wiengmoon et al., 2011). On the other hand, larger or interconnected carbides increase the number of anodic and cathodic sites, accelerating corrosion at the carbide-matrix interfaces and leading to extensive material loss (Zhang et al., 2020). Heat treatment has mixed effects on corrosion resistance in acidic environments. While it improves carbide distribution and reduces segregation, the formation of secondary carbides depletes chromium from the matrix, making it more vulnerable to acid attack (Su et al., 2019). Since sulphuric acid aggressively dissolves the matrix, the increased carbide volume after heat treatment can sometimes worsen corrosion by increasing the number of galvanic sites where anodic dissolution can occur (Farquhar et al., 2021). This presents a clear contrast to the benefits of heat treatment in NaCl and NaOH environments, where it generally improves corrosion resistance by refining carbide distribution. In acidic environments, however, the same process can worsen corrosion performance due to chromium depletion caused by secondary

carbide precipitation. Figure 2.6 shows characteristic surfaces after corrosion of hypoeutectic HCCIs in different corrosive media as illustrated by Abd El-Aziz et al. (2015).

Several key factors influence the corrosion resistance of high-chromium cast irons:

1. Carbide Volume and Distribution—A higher volume of carbides can increase wear resistance but may also lead to greater microgalvanic corrosion if not evenly distributed (Yang et al., 2009).
2. Chromium Content—A higher Cr content in the matrix promotes the formation of a strong passive film, enhancing corrosion resistance (Tang et al., 2011).
3. Microstructure Homogeneity—Heat treatment helps redistribute carbides and chromium, reducing segregation and weak points where corrosion can initiate (Sarac & Dikici, 2019).
4. Electrolyte Environment—Chlorides promote pitting, alkaline solutions favour passivation, and acidic solutions cause active dissolution (Liu et al., 2023).
5. Heat Treatment Effects—Heat treatment can improve corrosion resistance in chloride and alkaline solutions but may increase corrosion rates in acidic solutions due to secondary carbide precipitation (Moslemi et al., 2011).

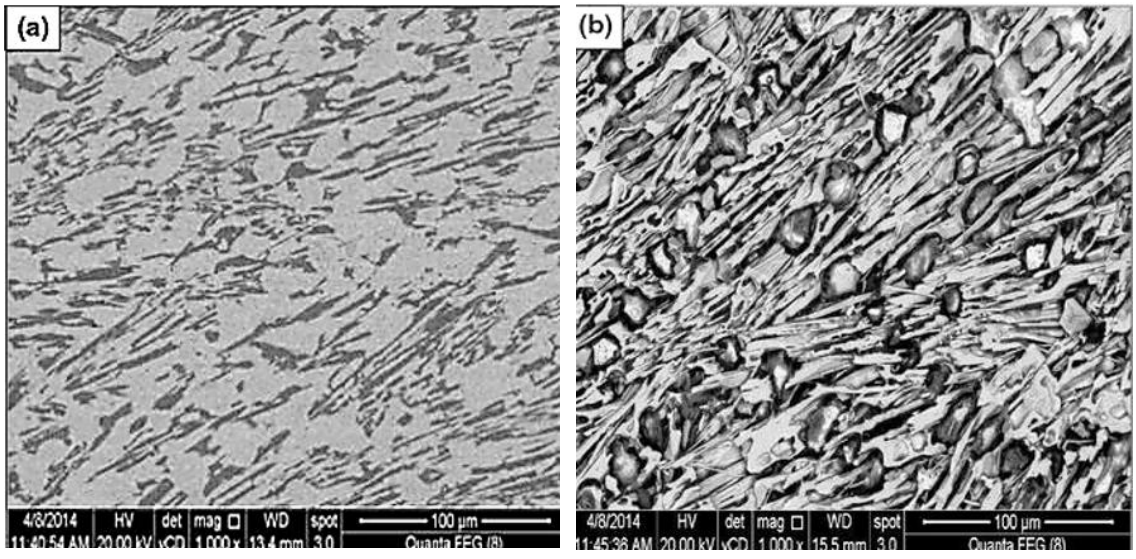

Figure 2.6: Characteristic surfaces after corrosion of hypoeutectic HCCIs in different 0.5M NaOH (a) and 0.5M H_2SO_4 (b) as illustrated by Abd El-Aziz et al. (2015).

The corrosion behaviour of high-chromium white cast irons is highly dependent on environmental conditions, carbide morphology, and chromium availability. In chloride

solutions, pitting and microgalvanic corrosion dominate, with finer carbide dispersion and heat treatment improving resistance. In NaOH, selective carbide dissolution promotes gradual passivation, with homogeneous carbide networks offering the best protection. In H_2SO_4, active matrix dissolution and galvanic corrosion lead to the highest corrosion rates, as the passive film is constantly attacked. Heat treatment generally improves corrosion resistance in neutral and alkaline conditions but may have negative effects in acidic environments due to chromium depletion. Optimising the Cr/C ratio and ensuring a homogeneous microstructure are critical strategies for enhancing corrosion resistance in HCCIs (Wiengmoon et al., 2011; Yan et al., 2020; Liu et al., 2023).

Corrosion testing methods such as Open Circuit Potential (OCP) and potentiodynamic polarisation are widely applied in evaluating the corrosion performance of metallic alloys, including high-chromium cast irons (HCCIs). While these techniques offer valuable insights, they also come with important limitations that restrict their reliability and interpretation, especially under complex or aggressive environmental conditions.

One of the main limitations of OCP testing is its qualitative nature. Although it is a convenient, non-destructive method used to assess the corrosion tendency of materials, it does not provide direct information on corrosion rates or mechanisms. For example, Hemkemeier et al. (2022) used OCP to monitor early corrosion activity in reinforced concrete systems containing industrial waste products such as sugarcane bagasse ash sand (SBAS) and water treatment plant sludge (WTPS). Their findings confirmed that while OCP could indicate the onset of corrosion, it lacked the capacity to quantify it or explain how corrosion progressed over time. Similarly, Cesiulis and Tsyntsaru (2009) highlighted that OCP is best used as an initial indicator and should be supported by additional techniques for a more accurate assessment.

The reliability of OCP is further limited by its sensitivity to experimental conditions, which can heavily influence the measured potential. Hemkemeier et al. (2022) demonstrated that variations in specimen immersion, partial versus full, and the adoption of wetting and drying cycles significantly altered corrosion results. Specifically, partial immersion combined with drying cycles led to the earlier appearance of corrosion, attributed to increased oxygen availability and higher chloride concentration near the exposed surface. These findings reveal that minor changes in test setup can cause major differences in output, reducing the consistency and reproducibility of OCP measurements.

Compounding these issues is the lack of standardised procedures for OCP testing. Hemkemeier et al. noted that there is no consensus on critical experimental aspects, including the type of reference electrode, immersion level, and accelerated ageing protocols. While their study found the reference electrode type to be of less importance, other variables had a considerable impact on the results. Without standardisation, it becomes difficult to compare data across studies, increasing the risk of misinterpretation or error in material selection and design decisions.

Another significant drawback of OCP is its susceptibility to environmental factors. Parameters such as oxygen levels, temperature, and chloride ion concentration can all shift the measured potential, sometimes misleadingly. Yuan et al. (2015) observed that OCP values became more noble as the exposed substrate area and the corrosion rate increased during corrosion tests of galvanised steel in NaCl solution. This finding contradicts the common assumption that a more positive potential indicates better corrosion resistance, showing that environmental context must be carefully considered when interpreting OCP results.

In more complex or inhomogeneous environments, the application of OCP becomes increasingly difficult. Tan (2011) reported that corrosion measurement in highly resistive and non-uniform media, such as concrete, soils, or porous matrices, faces challenges like IR drop, non-uniform polarisation current distribution, and instability in sensor placement. These limitations can result in poor resolution or misleading results, particularly when attempting to monitor localised corrosion or subtle electrochemical changes across a structure.

OCP reproducibility is also compromised in environments like NaOH and H_2SO_4, where the electrochemical conditions are especially sensitive to time, surface preparation, and electrolyte chemistry. In NaOH, slight differences in polishing or cleaning, variation in temperature, and dissolved oxygen levels can all alter the rate and extent of passive film formation (Ahmadian et al., 2014; Lynch et al., 2020; Ma et al., 2020). Time-dependent stabilisation and heat-treatment-induced secondary carbide precipitation can influence chromium availability in the matrix, further complicating results (Moslemi et al., 2011). Similarly, in H_2SO_4, the aggressive nature of sulphate ions causes continuous breakdown and reformation of the passive film. This, combined with hydrogen gas evolution, temperature variations, and reference electrode drift, makes it difficult to reproduce identical OCP readings between tests (Yue et al., 2018; Deng et al., 2018; Feng et al., 2021; Su et al., 2019; Atiyah & Albusalih, 2023; Shen et al., 2020; Farquhar et al., 2021). These factors highlight the time and condition-dependent nature of OCP measurements in highly reactive environments.

Potentiodynamic testing, often used alongside OCP, also presents key limitations. One major issue is its dependence on high electrolyte conductivity. In their investigation of stainless steel exposed to biofuels, Sorg and Ladwein (2009) found that the high resistance of low-conductivity liquids exceeded the voltage output capabilities of conventional electrochemical equipment, rendering potentiodynamic testing ineffective. They instead employed electrochemical impedance spectroscopy (EIS), which proved better suited to low-conductivity media. This example underscores how the test environment can restrict the use of potentiodynamic methods.

Beyond conductivity concerns, potentiodynamic testing is also limited in its ability to detect localised corrosion, which is responsible for the majority of real-world corrosion failures. Tan et al. (2009) stressed that traditional electrochemical methods, such as OCP, linear polarisation resistance, and even EIS, often fail to capture the spatial and temporal dynamics of localised attacks, such as pitting and crevice corrosion. They highlighted that up to 70–90% of corrosion-related failures stem from these localised mechanisms and recommended alternative methods like electrochemical noise analysis and wire beam electrode techniques, which provide better resolution for monitoring small-scale corrosion activity.

Furthermore, potentiodynamic testing may not accurately simulate real-world service conditions, especially when variables like mechanical stress, flow dynamics, and pH fluctuations are present. Yan (2020) showed that applying tensile stress in a weak acid environment caused the corrosion rate of steel to rise sharply, even though OCP readings did not change significantly. Their experiments, which included linear polarisation resistance and EIS, revealed that corrosion behaviour is highly stress-sensitive. This suggests that conventional testing in static, stress-free environments may overlook critical degradation mechanisms that only appear under load or in dynamic systems.

Another limitation of potentiodynamic polarisation, particularly when using the Tafel extrapolation technique, lies in the underlying assumptions and experimental constraints that can introduce significant errors in corrosion rate determination. One major assumption is that of uniform corrosion, that is, the material corrodes evenly across the entire exposed surface (Betts et al., 2017). However, in many real-world scenarios, especially during the initial stages of corrosion, localised processes such as pitting, crevice attack, or microgalvanic effects may dominate. This non-uniformity leads to discrepancies between the actual corrosion behaviour and the simplified uniform model assumed in Tafel analysis, thereby reducing the accuracy of

the calculated corrosion current density (Icorr). Additionally, the method is ideally suited for irreversible electrochemical reactions, yet many alloy-environment combinations do not strictly follow this behaviour (Betts et al., 2017). For instance, materials such as aluminium or passive stainless steels in neutral saline environments often exhibit complex surface interactions, where the reaction pathways include reversible steps or diffusion-limited processes. In these systems, it becomes exceedingly difficult to extract reliable Tafel slopes, which are crucial for extrapolating the linear sections of the polarisation curve. As a result, the estimated corrosion rates can deviate significantly from actual performance.

The lack of well-defined Tafel regions in some potentiodynamic curves further complicates analysis. In certain cases, the anodic and cathodic branches do not exhibit distinct linear behaviour over a sufficient potential range. This may be due to early passivation, mixed control mechanisms, or fluctuating surface states. Without clear linear segments, extrapolation becomes highly subjective and prone to error, increasing the uncertainty of Icorr values (Rybalka et al., 2021).

Experimental variables can also have a substantial impact on the reliability of the results. Poorqasemi, Abootalebi, et al. (2009) and Poorqasemi, Haqdar, et al. (2009) mention that one such factor is the formation of corrosion product films on the metal surface during testing. These films, especially when they act as passive layers, can increase the polarisation resistance and suppress electrochemical reactions. Consequently, the corrosion rate inferred from Tafel extrapolation may appear higher than values determined by gravimetric (weight loss) methods, which account for long-term material degradation. The discrepancy arises because electrochemical measurements capture short-term behaviour influenced by surface film formation, while gravimetric techniques measure actual material loss over time.

Moreover, scan rate and starting overpotential selection play a critical role in test accuracy (Fischer et al., 2019). A scan rate that is too slow may allow surface reactions or film formation to evolve during the measurement, while a fast scan may miss important kinetic features. Similarly, the choice of starting overpotential, if too far from the corrosion potential, can introduce transient effects or hysteresis, distorting the Tafel slope. Research has shown that these factors can contribute to deviations of up to 50% in the measured corrosion current, further highlighting the need for careful experimental design and parameter selection.

In summary, while Tafel extrapolation is a widely used technique in corrosion science, its effectiveness is limited by assumptions of uniform corrosion, strict irreversibility, the need for

well-defined linear regions, sensitivity to surface film formation, and vulnerability to scan rate and overpotential selection. These challenges must be addressed through careful data interpretation, supplementary testing, and, where possible, cross-validation with other methods such as weight loss measurements or electrochemical impedance spectroscopy (EIS).

Taken together, these findings demonstrate that while OCP and potentiodynamic tests are valuable tools in corrosion assessment, they are not without flaws. Their inability to capture corrosion rates accurately, sensitivity to test setup and environment, lack of standardisation, and failure to detect or simulate localised and real-world conditions limit their usefulness when used in isolation. Therefore, to obtain a complete and reliable picture of corrosion performance, especially for complex alloys like HCCIs, these methods should be used in combination with complementary techniques such as electrochemical impedance spectroscopy (EIS), immersion testing, microstructural analysis (SEM/EDS), and localised electrochemical methods. Only by integrating multiple testing strategies can we ensure accurate evaluation of corrosion behaviour in demanding industrial environments.

2.8 Recent Advancements in the Study of HCCIs

Recent advancements in the study of HCCIs have introduced a range of new methodologies that are reshaping how researchers understand the effects of composition on mechanical performance. Traditional approaches have often relied on labour-intensive experimental procedures to investigate the influence of chromium, carbon, and other alloying elements on properties such as hardness, fracture toughness, wear, and corrosion resistance. However, the integration of data-driven modelling, computational tools, advanced heat treatment strategies, and high-resolution microstructural characterisation offers far more efficient and insightful ways to optimise HCCI alloys.

One of the most significant changes in recent years is the application of machine learning to materials research. Using algorithms trained on large datasets, researchers are now able to predict key mechanical properties, such as Brinell hardness, tensile strength, and ductility, based on composition with high accuracy. These models, which have already shown promising results in similar alloys like ferritic ductile iron, are being adapted to HCCIs to assist in rapid alloy development. By feeding in variations of chromium, carbon, and trace alloying elements, it is now possible to generate reliable predictions for mechanical behaviour, reducing the need for extensive trial-and-error experimentation. This is particularly valuable in studying the

effects of the Cr/C ratio, which plays a fundamental role in governing carbide formation and matrix structure in HCCI alloys (Gu et al., 2023).

Gu et al. (2023) demonstrated the success of this approach by building a composition property dataset for ferritic ductile iron and using several machine learning algorithms to predict key mechanical properties such as tensile strength, Brinell hardness, yield strength, and elongation. Their models achieved correlation coefficients above 0.96 and mean absolute percentage errors below 5%, confirming the high predictive accuracy of the machine learning technique. Importantly, they also used thermodynamic calculations to predict phase compositions, which helped validate the reliability of the machine learning outputs. This combined approach not only predicted mechanical properties but also revealed how individual elements influenced performance, offering strong guidance for designing new alloys with improved strength and toughness. The success of this methodology in ductile iron research highlights its potential for high-chromium cast irons, where similar composition–property relationships can be established. Applying machine learning in this context allows for more efficient alloy optimisation, particularly in balancing hardness, toughness, and wear resistance through targeted control of the Cr/C ratio and other alloying additions.

Complementing this, computational techniques such as the Group Method of Data Handling (GMDH) have allowed for the creation of both linear and non-linear models that map the relationships between chemical composition and mechanical properties. This approach has proven especially useful in identifying how changes in the Cr/C ratio impact properties like hardness and toughness (Tokova & Savchenko, 2019). By modelling interactions between alloying elements, researchers can now predict not only property outcomes but also the potential risks of carbide coarsening, matrix brittleness, or chromium depletion. This level of detailed predictive insight was previously unattainable with traditional analytical methods and allows for much more refined control over alloy design. In addition to machine learning and data-modelling techniques, the use of Thermo-Calc has been particularly helpful in reducing experimental workload during alloy design. Thermo-Calc allowed for phase prediction at various temperatures and compositions, making it possible to forecast carbide types and their stability across different Cr/C ratios. This significantly cut down the amount of trial-based experimental work that would otherwise have been necessary to determine phase stability and solidification behaviour. Instead of casting multiple test samples for phase identification, preliminary simulations in Thermo-Calc guided the selection of promising compositions. This

not only saved time and resources but also improved the efficiency of the entire alloy development process.

Alongside these computational advances, developments in heat treatment techniques are making it possible to fine-tune the microstructure of HCCIs in order to meet specific performance requirements. Conventional as-cast HCCIs often suffer from uneven carbide distribution or brittle grain boundaries, particularly at high Cr/C ratios. Through methods such as austempering and quenching and partitioning (Q&P), researchers are now able to transform the microstructure after casting to improve both toughness and strength. Austempering promotes the formation of acicular ferrite and retained austenite, which together enhance ductility and impact resistance without significantly compromising hardness (Alves et al., 2018). These approaches allow for the optimisation of carbide morphology and matrix toughness, helping to overcome the classic trade-off between wear resistance and brittleness in HCCIs.

Alves et al. (2018) demonstrated the benefits of austempering in their study on ductile cast irons, where they analysed the microstructural evolution and mechanical properties of a commercial alloy subjected to different austempering temperatures. The resulting microstructures consisted of acicular ferrite (bainite), retained austenite with high carbon content, and nodular graphite, features that contributed to the observed improvements in mechanical performance. Using techniques such as optical microscopy, scanning electron microscopy, and x-ray diffraction, they characterised three different grades of austempered ductile iron (ADI), each processed to achieve a specific strength level. Their tensile and impact testing at room temperature revealed a strong link between austempering temperature and mechanical behaviour. The sample austempered at 280°C exhibited the highest tensile and yield strength, reaching 1599 MPa and 1427 MPa, respectively, while the sample treated at 320°C showed the highest Charpy impact energy (99.90 J) and the greatest volume fraction of retained austenite (27%). These results confirm that austempering temperature directly affects the balance between strength and toughness, enabling precise control over mechanical performance through heat treatment.

This study highlights how principles from ADI research can be applied to HCCIs, where tailored heat treatment strategies such as austempering can refine the matrix and control phase transformation, leading to materials with improved toughness and wear resistance. When

adapted to high-Cr alloys, such strategies offer a valuable means of enhancing impact performance without sacrificing the high hardness needed for wear-critical applications.

Understanding how different processing methods affect the structure of HCCIs has improved a lot thanks to modern characterisation tools. Scanning Electron Microscopy (SEM) is widely used to examine features like carbides, grain size, and cracks. This helps us see how elements such as chromium and carbon form different structures in the alloy. However, Electron Backscatter Diffraction (EBSD), which is an advanced SEM technique, allows us to go even further. EBSD gives us detailed information about the crystal orientation, phase boundaries, grain structure, and internal strain of the material. It can do this with a very fine resolution, down to tens of nanometers, which is useful for studying HCCIs, where small changes in microstructure can affect hardness, wear, and toughness, particularly after heat treatment through secondary carbide precipitation (Vespucci et al., 2015).

EBSD works by capturing patterns called Electron Backscatter Patterns (EBSPs), which form when the electron beam hits a crystalline sample. These patterns are then analysed to work out the orientation of the crystals in the material. Recent software improvements have made this process more accurate. Some researchers have developed new methods to better detect and measure the angles between crystal planes, making EBSD results more precise (Britton et al., 2018; Zhang et al., 2021). This kind of accuracy helps identify how carbides are arranged and whether there are any issues like misorientation or strain that could lead to cracks or wear.

Recent improvements in EBSD equipment have made it even more powerful. Direct electron detectors, such as Timepix, now allow us to collect EBSPs with much better detail than older systems, which relied on converting electrons to light and back again. These new detectors work well even at lower beam energies (less than 5 keV), which helps improve resolution and reduces the area affected in the sample. They also make it possible to study lighter or lower-density materials, which were difficult to analyse before. Using energy filtering, where only electrons above a certain energy are used, also increases image contrast and reveals finer details in the crystal structure. These improvements help researchers study small carbides and subtle strain patterns that are important in understanding wear and corrosion in HCCIs. When even higher resolution is needed, especially in very small grains or highly deformed areas, Transmission Kikuchi Diffraction (TKD) is used. TKD works with very thin samples and gives crystal orientation maps with resolution better than 10 nanometers (Gao et al., 2021). TKD and high-resolution EBSD (HR-EBSD) are especially useful for looking at microstructural changes

caused by heat treatment, deformation, or phase transformation in HCCIs. These techniques help explain how certain features, like carbide-matrix boundaries, affect mechanical behaviour. The way EBSD data is analysed has also improved. New software and toolkits allow for faster and more accurate processing of large datasets. These tools can track grain changes during experiments and even use machine learning to find patterns in the data (Adams et al., 2021; Yi et al., 2024). This is especially useful in HCCI research, where many small changes in structure can have a big effect on performance.

Along with EBSD, X-Ray Diffraction (XRD) remains an important method for identifying phases in the alloy. XRD is very good at detecting the main types of carbides, like M_7C_3 and $M_{23}C_6$, as well as retained austenite and martensite. These phases influence hardness, toughness, and wear resistance. However, XRD gives information averaged over a large area and does not show where these phases are located. This is where EBSD is helpful; it adds spatial detail and shows how these phases are arranged in the microstructure. By combining XRD and EBSD, researchers get a much clearer picture of how the material is built and how it will behave in real applications.

Together, SEM, EBSD, and XRD give a complete set of tools to study the structure and performance of HCCIs. SEM shows the shape and size of features, XRD identifies the types of phases present, and EBSD links these to crystal structure, orientation, and strain. These techniques are essential for understanding how the Cr/C ratio, heat treatment, and alloying affect the properties of HCCIs, especially hardness, wear resistance, and corrosion behaviour.

Another important area of development is in alloying strategies and hardfacing techniques. Recent studies have explored the benefits of adding elements such as niobium, molybdenum, and titanium, which form complex carbides and carbonitrides that enhance both wear and corrosion resistance (Kishore et al., 2023). These fine, stable carbides not only increase surface hardness but also help resist crack initiation and propagation under abrasive or cyclic loading. Hardfacing technologies have also evolved, allowing for HCCI layers to be deposited onto critical components in demanding industrial environments. This targeted application of wear-resistant material, when combined with controlled alloy design and heat treatment, extends component life while maintaining cost efficiency. In addition, more advanced wear and fatigue testing methodologies are being introduced to evaluate how HCCIs perform under realistic service conditions. These tests now account for factors such as operating temperatures, contact pressures, and lubrication effects, offering a much clearer picture of how the material will

behave in practical settings. When coupled with predictive models and microstructural data, these tests validate the design decisions made during alloy development and help to further refine the relationships between composition, processing, and performance (Devlin, 2021).

Together, these innovations are driving a fundamental shift in how researchers and engineers study and design HCCIs. Rather than relying on general guidelines and post-failure analysis, modern research enables a proactive approach: one that predicts performance from the outset and allows fine-tuning of every stage, from alloy composition and casting to heat treatment and application. This integrated framework is making it possible to design HCCIs that not only meet but exceed the requirements for hardness, wear resistance, toughness, and corrosion resistance in even the harshest industrial environments.

2.9 Effect of Heat Treatment and Service Conditions on Mechanical Properties of HCCIs

Recent studies have highlighted the significant role of heat treatment in enhancing the mechanical properties of HCCIs. Heat treatments such as quenching and tempering are widely used to refine the microstructure, leading to improved hardness, wear resistance, and toughness (Guo et al., 2018; Zhang et al., 2022; Zhong et al., 2022). The heat treatment process enhances carbide morphology and promotes the precipitation of secondary carbides, which contributes to increased hardness and wear resistance while maintaining sufficient impact toughness. Sudhakar et al. (2022) demonstrated that heat-treated HCCI samples exhibited a more homogeneous carbide distribution, leading to a slight increase in toughness compared to as-cast samples. These findings indicate that, although the Cr/C ratio and casting conditions play a crucial role in determining the mechanical properties of HCCI, heat treatment serves as an additional refinement tool, further enhancing microstructural stability and performance. This aspect is particularly important for industrial applications requiring high wear resistance combined with impact toughness, such as mining and milling operations.

The type and distribution of carbides within the HCCI matrix play a fundamental role in determining hardness, wear resistance, and fracture toughness. Studies suggest that M_7C_3 carbides provide superior hardness and wear resistance, whereas $M_{23}C_6$ carbides contribute to better fracture toughness (Oanh & Viet, 2020; Ping et al., 2021; Yulianto et al., 2021). A well-balanced ratio of these carbides ensures that the alloy maintains resistance to surface wear while simultaneously absorbing impact energy without failure. Du et al. (2024) suggested that this balance could be optimised by precise control of the Cr/C ratio during alloy manufacturing.

Excessive hard carbides may increase brittleness, leading to reduced toughness, whereas too few carbides can result in higher wear resistance (Shi & Zhang, 2017; Guo et al., 2021). Fine-tuning carbide phases through careful composition control and heat treatment is therefore essential to achieving the best possible mechanical properties for HCCI used in severe service environments.

While microstructural characteristics significantly influence the performance of HCCIs, external service conditions also play a crucial role. In high-wear environments such as mining and milling, the interaction between hardness, wear resistance, and fracture toughness determines overall durability. Studies have shown that HCCI alloys optimised for these properties significantly reduce maintenance costs and downtime in industrial applications (Yang & Li, 2012; Guo et al., 2021). For example, in the mining industry, HCCI components with precisely controlled Cr/C ratios demonstrate high resistance to extreme abrasion and impact, thereby increasing equipment reliability and longevity (Panichkin et al., 2023; Goto et al., 2023; Du et al., 2024). The ability to optimise HCCI for specific operational conditions reinforces the importance of understanding how microstructural features influence mechanical properties.

Decades of research have contributed to the development of theoretical models that describe the mechanical behaviour of HCCI under varying conditions. Recent investigations have focused on modelling carbide nucleation and growth, providing a deeper understanding of the influence of the Cr/C ratio on alloy properties. One such approach is the phenomenological model, which explains the formation of carbides from carbon-rich regions during solidification (Li et al., 2023). This model is essential in predicting mechanical properties based on carbide distribution and refining alloy design for optimised performance. Additionally, studies have explored the associative perception framework, which analyses how HCCI responds to fluctuating service conditions. However, experimental studies on surface roughness and wear performance remain relatively limited. Future research should incorporate detailed wear studies to bridge the gap between theoretical predictions and real-world applications. The integration of modelling and experimental validation will enhance the predictive accuracy of the performance of HCCIs under extreme conditions.

The mechanical properties of HCCI, hardness, wear resistance, and fracture toughness are primarily dictated by its microstructural balance, which in turn is controlled by the Cr/C ratio. A well-balanced Cr/C ratio ensures the formation of a homogeneous, fine carbide network

within an austenitic matrix, optimising mechanical performance (Ma et al., 2006; Huang et al., 2013; Pourasiabi & Gates, 2022). Research consistently highlights that maintaining the correct Cr/C ratio is essential to prevent excessive brittleness or poor wear resistance. Furthermore, microstructural adjustments through heat treatment further refine carbide size, distribution, and morphology, improving the overall mechanical integrity of HCCI.

By combining experimental data, theoretical modelling, and process optimisation, researchers have developed guidelines for designing and processing HCCI components that meet industrial performance standards. These insights are crucial for extending the service life of HCCI-based materials in high-stress environments, where a precise balance between hardness, wear resistance, and toughness is required for optimal performance.

2.10 Research Gaps and Rationale for the Current Study

Despite the extensive research on HCCIs, there are still key gaps in understanding how the Cr/C ratio and solidification cooling rates collectively influence the as-cast and heat-treated microstructure. While previous studies have examined the effects of Cr/C ratio on phase stability, mechanical properties, and microstructural evolution (Bedolla-Jacuinde et al., 2005; Ortega-Cubillos et al., 2015; Stachowiak et al., 2015; Abdel-Aziz et al., 2017), and others have looked at how cooling rates impact carbide formation and distribution (Zhang et al., 2018; Sasaguri et al., 2019; Goto et al., 2023; Panichkin et al., 2023), these findings do not fully address how both parameters interact during solidification and influence final material performance, the core focus of the first and second research questions of this study. Most studies have either focused on optimising alloy composition in the as-cast condition or on evaluating the effects of heat treatment, but without fully accounting for how initial solidification microstructure affects subsequent thermal processing outcomes and mechanical behaviour (Karantzalis et al., 2009; Ai et al., 2011; Zhang et al., 2022). This is particularly relevant to research questions 1 and 2, which seek to understand the role of the Cr/C ratio in microstructural evolution and its consequences on hardness and toughness. This gap is significant because the solidification process influences carbide morphology, which in turn affects how the material responds to heat treatment and ultimately determines mechanical performance. A deeper understanding of this relationship is essential for developing HCCI components with optimised properties for wear and corrosion resistance.

Another critical limitation in the current literature is the lack of detailed exploration of microstructural variations caused by different Cr/C ratios combined with varied cooling rates.

Many studies have reported trends in carbide size, distribution, and volume fraction as functions of cooling rate or composition separately, yet their combined effects remain underexplored (Panichkin et al., 2023; Goto et al., 2023; Du et al., 2024). While it is well established that rapid cooling refines the microstructure and that an optimal Cr/C ratio enhances carbide stability, few studies have addressed how these two parameters together influence the carbide network and mechanical response, which are central to the second and third research questions regarding fracture toughness and corrosion/wear performance. This limits the ability to predict performance in real-world applications where both rapid cooling during casting and heat treatments are standard industrial practices. Additionally, the influence of non-equilibrium solidification on carbide precipitation and subsequent heat treatment response has not been adequately studied, leaving uncertainties in optimising processing parameters for enhanced wear resistance, hardness, and toughness (Siekaniec et al., 2022; Sudhakar et al., 2022).

This research aims to bridge these existing gaps by adopting an integrated approach that simultaneously considers both the Cr/C ratio and cooling curve characteristics to understand the microstructural evolution of HCCIs. This directly supports all three research questions, which aim to identify the microstructural effects of Cr/C ratio, evaluate its impact on mechanical properties, and understand performance in corrosive and abrasive environments. Unlike previous studies that treat alloy composition and cooling effects separately, this work explores their combined influence on as-cast and heat-treated microstructures and resulting properties. The study will integrate experimental investigations with advanced characterisation techniques to provide a comprehensive understanding of how these parameters interact. Key methods will include:

- Thermodynamic simulations using ThermoCalc to model phase transformations and carbide precipitation in non-equilibrium conditions.
- Cooling curve analysis to experimentally track solidification behaviour, identify critical temperatures, and assess the influence of different Cr/C ratios on phase formation and undercooling dynamics.
- Microstructural analysis using scanning electron microscopy (SEM) and energy-dispersive spectroscopy (EDS) to characterise carbide morphology, distribution, and matrix transformations.

By linking these techniques to both solidification and subsequent microstructural evolution, the study addresses the limitations of previous work, where the impact of as-solidified

microstructure on mechanical properties was considered in isolation or without connection to alloy composition and cooling behaviour. While heat treatment is included as a secondary factor, the primary focus remains on understanding how Cr/C ratio and cooling rate shape the initial microstructure. This sets the foundation for answering the third research question by correlating microstructural features with wear and corrosion test results. This integrated approach is expected to generate valuable insights for optimising alloy design, casting conditions, and property control to enhance wear and corrosion resistance in demanding industrial environments.

Understanding the Cr/C ratio and cooling rate effects in HCCI has significant practical implications. Industries such as mining, petrochemical processing, and milling rely on HCCI components to withstand harsh environmental conditions that demand exceptionally high hardness, wear resistance, and corrosion resistance. The third research question is directly aligned with this concern, seeking to relate microstructural characteristics to real-world performance metrics. The results will guide alloy design and processing improvements, helping to reduce maintenance costs, extend service life, and improve overall operational efficiency.

HCCIs are widely known for their high hardness and superior resistance to wear and corrosion (Abd El-Aziz et al., 2015). Many researchers, including Bedolla-Jacuinde et al. (2005), Karantzalis et al. (2009), Wiengmoon et al. (2011), and Ngqase & Pan (2020), have focused on improving these properties, as they are essential in engineering applications. The exceptional wear and corrosion resistance of HCCI is primarily attributed to its high carbide volume fraction, which is embedded in an austenitic matrix. These carbides, including M_3C, M_7C_3, $M_{23}C_6$, and M_3C_2 form under different chemical compositions and heat-treatment conditions (Abd El-Aziz et al., 2015).

Both chromium and carbon are critical elements in determining the ultimate mechanical properties of HCCI. Chromium, the primary alloying element, enhances corrosion resistance by forming M_7C_3 carbides that promote a protective oxide layer against corrosive attack (Fan et al., 2022). Carbon, on the other hand, influences carbide shape and formation, with higher carbon levels producing larger primary carbides, which increase hardness and wear resistance (Guo et al., 2021). While extensive research has been conducted on the independent effects of Cr and C, the synergistic influence of their ratio (Cr/C) is less understood, particularly in connection with performance outcomes, an area directly investigated in Research Questions 1 and 2.

Research on the Cr/C ratio in HCCI has shown that it significantly affects phase diagrams, mechanical properties, and wear resistance (Abd El-Aziz et al., 2015; Sasaguri et al., 2019; Liu et al., 2025). Studies suggest that a Cr/C ratio below 10 leads to a sharp increase in hardness but at the cost of reduced toughness. Optimal wear resistance is achieved when the Cr/C ratio is between 8 and 11, as this provides balanced hardness and impact resistance under both high-stress and low-stress abrasion conditions (Sasaguri et al., 2019). Additionally, the Cr/C ratio influences the transformation behaviour of HCCI during cooling. Higher Cr/C values slightly increase the pearlite transformation temperature and extend the transformation time, with the maximum post-transformation hardness occurring at a Cr/C ratio of 6 before declining (Sasaguri et al., 2019).

Further research is needed to explore the combined effects of Cr and C in HCCI, particularly in relation to solidification and cooling conditions. Guo et al. (2021) found that a low Cr/C ratio results in more carbide formation, increasing hardness and wear resistance but reducing toughness. The shape and size of carbides also matter; rod-like carbides enhance wear resistance but can increase brittleness (Wang et al., 2018). Conversely, a higher Cr/C ratio forms fewer carbides, improving toughness but compromising wear resistance. Additionally, carbides influence corrosion resistance, as more carbides reduce exposed surface area, minimising corrosion attack (Gong et al., 2023). The microstructure and carbide morphology, including size, shape, and distribution, dictate the performance of HCCI in different environments. Heat treatment further modifies this behaviour, adding another layer of complexity. Therefore, precisely controlling the Cr/C ratio, along with carbide morphology, is crucial to addressing the performance-based questions posed in this research.

In South Africa, high-chrome cast irons are widely used in mining, processing, and marine environments, where acidic and basic conditions accelerate wear and corrosion (Singh, 2016). Failures in these industries often result in high repair costs and equipment downtime. Understanding how the Cr/C ratio influences microstructure is essential for preventing such failures and improving material performance. Bedolla-Jacuinde et al. (2005) found that chromium-rich carbides enhance corrosion resistance by minimising reactive surface areas, but this requires precise control over alloy composition. This context underscores the need for application-specific microstructural optimisation, reinforcing the industrial relevance of Research Question 3.

This research will contribute to understanding how microstructure optimisation can improve HCCI for wear and corrosion resistance, ensuring that specific Cr/C ratios are tailored for industrial applications. This knowledge will guide future alloy design, allowing engineers to customise HCCI for different operating conditions, ultimately reducing maintenance costs and extending component lifespan.

2.11 Chapter Summary

This chapter provided a comprehensive review of the literature on high-chrome cast iron (HCCI), focusing on its composition, microstructure, thermal processing, and mechanical properties. Section 2.8 presented the newer techniques that are being implemented in the study of HCCIs to increase efficiency and experimental analysis accuracy as well as cutting down on intensive labour, allowing focus on the important aspects of the analysis. In Section 2.9, we examined the effects of heat treatments such as austenisation, quenching, and tempering on HCCI, highlighting how these treatments modify the microstructure by refining carbide size and distribution, as well as relieving residual stresses. These changes consequently enhance key mechanical properties, including hardness, wear resistance, and fracture toughness, particularly when optimised alongside the Cr/C ratio.

Section 2.10 identified several critical research gaps in existing literature. Previous studies have independently investigated the influence of the Cr/C ratio and cooling rates on microstructural evolution. However, few have explored these factors in combination, particularly in the transition from the as-cast to the heat-treated state. Due to the limited focus on the combined effects of these variables, further research is required to provide a more comprehensive understanding of HCCI processing. This knowledge is essential for optimising alloy design and component performance in wear and corrosion-intensive industries.

Sections 2.1 to 2.7 summarised the key findings of the literature review and theoretical framework, underscoring the significance of the synergistic effects of alloying elements, cooling rate, and thermal treatment on the microstructural evolution and mechanical performance of HCCI. The review has established a strong foundation for the research objectives, which seek to integrate these parameters to optimise HCCI for specific industrial applications. Subsequent chapters will now transition to methodology, addressing the identified research gaps by incorporating experimental investigations, assessment standards, and computational modelling. This approach will bridge the gap between theoretical knowledge

and practical application, ultimately contributing to the development of higher-performance materials for industrial use.

2.12 References

Abd El-Aziz, K., Zohdy, K., Saber, D., & Sallam, H. E. M. (2015). Wear and Corrosion Behaviour of High-Cr White Cast Iron Alloys in Different Corrosive Media. *Journal of Bio- and Tribo-Corrosion*, *1*(4).

Adams, D., Miles, M. P., Homer, E. R., Brown, T., Mishra, R. K., & Fullwood, D. T. (2021). Phase determination in dual phase steels via HREBSD-based tetragonality mapping. *Journal of Microscopy*, *282*(1), 60–72.

Ahmadian, Z., Danaee, I., & Golozar, M. A. (2014). Effect of surface treatment on corrosion resistance of 304 stainless steel implants in Tyrode solution. *Archives of Metallurgy and Materials*, *59*(1), 25–30.

Ai, Y.-L., Chen, W.-H., Ding, J.-Y., & He, W. (2011). Heat treatment process of low carbon high chromium white cast iron. *Jinshu Rechuli/Heat Treatment of Metals*, *36*(6), 107–110.

Alves, V. C. C., Baracho, L. L. de A., Dos Santos, C. T. A., Lopes, L. C. R., Silva, É. dos R., Freitas Da Silva, F. R., Da Fonseca, G. S., Leal, R. H., & Fonseca, M. da P. C. (2018). Correlation between microstructure and mechanical properties of austempered ductile irons. *Materials Science Forum*, *925 MSF*, 203–209.

Aslam, R. (2023). Potentiodynamic polarization methods for corrosion measurement. In *Electrochemical and Analytical Techniques for Sustainable Corrosion Monitoring: Advances, Challenges and Opportunities* (25–37).

Baharudin, B. A., Ayob, F., Abdul Rahim, A., Mustapha, M., Ismail, A., Ab Rahman, F., & Ismail, A. (2022). Investigation on the Mechanical and Microstructural Characteristics of Diffusional Bonded Gray Cast Iron and Low Carbon Steel. In *Advanced Structured Materials* 167, (245–262).

Betti, Z. A., & Ataiwi, A. H. (2020). Mechanical properties of 27Cr- white cast iron subjected to sub-zero heat treatments. *AIP Conference Proceedings*, *2213*.

Betts, A. J., Cassidy, J. F., & Culliton, D. (2017). Accurate assessment of instantaneous corrosion rates. *Corrosion and Prevention 2017*, *2017-November*.

Britton, T. B., Tong, V. S., Hickey, J., Foden, A., & Wilkinson, A. J. (2018). AstroEBSD: Exploring new space in pattern indexing with methods launched from an astronomical approach. *Journal of Applied Crystallography*, *51*(6), 1525–1534.

Camurri, C., Maril, J., & Romero, E. (2021). Effect of the morphology, size, distribution and homogeneity of carbides and matrix on wear resistance in high Cr-alloys white cast iron. *Materials Science Forum*, *1016 MSF*, 56–62.

Cesiulis, H., & Tsyntsaru, N. (2009). Non-destructive method for assessing thin oil films. *BALTTRIB 2009 - 5th Int. Conference, Dedicated to Lithuanian Millennium, 85th Anniversary of Lithuanian University of Agriculture, and 60th Anniversary of Department of Mechanical Engineering, Proc.*, 59–63.

Chen, J., Yan, W., Li, H., Lu, C.-G., & Fan, X.-H. (2006). Effect of solidification rate on primary phase M7C3 of high chromium cast iron. *Zhuzao Jishu/Foundry Technology*, *27*(6), 591–593.

Chen, L., Zhang, W., Lu, W., Wei, B., Huo, S., Wang, Y., & Zhou, Y. (2023). Low thermal conductivity of dense (TiZrHfVNbTa)Cx high-entropy carbides by tailoring carbon stoichiometry. *Journal of Advanced Ceramics*, *12*(1), 49–58.

Demmel, F., Hennet, L., & Jakse, N. (2021). The intimate relationship between structural relaxation and the energy landscape of monatomic liquid metals. *Scientific Reports*, *11*(1).

Deng, Y., Zhang, J., & Jiao, K. (2018). Viscosity measurement and prediction model of molten iron. *Ironmaking and Steelmaking*, *45*(8), 773–777.

Devlin, M. T. (2021). Tribology and Wear Modeling and Testing. In *Encyclopedia of Materials: Metals and Alloys* (vol589–595).

Feng, G., Jiao, K., Zhang, J., & Gao, S. (2021). High-temperature viscosity of iron-carbon melts based on liquid structure:The effect of carbon content and temperature. *Journal of Molecular Liquids*, *330*.

Fischer, D. A., Vargas, I. T., Pizarro, G. E., Armijo, F., & Walczak, M. (2019). The effect of scan rate on the precision of determining corrosion current by Tafel extrapolation: A numerical study on the example of pure Cu in chloride containing medium. *Electrochimica Acta*, *313*, 457–467.

Galvan, E., Malak, R. J., Gibbons, S., & Arroyave, R. (2014). Constraint satisfaction approach to the design of multi-component, multi-phase alloys. *Proceedings of the ASME Design Engineering Technical Conference*, *2B*.

Gao, S., Huang, M., Wang, J., & Ma, Q. (2021). Researchprogress of electron backscatter diffraction in the area of characterization technology. *Cailiao Kexue Yu Gongyi/Material Science and Technology*, *29*(3), 8–15.

Gasan, H., & Erturk, F. (2013). Effects of a destabilization heat treatment on the microstructure and abrasive wear behaviour of high-chromium white cast iron investigated using different characterization techniques. *Metallurgical and Materials Transactions A: Physical Metallurgy and Materials Science*, *44*(11), 4993–5005

Gong, P., Zhao, Y., Yang, H., & Wang, N. (2017). Effects of carbon and chromium content and heat treatment on mechanical properties of high chromium cast iron. *Jinshu Rechuli/Heat Treatment of Metals*, *42*(9), 137–142.

Goto, I., Fukuchi, K., & Kurosawa, K. (2023). Effects of solidification conditions on the microstructural morphologies and strengths of hypereutectic high-chromium white cast iron castings. *Materials Science and Engineering: A*, *886*.

Gu, J., Liu, S., Si, J., & Zhang, Z. (2024). Microstructure Evolution and Properties of Nitrogen-Bearing Hypereutectic High Chromium Cast Iron after Quenching. *Journal of Materials Engineering and Performance*.

Gu, S., Yao, Z., Li, M., Qu, N., Bu, E., Bai, X., Liu, Y., Lai, Z., & Zhu, J. (2023). Mechanical properties prediction of ferrite ductile iron via machine learning. *Physica Scripta*, *98*(12), 126003.

Guitar, M. A., Nayak, U. P., Britz, D., & Mücklich, F. (2020). The Effect of Thermal Processing and Chemical Composition on Secondary Carbide Precipitation and Hardness in High-Chromium Cast Irons. *International Journal of Metalcasting*, *14*(3), 755–765.

Guitar, M. A., Scheid, A., Nayak, U. P., Nakamura, L., Ponge, D., Britz, D., & Mücklich, F. (2020). Quantification of the Phase Transformation Kinetics in High Chromium Cast Irons Using Dilatometry and Metallographic Techniques. *Metallurgical and Materials Transactions A: Physical Metallurgy and Materials Science*, *51*(8), 3789–3801.

Gundlach, R. B., & Tartaglia, J. M. (2024). Effects of Silicon in High-Cr White Cast Irons. *International Journal of Metalcasting*, *18*(3), 1843–1853.

Guo, Q., Fu, H., Guo, X., Xing, Z., & Lin, J. (2021). Effect of carbon content on microstructure evolution and properties of hypereutectic high chromium cast iron. *Surface Review and Letters*, *28*(10).

Guo, Z. H., Xiao, F. R., Lu, S. L., Li, H. Y., & Liao, B. (2016). Effects of heat-treatment on the microstructure and wear resistance of a high-chromium cast iron for rolls. *Advances in Materials Science and Engineering*, *2016*.

Habib, K. (2015). Evaluation of transit stray current interference by optical interferometry methods. *Journal of Materials and Environmental Science*, *6*(7), 1902–1906.

Hagemann, P., Kawalla, R., Korpała, G., & Schmidtchen, M. (2012). The influence of the initial state on the softening and precipitation kinetics in hot metal forming. *Materials Science Forum*, *706–709*, 1397–1402.

Hemkemeier, T. A., Almeida, F. C. R., Sales, A., & Klemm, A. J. (2022). Corrosion monitoring by open circuit potential in steel reinforcements embedded in cementitious composites with industrial wastes. *Case Studies in Construction Materials*, *16*.

Huang, J.-S., Chen, H.-R., Zeng, X.-M., Zhu, L. X., & Jin, D.-H. (2008). Heat treatment process of Cr20 high Cr white cast iron refiner plates. *Jinshu Rechuli/Heat Treatment of Metals*, *33*(6), 101–104.

Huang, P., Ji, X.-L., Wu, H.-C., Shan, Y.-P., & Wang, K.-P. (2019). Effects of Cooling Rate on Solidification Structure and Wear Resistance of High Chromium Cast Iron. *Zhuzao/Foundry*, *68*(8), 854–859.

Huang, Y., Long, M., Liu, P., Chen, D., Chen, H., Gui, L., Liu, T., & Yu, S. (2017). Effects of Partition Coefficients, Diffusion Coefficients, and Solidification Paths on Microsegregation in Fe-Based Multinary Alloy. *Metallurgical and Materials Transactions B: Process Metallurgy and Materials Processing Science*, *48*(5), 2504–2515.

Ibrahim, M. M., El-Hadad, S., & Mourad, M. (2021). Influence of Niobium Content on the Mechanical Properties and Abrasion Wear Resistance of Heat-Treated High-Chromium Cast Iron. *International Journal of Metalcasting*, *15*(2), 500–509.

Imurai, S., Thanachayanont, C., Pearce, J. T. H., Tsuda, K., & Chairuangsri, T. (2014). Effects of Mo on microstructure of as-cast 28 wt.% Cr-2.6 wt.% C-(0-10) wt.% Mo irons. *Materials Characterization*, *90*, 99–112.

Karantzalis, A. E., Lekatou, A., & Mavros, H. (2009). Microstructural Modifications of As-Cast High-Chromium White Iron by Heat Treatment. *Journal of Materials Engineering and Performance*, *18*(2), 174–181.

Karantzalis, E., Lekatou, A., & Mavros, H. (2009). Microstructure and properties of high chromium cast irons: Effect of heat treatments and alloying additions. *International Journal of Cast Metals Research*, *22*(6), 448–456.

Kishore, K., Sarkar, K., & Arora, K. S. (2023). Effect of alloying elements on microstructure, wear, and corrosion behaviour of Fe-based hardfacing. *Welding in the World*, *67*(11), 2463–2475.

Kootsookos, A., & Gates, J. D. (2004). The effect of the reduction of carbon content on the toughness of high chromium white irons in the as-cast state. *Journal of Materials Science*, *39*(1), 73–84.

Kopycinski, D., Guzik, E., Siekaniec, D., & Szczesny, A. (2014). Analysis of the high chromium cast iron microstructure after the heat treatment. *Archives of Foundry Engineering*, *14*(3), 43–46.

Le Nué, C., Gallo, S. C., Vahid, A., Taherishargh, M., Attar, H., Fabijanic, D., & Barnett, M. (2024). Influence of Cooling Rate After Destabilization on Microstructure and Hardness of a High-Cr Cast Iron. *Metallurgical and Materials Transactions A: Physical Metallurgy and Materials Science*, *55*(6), 1722–1727.

Liu, E.-Z., Sun, S.-C., Tu, G.-F., Zheng, Z., Tong, J., & Guo, Y. (2008). Effects of heat treatments on structure and properties of a high chromium cast iron. *Jinshu Rechuli/Heat Treatment of Metals*, *33*(9), 29–32.

Li, D., Liu, L., Zhang, Y., Ye, C., Ren, X., Yang, Y., & Yang, Q. (2009). Phase diagram calculation of high chromium cast irons and influence of its chemical composition. *Materials and Design*, *30*(2), 340–345.

Li, J., Zhang, C., Jiang, B., Zhou, L., & Liu, Y. (2016). Effect of large-size M23C6-type carbides on the low-temperature toughness of martensitic heat-resistant steels. *Journal of Alloys and Compounds*, *685*, 248–257.

Li, Y., Zhu, P. X., Tang, C., & Sun, Z. (2022). Effects of Quenching Medium on Microstructure and Mechanical Properties of High Chromium Cast Iron. *Crystals*, *12*(10).

Liu, S., Li, J., Su, X., Cui, S., Zhang, H., & Ren, Z. (2025). Effect of Cr:C ratio on open three-body wear resistance of squeeze cast high chromium cast iron. *Tribology International*, *202*.

Lou, D., Liu, D., He, C., Bennett, P., Chen, L., Yang, Q., Fearon, E., & Dearden, G. (2016). Effect of Cr/C Ratio on Microstructure and Corrosion Performance of Cr3C2-NiCr Composite Fabricated by Laser Processing. *Journal of Materials Engineering and Performance*, *25*(1), 312–319.

Lynch, B., Wang, Z., Ma, L., Paschalidou, E.-M., Wiame, F., Maurice, V., & Marcus, P. (2020). Passivation-Induced Cr and Mo Enrichments of 316L Stainless Steel Surfaces and Effects of Controlled Pre-Oxidation. *Journal of The Electrochemical Society*, *167*(14), 141509.

Ma, L., Pascalidou, E. M., Wiame, F., Zanna, S., Maurice, V., & Marcus, P. (2020). Passivation mechanisms and pre-oxidation effects on model surfaces of FeCrNi austenitic stainless steel. *Corrosion Science*, *167*.

Ma, Y. P., Li, X. L., & Yang, L. (2011). Effects of Carbon Concentration Variation on Primary Austenite Stability of High Chromium Cast Iron. *Advanced Materials Research*, *154–155*, 1684–1688.

Ma, Y.-P., Li, J., Liu, Y.-G., Zhao, F., & Li, Z.-Y. (2006). Effects of carbon content variation on primary austenite stability of high chromium cast iron. *Zhuzao/Foundry*, *55*(10), 1079–1081.

Ma, Y.-P., Li, X., & Yang, L. (2011). Effects of carbon concentration variation on primary austenite stability of high chromium cast iron. *Advanced Materials Research*, *154–155*, 1684–1688.

Nayak, U. P., Guitar, M. A., & Mücklich, F. (2020). A comparative study on the influence of chromium on the phase fraction and elemental distribution in as-cast high chromium cast irons: Simulation vs. experimentation. *Metals*, *10*(1).

Oanh, N. T. H., & Viet, N. H. (2020). Precipitation of M23C6 secondary carbide particles in Fe-Cr-Mn-C alloy during heat treatment process. *Metals*, *10*(2).

Panichkin, A., Kenzhegulov, A., Mamaeva, A., Uskenbayeva, A., Kshibekova, B., Imbarova, A., & Alibekov, Z. (2023). Effect of Carbon and Cooling Rate on the Structure of Hypereutectic High Chromium Cast Iron in the Cast State and after Heat Treatment. *Journal of Composites Science*, *7*(12).

Panichkin, A., Wieleba, W., Kenzhegulov, A., Uskenbayeva, A., Mamaeva, A., Imbarova, A., Kvyatkovskii, S., & Kasenova, B. (2023). Effect of thermal treatment of chromium iron melts on the structure and properties of castings. *Materials Research Express*, *10*(8).

Poolthong, N., Nomura, H., & Takita, M. (2004). Effect of heat treatment on microstructure and properties of semi-solid chromium cast iron. *Materials Transactions*, *45*(3), 880–887.

Purevdorj, B., Ariunbolor, P., Temuulen, P., & Khavalbolot, K. (2024). Microstructure and Mechanical Properties of 28% High Chromium White Cast Iron. In *Materials Science Forum 1133*, 17–23.

Poorqasemi, E., Abootalebi, O., Peikari, M., & Haqdar, F. (2009). Investigating accuracy of the Tafel extrapolation method in HCl solutions. *Corrosion Science*, *51*(5), 1043–1054.

Poorqasemi, E., Haqdar, F., & Abootalebi, O. (2009). A study on the accuracy of the Tafel extrapolation method in HCl. *ECS Transactions*, *19*(29), 191–203.

Prasanna Kumar, T. S., Hernandez-Morales, B., & Totten, G. E. (2014). "Reference quench probe" - An alternative probe design for in-situ estimation of cooling rates, heat flux, and hardenability during immersion quenching of hardenable steels. *Materials Performance and Characterization*, *3*(4), 371–394.

Rybalka, K. V., Beketaeva, L. A., & Davydov, A. D. (2021). Estimation of Corrosion Rate of AISI 1016 Steel by the Analysis of Polarization Curves and Using the Method of Measuring Ohmic Resistance. *Russian Journal of Electrochemistry*, *57*(1), 16–21.

Rost, C. M., Borman, T., Hossain, M. D., Lim, M., Quiambao-Tomko, K. F., Tomko, J. A., Brenner, D. W., Maria, J. P., & Hopkins, P. E. (2020). Electron and phonon thermal conductivity in high entropy carbides with variable carbon content. *Acta Materialia*, *196*, 231–239.

Saal, J. E., Berglund, I. S., Sebastian, J. T., Liaw, P. K., & Olson, G. B. (2018). Equilibrium high entropy alloy phase stability from experiments and thermodynamic modeling. *Scripta Materialia*, *146*, 5–8.

Sakai, T., & Miura, H. (2010). Mechanisms of ultrafine grain formation in severe plastic deformation. *Materials Science Forum*, *638–642*, 98–103.

Sakai, T., & Miura, H. (2012). Ultrafine grain formation in aluminum alloys during hot severe plastic deformation. *Materials Science Forum*, *706–709*, 1829–1834.

Sasaguri, N., Yamamoto, K., Yokomizo, Y., & Matsubara, Y. (2019). Effect of Cr/C value on behaviour of continuous cooling transformation in plain high chromium cast iron. *Materials Transactions*, *60*(12), 2537–2541.

Scandian, C., Boher, C., de Mello, J. D. B., & Rézaï-Aria, F. (2009a). Effect of molybdenum and chromium contents in sliding wear of high-chromium white cast iron: The relationship between microstructure and wear. *Wear*, *267*(1–4), 401–408.

Shi, L., & Zhang, F.-Y. (2017). Effect of Heat Treatment on Microstructure and Properties of Cr26 High Chromium Cast Iron. *Zhuzao/Foundry*, *66*(4), 408-410and417.

Shimizu, K., Purba, R. H., Kusumoto, K., Yaer, X., Ito, J., Kasuga, H., & Gaqi, Y. (2019). Microstructural evaluation and high-temperature erosion characteristics of high chromium cast irons. *Wear*, *426–427*, 420–427.

Siekaniec, D., Kopyciński, D., Tyrała, E., Guzik, E., & Szczęsny, A. (2022). Optimisation of Solidification Structure and Properties of Hypoeutectic Chromium Cast Iron. *Materials*, *15*(18).

Sorg, M., & Ladwein, T. (2009). Investigation of the pitting corrosion behaviour of stainless steels in ethanol containing fuels. *NACE - International Corrosion Conference Series*.

Stan, I., Anca, D. E., Riposan, I., & Stan, S. (2023). Solidification pattern of 4.5%Si ductile iron in metal mould versus sand mould castings. *Journal of Thermal Analysis and Calorimetry*, *148*(5), 1805–1817.

Stan, S., Chisamera, M., Riposan, I., & Barstow, M. (2012). Application of thermal analysis to monitor the quality of hypoeutectic cast irons during solidification in sand and metal moulds. *Journal of Thermal Analysis and Calorimetry*, *110*(3), 1185–1192.

Stan, S., Chisamera, M., Riposan, I., Neacsu, L., Cojocaru, A. M., & Stan, I. (2017). Technique Incorporating Cooling & Contraction / Expansion Analysis to Illustrate Shrinkage Tendency in Cast Irons. *IOP Conference Series: Materials Science and Engineering*, *209*(1).

Strobl, S., & Haubner, R. (2020). Investigation of the diffusion couple ductile cast iron / iron. *Defect and Diffusion Forum*, *405 DDF*, 54–59.

Sudhakar, A. N., Markandeya, R., Srinivasa Rao, B., Ajoy, K. P., & Kaushik, D. (2022). Effect of alloying elements on the microstructure and mechanical properties of high chromium white cast iron and Ni-Hard iron. *Materials Today: Proceedings*, *61*, 1006–1014.

Sun, Y.-F., Yu, G.-W., Zhao, J.-Y., Li, Z.-M., Shi, A.-J., & Liu, X.-F. (2008). Effects of heat treatment on microstructure and properties of high chromium tungsten-containing cast iron. *Jinshu Rechuli/Heat Treatment of Metals*, *33*(9), 91–94. \

Tan, Y. (2011). Experimental methods designed for measuring corrosion in highly resistive and inhomogeneous media. *Corrosion Science*, *53*(4), 1145–1155.

Tan, Y., Lepkova, K., Bailey, S., & Gubner, R. (2009). A critical review on various corrosion testing and monitoring techniques. *49th Annual Conference of the Australasian Corrosion Association 2009: Corrosion and Prevention 2009*, 11–19.

Tang, X. H., Chung, R., Pang, C. J., Li, D. Y., Hinckley, B., & Dolman, K. (2011). Microstructure of high (45wt.%) chromium cast irons and their resistances to wear and corrosion. *Wear*, *271*(9–10), 1426–1431.

Tkacz, J., Minda, J., Fintová, S., & Wasserbauer, J. (2016). Comparison of electrochemical methods for the evaluation of cast AZ91 magnesium alloy. *Materials*, *9*(11).

Tokova, O., & Savchenko, Y. (2019). Modelling of Dependence of Mechanical Properties of Cast Iron on Chemical Composition of Raw Materials. *International Scientific and Technical Conference on Computer Sciences and Information Technologies*, *1*, 179–182.

Touhami, R. C., Mechachti, S., Bouhamla, K., Hadji, A., & Khettache, A. (2023). Wear Behaviour and Microstructure Changes of a High Chromium Cast Iron: The Combined Effect of Heat Treatment and Alloying Elements. *Metallography, Microstructure, and Analysis*, *12*(4), 580–590.

Vespucci, S., Winkelmann, A., Naresh-Kumar, G., Mingard, K. P., Maneuski, D., Edwards, P. R., Day, A. P., O'Shea, V., & Trager-Cowan, C. (2015). Digital direct electron imaging of energy-filtered electron backscatter diffraction patterns. *Physical Review B - Condensed Matter and Materials Physics*, *92*(20).

Wan, Y., Gao, S., Li, M. hua, Zhang, L. qiang, Wen, Y. hong, & Song, M. ming. (2021). Enrichment characteristic of carbon atoms in solid-liquid zone of high carbon steel under different directional solidification rates. *China Foundry*, *18*(5), 488–496.

Wang, J., Zeng, M., Yang, H.-S., Liu, H.-H., Sun, Z.-P., Shen, B.-L., & Huang, S.-J. (2005). Effect of heat treatment on microstructure of a high chromium cast iron. *Cailiao Rechuli Xuebao/Transactions of Materials and Heat Treatment*, *26*(6), 75–79.

Wiengmoon, A., Pearce, J. T. H., & Chairuangsri, T. (2011). Relationship between microstructure, hardness and corrosion resistance in 20 wt.%Cr, 27 wt.%Cr and 36 wt.%Cr high chromium cast irons. *Materials Chemistry and Physics*, *125*(3), 739–748.

Xia, Y.-J., Wang, F.-M., & Wang, J.-L. (2011). Simulation of Secondary Dendritic Arm Spacing of Free Cutting Steel 38MnVS. *Journal of Iron and Steel Research International*, *18*(6), 54-73.

Xu, J., Xiang, M., Dang, B., & Jian, Z. (2017). Relation of cooling rate, undercooling and structure for rapid solidification of iron melt. *Computational Materials Science*, *128*, 98–102.

Yan, W. (2020). Effect of mechanical stress on electrochemical corrosion of X65 carbon steel in CO2 saturated brine. *Materialpruefung/Materials Testing*, *62*(8), 803–808.

Yang, B., Peng, Q., Milkereit, B., Springer, A., Liu, D., Rettenmayr, M., Schick, C., & Keßler, O. (2021). Nucleation behaviour and microstructure of single Al-Si12 powder particles rapidly solidified in a fast-scanning calorimeter. *Journal of Materials Science*, *56*(22), 12881–12897.

Yang, C.-K., & Li, W. (2012). Effects of carbon contents on microstructure and wear resistance of the hypereutectic high chromium cast iron. *Zhuzao/Foundry*, *61*(12), 1393–1396.

Yang, W., Wei, J., & Huang, Z. (2007a). Microstructure in Fe-Cr-C hardfacing alloys with high C and Cr. *Hanjie Xuebao/Transactions of the China Welding Institution*, *28*(3), 85–88.

Yi, H., Zeng, X., & Guan, D. (2024). Data Science Approach for EBSD Data Processing and Materials Design for Magnesium Alloy. *Minerals, Metals and Materials Series*, 49–53.

Yu, H., Song, C., Cheng, F., Gao, Z., Chen, X., Wang, Y., & Zhang, Y. (2021). Microstructure and properties of a hypoeutectic high-Cr cast iron under different heat treatment conditions. *Jinshu Rechuli/Heat Treatment of Metals*, *46*(8), 56–60.

Yuan, X., Zhang, J., Zhang, S., Tan, T., & Ma, X. (2015). Corrosion behaviour of galvanized steel with exposed substrate in a marine environment. *Materials Performance*, *54*(2), 24–26.

Yue, Y., Liu, C., Shi, P., & Jiang, M. (2018). Passivity of stainless steel in sulphuric acid under chemical oxidation. *Corrosion Engineering Science and Technology*, *53*(3), 173–182.

Zhang, Y., Shen, Y., Peng, F., Jiang, C., Li, W., Miao, H., Huang, F., & Zeng, Y. (2021). Method for acquiring accurate coordinates of the source point in electron backscatter diffraction. *Journal of Microscopy*, *284*(3), 233–243.

Zhang, S., Zhang, H.-W., Miao, M., Feng, M.-M., Lei, H., & Wang, Q. (2021). Cellular automaton simulation on cooperative growth of M7C3 carbide and austenite in high Cr cast irons. *Wuli Xuebao/Acta Physica Sinica*, *70*(21).

Zhang, Z., Koyama, M., Wang, M. M., Tsuzaki, K., Tasan, C. C., & Noguchi, H. (2018). Microstructural mechanisms of fatigue crack non-propagation in TRIP-maraging steels. *International Journal of Fatigue*, *113*(January), 126–136.

Zhao, J., Jiang, Z., & Wei, D. (2013). Analysis of elemental segregation in a microalloyed cast steel. *Advanced Materials Research*, *652–654*, 2465–2468.

Zhao, Z., Song, R., Zhang, Y., Yu, P., & Pei, Y. (2021). Co-orientation relationship between secondary carbides and adjacent ferrite after quenching and tempering in high chromium cast iron. *Vacuum*, *184*.

Chapter 3: Materials and Methods

3. Process Overview

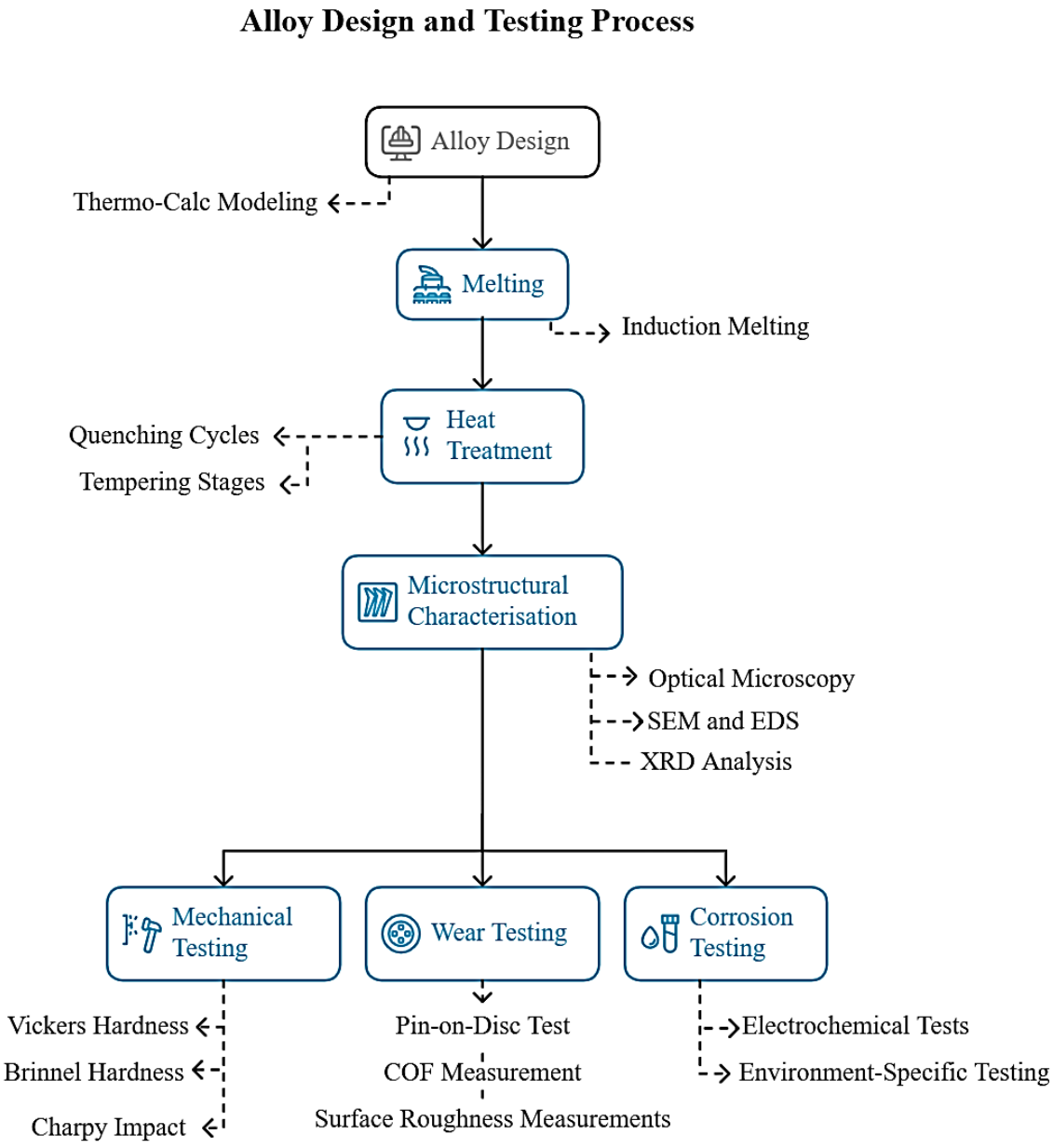

Figure 3:1 Alloy Design and Testing Process

3.1 Materials

3.1.1 Casting

Three batches of alloys were cast, varying the C and Cr content. Table 3.1 shows the composition of the alloys.

Table 3.1: Composition of the three cast iron batches

	Element (wt%)										
Sample	**C**	**Mn**	**S**	**P**	**Si**	**Cr**	**Cr**	**N**	**Cu**	**Fe**	**Cr/C ratio**
P1	1.98	0.28	0.022	0.029	0.2	24.01	24.01	0.22	0.03	49.22	12.13
P2	2.78	0.28	0.019	0.026	0.17	23.97	23.97	0.23	0.03	48.53	8.62
P3	2.96	0.29	0.02	0.027	0.18	23.87	23.87	0.23	0.03	48.52	8.06

Prior to casting, the intended composition was calculated for specific values, after which ThermoCalc was employed to estimate the resulting phases in HCCIs, their total atomic percentages, as well as the temperatures at which the transformations occurred under equilibrium conditions. The resulting Cr/C ratios were used in order to bias the results for better analyses of the cooling behaviour of HCCIs as well as the changes that occur in the microstructure pertaining to carbide volume, size, shape, and morphology through large and minor changes in the C content. The Cr was intended to be fixed. However, due to differences in the casting process, including unintended spillages, weight alterations in raw materials, and the conducting of the casting process, the actual results slightly changed. The following process was followed for casting. Moulds were made using chromite sand, which was mixed with the binding agent bentonite and water. Mixing was done with a sand mixer for 1 min 30 seconds, just in time to ensure that the sand was well mixed but not long enough to bind in the mixer. After thoroughly mixing, the sand was then poured and packed into a wooden pattern and compacted. The sand was left to solidify for approximately 15 minutes. The mould was then released from the pattern and left to harden for a few days. The raw materials, which consisted of iron scrap, iron remelt, Fe-Cr, Fe-Mo, and sascurb, were heated up in a 40 kg induction furnace to 1500°C and left to completely melt and thoroughly mix. A scoop of the metal was taken from the melt and poured into thermal analysis quick cups, which had thermocouples that were then connected to Nova software. As the molten metal cooled down and solidified,

the thermocouples transferred the cooling curve data to Nova, which drew a solidification cooling curve for each of the cups. After getting the graphs, the molten melt was poured into the moulds. With each pour into the moulds, the remaining composition of the melt was adjusted to fit the second composition, then ultimately the third composition. The casts, as seen in Figure 3.2, were left to solidify overnight. The same procedure was repeated for all 3 batches of cast, whose compositions are reported in Table 3.1.

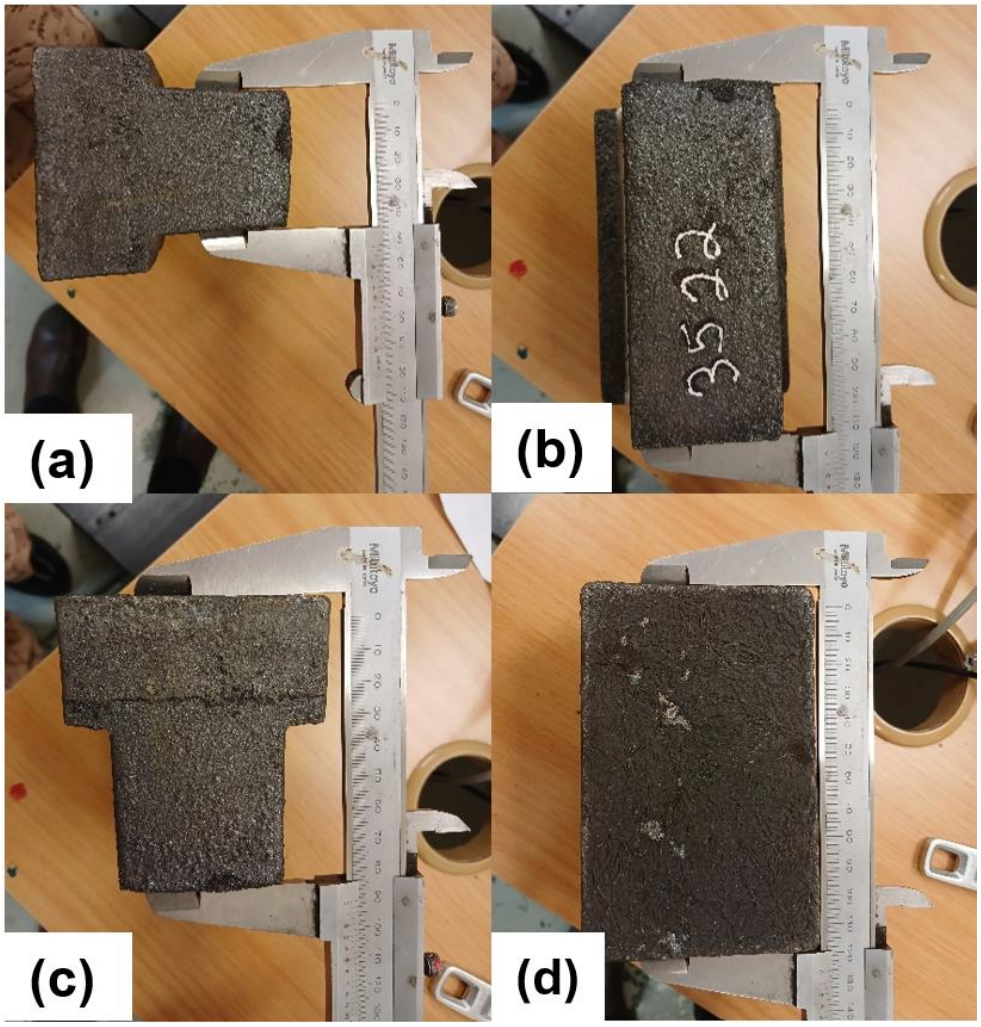

Figure 3.2: High chrome cast iron ingots

3.2 Methods

3.2.1 Sample Preparation

The samples are cut into 10×10×5 mm using a Gold San computer numerical control wire-cutting electrical discharge machine. The samples were mounted using bakelite using a Struers Bainmount Twin H Auto Specimen Mounting Press. The mounted samples were taken for grinding and polished to give a mirror surface finish using grit paper from P400 to P1200.

Using MD-Chem polishing cloth, the samples were polished at a speed of roughly 120 to 150 rpm using a Struers Tegramin-20 automatic polishing machine until a mirror surface was achieved. Non-crystallising colloidal silica was used to achieve the mirror finish required. The samples were etched using Murakami's reagents for 60 seconds using the immersion technique, then rinsed with distilled water.

3.2.2 Heat Treatment

Heat treatment was performed using the Bohler steel muffle furnace on three samples of each of the compositions. The following heat treatment procedure followed is represented by Figure 3.3. This heat treatment procedure was informed by (China Patent No. CN102899469B, 2013). This particular procedure was chosen as the owners of the invention claimed the specific procedure improved the toughness of the high chrome cast iron while preserving the wear resistance of the material. The procedure was reported to improve the toughness of the material by refining grains from the continuous plate-like structure common to high chrome cast iron to thicker spherical shapes in Cr28 alloy. Additionally, the procedure was reported to promote better diffusion to get a more uniform microstructure, which effectively refines the grains, thereby improving toughness.

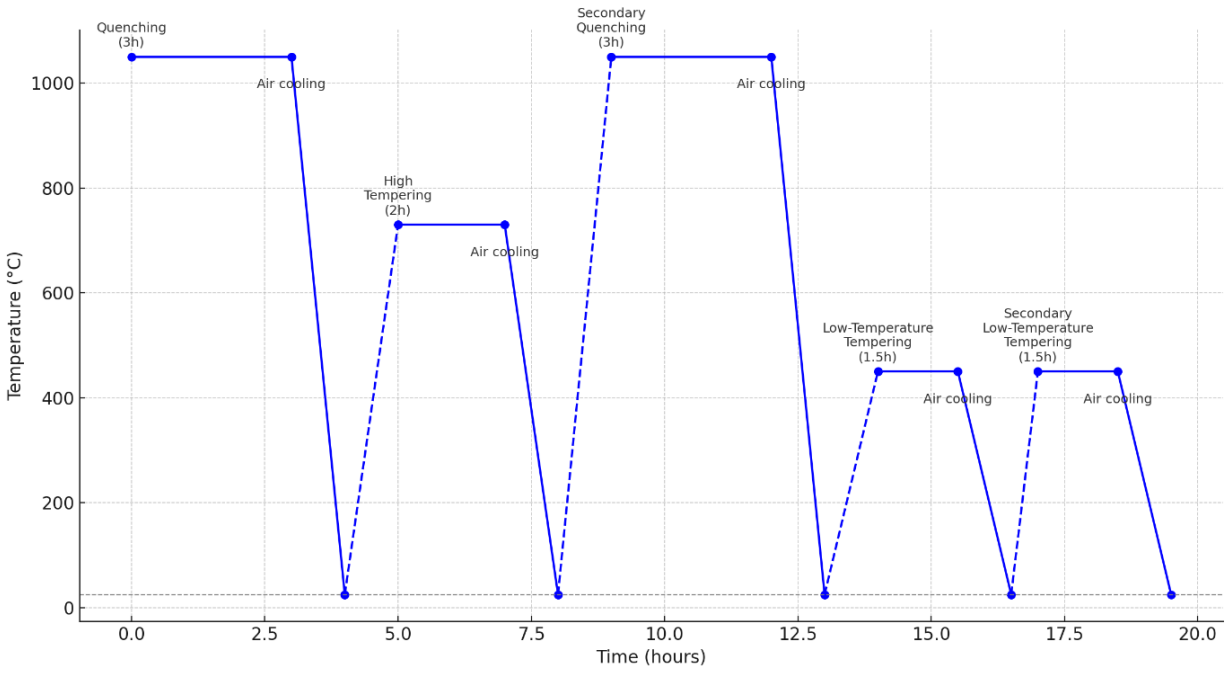

Figure 3.3: Heat treatment procedure followed for HCCI samples as designed in China Patent No.CN102899469B (2013).

3.2.3 Hardness Testing

Hardness testing for both the as-cast and heat-treated batches was done using the FutureTech Vickers Hardness tester (FM-800) equipped with a diamond indenter according to ASTM E92 standards as in ASTM E92-17 (2017), with the load set to 300 gf at 10 seconds dwell time. The hardness value of the samples for both as-cast and heat-treated batches was obtained by averaging at least five indentations made to each sample across three separate samples of the same composition, for a total of 15 indentations for one composition. Bulk hardness on larger samples was also done using a Brinell hardness indenter for bulk hardness analysis on the samples, as the material consists of two phases that cannot be accurately covered by the Vicker's hardness indenter. The indentations were done using ASTME10-15 standards with parameters shown in Table 3.2 (ASTM E10-15, 2012).

Table 3.2: Testing parameters for Brinell testing

Brinell Hardness	**Ball Diameter D (mm)**	**Force Diameter Ratio**	**Nominal Value of Test Force, F**		**Recommended Hardness Range HBW**
			N	kgF	
HBW 10/3000	10	30	29420	3000	95.5 to 650

3.2.4 Wear Testing

The pin-on-disc wear tests, dry abrasion tests, were conducted according to ASTM G99 standards, as in ASTM G99-23 (2023) , on a CSM ball-on-disk tribometer. The tests were conducted at room temperature, under a 10 N load for 1 km using a 6 mm Al_2O_3 ball. Alumina wear balls are preferred over 100Cr6 steel balls when testing high-chromium cast iron (HCCI) samples because they provide more accurate and controlled wear measurements. Unlike 100Cr6, which is metallic and similar in hardness to HCCI, alumina is a much harder ceramic material that resists deformation and wear. This ensures that most of the wear occurs on the HCCI sample, not the ball, allowing for a clearer assessment of the wear resistance of the alloy. Additionally, the chemical inertness of the alumina ball prevents reactions with the metal surface and avoids metal-to-metal adhesion, which can distort results (Pelleg, 2016). The white ceramic surface also makes it easier to observe material transfer from the HCCI sample, especially when adhesive wear occurs. As a result, alumina offers a more stable and reliable counterbody in tribological tests, especially under standards like ASTM G133, which recommend minimal wear on the ball. The total time came to 1 hr 23 mins. Table 3.3 shows the parameters used during the tests.

Table 3.3: Pin-on-disc wear testing parameters

Testing parameters	Values
Sliding speed	0.10 m/s
Sliding distance	1000 m
Nominal load	10 N
Acquisition radius	6 mm
Humidity	40%
Testing temperature	20±5°C

The traditional method was used to determine the wear volumes of the high chrome cast iron alloys based on the wear track's average maximum penetration depth (Bhushan, 1992). The average penetration depth technique is applied, assuming that the wear track has an elliptic curve, a profile of Hertzia. Using the Elcometer 7062 MarSurf PS10 surface roughness tester (profilometer) to measure the cross-sectional area of the wear scars by moving the stylus across the wear scar from the edge, the wear scar profiles of the alloys were analysed to obtain the data on the penetration depth of the wear tracks of the alloys. The HCCI alloys' wear volume (V_w) was determined using Equation 3.1.

$$V_w = A_w P d_{max} \quad \text{Equation 3.1}$$

Where: V_w= wear volume (mm^3), A_w = worn surface area (mm^2), and Pd_{max}= average penetration depth (mm). The specific wear rates (SWR) of the titanium alloys were calculated using Equation 3.2 (Archard, 1953; Kiefer, 2006).

$$SWR = \frac{V_W}{F \times s} \quad \text{Equation 3.2}$$

Where SWR = wear rate (mm^3 /Nm), F = load (N), and s = sliding distance (m). This procedure was followed for both the as-cast and heat-treated samples.

3.2.5 Corrosion Testing

The electrochemical potential dynamic corrosion tests were conducted as per ASTM G5-94, (1999) standards with a potential dynamic analogic polarisation measurement for both the as-cast and heat-treated batches. An A3 electrode electrochemical cell connected to a Gamry potentiostat setup was used for the testing. The electrolytes, 0.5M H_2SO_4, 0.5M NaOH, and 3.5 wt.% NaCl solutions, were used for each of the compositions of the sample. A platinum wire

was used as the counter electrode, and an Ag/AgCl 3.5M KCl electrode was used as the reference, with the exposed surface of the HCCI samples as the working electrode. The test began with running an open circuit potential (OCP) test for 3600 seconds, followed by a linear polarisation scan ranging from -0.5 to 1 V at a standard scan rate of 0.1667 mV/s at room temperature. After the tests, the calculation of the corrosion potential (Ecorr), corrosion current density (Icorr), and corrosion rates was done according to ASTM G59-97 standards (ASTM G59 Standards, 2020). The corrosion rate was calculated using Equation 3.3

$$CR = \frac{KI_{corr}\,EW}{\rho} \qquad \text{Equation 3.3}$$

where K = constant, EW = equivalent weight, and ρ = calculated density

3.2.6 Impact Toughness Testing

The samples were tested according to ISO 179 testing standards (ISO 179-2, 2020). As shown in Figure 3.4, the typical Charpy impact test specimen had a notch machined across one of the larger dimensions and measured 55 × 10 × 10 mm, as in Figures 3.3(a) and (b). The energy that a conventional notched specimen absorbs when it breaks under an impact load was measured by the Tinius Olsen Charpy impact testing machine and recorded. In this test, the specimen was held firmly at both ends while being struck with a hammer on a pendulum arm, with the hammer hitting in the opposite direction facing the notch as shown in Figure 3.4(c). By monitoring the decrease in motion of the pendulum arm, the energy absorbed by the specimen was precisely ascertained. Low temperatures, high strain rates (from impact or pressurisation), and stress concentrators like notches are crucial elements that influence the toughness of the material.

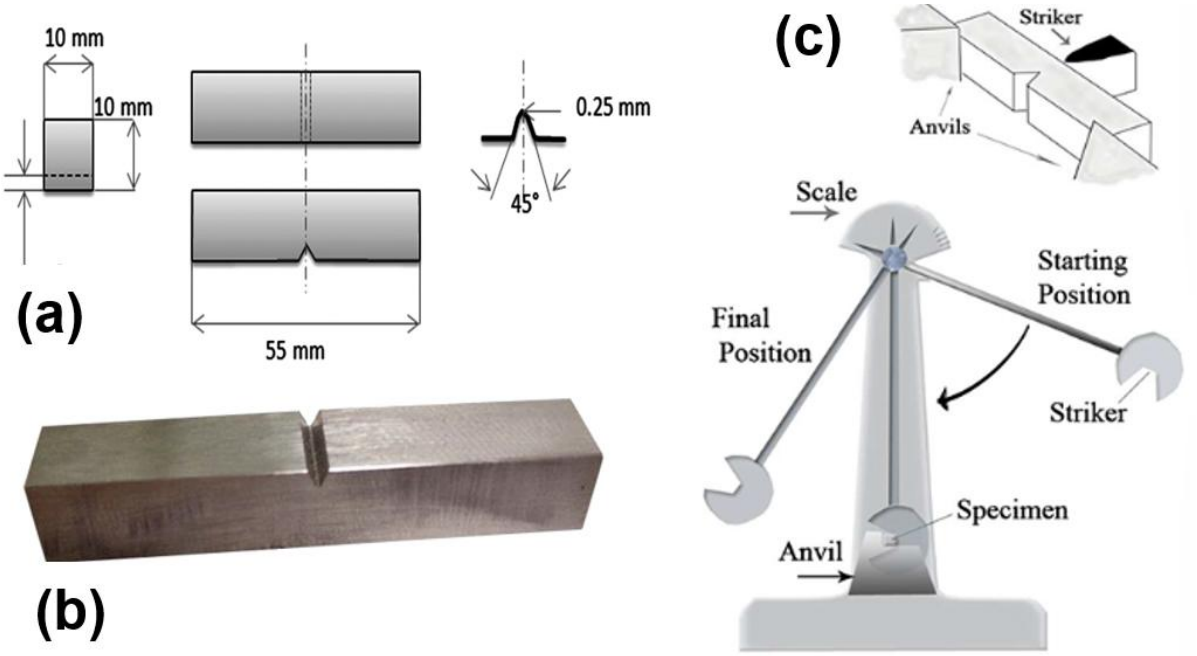

Figure 3.4: (a) The standard Charpy impact test sample dimensions used for the HCCI samples (Barbosa et al., 2012) (b) a photograph of one of the test samples and (c) shows the machine and the mechanism of the Charpy impact test (Charpy Impact Testing, 2024).

3.2.7 Microstructural Analysis and X-ray Diffraction

Microstructural analyses were done using the Carl Zeiss SmartSEM SIGMA 03-39 at magnifications ranging from 200 X to 15.00 kX using both secondary electron and electron backscattered imaging in order to study the microstructural characteristics, carbide morphology, and phase distribution. The samples were analysed at 20 kV at a current of 30 µAmps. Energy dispersive spectroscopy (EDS) analyses using an Oxford x-act PentaFET Precision Instrument with Inca for Windows 7 software to do spot and area analyses to help characterise the phases and other features of interest. The same analyses were done for the as-cast samples, heat-treated samples, and corroded and worn surfaces. Additional phase analysis was done using the X-ray diffraction technique with the parameters of a Co Kα radiation source [$\lambda = 1.78899$ Å] at 30 kV and 25 mA within the 2θ range of 20 to 120° at 25 °C. Failure analysis of the fracture surfaces after impact testing was done using a stereoscope in order to analyse the fracture patterns on the fractured surface.

3.3 References

Archard, J. F. (1953). Contact and rubbing of flat surfaces. *Journal of Applied Physics*, *24*(8), 981–988.

ASTM E10-15. (2012). Standard Test Method for Brinell Hardness of Metallic Materials. *ASTM International*, *June*, 1–36.

Barbosa, A. Q., Da Silva, L. F. M., Öchsner, A., Abenojar, J., & Del Real, J. C. (2012). Influence of the size and amount of cork particles on the impact toughness of a structural adhesive. *Journal of Adhesion*, *88*(4–6), 452–470.

Bhushan, B., & Majumdar, A. (1992). Elastic-plastic contact model for bifractal surfaces 53. In *Wear* (Vol. 153).

Method, S. T. (2000). *iTeh Standards iTeh Standards Document Preview*. *08*(Reapproved 1989), 3–4.

ISO 179-2: 2020, 2020. Plastics—Determination of Charpy Impact Properties—Part 2: Instrumented Impact Test.

Standard Reference Test Method for Making Potentiostatic and Potentiodynamic Anodic Polarization Measurements 1. (1999). 1-6

G02 Committee, 2017. Test method for wear testing with a pin-on-disk apparatus. ASTM International: West Conshohocken, PA, USA, 1-6.

E28 Committee, 2023. Test Methods for Vickers Hardness and Knoop Hardness of Metallic Materials. ASTM International.

Chapter 4: The Effects of Cr/C Ratio on the Microstructure of High Chrome Cast Iron

4.1 Introduction

The mechanical properties of HCCI, such as the hardness, toughness, wear, and corrosion resistance, are significantly affected by its microstructure, which comprises a hard carbide phase embedded in a softer matrix. The Cr/C ratio is a critical factor influencing the type, volume, and distribution of carbides within the microstructure. An increased Cr/C ratio typically reduces the carbide volume and promotes a more uniform distribution of carbides within the material, while a lower Cr/C ratio increases the carbide volume and promotes the growth of larger carbides within the microstructure (Kootsookos & Gates, 2004; Guo et al., 2021). Heat treatment is a frequently utilised procedure to refine the microstructural properties of high chrome cast iron, improving its mechanical properties. Quenching and tempering can enhance the carbide structure and convert the matrix to martensite as well as promote secondary carbide precipitation. To optimise HCCI for various industrial applications, this section explores how the Cr/C ratio influences the carbide volume, phases, and morphology, and how these, in turn, impact the resulting microstructural properties. This will be achieved by analysing the microstructure of the cast samples, followed by a discussion of the observations. Additional techniques, such as EDS and XRD analysis, will be utilised to gain a deeper understanding of the microstructure. Additionally, this chapter examines how heat treatment further modifies high chrome cast irons microstructural properties.

4.2 Role of Alloying Elements Composition on HCCI Samples

The composition of the three cast iron batches, obtained through spark analysis after casting, is shown in Table 4.1, along with their Cr/C ratios and carbide volumes. The goal for samples P1 to P3 was to increase the carbon content (1.98–2.96 wt%) from P1 to P3, representing the composition of hypoeutectic high-chromium cast iron, while keeping the chromium content relatively constant (>23 wt%). This introduced differences in the Cr/C ratio, as shown in Table 4.1. Silicon, nickel, manganese, and copper are present at low levels (<0.03 wt%), while molybdenum is higher at >1 wt%. Sulphur and phosphorous were also kept at low levels (<0.3 wt%). Iron makes up the majority of the composition, with a content of over 70 wt%. The carbide volume was calculated using a theoretical formula (Jacuinde et al., 2005).

$$\%CV = 12.33 \times \%wt.C + 0.55 \times \%wt.Cr - 15.2\% \quad \text{Equation 4.1}$$

Table 4.1: Composition of the three cast iron batches

	Elements(wt%)											
Sample	**C**	**Mn**	**S**	**Mo**	**P**	**Si**	**Cr**	**Ni**	**Cu**	**Fe**	**Cr/C ratio**	**Theoretical Carbide Volume (%)**
P1	1.98	0.28	0.022	1.09	0.029	0.2	24.01	0.22	0.03	72.14	12.13	22.42
P2	2.78	0.28	0.019	1.06	0.026	0.17	23.97	0.23	0.03	71.44	8.62	32.26
P3	2.96	0.29	0.02	1.08	0.027	0.18	23.87	0.23	0.03	71.31	8.06	34.43

4.3 Prediction of Phase Results using Thermocalc

The ThermoCalc phase diagrams and compositional data provide valuable insights into the formation of phases and their evolution across different temperatures for samples P1, P2, and P3. These phases include the liquid phase, metallic matrices (FCC_A1 and BCC_A2), and carbides (M_7C_3, M_3C_2, and $M_{23}C_6$). Each sample shows a unique phase behaviour due to differences in Cr/C ratio and other compositional factors, which significantly influence the final carbide volume. The predicted phase formation is based on thermodynamic principles, including equilibrium phase stability, solute redistribution, and carbide precipitation kinetics.

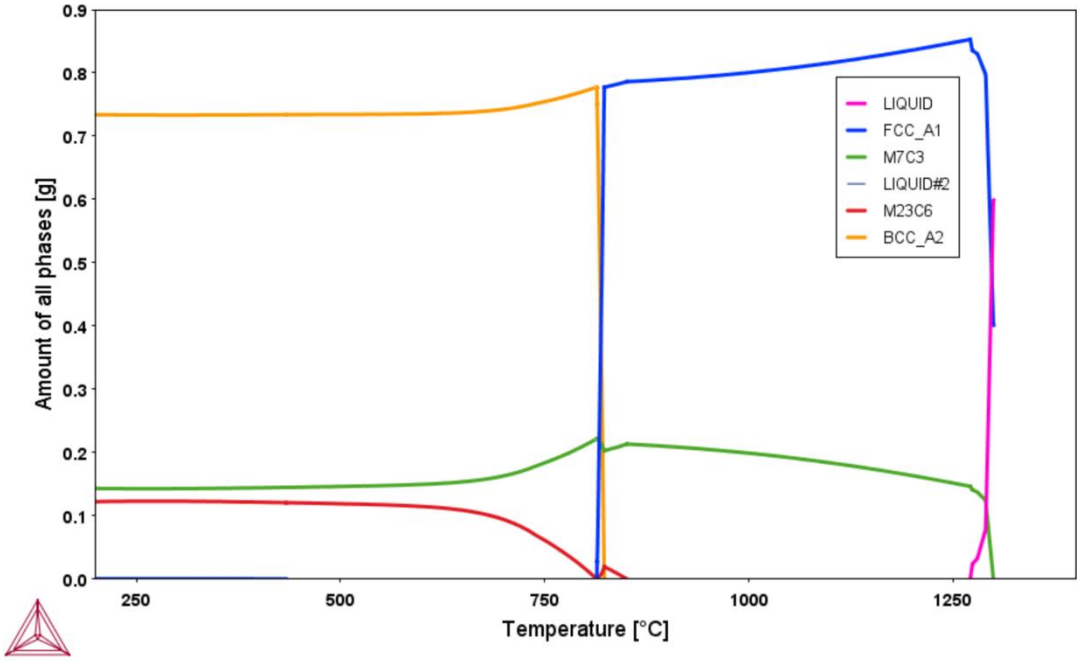

Figure 4.1: Predicted phase diagram for P1

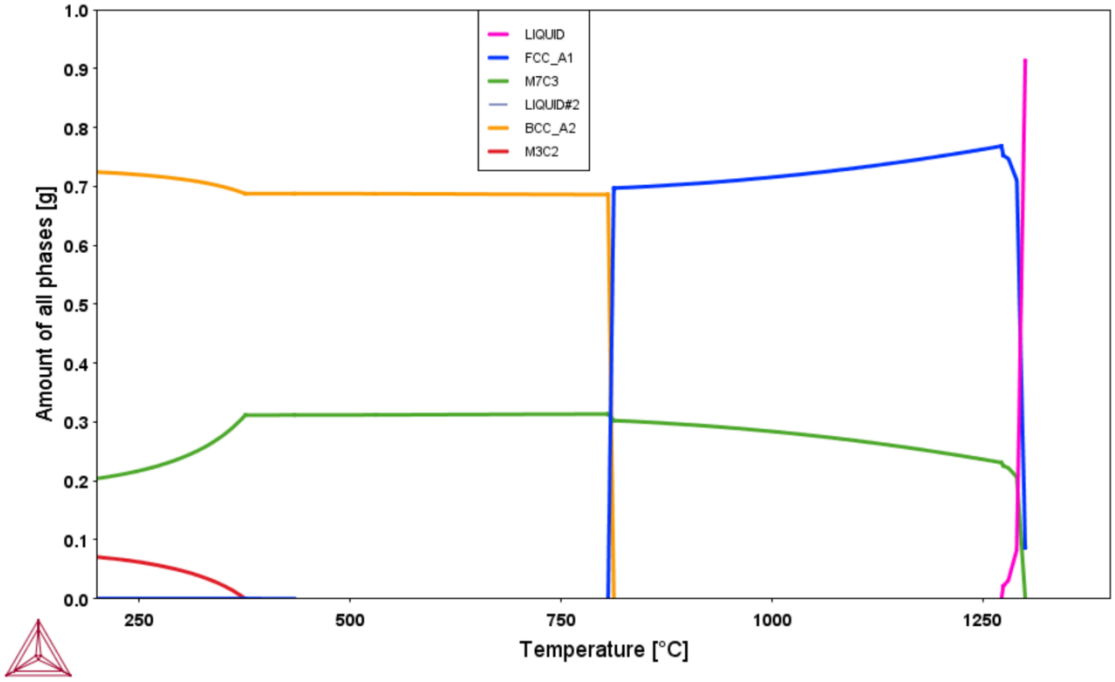

Figure 4.2: Predicted phase diagram for P2

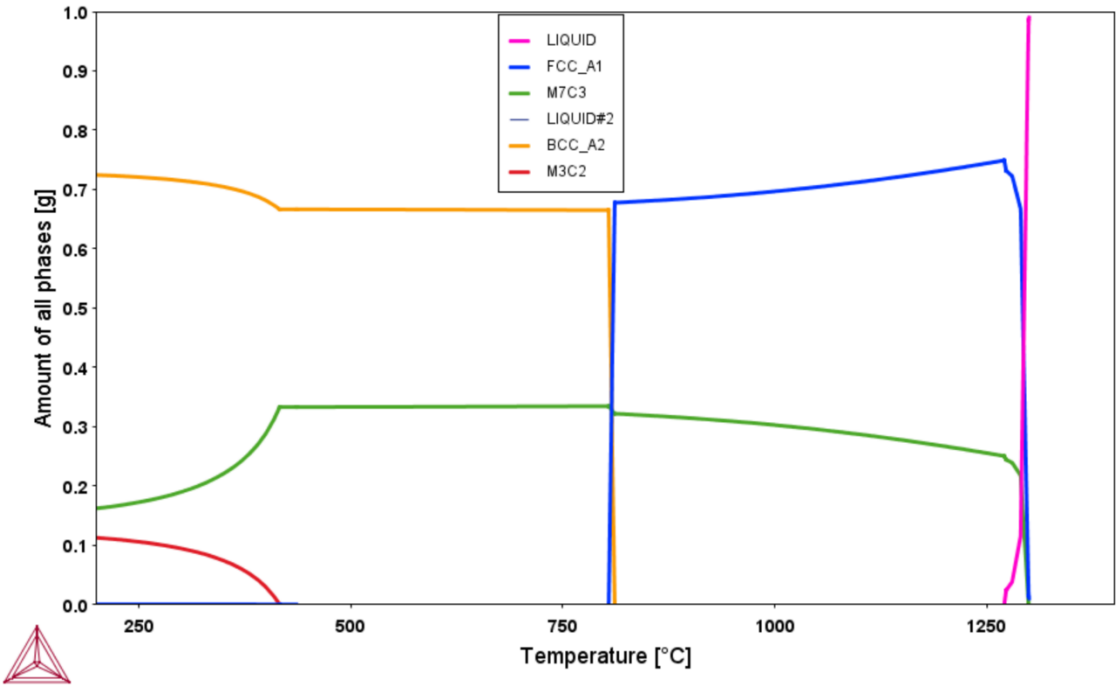

Figure 4.3: Predicted phase diagram for P2

Figure 4.1 shows the predicted phase diagram for P1. For P1, the liquid phase begins forming at approximately 1290°C and dominates at higher temperatures, disappearing when the formation of the first phase, FCC_A1, begins. The FCC_A1 phase (austenite) is the primary metallic matrix, beginning formation at ~1290°C from the liquid, where it accounts for about 80% of the volume. This gradually decreases until it completely disappears around 800°C when the BCC_A2 phase begins to form. Below 400°C, the BCC_A2 ferrite phase remains relatively stable, occupying ~73% of the microstructural volume. Carbide formation in P1 is dominated by the M_7C_3 phase, which forms at ~1290°C and steadily increases in volume before slightly decreasing when the $M_{23}C_6$ phase begins to form at ~850°C. $M_{23}C_6$ increases in volume until ~700°C, where it stabilises below 400°C. Below this temperature, the retained phases are ~73% BCC_A2 ferrite, ~15% M_7C_3, and ~12% $M_{23}C_6$ carbides. ThermoCalc predicts a total carbide volume of ~27%, which is slightly higher than the calculated carbide volume of 22.42% from the actual composition of the alloy presented in Table 4.1.

Figure 4.2 shows the predicted phase diagram for P2. For P2, the liquid phase forms at ~1290°C and transitions into FCC_A1 (austenite) and M_7C_3 carbides. FCC_A1 remains the dominant metallic matrix, accounting for approximately 65% of the volume above ~850°C, before gradually decreasing and disappearing as the BCC_A2 ferrite phase starts forming.

Below 400°C, BCC_A2 stabilises, occupying ~70% of the microstructure. M_7C_3 carbides form at ~1290°C and steadily increase in volume until ~400°C, where M_3C_2 carbides precipitate out, slightly reducing the M_7C_3 volume. Below 400°C, the retained phases are ~72% BCC_A2, ~21% M_7C_3, and ~7% M_3C_2 carbides. ThermoCalc predicts a total carbide volume of ~28%, which is lower than the calculated value of 32.26% shown in Table 4.1.

Figure 4.3 shows the predicted phase diagram for P3. For Sample P3, the liquid phase exhibits similar behaviour to P2, forming at ~1290°C and transitioning to FCC_A1, which remains stable up to ~850°C and accounts for ~65% of the volume before disappearing as the BCC_A2 phase starts forming. Below 400°C, BCC_A2 stabilises, occupying ~72% of the microstructure. Carbide formation is primarily driven by M_7C_3, which forms at ~1290°C and steadily increases until ~400°C, when M_3C_2 carbides precipitate, slightly reducing the M_7C_3 volume. Below 400°C, the retained phases are ~72% BCC_A2, ~17% M_7C_3, and ~11% M_3C_2 carbides. ThermoCalc predicts a total carbide volume of ~28%, which is lower than the calculated value of 34.43% in Table 4.1.

Although there is a marginal difference between the predicted carbide volume from Thermo-Calc and those obtained from the actual composition of the alloys, one common trend is that the progression from P1 to P3 demonstrates an increase in carbide volume, with P3 having the highest carbide fraction. Across all samples, the stability of the FCC_A1 matrix decreases as the carbide volume increases. The BCC_A2 ferrite phase was the highest phase retained across all three samples, taking about ~70% of the whole volume of the microstructure. This predicts that the ferrite phase is the phase that would make up the matrix, while the carbides would take up to 30% of the volume.

4.4 Cooling Curves of the HCCI Samples

Figure 4.4 illustrates the cooling behaviour of P1 during the casting process. The alloy followed a typical cooling pattern for hypoeutectic cast irons, cooling in a liquid cooling region reaching the liquidus temperature (TL) where solidification begins, followed by a dual phase liquid and solid region where the remaining liquid fully solidifies as the temperature decreases over a period of time. The pouring temperature was ~1280ºC. Cooling in the liquid region (green) continued until the liquidus temperature (TL) of ~1270ºC was reached after ~21 seconds.

Solidification began at this point (red) and was completed in 23 seconds at ~1200°C, bringing the total solidification time to 44 seconds.

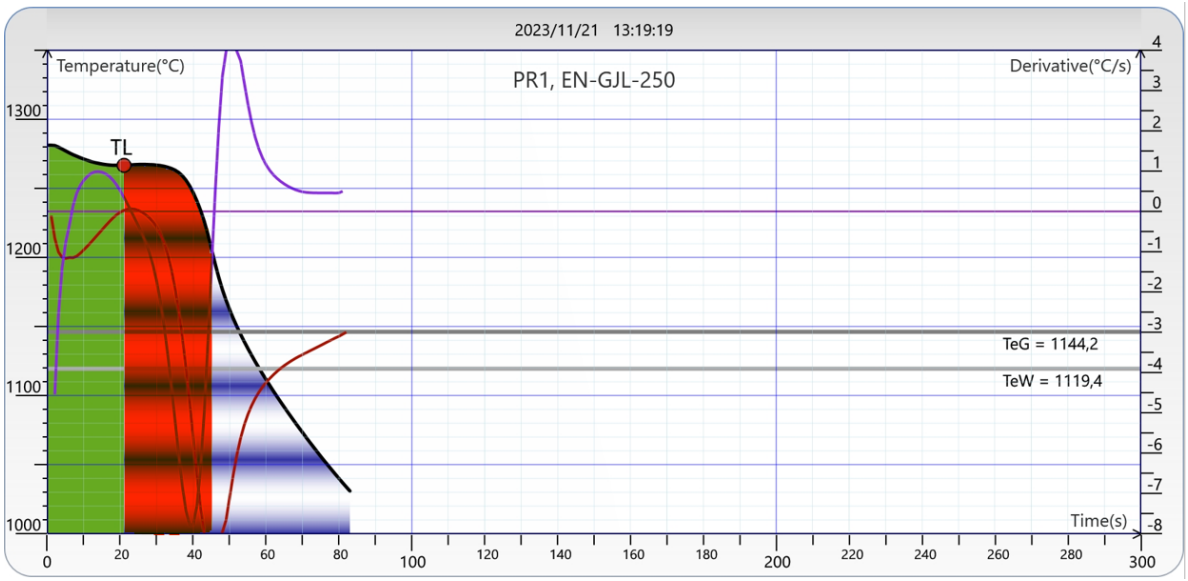

Figure 4.4: Cooling curve showing cooling behaviour for P1

The cooling behaviour of P2, shown in Figure 4.5, followed a similar pattern but with significant differences. The pouring temperature was also ~1280ºC, but the liquidus temperature was reached after ~41 seconds, resulting in a longer liquid cooling region compared to P1. Solidification in P2 took ~59 seconds, bringing the total solidification time to ~100 seconds, indicating a significantly longer total solidification time.

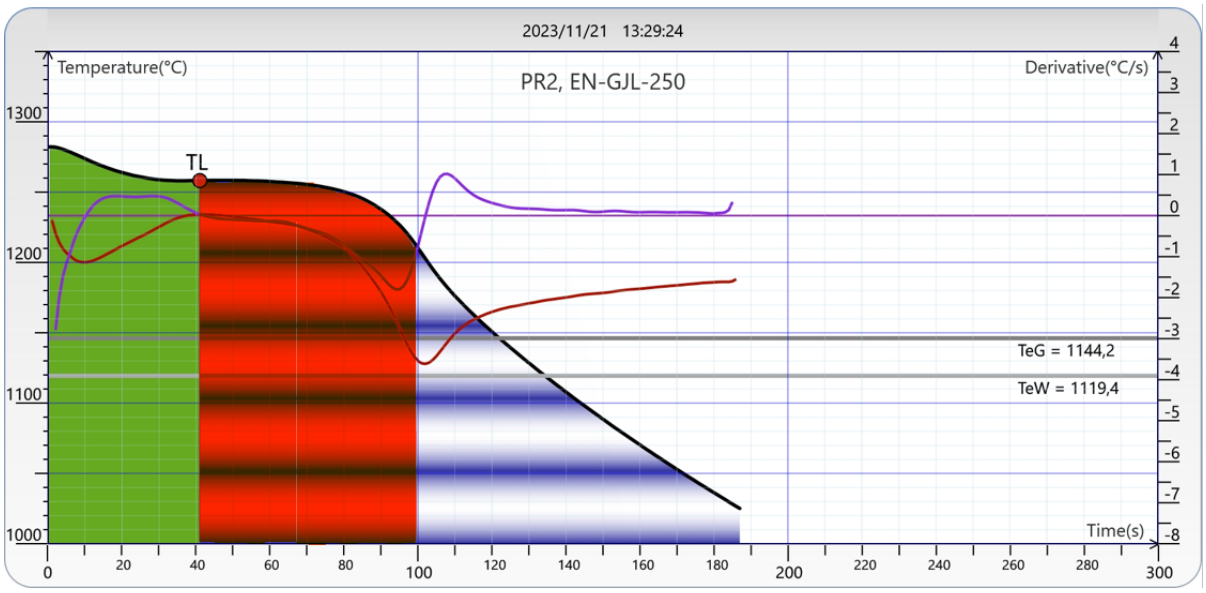

Figure 4.5: Cooling Curve showing cooling behaviour for P2

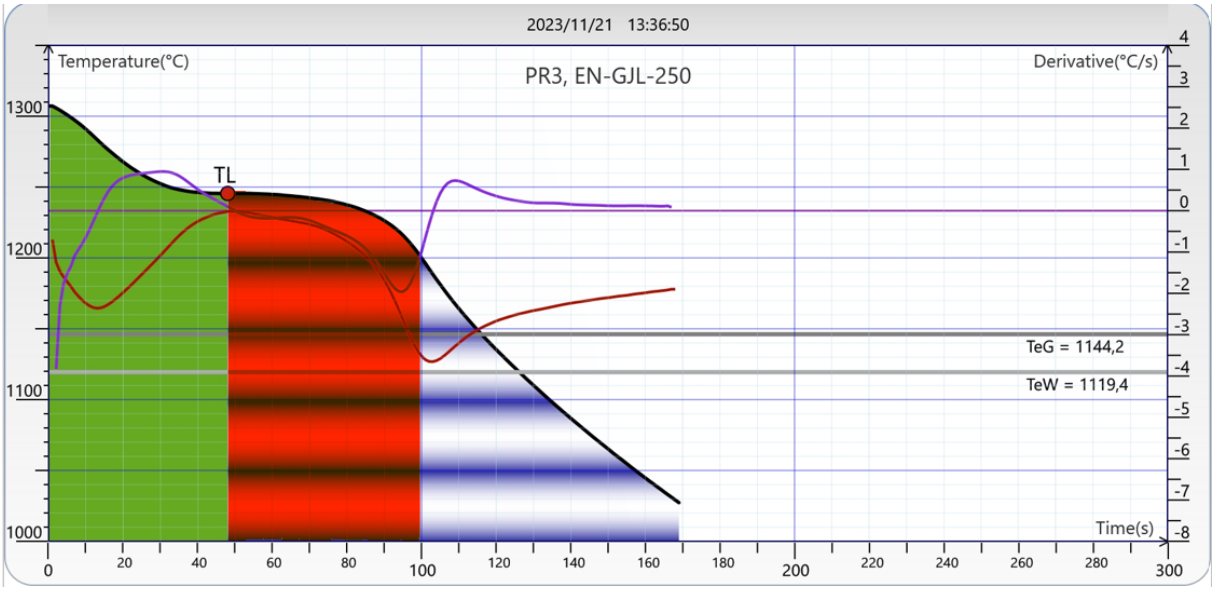

Figure 4.6: Cooling Curve showing cooling behaviour for P3

Similarly, P3 followed the general cooling pattern of P1 and P2, as shown in Figure 4.6. However, P3 was poured at a higher temperature of ~1310ºC, likely due to being held in the furnace longer. It took ~47 seconds for P3 to reach the liquidus temperature, which is ~6 seconds longer than P2. Despite this, P3 had a shorter liquid cooling region than P2, cooling faster at ~1.06 ~1.06ºC/s compared to that of P2 at ~0.54ºC/s. This faster cooling rate, combined with the higher pouring temperature, accelerated heat extraction and the onset of solidification. Total solidification in P3 was completed at ~100 seconds, like in P2.

4.5 Microstructures of As-cast HCCI Samples

The microstructures of samples P1 to P3 after the casting process are shown in Figures 4.7a–c. Table 4.2 shows the actual average primary carbide size along with their variance and primary and eutectic carbide volume. In Figure 4.7a, sample P1, with a Cr/C ratio of 12.13 and a calculated carbide volume of 22.42%, displays a dendritic microstructure (light phase) characterised by fine carbides and visible separation of matrix and primary carbides with wider dendrite arm spacing in between them, attributable to its low carbon content (1.98%). However, the actual average size shows that P1 has a carbide volume of ~26.26%. Additionally, P1 shows more directional needle-like-shaped primary carbides. Sample P1 in Table 4.2 also has the lowest average primary carbide volume of 143µm amongst the as-cast samples. The standard deviation of the primary carbides also presents low, showing it has a smaller carbide size difference, and the carbides are of uniform size with marginal differences.

Table 4.2: Average carbide size and volume of as-cast and heat-treated HCCIs

	Carbide Size		Carbide Volume
Sample	**Perimeter (µm)**	**Carbide Size Variance(µm)**	**Carbide volume (%)**
P1	143.90	±23.69	26.26±2.28
P2	217.11	±45.37	37.27±3.27
P3	1431.85	±1433.36	42.90±5.35

Figure 4.7b showing the microstructure of P2 with a Cr/C ratio of 8.62, confirms a higher theoretical volume fraction of carbides (32.36%) as indicated in Table 4.1. However, the actual values present a bit higher at ~37.27%. The microstructure of P2 (Figure 4.7b) shows a more defined interconnected carbide network made up of hexagonal-shaped primary carbides and finer eutectic carbides. The matrix in P2 remains predominantly austenitic, but the carbides have either rounded, hexagonal, or acicular morphology, which are evenly dispersed throughout the microstructure. P2 in Table 4.2 also shows that it has coarser grains than P1 with an average primary carbide size of 217 µm. P2 also shows a relatively low carbide size variation, showing that the primary carbides are mostly of uniform size.

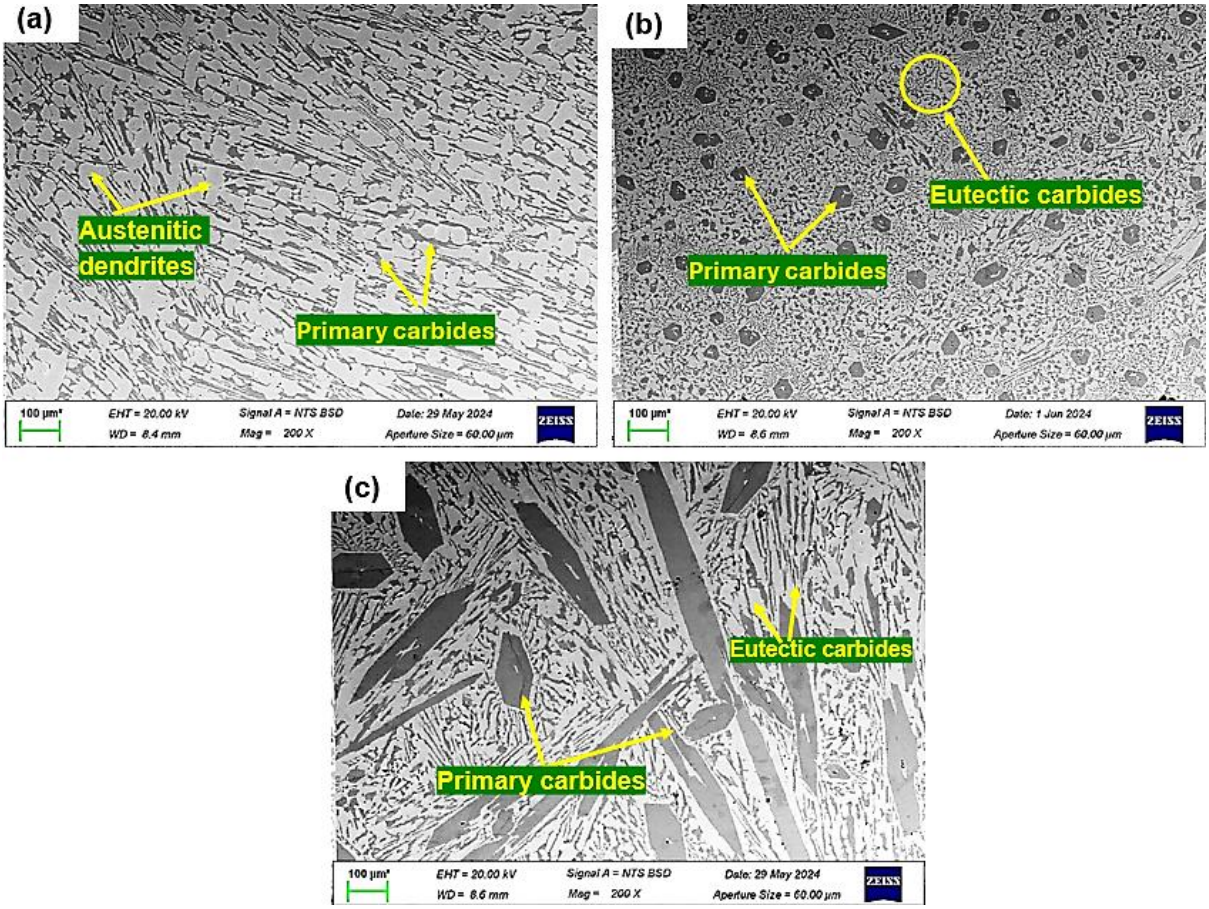

Figure 4.7: SEM image showing the microstructure of P1(a), P2(b) and P3(c). Light phase is the matrix; dark phase is the carbides.

In Figure 4.7c, P3, with the lowest Cr/C ratio of 8.06 and the slightly higher theoretical carbide volume than P2 of 34.43% (Table 4.1), displays extensive carbide networks. However, the actual carbide volume presents a bit higher at ~42.90%. The primary carbides in P3 are significantly coarser and more continuous than those in P1 and P2. The volume of the matrix appears substantially covered by the primary and eutectic carbides. Additionally, P3 shows the greatest carbide size amongst the as-cast samples at an average of 1431 µm. P3 also shows the greatest variation in primary carbide size, with the variation coming to ±1433.36. This indicates the inconsistent size in the primary carbide sizes in thematrix. Across the three samples, the carbide volume and morphology progressively change, with P3 showing the most pronounced features of carbide coarsening and boundary segregation.

4.5.2 EDS Results of As-cast HCCI Samples

Figure 4.8a-f shows the EDS analysis of the matrix of alloys P1, P2 and P3. The matrix for all samples is dominated by Fe and Cr. This is characteristic of an austenitic matrix observed in the light phase in Figure 4.7. Austenite in high chromium cast irons is usually the light phase

in SEM images due to its lower chromium content compared to carbides. Additionally, in cast iron, Cr is an austenite stabiliser. (Ma et al., 2011).

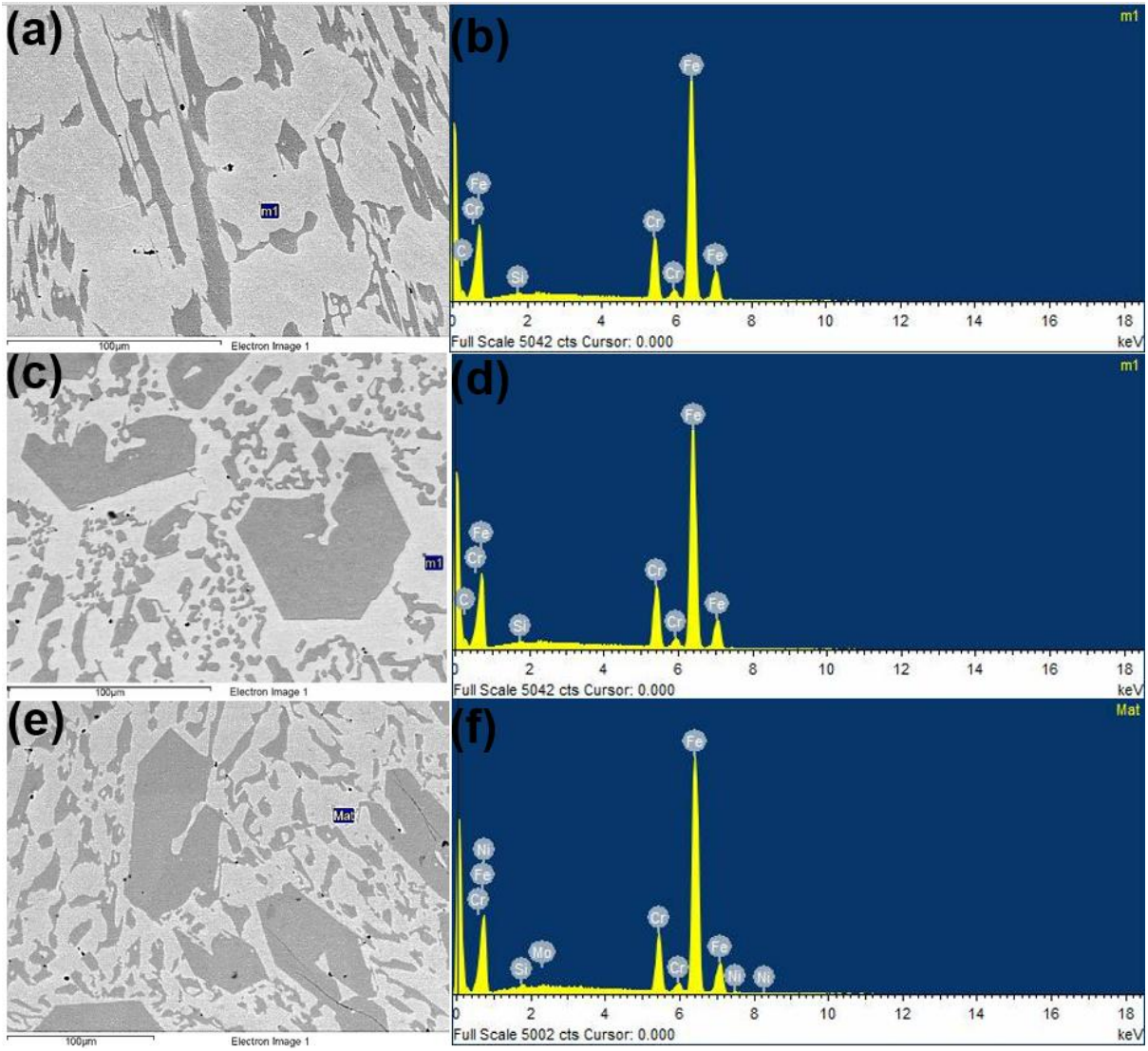

Figure 4.8: SEM spot analysis for the matrix of P1(a), P2(c) and P3(e) and the corresponding spectrum for the analysis P1(b), P2(d) and P3(f).

EDS analysis of the light phase typically shows higher Fe content and lower Cr, indicating it is part of the metallic matrix (Purevdorj et al., 2024). The matrix in high chromium cast iron is primarily Fe with small amounts of Cr because chromium preferentially forms carbides during solidification. While some Cr remains in the matrix to stabilise the austenitic structure, most of it is used up in the carbide phases, leaving Fe as the dominant component of the metallic matrix. These observations agree with common observations for HCCI matrices, such as those by Scandian et al. (2009), Karantzalis et al. (2009) and Guitar et al. (2020). The detection of silicon could potentially be caused by residue from colloidal silica used in polishing.

Figure 4.9a-f shows the EDS results for the carbides in samples P1, P2, and P3 along with their corresponding spot analysis images. The spectrums for carbides (Figure 4.9b, d and f) show high peaks for Cr, followed by Fe, along with smaller peaks for C in all three samples. This pattern is typical of chromium carbides, likely M_7C_3 or $M_{23}C_6$, where "M" represents Cr and Fe. In contrast, the matrix spectrum (Figures 4.8 b, d, and f) shows a higher concentration of Fe with some Cr. The EDS spectrum for carbides shows significantly more Cr than Fe in the carbides because chromium is naturally the dominant element in M_7C_3 carbides. According to Wiengmoon et al. (2011), chromium has a strong tendency to bond with carbon, making it the main component in carbide formation, particularly in high chromium cast irons where chromium is abundant. Iron, while present, substitutes for chromium to a lesser extent because chromium is more effective at forming stable carbides like M_7C_3 and tends to concentrate in the carbides rather than in the matrix. Additionally, during solidification, chromium segregates into the carbides, further increasing their Cr content (Guitar et al., 2020).

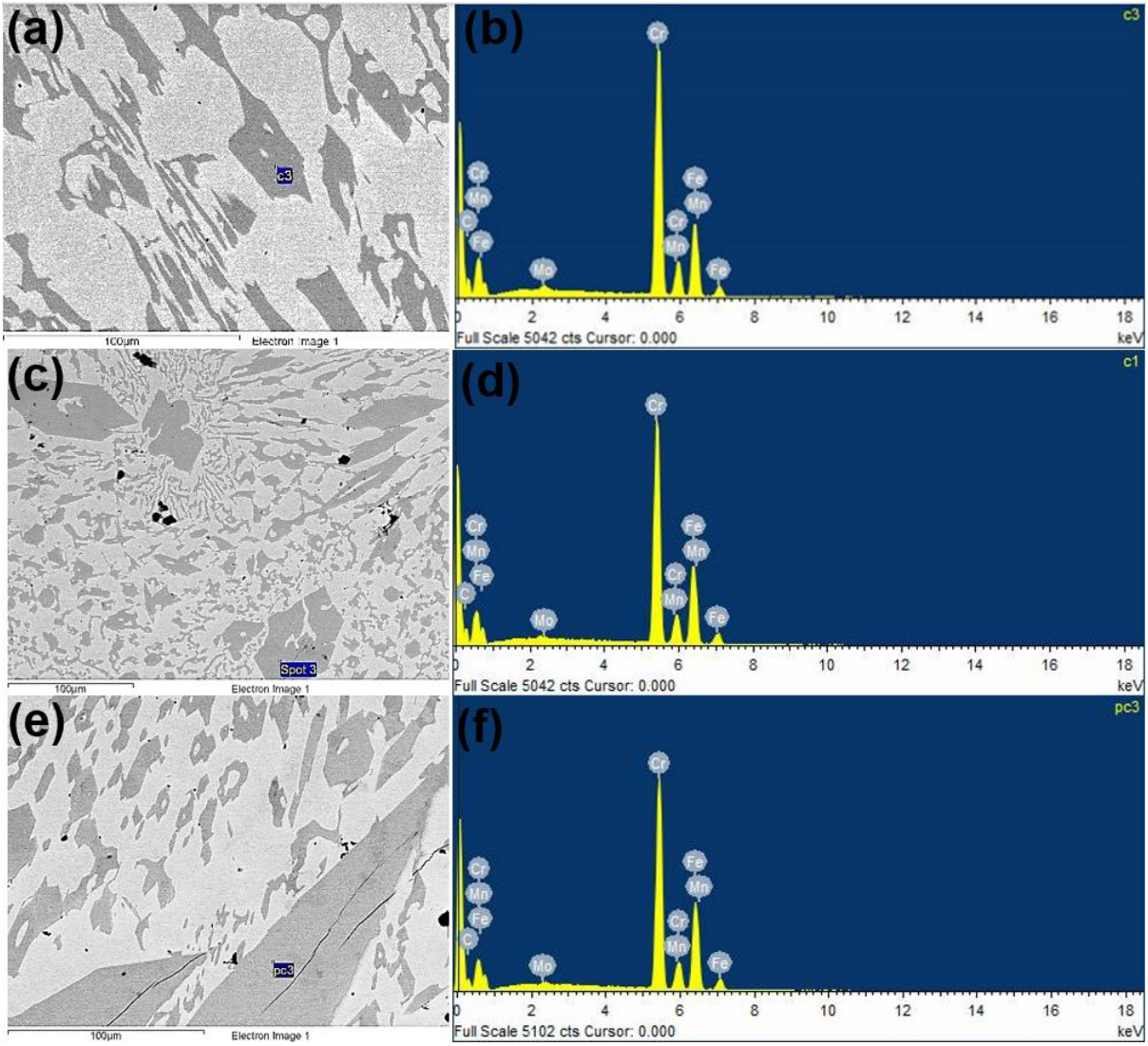

Figure 4.9: SEM spot analysis for the carbides of P1(a), P2(c) and P3(e) and the corresponding spectrum for the analysis P1(b), P2(d) and P3(f).

From the EDS analysis alone, the carbide type is inconclusive and requires additional XRD analysis. However, considering that the microstructures were obtained from as-cast alloys, the carbides are more likely to be M_7C_3 than $M_{23}C_6$, as $M_{23}C_6$ is typically associated with heat treatment and appears smaller and more rounded. The larger, hexagonal carbides observed in the microstructure are characteristic of M_7C_3. This is supported by studies such as those by Guo et al. (2016); Li et al. (2016) and Oanh & Viet (2020).The presence of Mo in the EDS peaks suggests that molybdenum contributes to carbide formation, enhancing their properties. The Mn peak, however, is likely an overlap with Fe, as Mn is present in such low quantities that it cannot be accurately detected.

4.5.3 XRD results of As-cast HCCI Samples

Figures 4.10a-c shows the XRD results for the as-cast conditions of P1, P2, and P3. The results show peaks corresponding to austenite (γ-phase) and M_7C_3 carbides. These peaks are observed at specific angles of 2θ, and their positions and intensities reveal the phases present in each alloy. For P1, Figure 4.10a, the major peak for austenite is observed around 60º, while for P2, Figure 4.10b, and P3, Figure 4.10c, the major peaks for austenite are observed around 50º with smaller ones observed at 60º and 90º for P3. The peaks for M_7C_3 carbides appear at approximately 44°, 50°, and 60°, with a few additional ones in between.

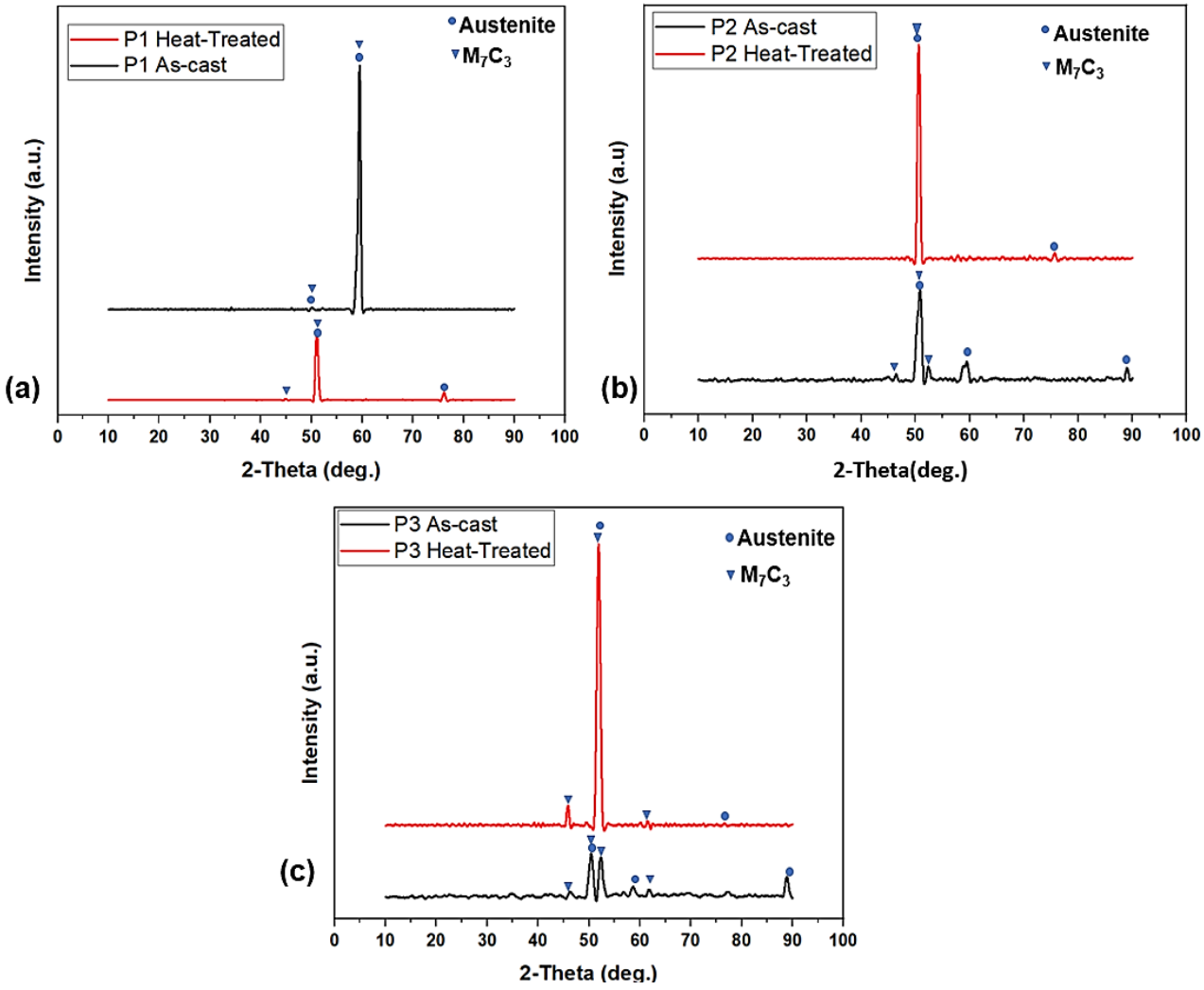

Figure 4.10: XRD patterns for samples P1 (a), P2 (b), and P3 (c) as-cast and after heat-treatment.

The specific angles for these peaks are consistent across the alloys, but the relative intensities of the austenite and M_7C_3 peaks vary significantly. P1 shows the strongest austenite peaks and weaker M_7C_3 peaks, reflecting its austenite-dominated microstructure. In contrast, P2 and P3 show relatively more peaks detecting M_7C_3, with P3 exhibiting higher intensity peaks of M_7C_3

phase and comparatively weak austenite peaks, indicating a progressively higher carbide volume fraction and reduced metallic matrix.

The observed peaks and their positions match those reported in literature for high chromium cast irons. Studies such as Li et al. (2009), Guitar et al. (2020), and Touhami et al. (2023) report similar 2θ angles for austenite and M_7C_3 carbides. The XRD results confirm the phases observed in the SEM images are M_7C_3 carbides in an austenitic matrix. In P1 in Figure 4.10a, the weaker M_7C_3 peaks correspond to the finer and more dispersed carbides seen in the microstructure. For P2 in Figure 4.10b, the detection of both austenite and M_7C_3 through peak intensities reflects the higher carbide volume in the austenitic matrix observed in the SEM. In P3 shown in Figure 4.10c, the dominant M_7C_3 peaks align with the extensive and interconnected carbide networks seen in the microstructure. Overall, the XRD results corroborate the phase distribution and morphology observed in the SEM images.

4.6 Microstructures of Heat-Treated HCCI Samples

Figure 4.11a-c shows the SEM images of P1 after heat treatment (P1ht), P2 after heat treatment (P2ht), and P3 after heat treatment (P3ht) exhibiting notable microstructural changes. Table 4.3 shows the average primary carbide size of as-cast and heat-treated HCCI samples determined through ImageJ analysis. The carbide volume could not be determined using this technique, as the secondary carbides were too fine to be detected accurately for analysis. In Figure 4.11a, P1ht shows a significantly finer microstructure, indicating substantial grain refinement. The M_7C_3 carbides in P1ht appear smaller, fragmented, and more densely distributed throughout the matrix, leading to a more compact and refined structure. This suggests that heat treatment facilitated carbide redistribution, promoting a more uniform dispersion of elements into the carbide and matrix phases. In contrast, the as-cast P1 microstructure displayed more directional primary carbides with a wider dendrite arm spacing in the austenitic matrix. The heat treatment process effectively reduced this directional arrangement, breaking up the primary carbides and leading to a denser, more homogeneous carbide network. The increased dense packing of carbides in P1ht further highlights the microstructural refinement, enhancing phase uniformity and reducing segregation effects compared to the as-cast state. This is evidenced by the decrease in carbide size shown in Table 4.3, where the average primary carbide significantly dropped to ~99.65 μm from ~1453.90 μm in the as-cast. Additionally, the carbide variance significantly dropped to $\pm$12.08 μm showing that after recrystallisation the primary carbides were all relatively the same size. This shows the effect of homogenisation that came with recrystallisation.

The microstructure of P2 in Figure 4.2b shows a relatively fine distribution of primary M_7C_3 carbides, which are blocky and hexagonal in shape and homogeneously dispersed within the matrix. In contrast, P2ht exhibits coarser primary M_7C_3 carbides that are larger and more prominent. This is evidenced by the large change observed in the grain size of the P2ht versus P2 with the P2ht increasing to an average grain size of $\pm$570.01μm from $\pm$143.90 μm in P1.This coarsening occurs due to the prolonged growth of carbides at elevated temperatures, leading to greater variation in the sizes of both primary and eutectic carbides. The increased variation in primary carbide size as seen in Table 4.3 in P2ht of $\pm$612.22 μm is evidence of this. Distinct growth patterns are visible in the heat-treated sample, highlighting this increased carbide size variance. Despite the coarsening of primary carbides, the matrix in P2ht retains its refinement and homogeneity. This suggests that some redistribution of alloying elements has occurred, reducing segregation of elements between the carbides and the matrix compared to the as-cast sample. As a result, while the primary carbides in P2ht are coarser than in as-cast P2, the overall matrix appears to remainins uniformly covered by eutectic M_7C_3 carbides. The redistribution of elements plays a key role in maintaining phase homogeneity and ensuring a more uniform microstructure despite the differences in carbide size.

The microstructure of P3 in Figure 4.11c shows large, elongated primary M_7C_3 carbides arranged in an austenitic matrix in an interconnected pattern, with visibly less connectivity between the primary and eutectic carbides. These carbides are sharply defined and aligned, giving the microstructure a strong directional appearance. In contrast, the microstructure of P3ht retains its coarse primary carbides; however, they are now less continuous and plate-like, appearing more blocky in shape. Table 4.3 shows the reduction in primary carbide size in P3ht of $\pm$1056.26 μm from $\pm$1431.85 μm. The network of primary and eutectic carbides in P3ht appears more interconnected than in the as-cast sample, reducing the strong directional effect seen in P3. Additionally, while the primary carbides remain coarse, their elongation is more limited, contributing to a structure where the carbide network is more evenly spread throughout the matrix rather than forming distinct, elongated patterns. The carbide variation also decreased from $\pm$1433.36 μm in as-cast P3 to $\pm$1032.81 μm which indicates that the size difference of the carbides was also decreased, however the retained high variance carbides still remained the coarsest amongst the heat-treated samples.

Table 4.3: Average primary carbide size of as-cast and heat-treated HCCIs.

	Carbide Size	
Sample	**Perimeter (µm)**	**Carbide Size Variance(µm)**
P1	143.90	±23.69
P2	217.11	±45.37
P3	1431.85	±1433.36
P1ht	99.65	±12.08
P2ht	570.01	±612.22
P3ht	1056.26	±1032.81

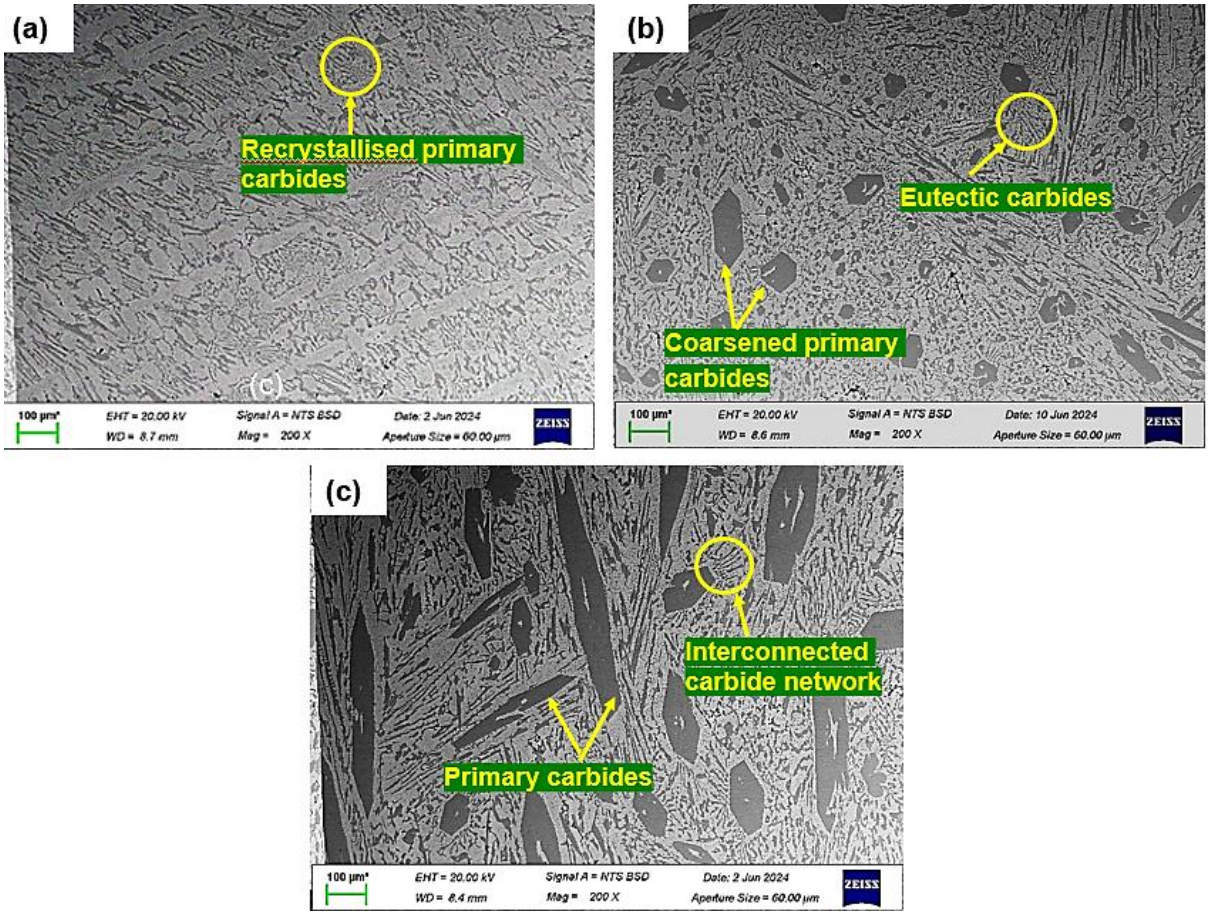

Figure 4.10: SEM images of microstructures after heat-treatment for P1ht(a), P2ht(b) and P3ht(c).

SEM images showing precipitates in the matrix at 5000x magnification are shown in Figure 4.12 a-c. In addition to the observed changes above, the high-resolution SEM images in Figure 4.12a-c confirm the presence of secondary carbides of M_7C_3 type as confirmed by the XRD in Figure 4.10 precipitated after heat treatment. These secondary carbides are much smaller and

rounder-shaped and embedded in the matrix compared to the primary and eutectic carbides found in the as-cast microstructure. The redistribution of chromium and carbon during heat treatment is critical in promoting the growth and refinement of these secondary carbides, making the microstructure more homogeneous (Guo et al., 2016). The Cr/C ratio plays a significant role in this process by influencing the availability of free carbon and chromium and the stability of carbide phases.

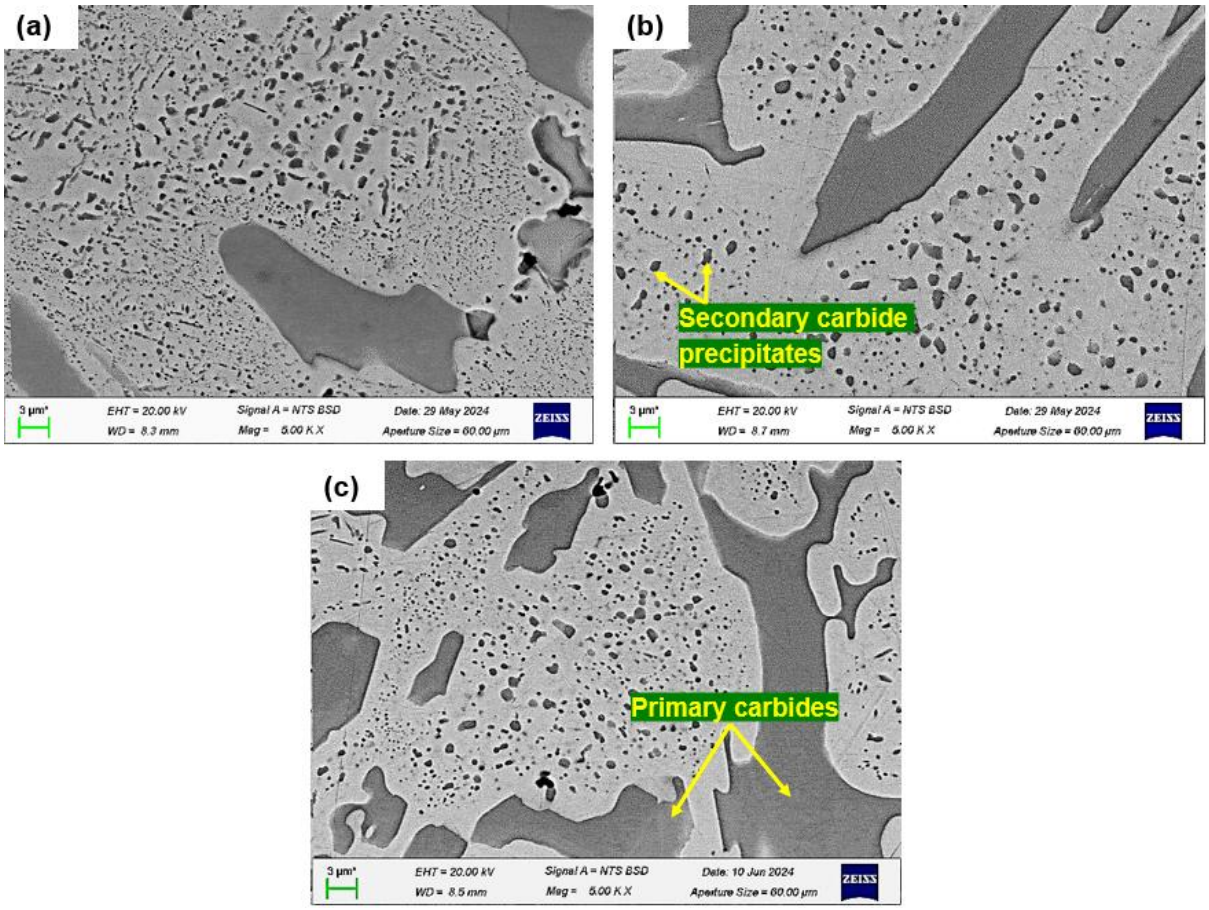

FiFigure 4.11: SEM images showing precipitates in the matrix of P1ht(a), P2ht(b) and P3ht (c) at 5000x.

4.6.1 EDS Results of Heat-Treated HCCI Samples

The EDS spectrum in Figure 4.13b shows the composition of the secondary carbides spot analysis done as shown in Figure 4.13a. The pattern in this spectrum is similar to the patterns observed for the primary carbides in the as-cast microstructure. This is characterised by prominent Cr peaks, with Fe peaks nearly as high and the presence of C and Mo in the carbides. These results suggest that the precipitated carbides could be of the M_7C_3 type. However, the analysis is inconclusive because the analysed spots were too small, and the detector could have

been analysing the surrounding areas as well. This may have introduced bias to the results. To confirm these observations, additional techniques such as XRD should be used.

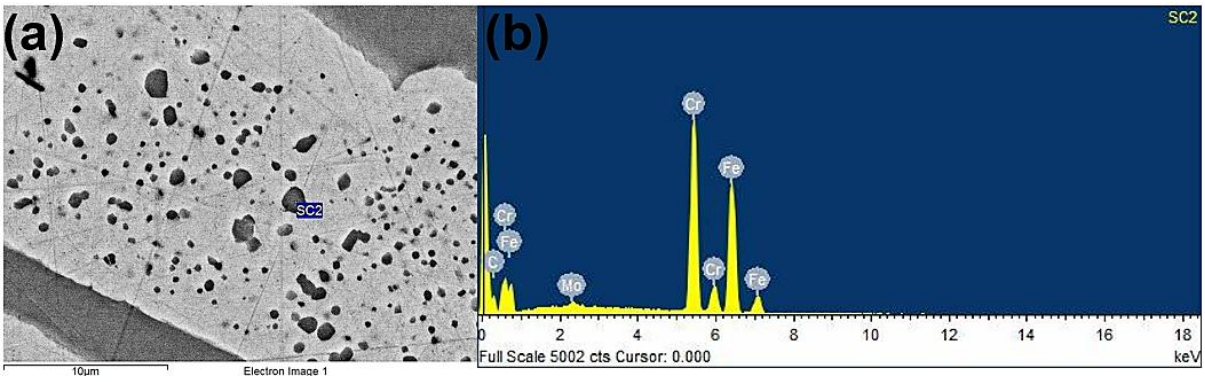

Figure 4.12: EDS a) image of spot analysis done of carbide and b) spectrum of the spot analysis.

4.6.2 XRD Results of Heat-Treated HCCI Samples Microstructure

The XRD in Figures 5.10a-c confirms the precipitation of carbides of the M_7C_3 nature. The major peaks of the austenite and M_7C_3 carbides are seen at a 2θ angle of 50º and additional austenite angles around 75º. P3 in Figure 4.10c has additional peaks for M_7C_3 carbides around 45º and 60º. Additionally, the peaks are of higher intensities than for P1 to P3 as-cast, confirming the overall increase of carbides in the matrix. This result can also be related to the heat treatment process and the differences in Cr/C ratios between P2ht and P3ht. The transformation and precipitation of secondary carbides observed in the findings of the microstructural and EDS analyses are validated by the XRD confirming the evolution of the material during heat treatment.

4.7 Discussion

4.7.1 Solidification Kinetics of the As-Cast HCCIs

The cooling behaviour of hypoeutectic high-chromium cast irons is influenced by several key factors that govern heat extraction, solidification kinetics, and final microstructure development. The chemical composition, particularly the Cr/C ratio, affects how phases nucleate and grow, as chromium promotes carbide formation while carbon influences thermal conductivity and heat dissipation (Yang & Li, 2012; Gong et al., 2017). Cooling rate plays a crucial role in determining primary phase formation, dendritic structure, and carbide morphology, with faster cooling refining microstructural features and slower cooling allowing for coarser growth (Chen et al., 2006; Huang et al., 2019). The carbide volume fraction impacts heat extraction efficiency, as carbides act as heat sinks but also release latent heat during

formation, which can momentarily slow cooling. Segregation effects, driven by variations in chromium and carbon distribution, further influence the way solidification progresses, affecting the size and continuity of carbides. Additionally, mould material, casting conditions, and thermal gradients contribute to variations in cooling behaviour by altering how efficiently heat is transferred away from the molten metal fast. These factors collectively determine the microstructure and mechanical properties of the final casting.

The differences in cooling behaviour and solidification times across the samples are influenced by their Cr/C ratios and cooling rates. Figure 4.4 shows the cooling curve for sample P1 with the highest Cr/C ratio (12.13); the total solidification time for this alloy was the shortest. High Cr/C ratios in high-chromium cast irons reduce carbide formation because the excess chromium limits the availability of free carbon needed to form carbides like M_7C_3 (Yang & Li, 2012). This results in fewer carbides precipitating, leading to shorter diffusion distances for alloying elements during solidification and facilitating faster heat extraction (Xu et al., 2017). Consequently, the solidification process is accelerated, resulting in a more refined microstructure. Studies like that of Lou et al.(2016) have shown that higher Cr/C ratios limit carbide precipitation, leading to faster solidification.

In Figure 4.5 , P2 (Cr/C = 8.62) and P3 (Cr/C = 8.06) in Figure 4.6, where the Cr/C ratio is significantly lower than P1 and marginally different between P2 and P3, the solidification kinetics can become a bit more complex. The cooling and solidification process is crucial in determining the final microstructure, particularly the size, distribution, and morphology of the primary and eutectic carbides. The solidification behaviour is influenced by several key factors, including cooling rate, Cr/C ratio, primary and eutectic carbide volume fraction, elemental segregation effects, and latent heat release during phase transformations. During the liquid cooling phase, heat may be removed from the molten alloy through three primary mechanisms: conduction, convection, and radiation (Li et al., 2022). However, the rate at which this heat is extracted is not uniform and depends on the thermal properties of the liquid metal, its composition, and interactions with the surrounding environment (e.g., mould material, heat sinks, and cooling conditions).

Between the two samples, P3 in Figure 4.6 exhibits a faster liquid cooling rate (1.06°C/s) compared to P2 (0.54°C/s). This difference can be attributed primarily to the higher carbon content in P3 (2.96% vs. 2.78% in P2), which influences thermal conductivity and heat dissipation efficiency. Carbon plays a significant role in the heat transfer mechanisms of molten

metals by affecting electron mobility and convective heat transfer (Guo et al., 2021). In metallic systems like HCCIs, heat is predominantly transported through free electron movement, meaning that elements influencing electron density impact thermal conductivity. Since carbon is a small interstitial element, it enhances electron mobility in the liquid phase, increasing thermal diffusivity and allowing heat to be transferred and dissipated more efficiently (Rost et al., 2020; Chen et al., 2023).

Additionally, carbon affects the formation of convection currents within the molten alloy. These currents arise due to temperature gradients, causing density variations in the melt. Higher carbon content in P3 may lower the viscosity of the liquid phase, enabling stronger convective flow and more efficient internal heat transport (Deng et al., 2018; Feng et al., 2021). This promotes faster cooling by reducing thermal resistance within the molten metal, further contributing to the higher cooling rate in P3. In contrast, P2, with its lower carbon content, may experience weaker convection-driven heat extraction, causing it to cool more slowly in the liquid state (Demmel et al., 2021; Feng et al., 2021). However, this occurs at a micro-level, as the differences in carbon between P2 and P3 are marginal.

Apart from carbon content, the carbide volume fraction also influences cooling behaviour. P3 has a slightly higher carbide volume (~34.43%) compared to P2 (~32.26%), meaning that slightly more nucleation of primary and eutectic carbides occurs. As carbides begin to form, they act as heat sinks, extracting heat from the surrounding liquid and accelerating heat removal from the system (Guo et al., 2016). Since P3 has more primary and eutectic carbides forming, this further increases its cooling rate. However, carbide formation also releases latent heat, which can temporarily slow down the cooling process in localised regions (Guo et al., 2021). The balance between heat extraction due to carbide formation and heat retention due to latent heat release plays a crucial role in determining the actual solidification kinetics of the alloy (Guo et al., 2016; Ibrahim et al., 2021).

Despite P3 cooling more quickly in the liquid state, the final carbide structure in P2 (Figure 4.7b) was finer, suggesting that the eutectic cooling stage played a more dominant role in shaping the microstructure. The slightly higher Cr/C ratio in P2 encouraged more nucleation sites for carbide formation, preventing excessive growth and leading to a more refined dispersion (Yang et al., 2007). On the other hand, P3 (Figure 4.7c), with its slightly lower Cr/C ratio and greater overall carbide volume, provided more room for carbide coalescence, allowing larger, more connected carbides to develop (Yang et al., 2007). Segregation likely

played a role as well. P3 may have retained more carbon and chromium in localised regions, delaying carbide precipitation and giving them additional time to grow and merge. Since both alloys completed solidification in the same time frame (100 seconds), the way heat was extracted during eutectic transformation had a stronger impact on primary and eutectic carbide morphology than the initial cooling rate in the liquid phase. The result was a more refined and dispersed carbide network in P2, while P3 exhibited coarser carbides that were more interconnected (Zhao et al., 2021; Gu et al., 2024). In the end, the rapid eutectic cooling in P2 and higher nucleation density resulted in a finer carbide structure, whereas the slightly slower eutectic solidification in P3 and greater carbide volume encouraged coarser growth, despite the faster initial cooling rate in the liquid phase.

4.7.2 Microstructure of As-Cast HCCIs

The microstructure of HCCIs is primarily determined by its chromium and carbon content, particularly in hypoeutectic compositions. Chromium is a strong carbide-forming element that stabilises the austenitic matrix and promotes carbide formation (Ma et al., 2011). Carbon plays a key role in determining the volume, size, and morphology of carbides, influencing the mechanical properties of the material (Imurai et al., 2014; Guo et al., 2021). A higher Cr/C ratio typically results in finer, more evenly distributed carbides, whereas a lower Cr/C ratio promotes the growth of larger, more interconnected carbide structures (Kootsookos & Gates, 2004; Guo et al., 2021). The balance between these two elements dictates the overall solidification behaviour, carbide formation, and matrix composition in HCCIs, affecting their mechanical performance.

The microstructure of HCCIs is significantly influenced by its carbon content. When the carbon content is below 2.45%, as seen in P1, the microstructure tends to be predominantly dendritic. This is because the first phase to solidify from the melt in lower-carbon compositions is austenite, which forms in a dendritic structure. This dendritic austenite structure is a common feature in hypoeutectic compositions, which contain less carbon than the eutectic (Guo et al., 2016; Ibrahim et al., 2021). The low carbon content slows carbide formation during solidification, allowing dendrites to develop as the primary phase (Ma et al., 2006). As cooling continues, carbides (dark phase) start to precipitate at the borders of the dendrites, preserving the dendritic pattern. The process of segregation occurs because elements like carbon, chromium, and other alloying elements distribute unevenly between the solid and liquid phases during solidification (Ma et al., 2006). This uneven distribution is due to differences in their solubility and partitioning behaviour, where elements less soluble in the solid phase, such as

carbon, are rejected into the liquid, while elements more soluble, such as chromium, concentrate in the solid (Huang et al., 2017). This segregation leads to regions with varying chemical compositions and wider dendrite arm spacing between the carbides and matrix (Ma et al., 2006).

Higher segregation levels of Cr and C in compositions with a higher Cr/C ratio can further increase dendrite arm spacing due to the uneven distribution of solute elements (Xia et al., 2011; Zhao et al., 2013; Wan et al., 2021). Chromium, which strongly partitions between the solid and liquid phases, accumulates at the solid-liquid interface, slowing down solidification and allowing for greater dendrite coarsening (Ma et al., 2006; Scandian et al., 2009). This delays nucleation and encourages the growth of fewer, more widely spaced dendrites. Additionally, the reduced availability of nucleation sites due to solute buildup further contributes to a coarser microstructure. This effect is particularly pronounced in hypoeutectic and near-eutectic compositions, where carbide formation is delayed, allowing the primary austenite dendrites to grow larger before carbide precipitation occurs. As a result, high Cr/C ratio compositions, due to their increased segregation tendencies, promote larger dendrite arm spacings (Ma et al., 2006; Wan et al., 2021).

The EDS and XRD analyses confirm the phase distribution and composition of the as-cast microstructures in P1, P2, and P3. The EDS analysis reveals that the light phases in the microstructure contain higher Fe and lower Cr, confirming that they are part of the metallic matrix, which is primarily austenitic. This is expected in high-chromium cast irons, where chromium preferentially forms carbides during solidification, leaving Fe as the dominant component in the matrix (Purevdorj et al., 2024). While some Cr remains in the matrix to stabilise the austenitic structure, most of it is concentrated in the carbides. This observation aligns with previous studies on high-chromium cast irons, such as those by Karantzalis et al. (2009), Scandian et al. (2009), and Nayak et al. (2020). Additionally, the XRD analysis confirms the presence of austenite and M_7C_3 carbides in all samples, supporting the observed microstructures and the phase distribution expected from their composition.

Figure 4.7a shows the SEM image of the microstructure in P1. The high Cr/C ratio in P1, as seen in Table 4.1, indicates that there is significantly more chromium relative to carbon, which influences the type and distribution of carbides formed. At this Cr/C ratio, the primary type of carbide expected is M_7C_3 (Abd El-Aziz et al., (2015); Shimizu et al., (2019). M_7C_3 carbides are favoured at elevated chromium levels because chromium has a strong affinity for carbon, which

stabilises the carbides (Scandian et al., 2009). The high Cr/C ratio ensures sufficient chromium availability to bind with carbon, leading to finer and more uniformly distributed primary carbides in the microstructure. The presence of these primary M_7C_3 carbides can also be attributed to the role of chromium in suppressing graphite growth and stabilising the austenitic matrix during solidification (Guitar et al., 2020).

Figure 4.7b shows the SEM image of the microstructure in P2. In contrast, P2 shows significant changes in its microstructure compared to P1. The decrease in the Cr/C ratio from P1 to P2 significantly affects the microstructure by increasing the volume and coarseness of some of the carbides in the matrix. It also defines the shape and morphology of the primary carbides, which appear as hexagonal-shaped carbides (Liu et al., 2025) surrounded by eutectic carbides (darker, finer phase), forming a network and increasing interconnection within the matrix. Carbon is crucial for the formation of both primary and eutectic carbides, which are present in the austenitic matrix (light phase) (Guo et al., 2021; Zhang et al., 2021). The higher carbon content and lower Cr/C ratio lead to increased carbide precipitation, promoting a more interconnected carbide structure.

Figure 4.7c shows the SEM image of the microstructure in P3. P3 exhibits a structure characterised by large, plate-like, extensive, and continuous primary carbides in a network of smaller eutectic carbides, attributable to its low Cr/C ratio. The elevated carbon content facilitates the substantial development of chromium carbides, particularly M_7C_3, which become more interconnected within the matrix (Zhang et al., 2021). The microstructure of P3 is less refined than that of P1 and P2, with larger primary carbides primarily forming along grain boundaries. The segregation of chromium and carbon at grain boundaries plays a crucial role. Guo et al. (2021) report that lower Cr/C ratios result in more carbon being available to combine with chromium, leading to the formation of larger primary carbides at these boundaries. This is because the grain boundaries act as preferential sites for carbide nucleation and growth due to the higher grain boundary energy state and the presence of solute atoms. This energy is higher at the grain boundaries due to the disrupted atomic structure and the presence of solute atoms, making these sites energetically favourable for nucleation processes. The presence of grain boundary primary carbides disrupts the continuity of the austenitic matrix, contributing to a coarser microstructure. The larger primary carbides in P3 suggest extended carbide growth during solidification, as the diminished Cr/C ratio promotes coarser carbide structures due to longer growth periods (Zhang et al., 2018).

Overall, these results confirm that the carbide content increases from P1 to P3, in line with their Cr/C ratios and carbide volume fractions. The combination of EDS and XRD analyses supports the presence of M_7C_3 carbides in an austenitic matrix, with the carbide distribution and morphology varying according to composition. These findings align with existing literature on high-chromium cast irons, reinforcing that chromium strongly bonds with carbon to form stable carbides during solidification, leading to distinct microstructural differences among the samples (Wiengmoon et al., 2011; Guitar et al., 2020).

4.7.3 High Chrome Cast Iron Samples: Microstructure versus Thermo-Calc Prediction

The microstructural results in Figure 4.7a-c and ThermoCalc predictions in Figure 4.1a-c show some similar trends, but there are also clear differences. Both methods show that the amount of carbides increases from P1 to P3 as the carbon content increases and the Cr/C ratio decreases. They also agree that M_7C_3 is the main carbide phase in all the samples, with smaller amounts of secondary carbides like $M_{23}C_6$ and M_3C_2 forming at lower temperatures. Similarly, both show that FCC_A1 (austenite) is the main matrix phase at high temperatures; however, in the Thermocalc prediction, the FCC_A1 phase transforms into BCC_A2 (ferrite) as the temperature drops.

Thermo-Calc prediction and the actual microstructural features did not agree completely in terms of the total amount of carbides. For P1, Thermo-Calc predicts 27% carbide volume, while the actual value is also approximately the same at ~26.26%. For P2 and P3, Thermo-Calc predicts 28% and 30%, respectively, but the actual values are higher at 37.26% and 42.90%, respectively. These differences arise because Thermo-Calc assumes equilibrium conditions, where all phases have enough time to fully form and stabilise (Galvan et al., 2014; Saal et al., 2018). In P1, the high Cr/C ratio (12.13) means there is more chromium available compared to carbon. Chromium strongly stabilises carbides like M_7C_3, making their formation more predictable under equilibrium conditions (Galvan et al., 2014). Since there is less excess carbon, carbide growth happens in a controlled way, reducing the chances of extra carbide formation during cooling. This makes the actual carbide volume closer to what Thermo-Calc predicts because the solidification process follows equilibrium more closely. In P2 and P3, the higher carbon content and reduced Cr/C ratios promote more extensive carbide formation, even under non-equilibrium conditions, which results in higher measured volumes than predicted (Panichkin et al., 2023).

Another key difference is in the shape and arrangement of the carbides. In P1, as observed in Figure 4.7a, the carbides are finer and more evenly spread, but in P2 and P3 (Figures 4.7b and c), some are coarser and more interconnected, often forming along grain boundaries. These features occur due to the effects of segregation of elements during solidification and the faster cooling rates, which Thermo-Calc does not simulate under non-equilibrium conditions (Panichkin et al., 2023; Sudhakar et al., 2022). This grain boundary segregation in P2 and P3 helps larger carbides grow in those areas, which increases the overall carbide volume.

ThermoCalc predicts a ferritic (BCC_A2) matrix for all three samples because it assumes equilibrium conditions where significant carbide formation depletes the matrix of chromium and carbon, stabilising ferrite. In contrast, the actual microstructures show an austenitic (FCC_A1)-dominated matrix. This happens because rapid cooling during solidification prevents complete carbide precipitation and chromium depletion, allowing the FCC_A1 phase to dominate in the actual samples (Panichkin et al., 2023; Gundlach & Tartaglia, 2024).

The formation of secondary carbides, like $M_{23}C_6$ and M_3C_2, also differs between Thermo-Calc and the microstructural results. Thermo-Calc predicts secondary carbide precipitation in all the alloy samples. However, secondary carbides need enough carbon to form, and with most of it already used during solidification, there is not enough left to promote the secondary precipitation of these carbides as predicted by ThermoCalc. ThermoCalc assumes the alloy cools slowly and reaches equilibrium, where primary carbides are stable and there is little drive for new carbide formation (Siekaniec et al., 2022; Goto et al., 2023; Panichkin et al., 2023). Additionally, the high chromium content stabilises the matrix, keeping chromium dissolved in the matrix instead of forming secondary carbides (Sasaguri et al., 2019). Fast cooling rates during casting could also inhibit secondary carbides from forming because there is not enough time for them to nucleate and grow (Sasaguri et al., 2019).

ThermoCalc gives a good idea of the general trends in phase and carbide formation across the samples, but it did not fully align with the practical results that were obtained. However, the observed microstructures reveal the impact of non-equilibrium conditions, such as rapid cooling, segregation, and kinetic constraints, which ThermoCalc did not account for. These factors explain the differences in carbide amounts, shapes, and the type of matrix seen in the samples.

4.7.4 Microstructure of Heat-Treated HCCIs

The differences between the as-cast and heat-treated microstructures in P1, P2, and P3 can be explained by the diffusion process and recrystallisation occurring during heat treatment and the impact of their corresponding Cr/C ratios. In P1 (Figure 4.7a), the elevated Cr/C ratio is essential for microstructural refinement. P1 displays slightly coarser, elongated primary carbides resulting from the segregation of chromium and carbon during solidification. The microstructure of P1ht in Figure 4.11a shows that heat treatment induces recrystallisation, facilitating the reorganisation of the matrix and the more uniform redistribution of alloying elements, or homogeneity (Ai et al., 2011). Heat treatment induces recrystallisation, which plays a crucial role in refining the microstructure by promoting the reorganisation of the matrix and facilitating the uniform redistribution of alloying elements. Heat treatment induces recrystallisation, which refines the microstructure by forming new, strain-free grains that replace deformed ones, reducing segregation and improving uniformity. At high temperatures, atoms move more freely, allowing chromium and carbon to redistribute more evenly between the matrix and carbides. This enhances carbide dispersion, transforming elongated carbides into more blocky shapes and creating a more balanced and stable structure. As a result, the matrix becomes more uniform, reducing weak points and improving mechanical properties like hardness, wear resistance, and toughness (Sakai & Miura, 2010, 2012; Hagemann et al., 2012). This transformation enhances the overall homogeneity of the microstructure by reducing elemental segregation effects and improving phase distribution. Furthermore, the elevated temperatures during heat treatment enhance diffusion-driven redistribution of alloying elements such as chromium and carbon. This reduces compositional gradients that may have developed during solidification, leading to a more balanced distribution of elements between the matrix and primary and eutectic carbides (Strobl & Haubner, 2020; Baharudin et al., 2022). As a result, carbide phases become more uniformly dispersed, refining their morphology and limiting excessive coarsening or elongation. The elevated chromium concentration stabilises finer carbides by forming strong bonds with carbon, hence reducing the availability of free carbon that promotes carbide development (Ai et al., 2011). This likewise diminishes carbon diffusion, preventing excessive coarsening. The elongated carbides in P1 decompose into smaller, more uniform particles, resulting in a finer, more homogeneous matrix in P1ht, in contrast to the coarse morphology of the as-cast state.

In P2 (Figure 4.7b), the reduced Cr/C ratio indicates an increased availability of carbon in relation to chromium, facilitating primary carbide growth during heat treatment. P2 exhibits relatively small, blocky hexagonal-shaped primary M_7C_3 carbides; however, in P2ht (Figure 4.11b), these carbides enlarge while retaining some homogeneity of carbide dispersion throughout the matrix. This introduces some variability in carbide size by increasing the size difference in the primary and eutectic carbides. However, some good interconnectedness in between carbides was maintained. Heat treatment helps spread alloying elements more evenly in the matrix, making the microstructure more uniform (Shi & Zhang, 2017). When the metal cools after casting, elements like chromium and carbon tend to separate unevenly between the solid and liquid parts, creating differences in composition. This can lead to an uneven distribution of primary and eutectic carbides. Heat treatment facilitates an increase in the movement of atoms at high temperature, allowing elements to mix more evenly throughout the matrix. At high temperatures, atoms move more freely, allowing elements to spread from areas with high concentrations to areas with low concentrations (Sun et al., 2008; Shi & Zhang, 2017). As a result, primary and eutectic carbide formation becomes more uniform, preventing excessive clustering or depletion of key elements in specific regions. This redistribution also refines the microstructure by reducing the likelihood of coarse, interconnected primary and eutectic carbides, leading to a more balanced phase distribution. Heat treatment also makes the matrix more stable by reducing segregation and encouraging the formation of a more uniform austenitic microstructure depending on the composition and heating conditions (Sun et al., 2008). With fewer areas of concentrated elements, the material becomes stronger and more stable, improving its overall performance. The coarsening of primary carbides predominates the microstructure in P2ht, consistent with research indicating that sometimes reduced Cr/C ratios in high-chromium cast irons result in larger, more interconnected carbides after heat treatment depending on the heat-treatment applied (Wang et al., 2005; Kopycinski et al., 2014).

The effect of the low Cr/C ratio in P3 is much stronger compared to P1. As seen in Figure 4.7c, P3 has large, elongated, plate-like primary carbides within the austenitic matrix. Heat treatment helps rearrange the microstructure by redistributing chromium and carbon, reducing segregation, and making the matrix more uniform, similar to what is seen in P2ht (Poolthong et al., 2004). This redistribution improves the connection between phases and leads to a more even spread of carbides throughout the matrix. The high carbon content in P3 encourages carbide growth, resulting in larger and more noticeable primary carbides in P3ht, as seen in Figure 4.11c. These carbides become more interconnected, forming network-like structures

where carbide particles merge or overlap, increasing interconnectedness after heat treatment (Guo et al., 2016). The heat treatment also facilitates recrystallisation of the primary and eutectic carbides, where some of the primary carbides become more blocky and hexagon-shaped from the long, continuous plate-like morphology observed in P3. In P3ht, the eutectic carbides are more evenly distributed throughout the matrix, giving it a more uniform appearance. However, the microstructure is still dominated by large, interconnected primary carbides. This confirms that a low Cr/C ratio encourages primary carbide growth and coarsening after heat treatment (Yang et al., 2021). While the primary carbides in P3ht remain coarse, they are now less continuous and plate-like, instead appearing more blocky in shape. The network of primary and eutectic carbides in P3ht is more interconnected than in the as-cast sample, reducing the strong directional effect observed in P3. Although the carbides are still large, their elongation is now more limited, resulting in a carbide network that is more evenly spread rather than forming long, distinct patterns.

Upon heating the high-chromium cast iron samples P1 to P3 beyond the austenitic temperature, the matrix experiences substantial alterations due to recrystallisation and phase transitions. At this elevated temperature, the matrix converts to austenite, a face-centered cubic (FCC) phase capable of dissolving substantial quantities of chromium and carbon, resulting in a supersaturated solution (Gasan & Erturk, 2013). This technique dissolves existing carbides and redistributes chromium and carbon uniformly throughout the matrix, minimising segregation of the phases. The Cr/C ratio and cooling rate are crucial factors influencing the final microstructure during cooling. An elevated Cr/C ratio enhances the chromium content in the matrix, hence stabilising the austenite phase and inhibiting its transformation into martensite (Ma et al., 2011). Upon cooling, secondary carbides, M_7C_3, precipitate from the supersaturated austenite matrix (Ma et al., 2011). These carbides diminish the carbon concentration in the matrix while preserving austenite as the predominant phase. The ultimate microstructure comprises an austenitic matrix with finely distributed secondary carbides of M_7C_3 type, along with primary and eutectic, as confirmed by the XRD results in Figure 4.10. In addition to the observed changes above, the high-resolution SEM images in Figure 4.12a-c confirm the presence of secondary carbides, such as M_7C_3 or $M_{23}C_6$, precipitated after heat treatment. These secondary carbides are finer and more evenly distributed in the matrix compared to the primary carbides found in the as-cast microstructure. The redistribution of chromium and carbon during heat treatment is critical in promoting the growth and refinement of these secondary carbides, making the microstructure more homogeneous (Guo et al., 2016). The Cr/C ratio plays a

significant role in this process by influencing the availability of free carbon and the stability of carbide phases.

Substantial changes occur during the high-temperature quenching stage, which takes place above 1000°C, and the subsequent tempering treatment. During quenching, rapid cooling prevents the formation of equilibrium phases, trapping Cr and C in the supersaturated matrix (Li et al., 2009). In the tempering stage, diffusion processes allow the precipitation of secondary carbides, primarily M_7C_3, within the matrix. These carbides are finer and more evenly dispersed, strengthening the austenitic matrix by impeding dislocation motion and improving hardness. The Cr/C ratio further influences this process; a high Cr/C ratio stabilises finer carbides and promotes a more uniform matrix, while a lower Cr/C ratio allows for larger carbide growth, contributing to the final distribution and morphology of the precipitated carbides.

Initially, $M_{23}C_6$ carbides form during the destabilisation heat treatment. With prolonged holding times, as observed in the heat treatment process outlined in Figure 3.2, these $M_{23}C_6$ carbides can transform into secondary M_7C_3 carbides (Guitar et al., 2020). This transformation involves a reorganisation of the carbide structure and further redistribution of Cr and C. The tempering stage specifically enhances this process, encouraging carbide precipitation and matrix strengthening.

4.8. Conclusion

The microstructural analysis of both as-cast and heat-treated high-chromium cast iron (HCCI) samples confirms the significant influence of the Cr/C ratio on carbide formation, distribution, and morphology. The findings show that a higher Cr/C ratio results in fewer, smaller, and more evenly distributed carbides, while a lower Cr/C ratio leads to more carbides that are larger and more interconnected. The solidification process showed that high Cr/C ratio alloys solidify faster due to limited carbide precipitation, allowing quicker heat removal. In low Cr/C ratio alloys, increased carbide formation affected heat flow, slowing down cooling in some areas and leading to a coarser microstructure. Element segregation played a key role, particularly in low Cr/C ratio alloys, where chromium and carbon gathered at grain boundaries, leading to the formation of large interconnected primary carbides. Heat treatment improved the distribution and shape of carbides by redistributing alloying elements and reducing segregation. It transformed elongated primary carbides into more compact, blocky structures and refined the overall microstructure. Secondary carbide precipitation, mainly M_7C_3, further modified the

austenitic matrix, particularly in high Cr/C ratio alloys. In low Cr/C ratio alloys, excessive carbide growth resulted in greater carbide interconnectivity, which may influence mechanical performance. Comparing the results with Thermo-Calc predictions, both the experimental and predicted trends showed an increase in carbide volume from P1 to P3, confirming the role of the Cr/C ratio in carbide formation. However, Thermo-Calc underestimated carbide content in low Cr/C ratio alloys, likely due to non-equilibrium solidification effects that it does not fully account for. The predicted ferritic matrix also differed from the observed austenitic matrix, as rapid cooling prevented complete carbide precipitation and chromium depletion. Overall, the study confirms that the Cr/C ratio has a strong effect on the carbide network and microstructural features of HCCI. Optimising the Cr/C ratio and applying controlled heat treatment can help refine carbide morphology, distribution, and stability, making it possible to tailor the microstructure for specific industrial applications.

4.8 References

Abd El-Aziz, K., Zohdy, K., Saber, D., & Sallam, H. E. M. (2015). Wear and Corrosion Behaviour of High-Cr White Cast Iron Alloys in Different Corrosive Media. *Journal of Bio- and Tribo-Corrosion*, *1*(4).

Ai, Y.-L., Chen, W.-H., Ding, J.-Y., & He, W. (2011). Heat treatment process of low carbon high chromium white cast iron. *Jinshu Rechuli/Heat Treatment of Metals*, *36*(6), 107–110.

Baharudin, B. A., Ayob, F., Abdul Rahim, A., Mustapha, M., Ismail, A., Ab Rahman, F., & Ismail, A. (2022). Investigation on the Mechanical and Microstructural Characteristics of Diffusional Bonded Gray Cast Iron and Low Carbon Steel. In *Advanced Structured Materials* 167, (245–262).

Chen, J., Yan, W., Li, H., Lu, C.-G., & Fan, X.-H. (2006). Effect of solidification rate on primary phase M7C3 of high chromium cast iron. *Zhuzao Jishu/Foundry Technology*, *27*(6), 591–593.

Chen, L., Zhang, W., Lu, W., Wei, B., Huo, S., Wang, Y., & Zhou, Y. (2023). Low thermal conductivity of dense (TiZrHfVNbTa)Cx high-entropy carbides by tailoring carbon stoichiometry. *Journal of Advanced Ceramics*, *12*(1), 49–58.

Demmel, F., Hennet, L., & Jakse, N. (2021). The intimate relationship between structural relaxation and the energy landscape of monatomic liquid metals. *Scientific Reports*, *11*(1).

Deng, Y., Zhang, J., & Jiao, K. (2018). Viscosity measurement and prediction model of molten iron. *Ironmaking and Steelmaking*, *45*(8), 773–777.

Feng, G., Jiao, K., Zhang, J., & Gao, S. (2021). High-temperature viscosity of iron-carbon melts based on liquid structure:The effect of carbon content and temperature. *Journal of Molecular Liquids*, *330*.

Galvan, E., Malak, R. J., Gibbons, S., & Arroyave, R. (2014). Constraint satisfaction approach to the design of multi-component, multi-phase alloys. *Proceedings of the ASME Design Engineering Technical Conference*, *2B*.

Gasan, H., & Erturk, F. (2013). Effects of a destabilization heat treatment on the microstructure and abrasive wear behaviour of high-chromium white cast iron investigated using different characterization techniques. *Metallurgical and Materials Transactions A: Physical Metallurgy and Materials Science*, *44*(11), 4993–5005

Gong, P., Zhao, Y., Yang, H., & Wang, N. (2017). Effects of carbon and chromium content and heat treatment on mechanical properties of high chromium cast iron. *Jinshu Rechuli/Heat Treatment of Metals*, *42*(9), 137–142.

Goto, I., Fukuchi, K., & Kurosawa, K. (2023). Effects of solidification conditions on the microstructural morphologies and strengths of hypereutectic high-chromium white cast iron castings. *Materials Science and Engineering: A*, *886*.

Gu, J., Liu, S., Si, J., & Zhang, Z. (2024). Microstructure Evolution and Properties of Nitrogen-Bearing Hypereutectic High Chromium Cast Iron after Quenching. *Journal of Materials Engineering and Performance*.

Guitar, M. A., Nayak, U. P., Britz, D., & Mücklich, F. (2020). The Effect of Thermal Processing and Chemical Composition on Secondary Carbide Precipitation and Hardness in High-Chromium Cast Irons. *International Journal of Metalcasting*, *14*(3), 755–765.

Guitar, M. A., Scheid, A., Nayak, U. P., Nakamura, L., Ponge, D., Britz, D., & Mücklich, F. (2020). Quantification of the Phase Transformation Kinetics in High Chromium Cast Irons Using Dilatometry and Metallographic Techniques. *Metallurgical and Materials Transactions A: Physical Metallurgy and Materials Science*, *51*(8), 3789–3801.

Gundlach, R. B., & Tartaglia, J. M. (2024). Effects of Silicon in High-Cr White Cast Irons. *International Journal of Metalcasting*, *18*(3), 1843–1853.

Guo, Q., Fu, H., Guo, X., Xing, Z., & Lin, J. (2021). Effect of carbon content on microstructure evolution and properties of hypereutectic high chromium cast iron. *Surface Review and Letters*, *28*(10).

Guo, Z. H., Xiao, F. R., Lu, S. L., Li, H. Y., & Liao, B. (2016). Effects of heat-treatment on the microstructure and wear resistance of a high-chromium cast iron for rolls. *Advances in Materials Science and Engineering*, *2016*.

Hagemann, P., Kawalla, R., Korpała, G., & Schmidtchen, M. (2012). The influence of the initial state on the softening and precipitation kinetics in hot metal forming. *Materials Science Forum*, *706–709*, 1397–1402.

Huang, P., Ji, X.-L., Wu, H.-C., Shan, Y.-P., & Wang, K.-P. (2019). Effects of Cooling Rate on Solidification Structure and Wear Resistance of High Chromium Cast Iron. *Zhuzao/Foundry*, *68*(8), 854–859.

Huang, Y., Long, M., Liu, P., Chen, D., Chen, H., Gui, L., Liu, T., & Yu, S. (2017). Effects of Partition Coefficients, Diffusion Coefficients, and Solidification Paths on Microsegregation in Fe-Based Multinary Alloy. *Metallurgical and Materials Transactions B: Process Metallurgy and Materials Processing Science*, *48*(5), 2504–2515.

Ibrahim, M. M., El-Hadad, S., & Mourad, M. (2021). Influence of Niobium Content on the Mechanical Properties and Abrasion Wear Resistance of Heat-Treated High-Chromium Cast Iron. *International Journal of Metalcasting*, *15*(2), 500–509.

Imurai, S., Thanachayanont, C., Pearce, J. T. H., Tsuda, K., & Chairuangsri, T. (2014). Effects of Mo on microstructure of as-cast 28 wt.% Cr-2.6 wt.% C-(0-10) wt.% Mo irons. *Materials Characterization*, *90*, 99–112.

Karantzalis, A. E., Lekatou, A., & Mavros, H. (2009). Microstructural Modifications of As-Cast High-Chromium White Iron by Heat Treatment. *Journal of Materials Engineering and Performance*, *18*(2), 174–181.

Karantzalis, E., Lekatou, A., & Mavros, H. (2009). Microstructure and properties of high chromium cast irons: Effect of heat treatments and alloying additions. *International Journal of Cast Metals Research*, *22*(6), 448–456.

Kootsookos, A., & Gates, J. D. (2004). The effect of the reduction of carbon content on the toughness of high chromium white irons in the as-cast state. *Journal of Materials Science*, *39*(1), 73–84.

Kopycinski, D., Guzik, E., Siekaniec, D., & Szczesny, A. (2014). Analysis of the high chromium cast iron microstructure after the heat treatment. *Archives of Foundry Engineering*, *14*(3), 43–46.

Li, D., Liu, L., Zhang, Y., Ye, C., Ren, X., Yang, Y., & Yang, Q. (2009). Phase diagram calculation of high chromium cast irons and influence of its chemical composition. *Materials and Design*, *30*(2), 340–345.

Li, J., Zhang, C., Jiang, B., Zhou, L., & Liu, Y. (2016). Effect of large-size M23C6-type carbides on the low-temperature toughness of martensitic heat-resistant steels. *Journal of Alloys and Compounds*, *685*, 248–257.

Li, Y., Zhu, P. X., Tang, C., & Sun, Z. (2022). Effects of Quenching Medium on Microstructure and Mechanical Properties of High Chromium Cast Iron. *Crystals*, *12*(10).

Liu, S., Li, J., Su, X., Cui, S., Zhang, H., & Ren, Z. (2025). Effect of Cr:C ratio on open three-body wear resistance of squeeze cast high chromium cast iron. *Tribology International*, *202*.

Lou, D., Liu, D., He, C., Bennett, P., Chen, L., Yang, Q., Fearon, E., & Dearden, G. (2016). Effect of Cr/C Ratio on Microstructure and Corrosion Performance of Cr3C2-NiCr Composite Fabricated by Laser Processing. *Journal of Materials Engineering and Performance*, *25*(1), 312–319.

Ma, Y. P., Li, X. L., & Yang, L. (2011). Effects of Carbon Concentration Variation on Primary Austenite Stability of High Chromium Cast Iron. *Advanced Materials Research*, *154–155*, 1684–1688.

Ma, Y.-P., Li, J., Liu, Y.-G., Zhao, F., & Li, Z.-Y. (2006). Effects of carbon content variation on primary austenite stability of high chromium cast iron. *Zhuzao/Foundry*, *55*(10), 1079–1081.

Ma, Y.-P., Li, X., & Yang, L. (2011). Effects of carbon concentration variation on primary austenite stability of high chromium cast iron. *Advanced Materials Research*, *154–155*, 1684–1688.

Nayak, U. P., Guitar, M. A., & Mücklich, F. (2020). A comparative study on the influence of chromium on the phase fraction and elemental distribution in as-cast high chromium cast irons: Simulation vs. experimentation. *Metals*, *10*(1).

Oanh, N. T. H., & Viet, N. H. (2020). Precipitation of M23C6 secondary carbide particles in Fe-Cr-Mn-C alloy during heat treatment process. *Metals*, *10*(2).

Panichkin, A., Kenzhegulov, A., Mamaeva, A., Uskenbayeva, A., Kshibekova, B., Imbarova, A., & Alibekov, Z. (2023). Effect of Carbon and Cooling Rate on the Structure of Hypereutectic High Chromium Cast Iron in the Cast State and after Heat Treatment. *Journal of Composites Science*, *7*(12).

Panichkin, A., Wieleba, W., Kenzhegulov, A., Uskenbayeva, A., Mamaeva, A., Imbarova, A., Kvyatkovskii, S., & Kasenova, B. (2023). Effect of thermal treatment of chromium iron melts on the structure and properties of castings. *Materials Research Express*, *10*(8).

Poolthong, N., Nomura, H., & Takita, M. (2004). Effect of heat treatment on microstructure and properties of semi-solid chromium cast iron. *Materials Transactions*, *45*(3), 880–887.

Purevdorj, B., Ariunbolor, P., Temuulen, P., & Khavalbolot, K. (2024). Microstructure and Mechanical Properties of 28% High Chromium White Cast Iron. In *Materials Science Forum 1133*, 17–23

Rost, C. M., Borman, T., Hossain, M. D., Lim, M., Quiambao-Tomko, K. F., Tomko, J. A., Brenner, D. W., Maria, J. P., & Hopkins, P. E. (2020). Electron and phonon thermal conductivity in high entropy carbides with variable carbon content. *Acta Materialia*, *196*, 231–239.

Saal, J. E., Berglund, I. S., Sebastian, J. T., Liaw, P. K., & Olson, G. B. (2018). Equilibrium high entropy alloy phase stability from experiments and thermodynamic modeling. *Scripta Materialia*, *146*, 5–8.

Sakai, T., & Miura, H. (2010). Mechanisms of ultrafine grain formation in severe plastic deformation. *Materials Science Forum*, *638–642*, 98–103.

Sakai, T., & Miura, H. (2012). Ultrafine grain formation in aluminum alloys during hot severe plastic deformation. *Materials Science Forum*, *706–709*, 1829–1834.

Sasaguri, N., Yamamoto, K., Yokomizo, Y., & Matsubara, Y. (2019). Effect of Cr/C value on behaviour of continuous cooling transformation in plain high chromium cast iron. *Materials Transactions*, *60*(12), 2537–2541.

Scandian, C., Boher, C., de Mello, J. D. B., & Rézaï-Aria, F. (2009a). Effect of molybdenum and chromium contents in sliding wear of high-chromium white cast iron: The relationship between microstructure and wear. *Wear*, *267*(1–4), 401–408.

Shi, L., & Zhang, F.-Y. (2017). Effect of Heat Treatment on Microstructure and Properties of Cr26 High Chromium Cast Iron. *Zhuzao/Foundry*, *66*(4), 408-410and417.

Shimizu, K., Purba, R. H., Kusumoto, K., Yaer, X., Ito, J., Kasuga, H., & Gaqi, Y. (2019). Microstructural evaluation and high-temperature erosion characteristics of high chromium cast irons. *Wear*, *426–427*, 420–427.

Siekaniec, D., Kopyciński, D., Tyrała, E., Guzik, E., & Szczęsny, A. (2022). Optimisation of Solidification Structure and Properties of Hypoeutectic Chromium Cast Iron. *Materials*, *15*(18).

Strobl, S., & Haubner, R. (2020). Investigation of the diffusion couple ductile cast iron / iron. *Defect and Diffusion Forum*, *405 DDF*, 54–59.

Sudhakar, A. N., Markandeya, R., Srinivasa Rao, B., Ajoy, K. P., & Kaushik, D. (2022). Effect of alloying elements on the microstructure and mechanical properties of high chromium white cast iron and Ni-Hard iron. *Materials Today: Proceedings*, *61*, 1006–1014.

Sun, Y.-F., Yu, G.-W., Zhao, J.-Y., Li, Z.-M., Shi, A.-J., & Liu, X.-F. (2008). Effects of heat treatment on microstructure and properties of high chromium tungsten-containing cast iron. *Jinshu Rechuli/Heat Treatment of Metals*, *33*(9), 91–94.

Touhami, R. C., Mechachti, S., Bouhamla, K., Hadji, A., & Khettache, A. (2023). Wear Behaviour and Microstructure Changes of a High Chromium Cast Iron: The Combined Effect of Heat Treatment and Alloying Elements. *Metallography, Microstructure, and Analysis*, *12*(4), 580–590.

Wan, Y., Gao, S., Li, M. hua, Zhang, L. qiang, Wen, Y. hong, & Song, M. ming. (2021). Enrichment characteristic of carbon atoms in solid-liquid zone of high carbon steel under different directional solidification rates. *China Foundry*, *18*(5), 488–496.

Wang, J., Zeng, M., Yang, H.-S., Liu, H.-H., Sun, Z.-P., Shen, B.-L., & Huang, S.-J. (2005). Effect of heat treatment on microstructure of a high chromium cast iron. *Cailiao Rechuli Xuebao/Transactions of Materials and Heat Treatment*, *26*(6), 75–79.

Wiengmoon, A., Pearce, J. T. H., & Chairuangsri, T. (2011). Relationship between microstructure, hardness and corrosion resistance in 20 wt.%Cr, 27 wt.%Cr and 36 wt.%Cr high chromium cast irons. *Materials Chemistry and Physics*, *125*(3), 739–748.

Xia, Y.-J., Wang, F.-M., & Wang, J.-L. (2011). Simulation of Secondary Dendritic Arm Spacing of Free Cutting Steel 38MnVS. *Journal of Iron and Steel Research International*, *18*(6), 54-73.

Xu, J., Xiang, M., Dang, B., & Jian, Z. (2017). Relation of cooling rate, undercooling and structure for rapid solidification of iron melt. *Computational Materials Science*, *128*, 98–102. h

Yang, B., Peng, Q., Milkereit, B., Springer, A., Liu, D., Rettenmayr, M., Schick, C., & Keßler, O. (2021). Nucleation behaviour and microstructure of single Al-Si12 powder particles rapidly solidified in a fast scanning calorimeter. *Journal of Materials Science*, *56*(22), 12881–12897.

Yang, C.-K., & Li, W. (2012a). Effects of carbon contents on microstructure and wear resistance of the hypereutectic high chromium cast iron. *Zhuzao/Foundry*, *61*(12), 1393–1396.

Yang, W., Wei, J., & Huang, Z. (2007a). Microstructure in Fe-Cr-C hardfacing alloys with high C and Cr. *Hanjie Xuebao/Transactions of the China Welding Institution*, *28*(3), 85–88.

Zhang, S., Zhang, H.-W., Miao, M., Feng, M.-M., Lei, H., & Wang, Q. (2021). Cellular automaton simulation on cooperative growth of M7C3 carbide and austenite in high Cr cast irons. *Wuli Xuebao/Acta Physica Sinica*, *70*(21).

Zhang, Z., Koyama, M., Wang, M. M., Tsuzaki, K., Tasan, C. C., & Noguchi, H. (2018). Microstructural mechanisms of fatigue crack non-propagation in TRIP-maraging steels. *International Journal of Fatigue*, *113*(January), 126–136.

Zhao, J., Jiang, Z., & Wei, D. (2013). Analysis of elemental segregation in a microalloyed cast steel. *Advanced Materials Research*, *652–654*, 2465–2468.

Zhao, Z., Song, R., Zhang, Y., Yu, P., & Pei, Y. (2021). Co-orientation relationship between secondary carbides and adjacent ferrite after quenching and tempering in high chromium cast iron. *Vacuum*, *184*.

Chapter 5: The Influence of Cr/C ratio on the Hardness and Fracture Toughness of High Chrome Cast Iron

5.1 Introduction

The mechanical properties of high chromium cast iron (HCCI), particularly hardness and toughness, are strongly influenced by its microstructure, which consists of a hard carbide phase embedded within a softer matrix. The Cr/C ratio plays a crucial role in determining the type, volume, and distribution of carbides within this microstructure (Guo et al., 2021). A higher Cr/C ratio typically results in a lower carbide volume and promotes a more uniform carbide distribution, which enhances toughness but reduces hardness. Conversely, a lower Cr/C ratio increases the carbide volume, leading to greater hardness but at the expense of reduced toughness (Kootsookos & Gates, 2004; Guo et al., 2021). Heat treatment is commonly employed to modify the hardness and toughness of HCCI. Processes such as quenching and tempering can refine carbide size and morphology while transforming the matrix into martensite, significantly increasing hardness. However, excessive carbide precipitation during heat treatment, particularly in alloys with a low Cr/C ratio, can lead to brittleness (Karantzalis et al., 2009; Zhang et al., 2024). To optimise HCCI for various industrial applications, this section investigates the relationship between Cr/C ratio, carbide volume, and their effects on hardness and toughness in both as-cast and heat-treated samples. This is achieved by analysing the hardness and toughness of the samples and discussing their results in relation to the microstructural characteristics influenced by the Cr/C ratio.

5.2 Hardness Characteristics of As-Cast HCCI Samples

Figure 5.1 shows the as-cast samples hardness frequency distribution plot. The hardness of the as-cast samples ranges from 300 to 750 HV. P1 has the lowest average hardness, followed by P2 and P3. P1 exhibits a relatively narrow data distribution, with the highest frequency occurring between 450 and 500 HV. Unlike P2 and P3, where most data clusters between 500 and 600 HV, the distribution of P1 skews slightly towards the lower hardness range, indicating its comparatively low characteristic hardness. P2 shows a broader data distribution compared to P1, with a peak frequency between 500 and 550 HV. The hardness values for P2 range from approximately 350 to 600 HV. Lower frequencies are observed in the higher hardness range (600+ HV), reflecting a wider variation in hardness and an overall trend towards higher values

than P1. P3 demonstrates a sharp and distinct hardness distribution, with a primary peak frequency between 550 and 600 HV and a secondary peak at 650 to 700 HV, indicating hardness segregation or two dominant hardness phases. The hardness of P3 extends significantly into the 600+ HV range, showing higher values compared to P1 and P2.

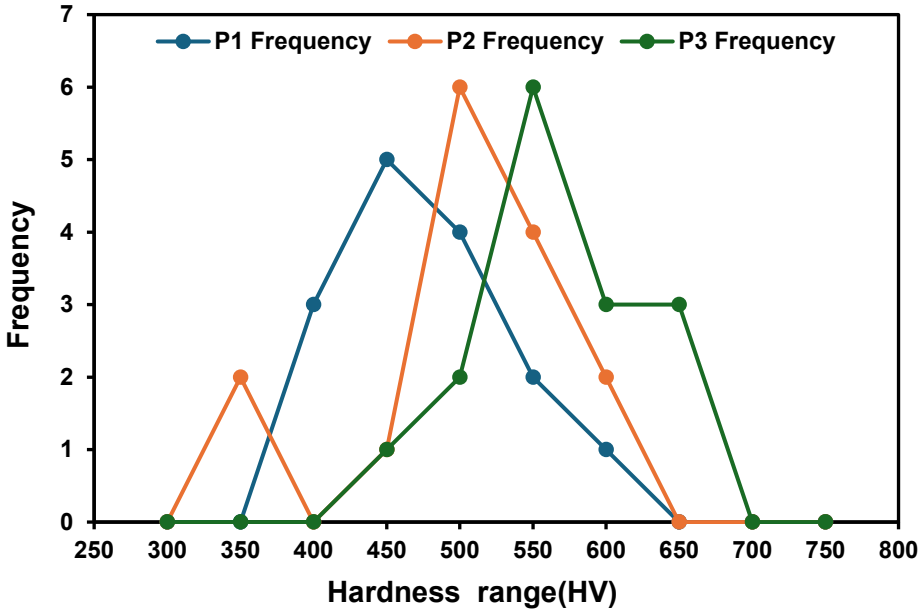

Figure 5.1: Frequency distribution plots of as-cast samples P1 to P3

Figure 5.2 shows the Brinell hardness results for sample P1 to P3. Brinell hardness tests in Figure 5.2 confirm that P1 has the lowest average bulk hardness value of 223 HBN, with an observed increase in Brinell hardness from P2 to 232 HBN, with P3 having the highest average hardness increasing to 240 HBN.

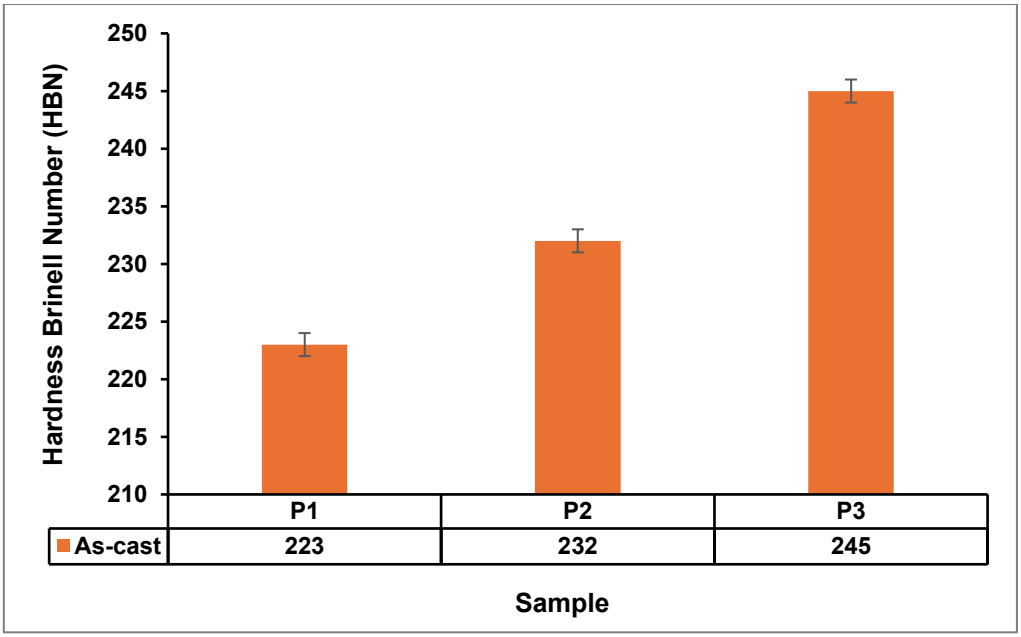

Figure 5.2: Brinell hardness results for as-cast samples P1 to P3

5.3 Hardness Characteristics of Heat-Treated Samples

Figure 5.3 shows the hardness frequency distribution of the post-heat-treated samples. For P1ht, the hardness increased after heat treatment, with its peak hardness shifting from 450–500 HV in the as-cast state to 500–550 HV. The distribution also broadened, with increased frequencies in the 500+ HV range, indicating enhanced hardness after heat treatment. In the case of P2ht, the peak hardness remained between 500 and 550 HV, similar to the as-cast state. However, the hardness distribution became broader, with values extending into the 600+ HV range, reflecting an increase in variability. While P2ht exhibited higher hardness values compared to P1ht, it also showed increased variability in hardness distribution, as frequencies in both the lower and higher ranges were observed. For P3ht, the primary hardness peak shifted notably after heat treatment, moving from 550–600 HV in the as-cast state to 600–650 HV. Frequencies extended into the 750 HV range, giving P3ht the highest hardness values among the heat-treated samples.

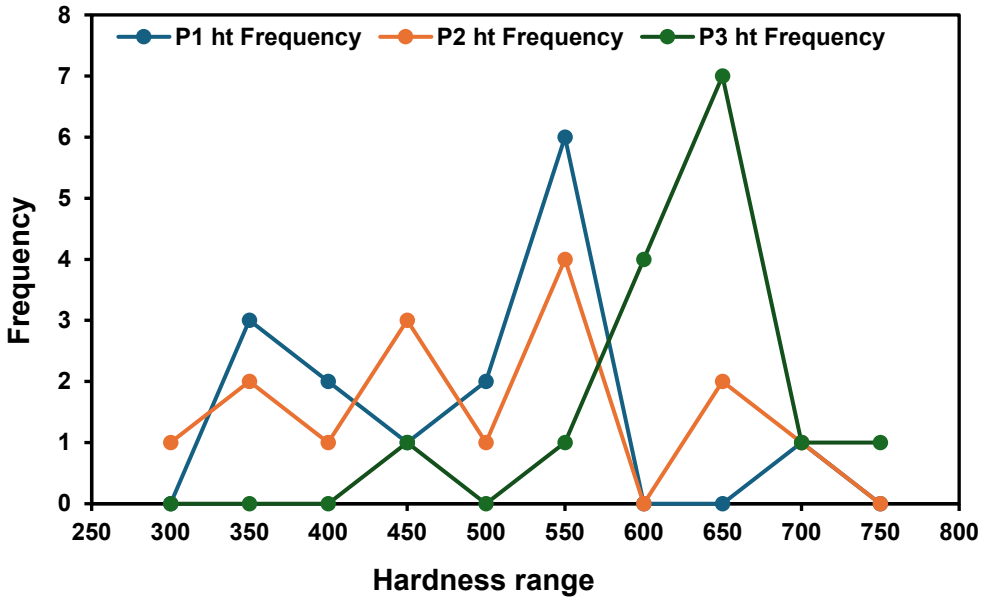

Figure 5.3: Frequency distribution plots of samples P1ht to P3ht.

Figure 5.4 shows the Brinell bulk hardness results of as-cast and heat-treated samples P1 to P3. The Brinell hardness confirmed the increase in the bulk hardness of the samples from P1ht to P3ht. Brinell hardness values for P1ht increased from 223 HBN to 341 HBN, while P2ht increased significantly from 232 HBN to 363 HBN after heat treatment, and P3ht increased from 245 HBN to 369 HBN, highlighting a significant improvement in hardness after heat treatment.

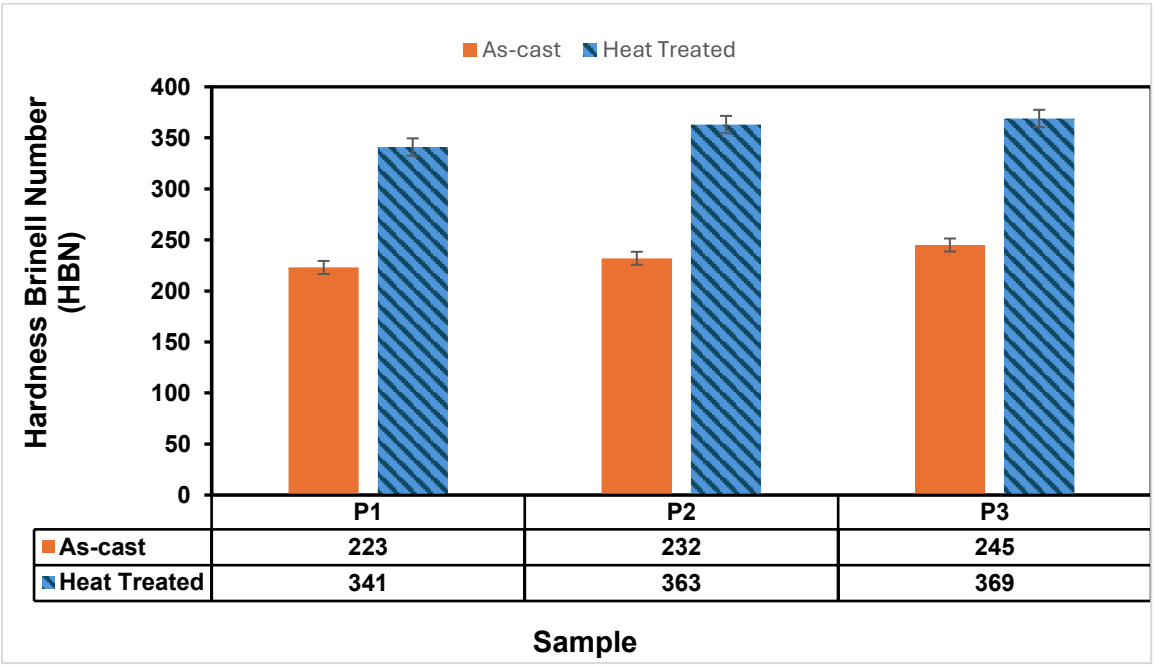

Figure 5.4: Brinell bulk hardness results of as-cast and heat-treated samples P1 to P3.

5.4 Fracture Toughness Characteristics of HCCI Samples

5.4.1 Charpy Impact Toughness of As-cast HCCI Samples

Table 5.1 shows the Charpy impact results for samples P1, P2 and P3 as-cast and after heat treatment. Figure 5.5a-c show the images captured using a stereomicroscope of P1ht samples after they underwent Charpy impact testing. P1, as shown in Figure 5.5a-c, exhibits a brittle mode of failure, with a relatively smooth fracture surface. The top view (Figure 5.5c) reveals dimples and an even fracture pattern, while the side view (Figure 5.5a) shows evidence of some deformation before failure. Its high Cr/C ratio, which resulted in a lower carbide volume and softer matrix, could enhance the ability of the material to absorb energy before fracturing. (Pourasiabi & Gates, 2022; Liu et al., 2025). Despite its brittle failure mode, P1 recorded the highest Charpy impact energy, with an average value of 10 J, as indicated in Table 5.1. This sample also had the lowest average hardness. P2 displays a brittle fracture mode with a more uneven surface compared to P1, as shown in Figure 5.6. The top view (Figure 5.6c) reveals more cleavage breakage with a rougher surface than P1 but smoother than P3. The side view (Figure 5.6a) indicates a somewhat uneven fracture surface, suggesting a ductile-to-brittle transition mode. This may result from the carbide morphology, which includes larger hexagonal primary M_7C_3 carbides with smaller eutectic M_7C_3 carbides in between. The side and top views (Figure 5.6a-c) both indicate a somewhat uneven fracture surface. The Charpy impact energy of P2 is the same as P1, with an average value of 10 J as recorded in Table 5.1. Figure 5.7a-c show the stereoscopic images showing the characteristic fracture failure pattern of P3. P3 predominantly exhibits a brittle mode of failure with minimal plastic deformation. The overall failure is characterised by cleavage breakage, with some localised plastic deformation observed in the top view (Figure 5.7c). The fracture surface shows a combination of smoother breakage areas and dimples, indicating localised ductile behaviour in certain regions. The side view (Figure 5.7a) confirms that the sample primarily fractures through cleavage, while smaller eutectic carbides contribute to deep dimples and limited plastic deformation in some areas. P3 absorbed the least amount of energy, with the lowest Charpy impact energy of 9 J. It also had the highest hardness. Overall, all samples exhibited brittle failure.

Table 5.1: Charpy impact test average values for sample P1, P2 and P3 before and after heat treatment.

	Charpy Impact Energy(J)					
	As-cast			Heat-Treated		
Sample	**Test 1**	**Test 2**	**Ave**	**Test 1**	**Test 2**	**Ave**
P1	10	10	10±0	9	9	9±0
P2	10	9	10±0.5	7.5	8.5	8±0.5
P3	9	9	9±0	7	7	7±0

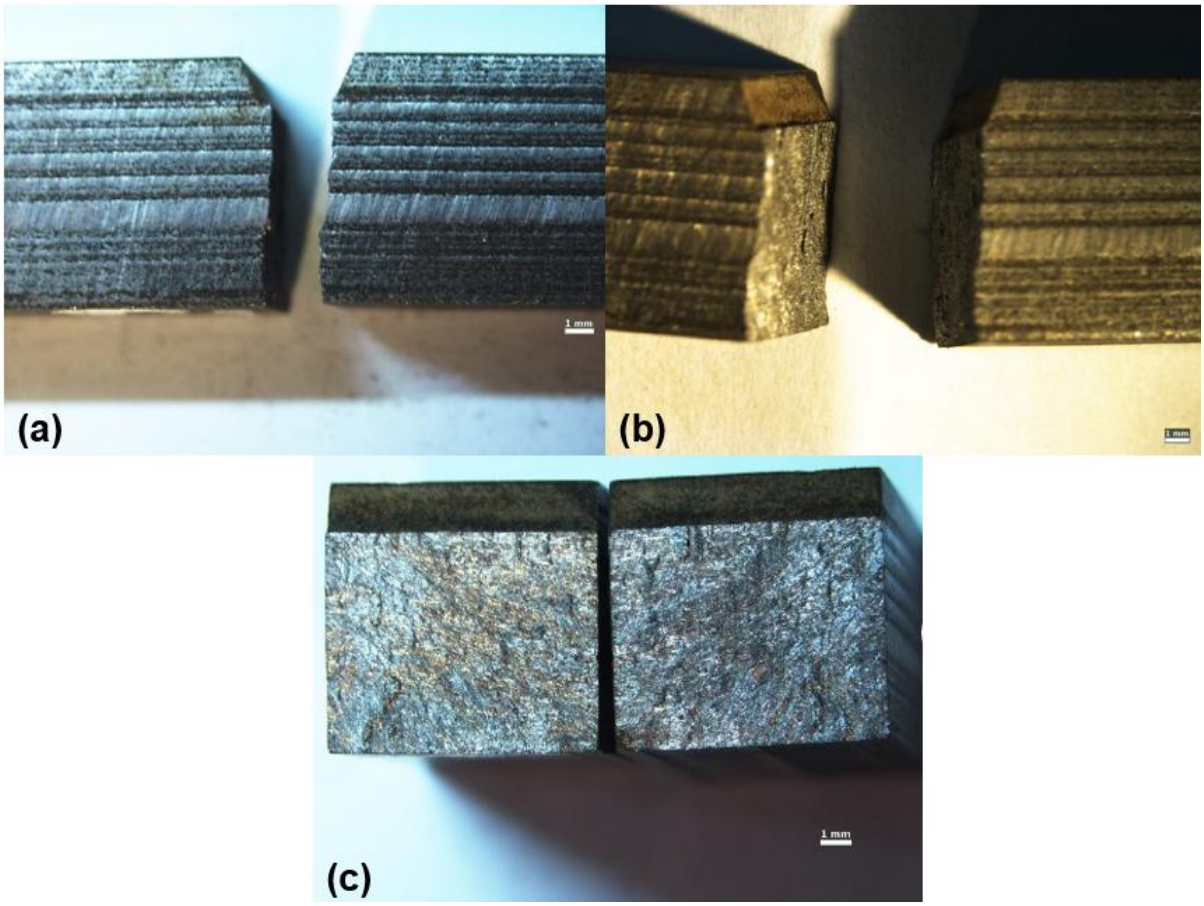

Figure 5.5: Charpy impact test average values for sample P1, P2 and P3 before and after heat treatment.

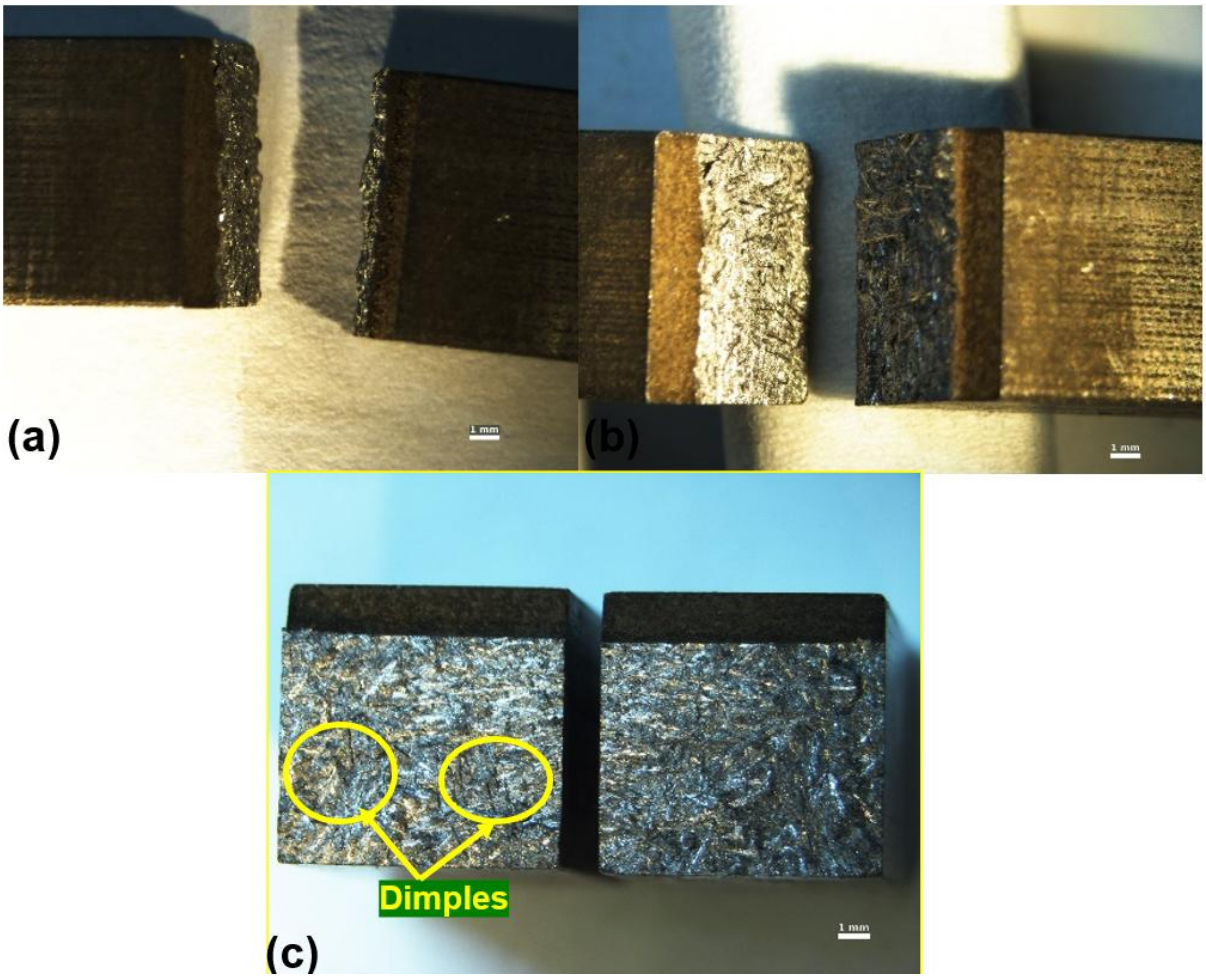

Figure 5.6: Stereomicroscopic images of P2 as-cast samples after Charpy impact testing a) side view, b) angled view, c) top view.

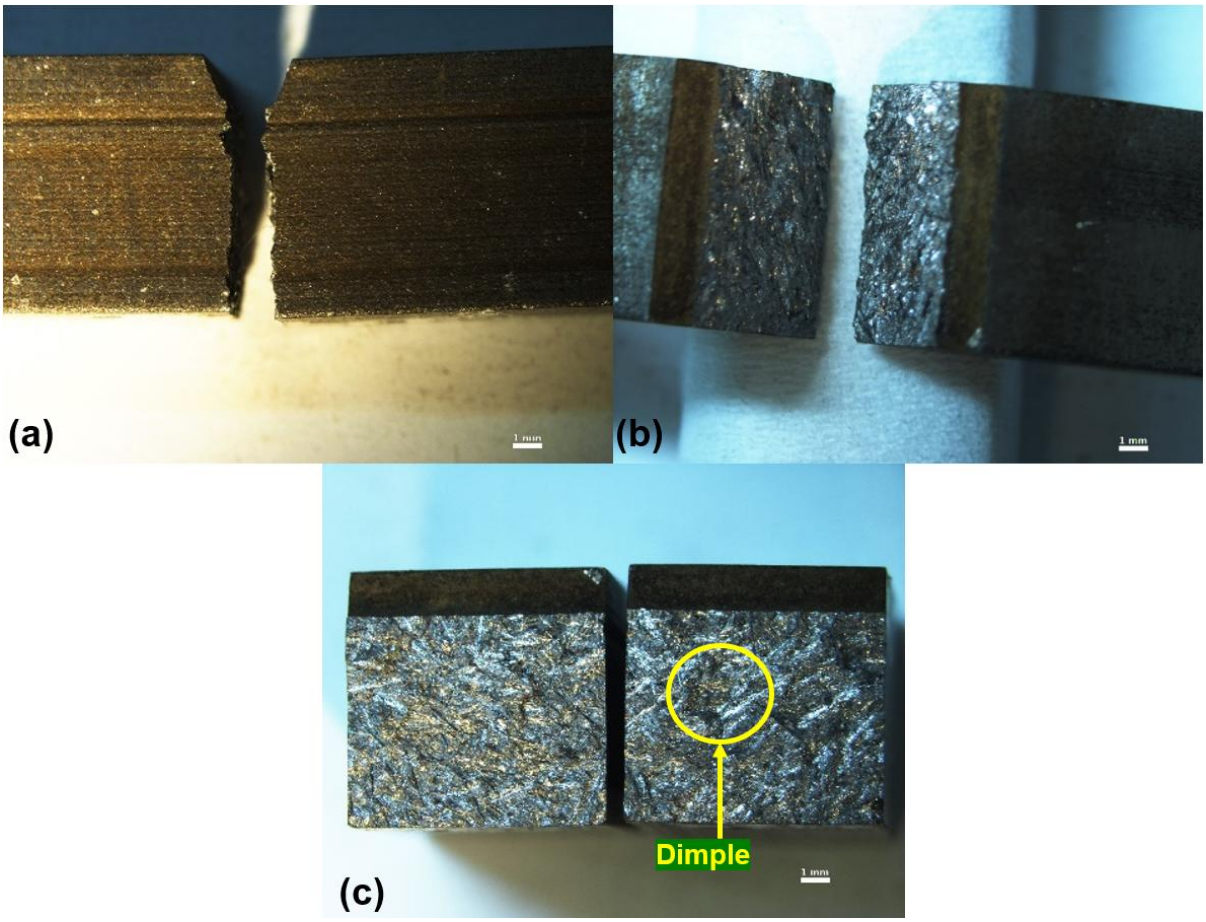

Figure 5.7: Stereomicroscopic images of P3 as-cast samples after Charpy impact testing a) side view, b) angled view, c) top view.

5.4.2 Charpy Impact Toughness for Heat-Treated Samples

Figure 5.8a-c shows the stereomicroscopic images of P1ht after Charpy impact testing. The side view (Figure 5.8a) reveals a relatively smooth fracture surface with no evidence of plastic deformation, indicating extremely brittle failure. The brittle failure is characterised by a cleavage mode of fracture with some fibrous zones. P1ht absorbed 9 J less energy than P1 in the as-cast state (10 J), but more energy than P2ht and P3ht, as indicated in Table 5.1. Figure 5.9a-c displays the stereomicroscopic images of P2ht. The side view (Figure 5.9a) shows no plastic deformation and reveals a fracture path that did not follow the same plane, indicating a tearing mechanism rather than simple splitting. The angled view (Figure 5.9b) highlights the heterogeneous fracture surface, while the top view (Figure 5.9c) reveals grooved patterns along the grain boundaries, suggesting crack initiation and propagation influenced by the presence of primary carbides. P2ht absorbed only 8 J of energy, showing a significant reduction in toughness compared to P1ht. The stereomicroscopic images of P3ht, shown in Figure 5.10a-c, reveal a smooth and planar fracture surface indicative of a highly hard and brittle material. The

side view (Figure 5.10a) highlights well-defined fracture edges with no sign of plastic deformation, confirming complete energy absorption failure. The angled view (Figure 5.10b) shows river lines aligned with the direction of carbide formation, and the top view (Figure 5.10c) shows cleavage planes with a uniform appearance. P3ht exhibited the lowest toughness, absorbing only 7 J of energy, as indicated in Table 5.1.

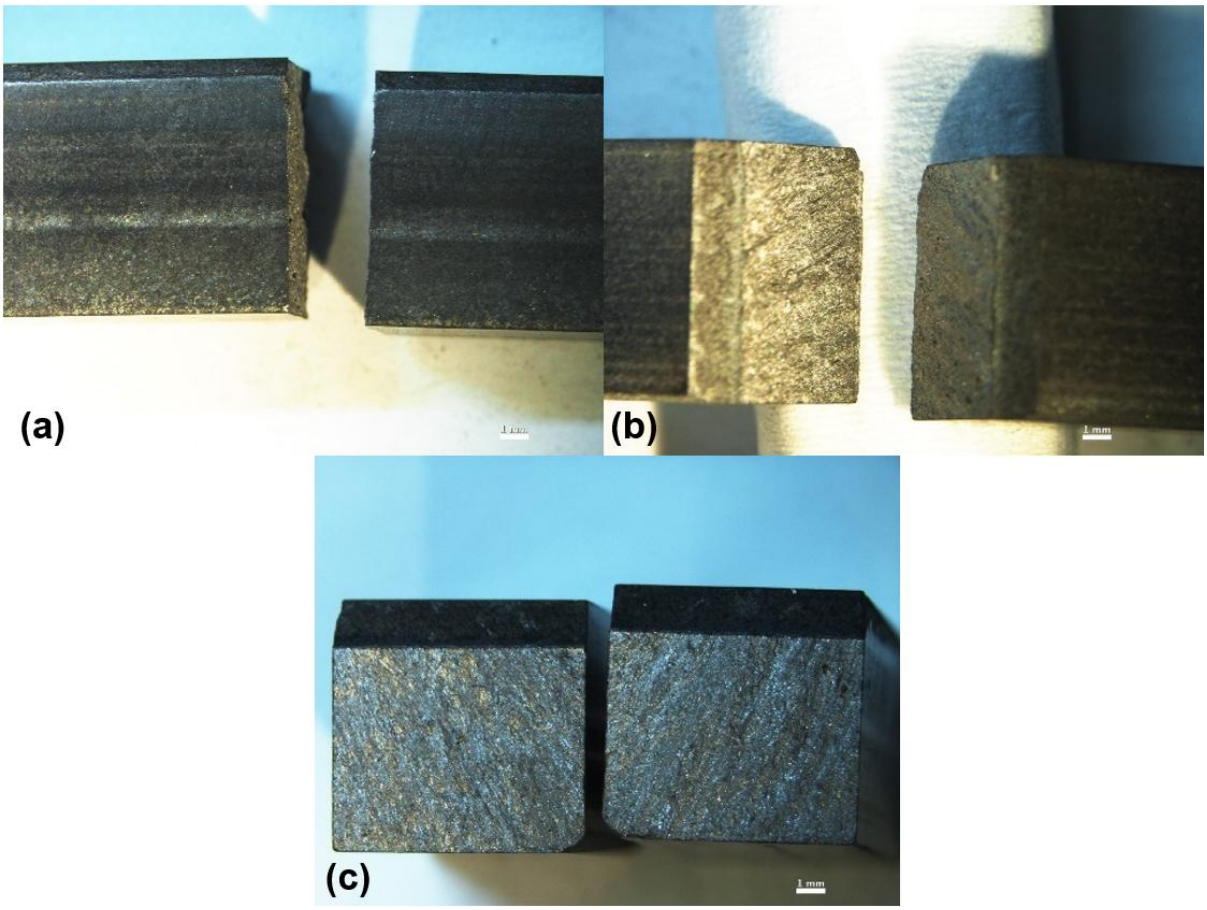

Figure 5.8: Stereomicroscopic images of P1ht samples after Charpy impact testing a) side view, b) angled view, c) top view.

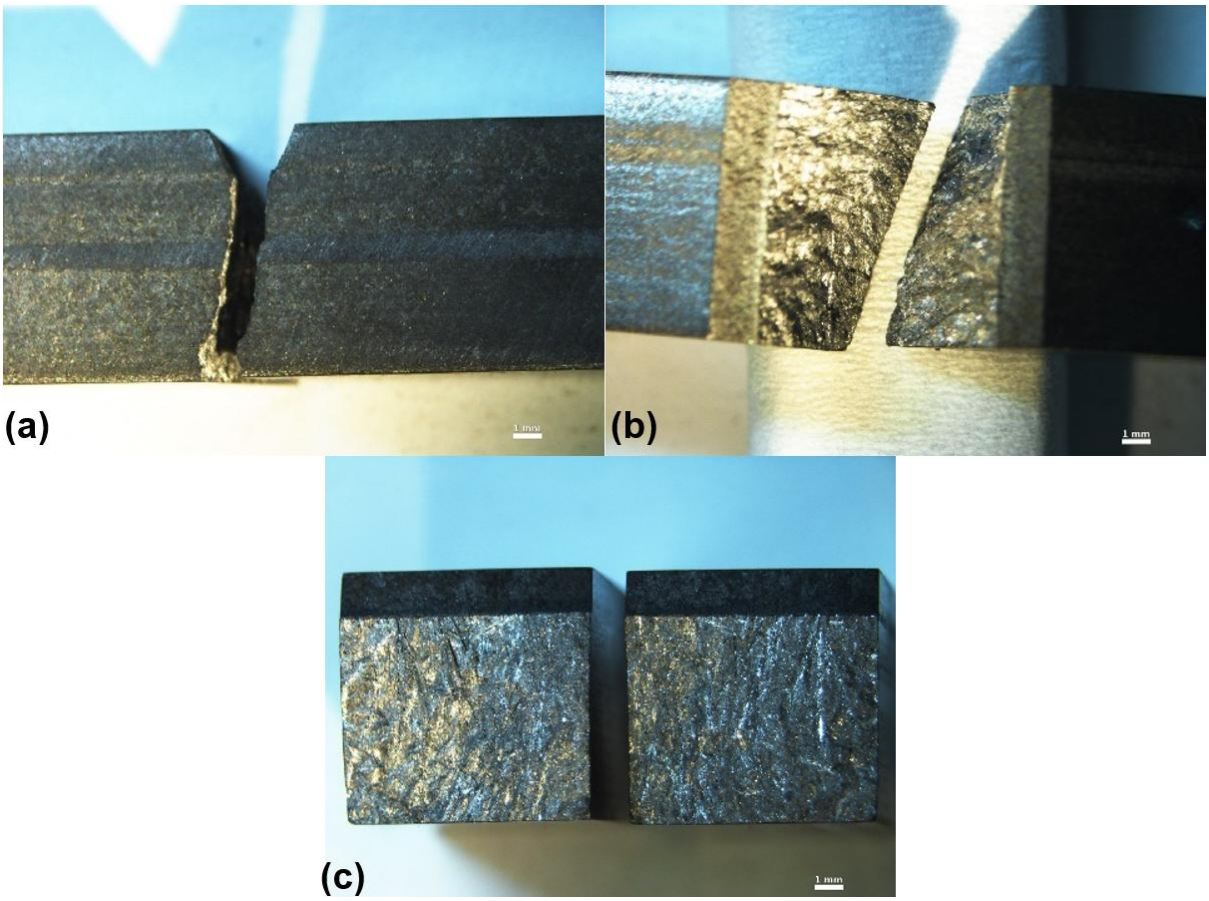

Figure 5.9: Stereomicroscopic images of P2ht samples after Charpy impact testing a) side view, b) angled view, c) top view.

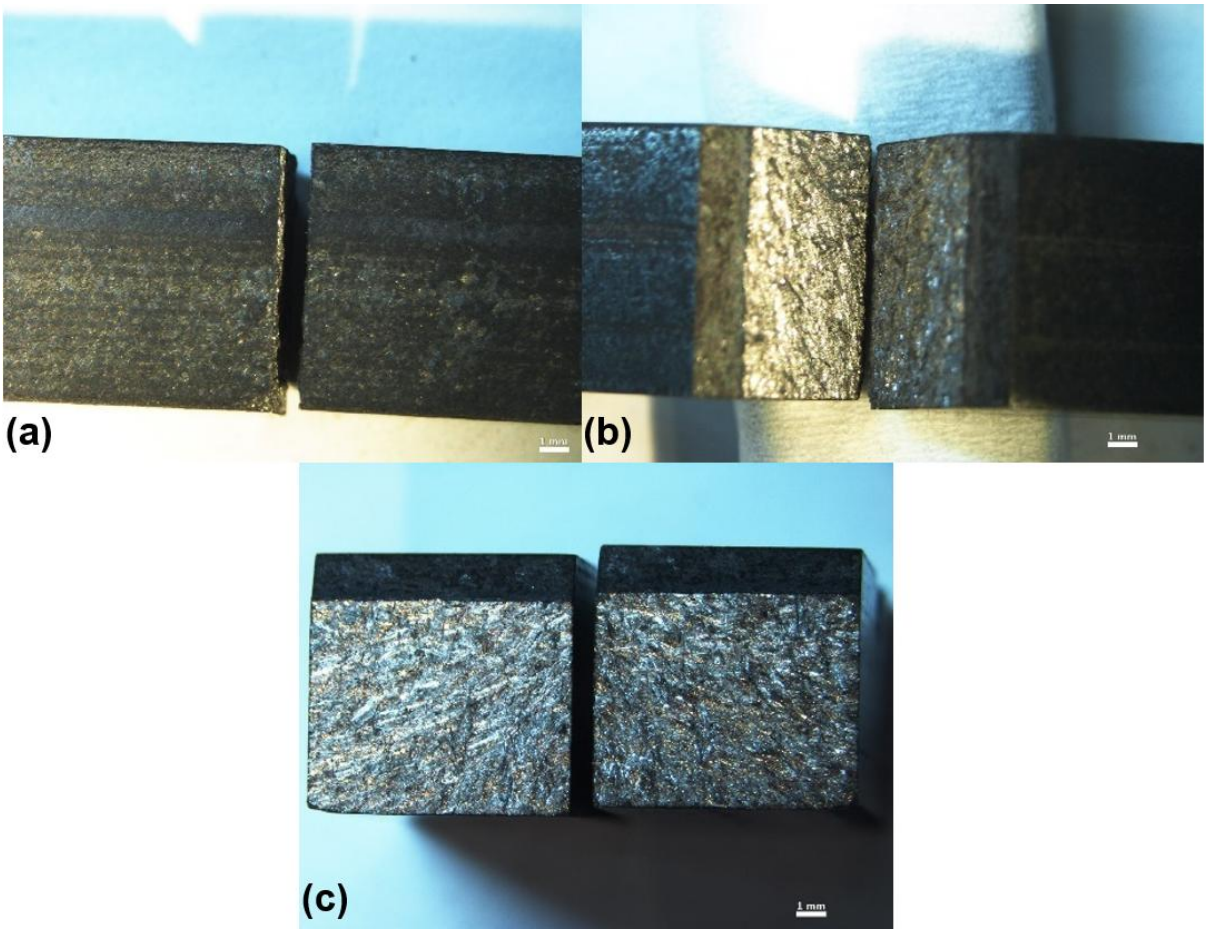

Figure 5.10: Stereomicroscopic images of P3ht samples after Charpy impact testing a) side view, b) angled view, c) top view.

5.5 Discussion

5.5.1 Hardness Characteristics of As-Cast and Heat-Treated HCCIs

The differences in hardness values from P1 to P3 as seen in Figure 5.1 can be attributed to variations in alloy compositions as seen in Table 4.1. Wang et al. (2019) mention that carbon content is a key factor in determining hardness. Higher carbon content generally increases hardness but also introduces brittleness due to the formation of carbides and other hard phases (Zhang et al., 2011). Since the difference in the Cr content in P1, P2, and P3 is so small, which is practically negligible, the impact of this difference is minor compared to the influence of carbon.

The Cr/C ratio plays a critical role in determining the type, size, morphology, and distribution of carbides in the microstructure, directly influencing the hardness of the material. A higher Cr/C ratio, as observed in P1 (Table 4.1), indicates relatively lower carbon content in the alloy. This reduces the volume fraction of carbides in the microstructure, as observed in Figure 4.7a,

as less carbon is available to form hard carbide phases such as M_7C_3. Consequently, the microstructure becomes more uniform, with fewer and less developed carbides. This uniformity reduces the number of hard phases that contribute to hardness, as carbides act as primary strengthening components by resisting deformation and impeding dislocation movement (Bedolla-Jacuinde et al., 2005). Liu et al. (2025) demonstrated that alloys with high Cr/C ratios tend to exhibit lower hardness due to fewer primary carbides forming, which results in a softer matrix. This trend is evident in P1 with the lower peak hardness frequency between 400 and 500 HV, which correlates with the lower carbide volume fraction. The absence of extensive carbide networks further explains the reduced hardness.

In P2, the increased carbon content and slightly lower Cr/C ratio contribute significantly to the formation and characteristics of the carbide network, directly affecting its hardness. The higher carbon content allows for the formation of a greater volume of M_7C_3 carbides, which are harder phases that act as primary barriers to dislocation movement, which increases hardness (Kootsookos & Gates, 2004; Guo et al., 2021). The primary and eutectic carbides are more in quantity. There are more coarse primary carbides distributed in finer eutectic carbides, forming an extensive eutectic carbide network as observed in Figure 4.7b. Such networks enhance hardness by providing a robust load-bearing microstructure that resists deformation under applied stresses (Hirose et al., 2011; Chung et al., 2013; Guo et al., 2021). The increased carbide volume, coupled with their coarser morphology, amplifies the hardness by increasing the ability of the alloy to resist deformation. The combination of extensive eutectic carbide networks and a higher carbide volume results in an intermediate peak hardness range of 500–550 HV in P2.

P3 exhibits the highest hardness, which can be attributed to its low Cr/C ratio and high carbon content, resulting in the highest carbide volume fraction. This composition promotes the formation of a heavily carbide-dominated microstructure, as observed in Figure 4.7c. The microstructure is characterised by large, plate-like primary M_7C_3 carbides and interconnected eutectic carbides. These carbides act as hard phases that significantly impede dislocation movement, enhancing the overall hardness of the material. The plate-like morphology of the primary M_7C_3 carbides provides increased resistance to deformation due to their large size and continuous nature, which effectively reinforces the austenite matrix (Inthidech & Matsubara, 2008; Wiengmoon et al., 2011). The eutectic carbides, which form networks around the primary carbides, further contribute to the hardness by filling intergranular regions and increasing the load-bearing capacity of the material (Lu et al., 2016; Wei et al., 2025). However, this microstructure also results in uneven carbide distribution, with localised areas dominated by

large primary carbides and regions where finer eutectic carbides are present. This heterogeneity is reflected in the hardness distribution, where a secondary peak in the 650 to 700 HV range indicates hardness segregation.

As a result of recrystallisation of the grains after heat treatment, the elongated primary carbides in P1 (4.7a) decompose into smaller, more uniformly distributed particles during heat treatment, creating the finer and more homogeneous matrix as seen in P1ht (Figure 4.11a). The refined microstructure improves the load-bearing capacity of the matrix, as the more uniform distribution of smaller eutectic carbides reduces stress concentration points and strengthens the material (Yang et al., 2009; Chung et al., 2013). This transformation from a coarse, widely dispersed primary carbide structure to a finer, more densely packed one directly contributes to the observed increase in hardness in P1ht. The Cr/C ratio ensured effective stabilisation of carbides, refining the microstructure and reducing defects (Yang et al., 2009; Chung et al., 2013).

The peak hardness in P2ht remained relatively unchanged because the coarsening of primary M_7C_3 carbides, which was caused by the decrease in Cr/C ratio, did not cause any significant alterations to the resulting hardness of the microstructure. This is attributed to the retained homogeneity of the primary and eutectic carbides within the matrix even after heat treatment. The growth of larger, interconnected carbides formed continuous or semi-continuous networks, contributing to the variation in carbide size in the microstructure. The increased variability in hardness, extending beyond 600 HV, is attributed to this heterogeneous distribution of coarsened primary carbides in between finer eutectic carbides and the additional formation of secondary carbides during heat treatment. Finely distributed secondary M_7C_3 carbides precipitated within the matrix, reinforced areas with lower primary carbide concentrations and more eutectic carbide concentrations (Chaus & Rudnickii, 2010; Pan et al., 2022). This dual effect created harder zones where both coarser primary carbides and secondary carbides were concentrated, while softer regions emerged in areas with smaller eutectic carbides. The interplay between the coarsened primary carbides in between finer eutectic carbides, finely distributed secondary carbides, and the retained homogeneity in the microstructure explains the broader hardness distribution in P2ht. P2ht exhibited a balance of localised hardening and softer zones, causing the observed variability.

P3ht exhibited the most significant increase in hardness after heat treatment due to its low Cr/C ratio and high carbon content, which promoted the formation of a carbide-dominated

microstructure. The low Cr/C ratio allowed the development of coarse, continuous carbide networks, particularly along grain boundaries, as observed in Figure 4.11c. These large, plate-like primary M_7C_3 carbides significantly enhanced hardness by providing strong barriers to deformation and creating a load-bearing framework within the material (Nam & Lee, 2008). Additionally, heat treatment facilitated the precipitation of secondary M_7C_3 carbides, which further strengthened the matrix in regions with fewer primary carbides. This combination of coarse primary carbides and finely distributed secondary carbides maximised hardness by impeding dislocation motion throughout the microstructure (Chaus & Rudnickii, 2010; Pan et al., 2022).

5.5.2 Fracture Toughness of As-Cast and Heat-Treated HCCIs

The fracture behaviour of HCCIs in both as-cast and heat-treated conditions highlights the relationship between hardness and fracture toughness. Each sample exhibits distinct fracture characteristics, influenced by carbide morphology, hardness, and the matrix composition. However, across all samples the primary mode of failure experienced was brittle failure.

In P1, the predominantly brittle failure with visible dimples and slight deformation indicating some ductile behaviour is linked to the high Cr/C ratio of P1, which results in a lower carbide volume and a softer matrix, allowing it to absorb more energy before fracturing (Pourasiabi & Gates, 2022; Liu et al., 2025). Even though P1 has the lowest hardness, it shows the highest Charpy toughness, as seen in Table 5.1. The reduced carbide content compared to P2 and P3 significantly decreases brittleness, making it more resistant to crack initiation and propagation (Antonov et al., 2017; Gadhikar et al., 2014). Because it lacks extensive carbide networks, the matrix plays a larger role in energy absorption, allowing for greater impact toughness. While carbides contribute to hardness by resisting deformation (Jain et al., 2021; Chen et al., 2022), the lower carbide fraction in P1 results in a softer, more uniform matrix that enhances ductility and impact resistance.

On the other hand, P2 exhibits a more brittle fracture mode, and the fracture surface shows more cleavage breakage than P1 but is smoother than P3. This pattern can be linked to its carbide morphology characterised by larger hexagonal primary M_7C_3 carbides in between smaller eutectic M_7C_3 carbides. The somewhat uneven fracture surface observed in the side and top views indicates a ductile-to-brittle transition failure, associated with its intermediate hardness. The microstructure (Figure 4.7b) contains more developed primary carbides than P1,

though they are finer than those in P3 (Figure 4.7c). Finer carbides contribute to a more uniform distribution and increased hardness by obstructing dislocation movement (Guan et al., 2018). Additionally, a uniform primary and eutectic carbide distribution helps reduce stress concentration zones, improving fracture toughness and making the material more resistant to crack propagation (Chung et al., 2013). This explains why P2 has the same Charpy toughness as P1, as seen in Table 5.1. Typically, hardness and toughness are inversely related but controlling primary and eutectic carbide growth through the Cr/C ratio can optimise both properties simultaneously. Studies by Shaw et al., (2012); Sun et al., (2021) and Zhang et al., (2023) have shown that refining WC grains into thin platelets can achieve this balance. The microstructure of P2 shows similar characteristics of this approach, providing higher hardness while maintaining moderate toughness. As a result, the Charpy toughness of P2 is equal to P1 but higher than P3.

The long plate-like primary M7C3 carbides characteristic of P3 serve as stress concentration points, making crack initiation and propagation easier (Guan et al., 2018; Heydari et al., 2024). The smaller eutectic carbides contribute to deep dimples in some areas. As a result, P3 deforms with minimal plastic deformation. P3 has the highest hardness due to its coarse carbide morphology. Additionally, eutectic M7C3 carbides further enhance hardness by resisting deformation. However, these coarse primary and eutectic carbide networks make the material more prone to brittle failure, as cracks propagate easily through large primary carbides (Guan et al., 2018). This trade-off between hardness and toughness is evident in the low Charpy impact toughness of P3.

Fracture toughness in all samples shows some variation following heat treatment. As demonstrated in Figure 5.8a-c, P1ht cracks in an extremely brittle manner without any signs of plastic deformation. The angled and top views show cleavage fracture with some fibrous zones, with the top view revealing a more uniform fracture surface than the as-cast state. This increased brittleness results from the hardness increase experienced in the sample following heat treatment. The grain refinement brought about by heat treatment and the secondary M_7C_3 carbides to precipitate improved hardness by filling areas formerly lacking more primary carbides. However, as carbide content increases, the hardness increases, leading to a brittle matrix. The hard carbides in increased volume limit the capacity of the matrix to absorb stress and deform plastic by restricting dislocation migration (Abdel-Aziz et al., 2017; Zhang et al., 2024). The precipitated secondary carbides occupy the once ductile areas, which increase the

susceptibility of the material to brittle fracture. Fewer soft zones to offset or deflect cracks mean that fractures spread more readily, thereby lowering the overall toughness even with higher hardness. However, P1ht still shows the best toughness among the heat-treated samples because of its rather smaller carbide content and finer carbide distribution.

P2ht shows an even more significant decrease in fracture toughness. The fracture surface, marked by cleavage planes and grooved patterns, suggests that crack initiation and propagation are influenced by both primary and secondary carbides. Its lower Cr/C ratio promotes the formation of more secondary carbides, which increases hardness but at the same time makes the material more brittle (Li et al., 2014; Guo et al., 2021). The observed tearing mechanism, rather than simple splitting, indicates that the fracture surface is more heterogeneous and that cracks do not always follow a straight cleavage path but are deflected due to microstructural features (Shterenlikht & Howard, 2004; Li et al., 2014). This behaviour is linked to the presence of large grains surrounded by smaller recrystallised grains, which can blunt and slow down micro-cracks to a limited extent. However, despite this localised crack-blunting effect, the overall reduction in toughness remains pronounced because the increased carbide content and less ductile matrix provide limited energy absorption before fracture (Ai et al., 2011; Chotěborský, 2013).

P3ht demonstrates the most brittle behaviour among the heat-treated samples. Its fracture surface is smooth and planar, with no evidence of plastic deformation, which confirms its very high hardness but also its brittleness. This behaviour is due to its low Cr/C ratio, which results in the highest volume of carbides and a microstructure heavily dominated by both primary and eutectic carbides. The large, plate-like primary carbides together with secondary carbides act as stress concentration points, making it easier for cracks to start and spread through the material (Guan et al., 2018). The presence of river lines on the fracture surface indicates that cracks tend to follow the alignment of the carbide structures, highlighting how these carbides control crack paths and promote brittle fracture. The well-defined, clean fracture edges further show that the material has very little capacity to absorb energy before breaking, which is typical of a very hard but brittle microstructure (Abdel-Aziz et al., 2017; Zhang et al., 2024). As a result of this carbide-rich and highly brittle structure, P3ht shows the lowest Charpy impact toughness among all the heat-treated samples.

Overall, the fracture behaviour of HCCIs in both as-cast and heat-treated conditions reflects the trade-off between hardness and toughness. While higher carbide content increases hardness,

it also promotes brittleness, reducing impact resistance. The heat-treated samples showed a considerable decrease in fracture toughness compared to the as-cast in order of decreasing Cr/C ratio, with P1ht retaining some energy absorption ability while P3ht completely lost energy absorption ability. Heat treatment further refines the microstructure and increases hardness, but at the expense of toughness, making the materials more prone to brittle failure.

5.6 Conclusion

The findings from as-cast to heat-treated samples illustrate the influence of the microstructure on hardness and resulting toughness. P1, with the lowest carbide volume and finer underdeveloped carbides, had the lowest hardness but slightly superior toughness. Conversely, as-cast P3, characterised by the highest carbide volume and coarsest carbides, exhibited the highest hardness but the least toughness. P2, possessing intermediate value for carbide volume and intermediate fineness of microstructure, exhibited hardness and toughness qualities that were intermediate between P1 and P3. Heat treatment considerably enhanced the hardness of all samples by refining the carbide structure and forming M7C3 secondary precipitates. However, this increase in hardness led to diminished toughness, particularly in samples with a higher volume of carbides, such as P2ht and P3ht. The pronounced carbide precipitation in these samples increased hardness but resulted in brittleness and diminished energy absorption. P2ht, with more developed carbides than P1 but finer than those in P3, achieved a better balance between hardness and toughness. The results show the critical influence of the carbide volume and microstructure on the mechanical characteristics of high chromium cast iron influenced by the Cr/C ratio. A decreased Cr/C ratio and increased carbide volume increases hardness but diminishes toughness, especially after heat treatment.

5.7 References

Abdel-Aziz, K., El-Shennawy, M., & Omar, A. A. (2017). Microstructural characteristics and mechanical properties of heat treated high-cr white cast iron alloys. *International Journal of Applied Engineering Research*, *12*(14), 4675–4686.

Ai, Y.-L., Chen, W.-H., Ding, J.-Y., & He, W. (2011). Heat treatment process of low carbon high chromium white cast iron. *Jinshu Rechuli/Heat Treatment of Metals*, *36*(6), 107–110.

Antonov, M., Yung, D. L., Goljandin, D., Mikli, V., & Hussainova, I. (2017). Effect of erodent particle impact energy on wear of cemented carbides. *Wear*, *376–377*, 507–515.

Bedolla-Jacuinde, A., Hernández, B., & Béjar-Gómez, L. (2005). SEM study on the M7C3 carbide nucleation during eutectic solidification of high-chromium white irons. *Zeitschrift Fuer Metallkunde/Materials Research and Advanced Techniques*, *96*(12), 1380–1385.

Chaus, A. S., & Rudnickii, F. I. (2010). Diffusion and secondary carbide precipitation in high-speed steels. *Defect and Diffusion Forum*, *297–301*, 1071–1076.

Chen, Z., Guo, Q., Fu, H., & Zhi, X. (2022). Effect of heat treatment on microstructure and properties of modified hypereutectic high chromium cast iron. *Materialpruefung/Materials Testing*, *64*(1), 33 – 54.

Chotěborský, R. (2013). Effect of heat treatment on the microstructure, hardness and abrasive wear resistance of high chromium hardfacing. *Agriculture Journals,* 59(1), 23–28

Chung, R. J., Tang, X., Li, D. Y., Hinckley, B., & Dolman, K. (2013). Microstructure refinement of hypereutectic high Cr cast irons using hard carbide-forming elements for improved wear resistance. *Wear*, *301*(1–2), 695–706.

Gadhikar, A. A., Sharma, A., Goel, D. B., & Sharma, C. P. (2014). Effect of carbides on erosion resistance of 23-8-N steel. *Bulletin of Materials Science*, *37*(2), 315–319.

Guan, J., Wang, L., Zhang, Z., Shi, X., & Ma, X. (2018). Fatigue crack nucleation and propagation at clustered metallic carbides in M50 bearing steel. *Tribology International*, *119*, 165–174.

Guo, Q., Fu, H., Guo, X., Xing, Z., & Lin, J. (2021). Effect of carbon content on microstructure evolution and properties of hypereutectic high chromium cast iron. *Surface Review and Letters*, *28*(10).

Heydari, A., Zarei-Hanzaki, A., Mahmoudi, M., Moshiri, A., Jaskari, M., Karjalainen, L. P., Balanian, H., & Abedi, H. R. (2024). Small crack growth behaviour and correlated microstructure-sensitivity during cyclic deformation of a high-chromium/carbon wrought tool steel. *Materials Science and Engineering: A*, *905*.

Hirose, M., Yamamoto, K., Miyahara, H., Sakata, K., & Ogi, K. (2011). Abrasion behaviour of high Cr-V-Nb cast iron. *Key Engineering Materials*, *457*, 243–248.

Inthidech, S., & Matsubara, Y. (2008). Effect of alloying elements on variation of micro-hardness during heat treatment of hypoeutectic high chromium cast iron. *Materials Transactions*, *49*(10), 2322–2330.

Jain, A. S., Chang, H., Tang, X., Hinckley, B., & Zhang, M. X. (2021). Refinement of primary carbides in hypereutectic high-chromium cast irons: a review. *Journal of Materials Science*, *56*(2), 999–1038.

Karantzalis, E., Lekatou, A., & Mavros, H. (2009). Microstructure and properties of high chromium cast irons: Effect of heat treatments and alloying additions. *International Journal of Cast Metals Research*, *22*(6), 448–456.

Kootsookos, A., & Gates, J. D. (2004). The effect of the reduction of carbon content on the toughness of high chromium white irons in the as-cast state. *Journal of Materials Science*, *39*(1), 73–84.

Li, X., Xie, W., Zhou, X., & Ma, Y. (2014). Influence of Ti, Nb, V, and Mo on morphology and properties of high chromium carbides. *Tezhong Zhuzao Ji Youse Hejin/Special Casting and Nonferrous Alloys*, *34*(8), 804–807.

Liu, S., Li, J., Su, X., Cui, S., Zhang, H., & Ren, Z. (2025a). Effect of Cr:C ratio on open three-body wear resistance of squeeze cast high chromium cast iron. *Tribology International*, *202*.

Liu, S., Li, J., Su, X., Cui, S., Zhang, H., & Ren, Z. (2025b). Effect of Cr:C ratio on open three-body wear resistance of squeeze cast high chromium cast iron. *Tribology International*, *202*.

Lu, L., Hou, L. G., Zhang, J. X., Wang, H. B., Cui, H., Huang, J. F., Zhang, Y. A., & Zhang, J. S. (2016). Improved the microstructures and properties of M3:2 high-speed steel by spray forming and niobium alloying. *Materials Characterization*, *117*, 1–8.

Nam, D., & Lee, S. (2008). Effects of tempering on microstructure, hardness, wear resistance, and fracture toughness of Cr_3C_2/steel surface composites fabricated by high-energy electron-beam irradiation. *Metallurgical and Materials Transactions A: Physical Metallurgy and Materials Science*, *39*(11), 2615–2625.

Pan, Y., Jin, T., Yuan, N., Ma, T., & Fu, H. (2022). Effect of austenitizing temperature on microstructure and properties of a high-speed cobalt steel. *Materialpruefung/Materials Testing*, *64*(8), 1122–1135.

Pourasiabi, H., & Gates, J. D. (2022). Effects of matrix chromium-to-carbon ratio on high-stress abrasive wear behaviour of high chromium white cast irons dual-reinforced by niobium carbides. *Tribology International*, *167*(November 2021), 107350.

Shaw, L. L., Luo, H., & Zhong, Y. (2012). WC-18wt.% Co with simultaneous improvements in hardness and toughness derived from nanocrystalline powder. *Materials Science and Engineering: A*, *537*, 39–48.

Shterenlikht, A., & Howard, I. C. (2004). Partition of Charpy fracture surface with digital image processing. In *International Journal of Fracture* (129).

Sun, J., Huang, Z., & Zhao, J. (2021). High-hard and high-tough WC-TiC-Co cemented carbide reinforced with graphene. *Materials Today Communications*, *29*.

Wang, X., Chen, Y., Wei, S., Zuo, L., & Mao, F. (2019). Effect of carbon content on abrasive impact wear behaviour of cr-si-mn low alloy wear resistant cast steels. *Frontiers in Materials*, *6*.

Wei, D., Mo, Z., Lu, J., Li, X., Weng, Y., Ren, X., & Hu, C. (2025). Eutectic resolidification and ultrafast self-quenching of the microstructure in the surface layer of high-speed steel by scanning electron beam treatment. *Vacuum*, *231*.

Wiengmoon, A., Pearce, J. T. H., & Chairuangsri, T. (2011). Relationship between microstructure, hardness and corrosion resistance in 20 wt.%Cr, 27 wt.%Cr and 36 wt.%Cr high chromium cast irons. *Materials Chemistry and Physics*, *125*(3), 739–748.

Yang, J., Wang, B., Yang, M., Ding, W.-C., Wang, P., & Luo, D.-J. (2009). Effect of instant modification on microstructure and properties of high chromium cast iron. *Zhuzao/Foundry*, *58*(2), 166–168.

Zhang, P., Li, S. X., & Zhang, Z. F. (2011). General relationship between strength and hardness. *Materials Science and Engineering: A*, *529*(1), 62–73.

Zhang, X., Li, C., Yang, X., & Di, X. (2024). Effect of Quenching-and-Tempering Heat Treatment on Mechanical Properties and Heat-Affected Zone Softening Behaviour of Ultra-High Strength Steel. *Journal of Materials Engineering and Performance*, *33*(1), 227–239.

Zhang, Y., Liu, Y., Huang, K., & Wang, L. (2023). Effects of Cr2(C,N) addition on microstructure and comprehensive mechanical properties of ultrafine cemented carbide. *Materials Science and Engineering: A*, *870*.

Chapter 6: The Influence of Microstructural Constituents on Wear Performance of High Chrome Cast Irons

6.1 Introduction

Wear occurs when a material gradually loses surface material due to friction and repeated contact with another surface. In industries such as mining and manufacturing, where components experience high friction and mechanical stress, selecting materials with high wear resistance is essential (Ortega-Cubillos et al., 2015). HCCI is widely used for this purpose because it contains hard carbides that reduce material loss by increasing resistance to wear (Filipovic, Korac & Gavrilovski, 2013). However, the wear performance of HCCI depends on several factors, including hardness, the size and volume of carbides, and their distribution within the material. These factors are directly influenced by the Cr/C ratio of the alloy. The results from the previous chapter highlight the significant role of carbide volume and microstructure in determining the mechanical properties of HCCI. A lower Cr/C ratio leads to an increased volume of carbides, which enhances hardness but may compromise toughness. Heat treatment further increases hardness, although this often comes at the expense of toughness. This chapter investigates the wear behaviour of high chromium cast iron and examines how these factors influence wear resistance. Both as-cast and heat-treated samples are tested to evaluate the effect of heat treatment on wear performance. The study analyses the coefficient of friction (COF) and wear rates to establish the relationship between friction and material loss, considering the microstructural characteristics of the alloy. By comparing wear tracks and examining worn surfaces, this chapter identifies which microstructural features offer the best protection against wear. The effect of carbide size, shape, and volume on wear resistance is discussed, along with the alloy composition that provides the optimal balance between hardness and durability.

6.2 Wear Resistance of As-Cast HCCIs

6.2.1 Coefficient of Friction Behaviour of As-HCCI Samples

Figure 6.1 shows the plot of coefficient of friction (COF) against time during the dry sliding wear experiments between the alumina ball and as-cast samples P1 to P3 surfaces. The COF plots show that all three samples, P1, P2, and P3 follow a similar trend, where the COF increases sharply at the beginning of the test during the running-in phase before stabilising after approximately 100–200 m running for 1000m in total. Among the samples, P3 has the highest COF, fluctuating between ~0.8 and 0.85 and drastically decreasing towards the end of the run to well below the COF of P1 and P2. P1 and P2 show the same COF behaviour with a COF between ~0.7 and 0.75, with P2 showing less aggressive fluctuation compared to P1. After the running-in phase, the COF remains relatively stable, with minor fluctuations observed in all samples and a drastic decrease observed in P3 from well above P1 and P2 to below P1 and P2 from ~800m.

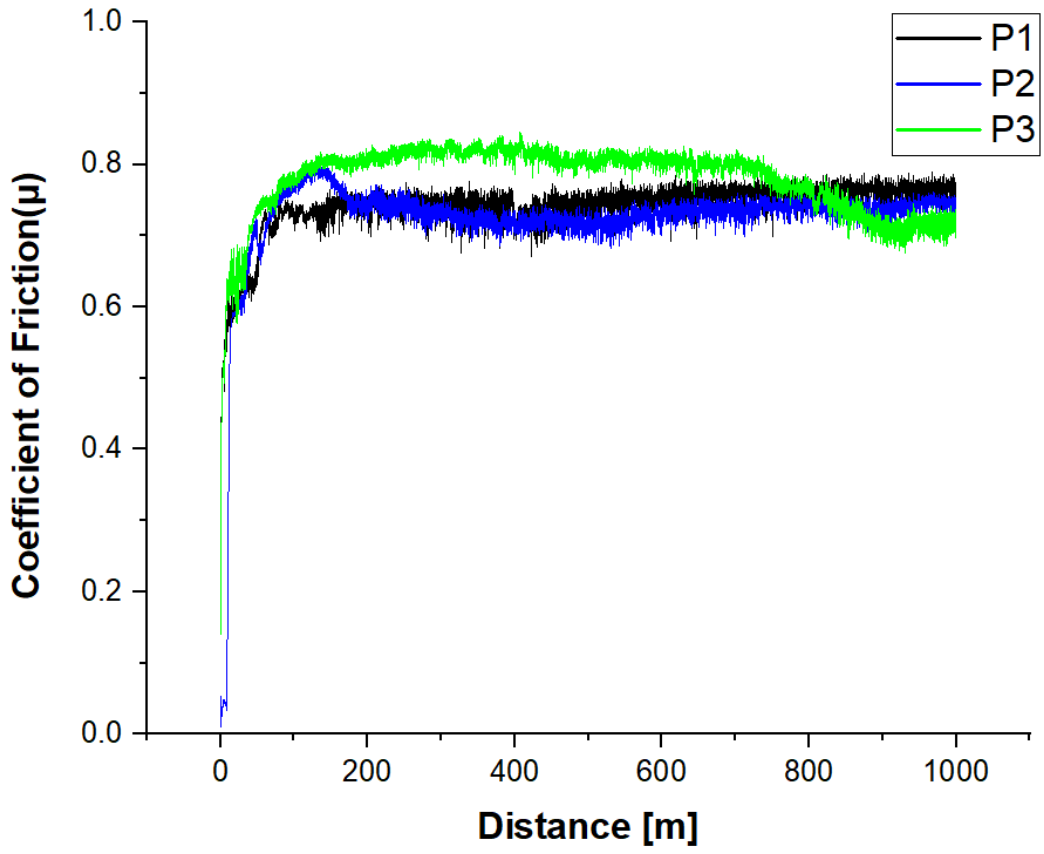

Figure 6.1: Coefficient of friction behaviour of as-cast samples P1 to P3 during dry sliding wear.

6.2.2 Wear Parameters and Wear Rates of the As-cast HCCI Samples

Table 6.1 shows wear parameters such as penetration depth, worn surface area, worn volume, and wear rate across the samples. The samples wear rate was calculated under Archard's theory of wear. The penetration depth versus width profiles is shown in Figure 6.2. The wear profiles reveal noticeable differences in penetration depth, worn surface area, and worn volume among the as-cast samples. P1 has the deepest penetration depth (0.037 μm), suggesting the most material loss at depth. P1 has a moderately worn surface area (44.3 mm^2) but the highest worn volume (0.0016 mm^3), indicating severe wear overall. P2 has a shallower penetration depth (0.019 μm), making it more resistant to deep wear than P1. However, it has the largest worn surface area (49.1 mm^2), indicating that wear is more evenly distributed rather than concentrated. Despite this, the worn volume for P2 remains relatively low at 0.0009 mm^3, indicating that it wears more uniformly. P3, with a penetration depth of 0.020 μm, has a slightly deeper wear scar than P2 but substantially less than P1. It has the smallest worn surface area (44.2 mm^2), indicating more localised wear. In addition, to having a thinner wear scar, P3 efficiently resists material loss, as seen by its worn volume matching P2 at 0.0009 mm^3.The results show that the wear experienced in P2 and P3 is the same wear rate, and the differences are in the wear behaviour.

Table 6.1: Dry sliding wear parameters for as-cast and heat-treated samples.

Sample	Penetration depth(μm)	Worn Surface Area(mm^2)	Worn Volume(mm^3)	Wear Rate (10^{-8} mm^3/Nm)
P1	0.037 ± 0.00285	44.3 ± 0.475	0.0017 ±0.00006	16.2 ± 10.9
P2	0.019 ± 0.00046	49.1 ± 0.15	0.0009 ± 0.000019	9.39 ± 1.97
P3	0.020 ± 0.00019	44.2 ± 0.235	0.0009 ± 0.000013	8.93 ±1.33
P1ht	0.033 ± 0.00600	47.8 ± 0.095	0.0016 ± 0.000025	15.9 ± 2.55
P2ht	0.021 ± 0.00272	46.4 ± 0.185	0.0015 ± 0.000014	9.74 ± 14.9
P3ht	0.021 ± 0.00169	47.8 ± 0.275	0.0010 ± 0.000074	9.37 ± 7.46

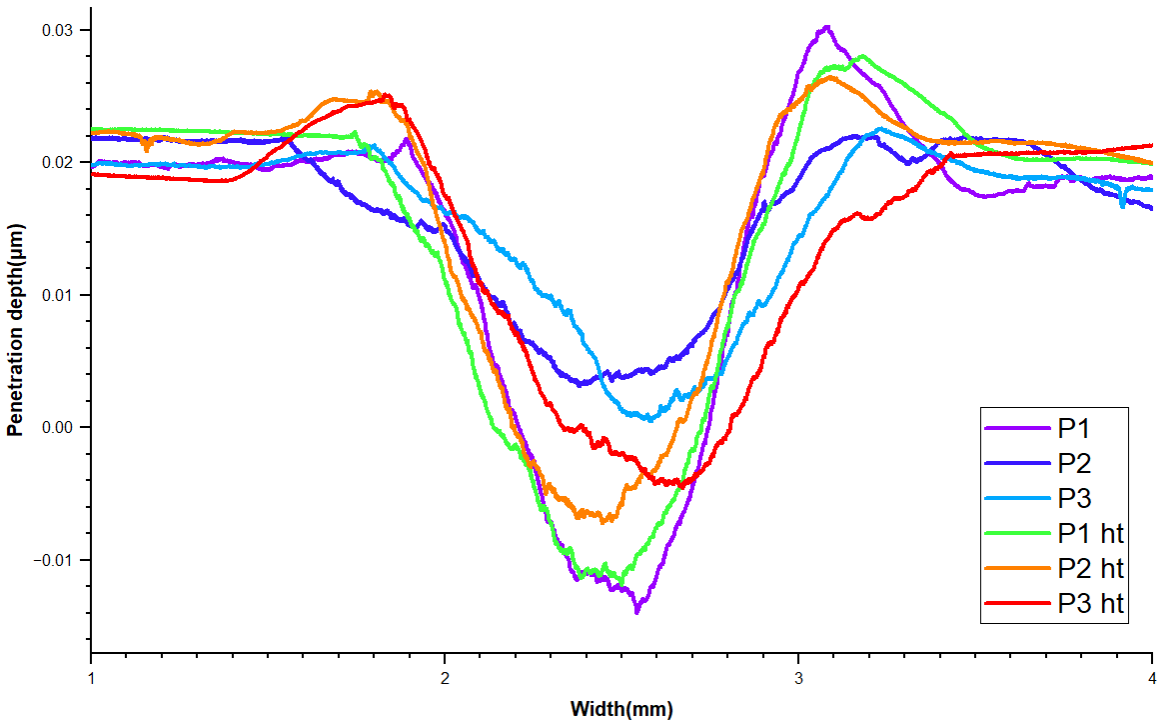

Figure 6.2: The penetration depth versus width of the wear scars obtained during dry sliding wear for the as-cast samples and heat-treated samples P1 to P3.

Figure 6.3 shows the wear rate trend for as-cast samples P1 to P3. The graph indicates that P1 has the highest wear rate at 16.2×10^{-8} mm³/Nm, followed by P2 at 9.39×10^{-8} mm³/Nm, and P3 has a marginally lower wear rate of 8.93×10^{-8} mm³/Nm compared to P2. Thus, the wear rate decreased progressively from P1 to P2 and P3, showing that P1 wears the most, while P2 and P3 are the more wear-resistant among the as-cast samples. The difference in the wear rate observed in P2 and P3 is marginally different; thus, they both wear the same.

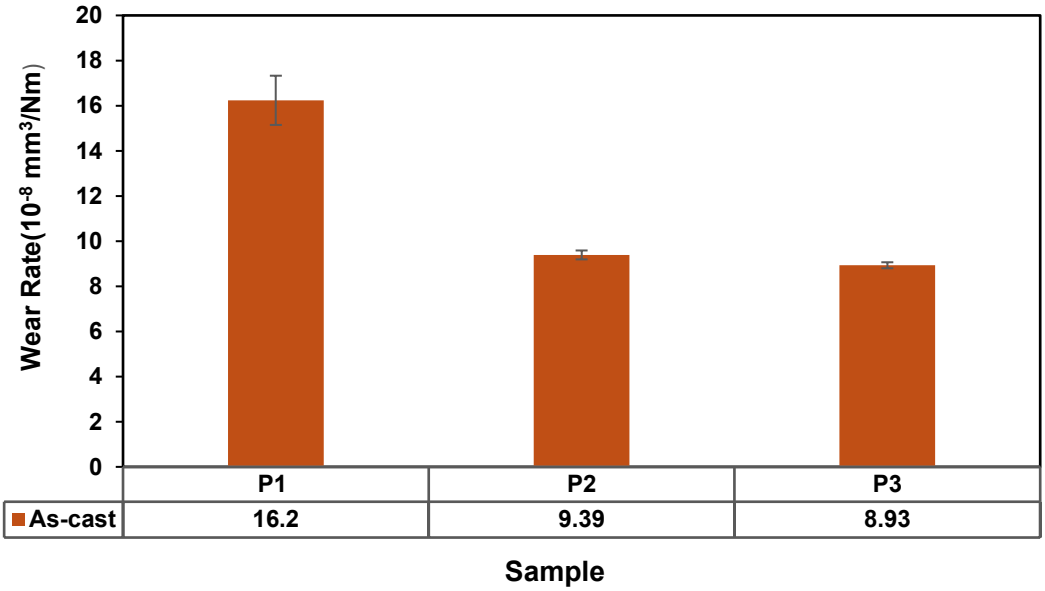

Figure 6.3: Wear rate trend for as-cast samples P1 to P3.

6.2.3 Wear Mechanism During Dry Sliding Wear of As-Cast High Chrome Cast Iron Samples

Figure 6.4 depicts the wear tracks of as-cast samples P1, P2, and P3 at low magnification (100x) in BSE and SE imaging. In P1 (images a and b), the wear track seems rough with large patches of material removal and deep grooves. The surface also shows significant ploughing marks and a rough surface, indicating abrasive wear. There is an accumulation of wear debris on the surface. The wear track in P1 consists of a combination of aggressive abrasive wear and adhesive wear. In P2 (images c and d), the wear track appears smoother than in P1, with less deep grooves. The dominant wear mechanism appears to be mild abrasive wear. There is still some wear debris accumulation on the surface, but in lesser quantities and it has less material tearing than P1. The grooves on the surface are not as deep, and the wear marks appear more controlled. P3 has mild abrasive and adhesive wear. In images e and f, the wear track appears the almost identical to that of P3; however with slightly more uniform wear. The surface grooves appear slightly finer and continuous, with minimal wear debris accumulation. Overall, there is only minor differences in the wear rack of P2 and P3, indicating they may wear at the same rate.

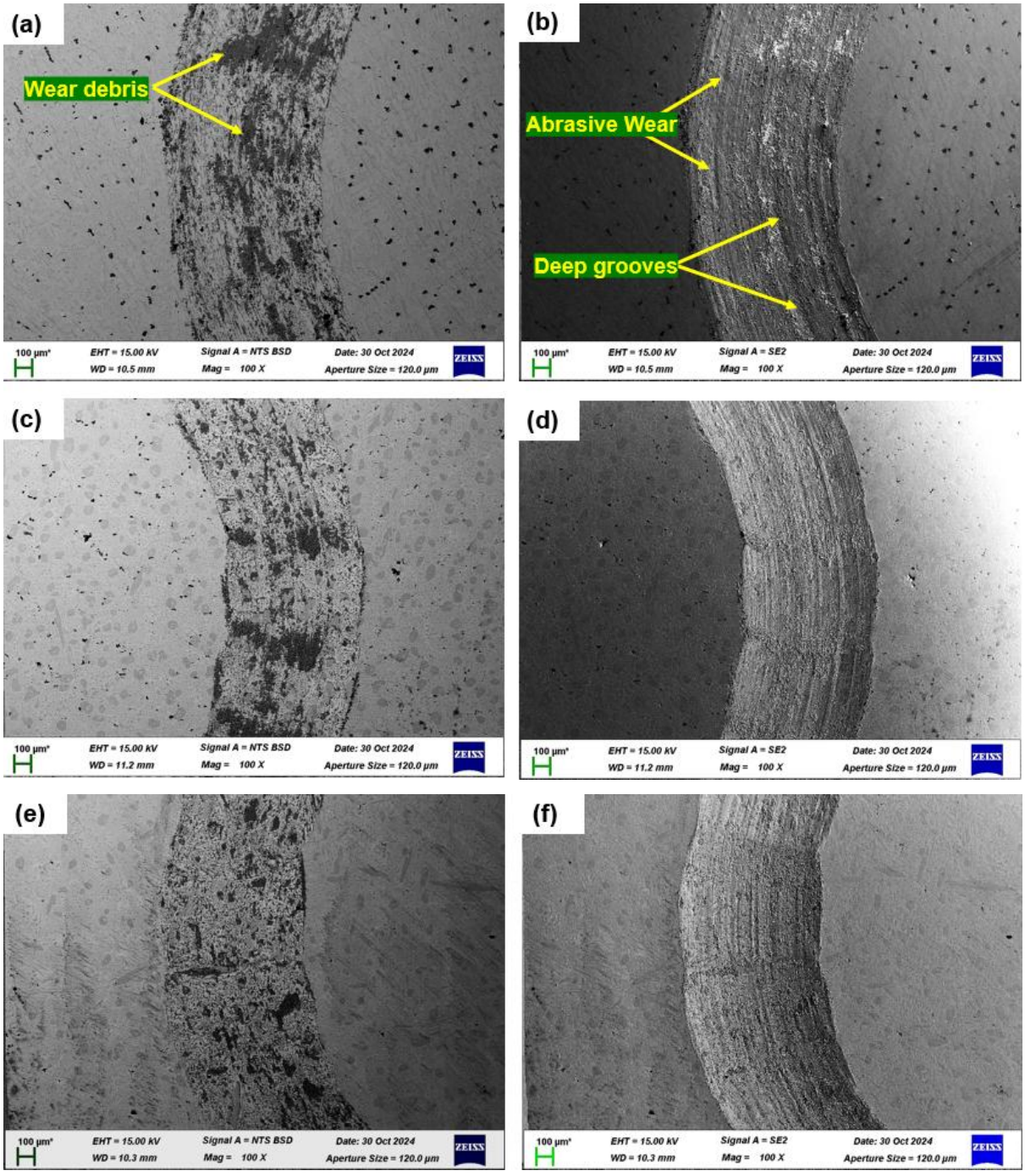

Figure 6.4: SEM images at 100x magnification of wear tracks for P1(a), P2(b) and P3(b) in BSE imaging and P1(b), P2(b) and P3(c) in SE imaging.

Figure 6.5a-f shows the scars for the corresponding samples at higher magnification (500×) in BSE and SE imaging. SEM images at 500× magnification show several types of abrasion and adhesion wear based on how carbides and the matrix react to sliding wear. Images a and b of sample P1 in Figure 6.5 reveal substantial material loss, deep grooves, and an uneven surface texture. Large parts of the matrix have been worn away, and debris is visible on the wear track. The absence of a developed and connected primary and eutectic carbide network causes

significant wear, with the matrix exhibiting obvious evidence of substantial deformation. P2 in images c and d in Figure 6.5 demonstrates a combination of two- and three-body abrasion, where the two-body abrasion is occurring from the debris attaching to the alumina ball and causing friction with the alloy surface and the three-body abrasion is occurring from the friction between the ball, the fractured carbide particles and the alloy surface. The track has moderately worn grooves with a mix of deep and shallow scratches. Primary M_7C_3 carbides remain embedded in the matrix, although some are visibly fractured. The surface texture indicates that the matrix and primary carbides are wearing at varying rates. For P3, images e and f in Figure 6.5 show finer wear tracks with shallow grooves and a more uniform wear pattern, indicating micro-level abrasion. The primary and eutectic carbides appear to be well integrated into the matrix, with evidence of primary carbide fracture.

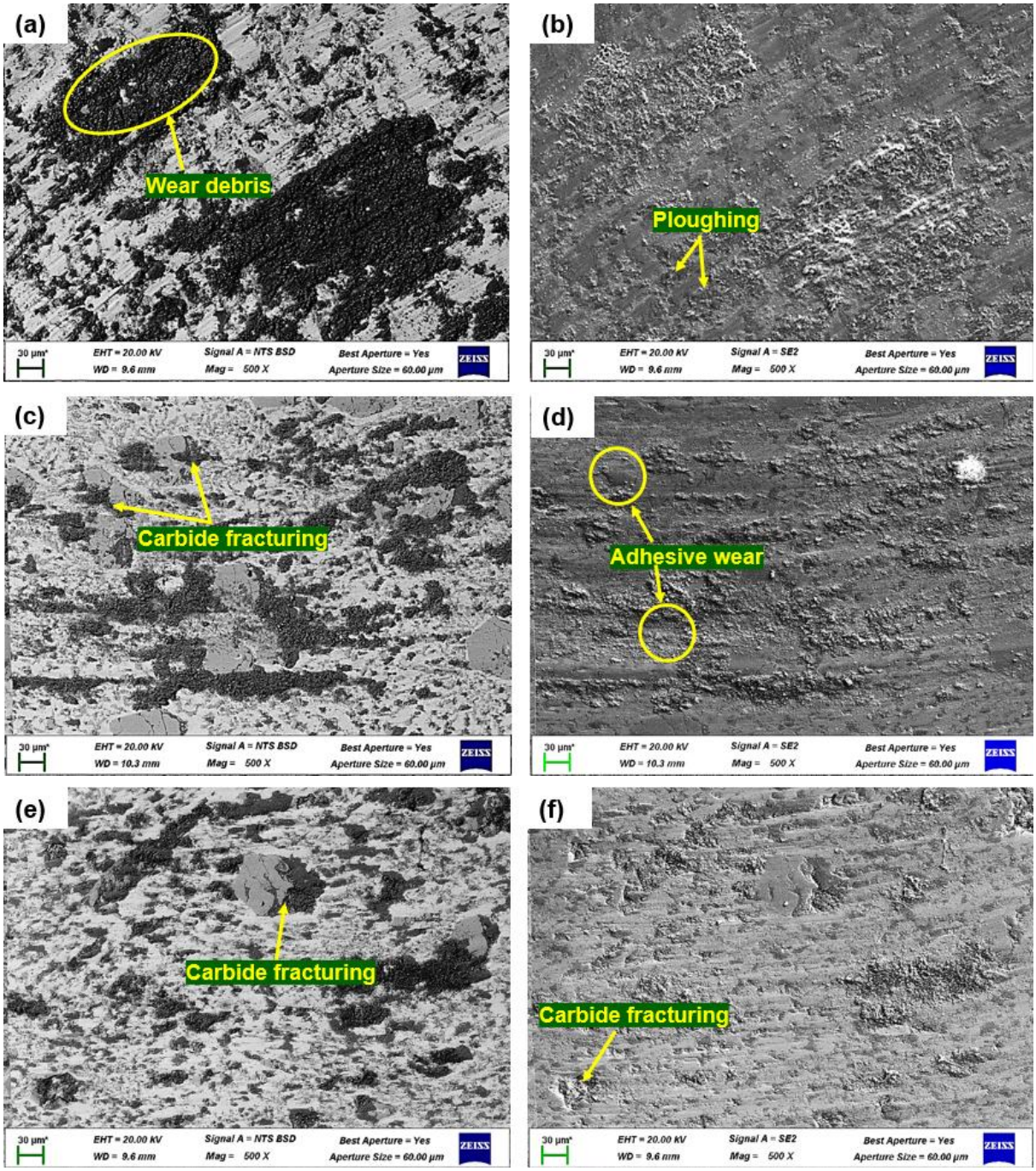

Figure 6.5: SEM images of wear tracks for P1(a), P2(c) and P3(e) at 500x magnification in BSE imaging and P1(b), P2(d) and P3(e) at 500x magnification in SE imaging.

6.2.4 Surface Topography of the Wear Surfaces for As-Cast and Heat-Treated HCCI Samples

The surface topography of the wear tracks for samples P1, P2, and P3 is shown in Figure 6.6 following dry sliding wear. For P1 Figure 6.6a, the wear surface of P1 is uneven and rough. Extensive material loss is observed as the high peaks and valleys seen on the surface. The surface displays deep scratches or grooves common of abrasive wear. The wear track surface is characterised by high material deformation, marked protrusions, and sharp edges, which

imply extreme wear. This extremely rough texture corresponds to plastic deformation and abrasive wear, where abrasive particles or asperities scrape away material. This is consistent with the aggressive fluctuations observed in the COF of P1 in Figure 6.1. For P2 (Figure 6.6b), the wear surface has a much smoother topography than P1. The fewer sharp peaks and valleys on the surface show mild abrasive wear. The surface has fewer prominent peaks and valleys, indicating mild abrasive wear. Though wear is still visible, it is more controlled than in P1 and therefore causes less material damage. This is most likely the result of a more homogeneously dispersed carbide structure, which helps to distribute the load and lessen the degree of wear experienced. This is also consistent with the COF of P2, which had less aggressive fluctuations than that of P1 in Figure 6.1.

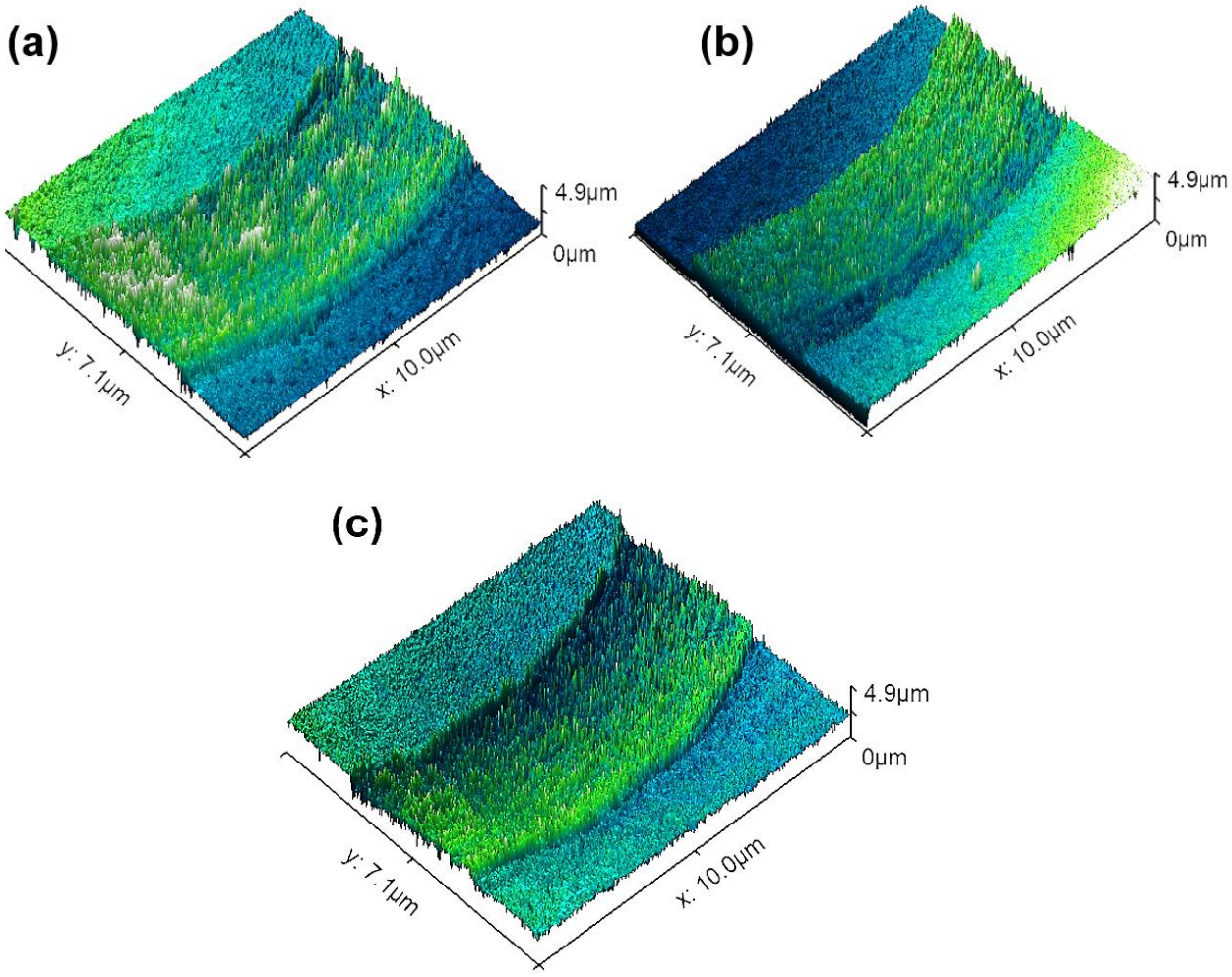

Figure 6.6: Surface topography of the wear surfaces for P1(a), P2(b) and P3(c) after dry sliding wear.

P3 (Figure 6.6c) has the most homogeneous topography among all the samples. Shallow, continuous grooves signify mild abrasive wear. The surface exhibits a well-distributed wear pattern that reflects a more steady wear process with more uniform material loss throughout.

This is consistent with the significant drop in COF towards the end observed in Figure 6.1. The homogeneous texture suggests that P3 has superior long-term wear resistance and less material deformation. These topography pictures taken generally imply that P3 has the most steady and more uniform wear behaviour in the long run, P1 shows the most severe wear while P2 shows an intermediate degree of wear. The variations in surface roughness draw attention to how the microstructure of every sample affects the wear rate.

6.2.5 Wear Balls After Dry Sliding Wear of As-Cast HCCI Samples

The wear surface of the alumina balls after dry sliding wear for the as-cast samples is shown in Appendix B-1a and b. The wear scars on the alumina balls were examined using a stereoscope, as shown in Figure 4.8. All the scars appeared almost perfectly round. According to Shaha et al. (2011), Hu et al. (2012), and Deleanu et al. (2022), severe wear would result in more irregular or elliptical scars, which was not the case in this study. The circular shape of the scars indicates that only mild wear occurred. Black or metallic marks and some significant amount of wear debris were clearly visible on the surface of the balls, showing that there was material transfer from the alloy samples to the alumina balls. This transfer was more noticeable than any actual damage to the balls themselves. The surface of the balls showed little to no significant damage. This is typical of adhesive wear, which was one of the wear mechanisms in this tribosystem. The wear on the alumina balls was considered negligible because the wear scars were very small. According to the ASTM G133-05 (Standard, 2010) standard, if the ball tip remains mostly round with only light abrasion, minor scratches, or a thin layer of transferred material after testing, it means that the flat alloy sample experienced most of the wear, and the ball did not suffer measurable damage (Standard, 2010). Authors Saikko, (2014); Ogunlana & Akinlabi, (2016) and D'Amato et al. (2017) also made the same observations. Therefore, no wear value was reported for the wear ball.

6.2.6 EDS Analysis of Wear Tracks for As-Cast HCCI Samples

The EDS spectrum in Figure 6.7b shows the composition of the wear debris area analysis done as shown in Figure 6.7a for sample P1. The spectrum shows dominant peaks of Fe followed by Cr and some C content. From these EDS results, the assumption that the majority of the debris was from the matrix with some from carbides could be plausible. The carbides in P1 were underdeveloped; therefore, the chances of them pulling out during wear are high, resulting in them being part of the debris seen in the spectrum. It is difficult to ascertain this information from the EDS alone, as there are a variety of factors that could bias the results. These include

the depth of the beam penetration if the debris was not thicker than 2 µm, consequently analysing the matrix or the carbide below which the debris was smeared. Additionally, the carbon content reported by the EDS spectra may not always be accurate, causing some bias to the results outputted.

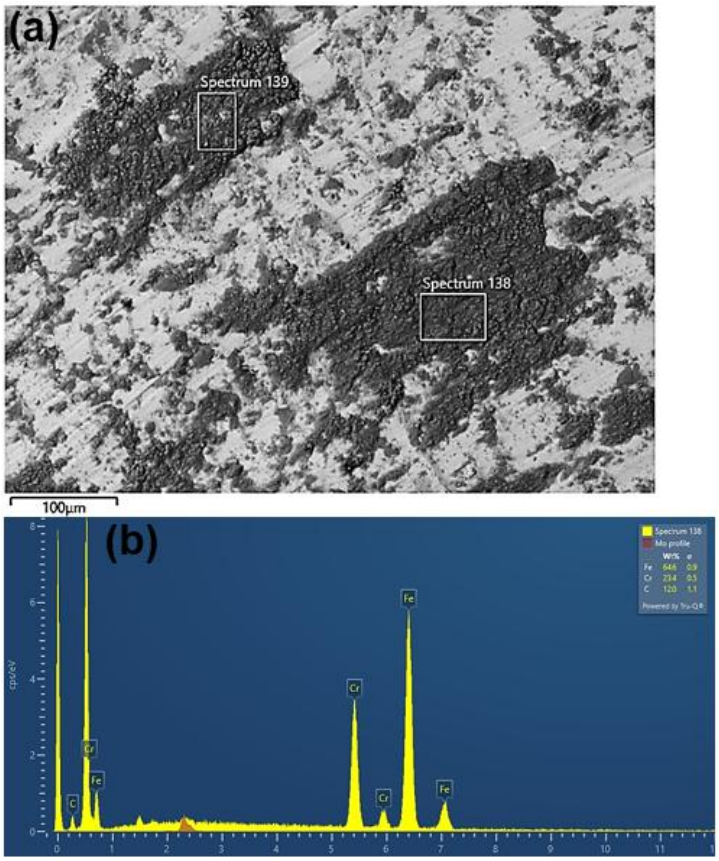

Figure 6.7: EDS a) image of area analysis done of wear debris and b) spectrum of the area analysis for P1.

The EDS spectra for P2 and P3 are shown in Figures 6.8 c and d, respectively, along with the images showing the areas where the analysis was done in images a and b. The spectra for both samples show dominant peaks of Fe followed by Cr and some C content. Similar inferences as made for sample P1 can be made here. The matrix was the primary worn material during wear testing, with some primary carbides fracturing and making up part of the debris. However, the results in this case are as well only indicative as the depth of the beam could have been analysing the material below the debris if the debris was not thicker than 2 µm. Additionally, the carbon content reported by the EDS spectra may not always be accurate, causing some bias to the results outputted.

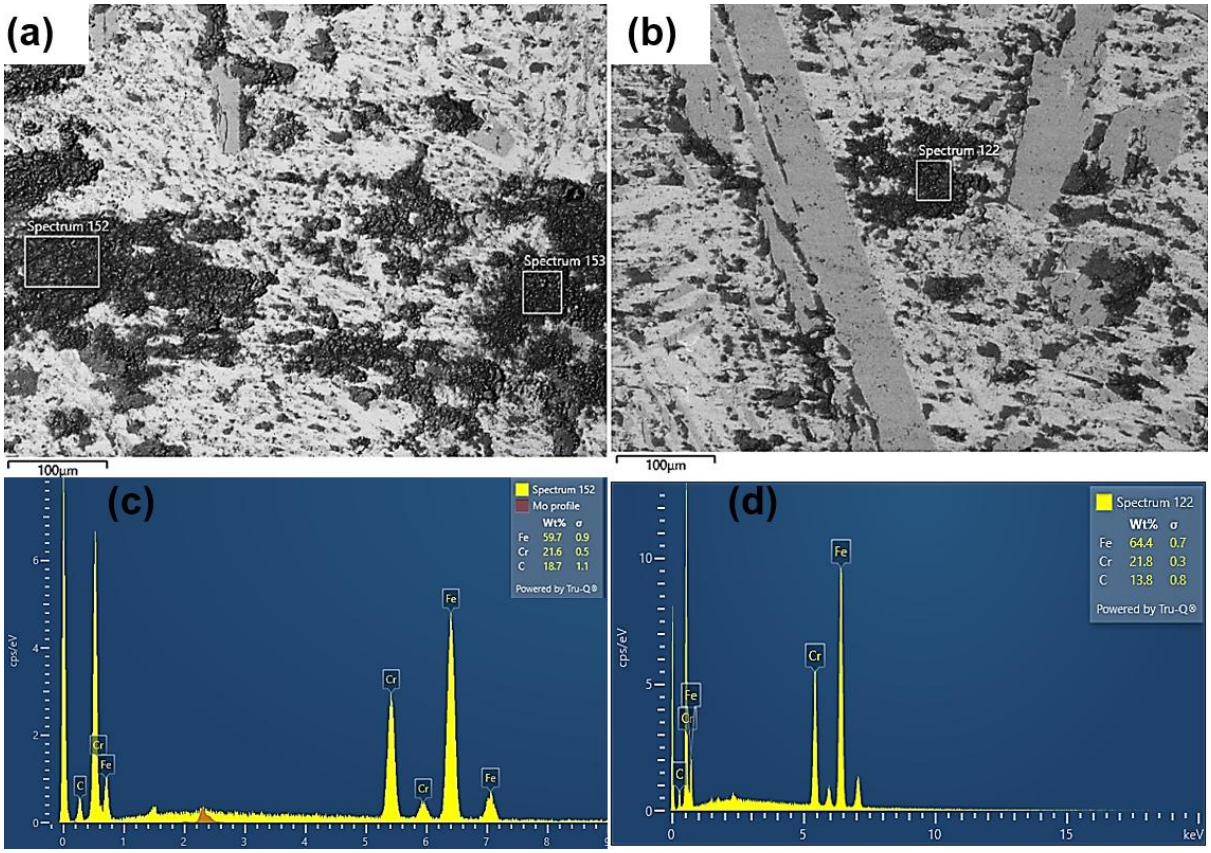

Figure 6.8: SEM images a) and b) showing the selected areas for EDS analysis in P2 and P3, respectively. The corresponding EDS spectra c) and d) present the elemental composition of the analysed regions.

6.3 Wear Resistance of Heat-Treated HCCIs

6.3.1 Coefficient of Friction of Heat-Treated HCCI Samples

P1ht to P3ht during dry sliding wear experiments between the alumina ball and as-cast samples P1 to P3 surfaces. The COF plots for P1ht, P2ht, and P3ht follow a similar pattern, with a sharp rise during the running-in phase before stabilising after about 100–200 m. The test covered a total distance of 1000 m, during which all three samples maintained relatively steady COF values, ranging between 0.7 and 0.8, with minor fluctuations. After heat treatment the three alloys exhibited similar COF behaviour and fluctuations. During the running-in phase, the COF rises as surface asperities come into contact, creating more resistance. As sliding continues, the surfaces smooth out, leading to a more stable frictional interaction. Once this phase is complete, the COF levels off, reflecting steady-state friction behaviour for the remainder of the 1000 m test. The three alloys fluctuate within similar COF ranges with each other, with marginal differences shown at the beginning of the running-in phase, caused by the different initial roughness of the surfaces. However, for the duration of the test, the differences in the tests all reached a peak and stabilised to the same COF.

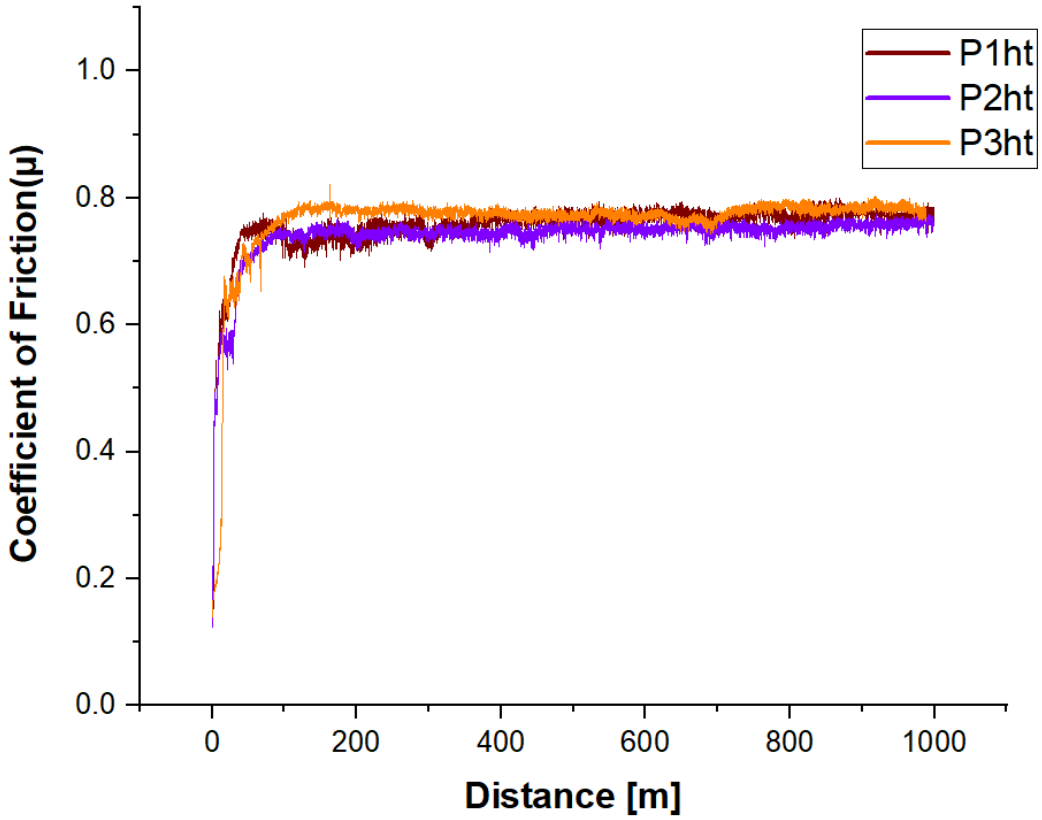

Figure 6.9: Coefficient of friction behaviour of heat-treated samples P1ht to P3ht during dry sliding wear.

When comparing the heat-treated samples (P1ht, P2ht, P3ht) to their as-cast counterparts (P1, P2, P3), in Figure 6.10 there are generally marginal increases in COF of P1ht and P2ht after heat treatment. This is with the exception of P3ht, which saw a noticeable decrease in COF. The COF for P3 was initially significantly higher than all samples as-cast and heat-treated until around 700 m in the running of the test, when it drastically dropped to below all the other samples. This can be attributed to increased hardness, homogenisation of the microstructures, and the precipitation of secondary carbides, which altered the microstructure and surface interactions during sliding. Figure 6.11 shows the trends of all the sample P1-P3 as-cast and heat-treated. The COF for P3 fluctuates above all samples for the majority of the test until it drops at ~700 m, where the COF drops below all samples.

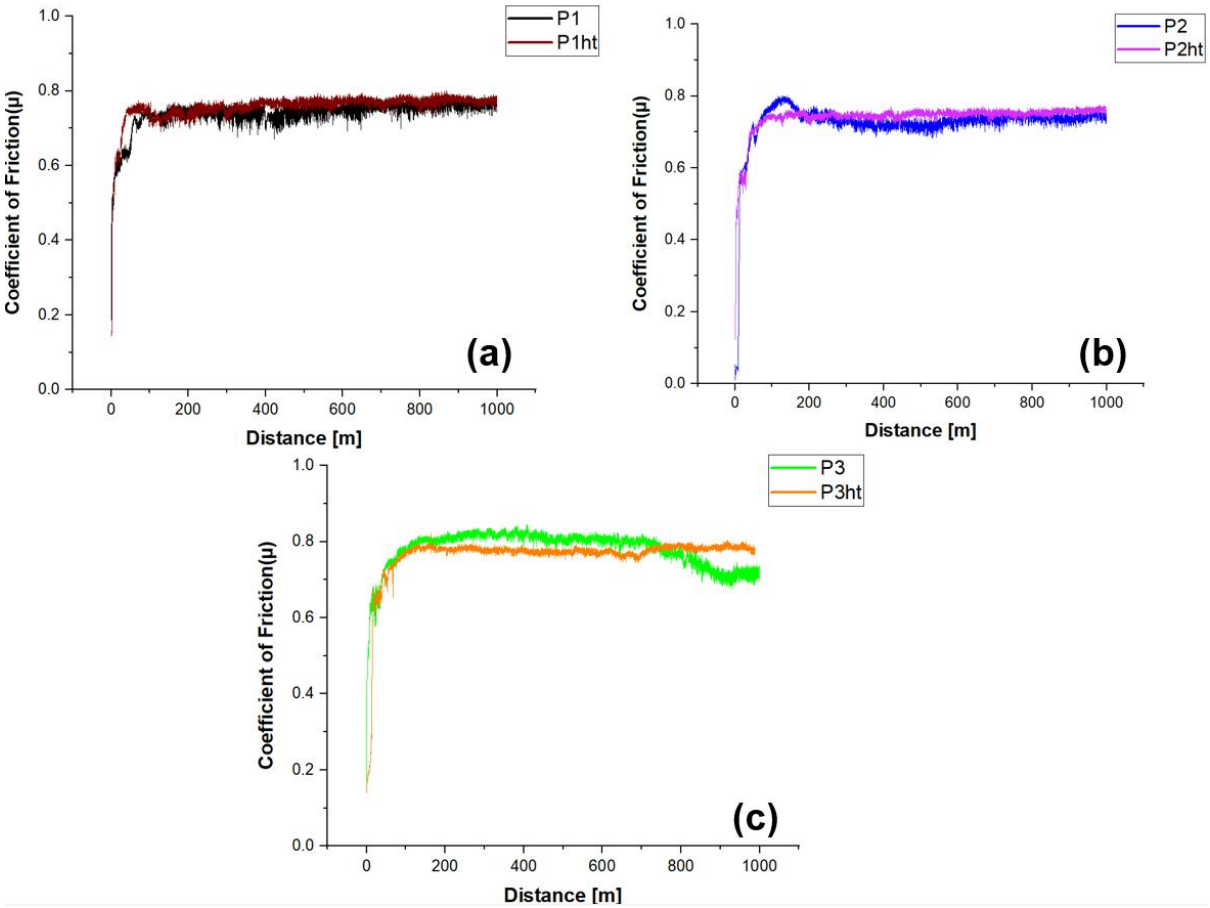

Figure 6.10: COF plots for the heat-treated plots and their as-cast counterparts during dry sliding wear.

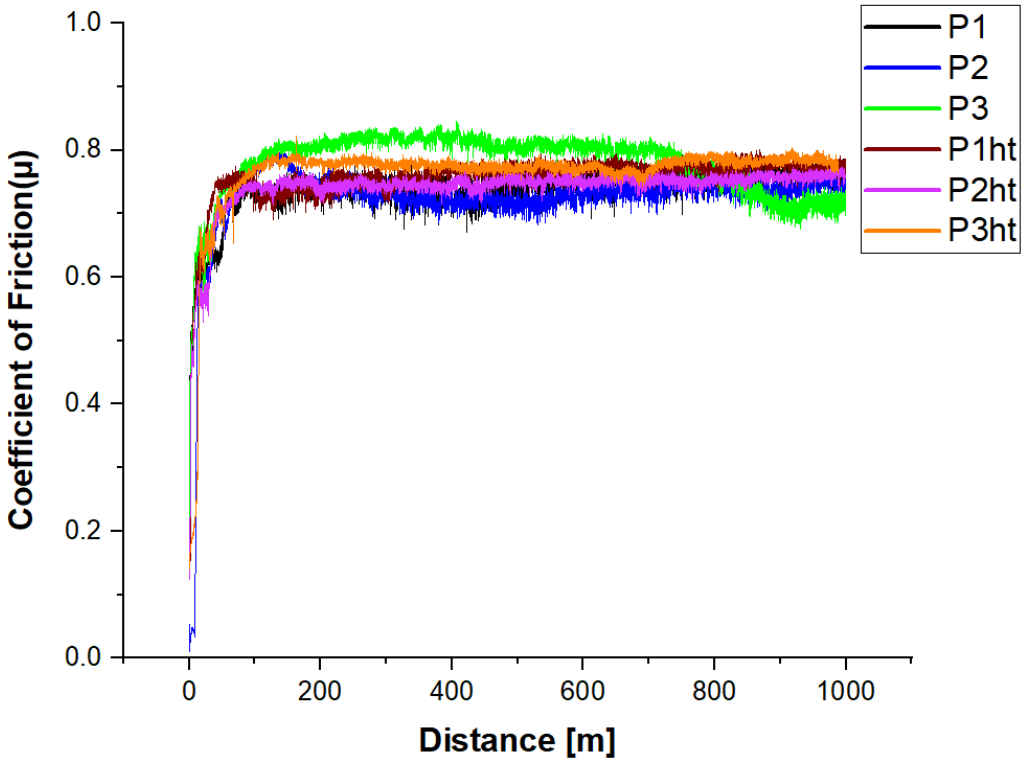

Figure 6.11: Coefficient of friction behaviour of as-cast samples heat-treated samples P1ht to P3ht during dry sliding wear.

6.3.2 Wear Parameters and Wear Rates of the Heat-Treated HCCI Samples

The wear profiles in Table 6.1 for the heat-treated samples (P1ht, P2ht, and P3ht) show changes in penetration depth, worn surface area, and worn volume due to heat treatment. P1ht has a penetration depth of 0.033 μm, which is lower than P1, meaning it resists wear better than the as-cast counterpart. However, its worn surface area increased to 47.8 mm², showing that wear is spread over a larger area instead of being deeply concentrated. Even with this improvement, P1ht still has the highest worn volume (0.0016 mm³) among the heat-treated samples, meaning it still wears the most. P2ht has a penetration depth of 0.021 μm, slightly deeper than as-cast P2, but its worn surface area is now smaller at 45.6 mm². This means that instead of spreading wear over a large surface, the material now wears slightly deeper. Even so, its worn volume is lower than P1ht at 0.0016 mm³, showing that its overall wear resistance has improved. P2ht and P3ht show a marginal difference in their wear resistance. However, P3ht had the lowest penetration depth of 0.020 μm. Its worn surface area increased to 47.5 mm², similar to P1ht, but its worn volume is the lowest at 0.0009 mm³. This suggests that heat treatment further strengthened the carbide morphology and size of P3ht, making it harder and more wear-resistant while allowing wear to spread out rather than penetrate deeply.

Figure 6.10 shows the wear rate trends of as-cast and heat-treated samples P1 to P3 after dry sliding wear. The wear rate for the heat-treated samples follows a clear pattern, with P1ht having the highest wear rate (15.9 × 10^{-8} mm^3/Nm), followed by P2ht (9.74 × 10^{-8} mm^3/Nm), and P3ht having the lowest wear rate (9.37 × 10^{-8} mm^3/Nm). P3ht remains the most wear-resistant, while P1ht experiences the most wear.

When comparing the as-cast and heat-treated samples in Figure 6.12, P1ht shows a slight improvement in wear resistance, with the wear rate dropping slightly from 16.2 × 10^{-8} mm^3/Nm in P1 to 15.9 × 10^{-8} mm^3/Nm in P1ht. On the other hand, P2ht experiences a marginal increase in wear rate, rising from 9.39 × 10^{-8} mm^3/Nm in P2 to 9.74 × 10^{-8} mm^3/Nm in P2ht. Similarly, P3ht also sees a marginal increase in wear rate compared to P3, going from 8.93 × 10^{-8} mm^3/Nm in P3 to 9.37 × 10^{-8} mm^3/Nm in P3ht. These results show that P1ht improved slightly, while P2ht and P3ht experienced marginal increases after heat- treatment. There are not many differences in the wear rates in the as-cast compared to the heat-treated.

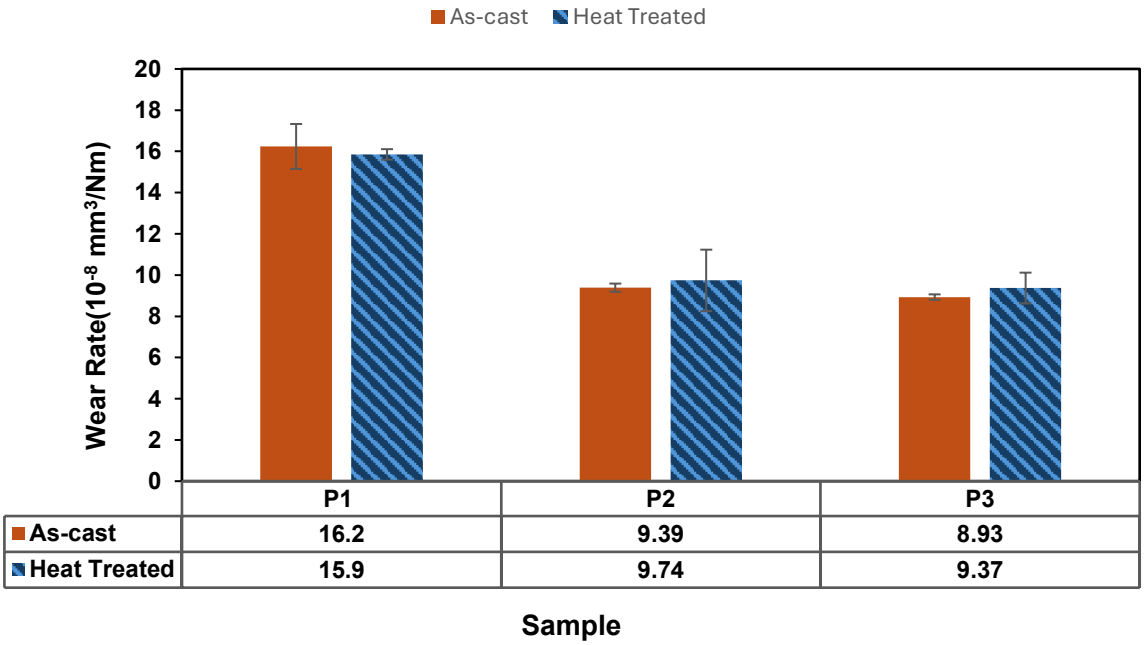

Figure 6.12: Wear rate trends of as-cast and heat-treated samples P1ht to P3ht.

6.3.3 Wear Mechanism During Dry Sliding Wear of Heat-HCCI Samples

Figure 6.13 shows the SEM images of wear tracks for heat-treated samples P1ht, P2ht, and P3ht at 100x magnification in BSE and SE imaging. In P1ht, images a and b, the wear tracks look more even, with a smoother surface and uniform grooves. There are no signs of deep ploughing marks, showing that the adhesive wear is less severe than in P1. The debris is spread out more evenly across the track, covering a larger surface area than in P1. The surface does

not have rough edges or large grooves, which suggests that the wear is not as aggressive as in P1. There are also signs of adhesive wear, with less material breaking off and a more uniform surface. The wear track in Figures 6.13c and d shows a rougher surface with an uneven pattern of wearing than P1ht. The surface consists of regions where more material has been removed than in others, giving the surface an uneven appearance. The surface also exhibits grooves and traces of material tearing, as well as minor debris accumulated in patches on the track; however, they are still relatively uniformly scattered across the track. There is evidence of sliding over primary carbides while material is removed from the matrix. Some regions contain deeper wear markings and deep scratches, indicating that wear was not distributed uniformly throughout the surface. The track shows signs of a more aggressive adhesive and abrasive wear pattern than in P1ht. The wear track in Figures 6.13e and f appears much smoother and more uniform compared to P1ht and P2ht. Unlike P1ht, which shows more material removal and uneven grooves, and P2ht, which has deep wear scars and fractured primary carbides, P3ht exhibits fine, continuous grooves with minimal material tearing. The wear surface in P3ht is more even, with evenly spaced grooves. There are fewer signs of severe plastic deformation or aggressive material loss compared to P1ht. The wear debris in P3ht similar to P2ht, showing finer and more evenly spread debris accumulation. The overall structure of the wear track for P3ht suggests similar wear resistance to P2ht, with P3ht experiencing more three-body abrasion than P3ht which experiences a balance between the modest abrasive and adhesive wear.

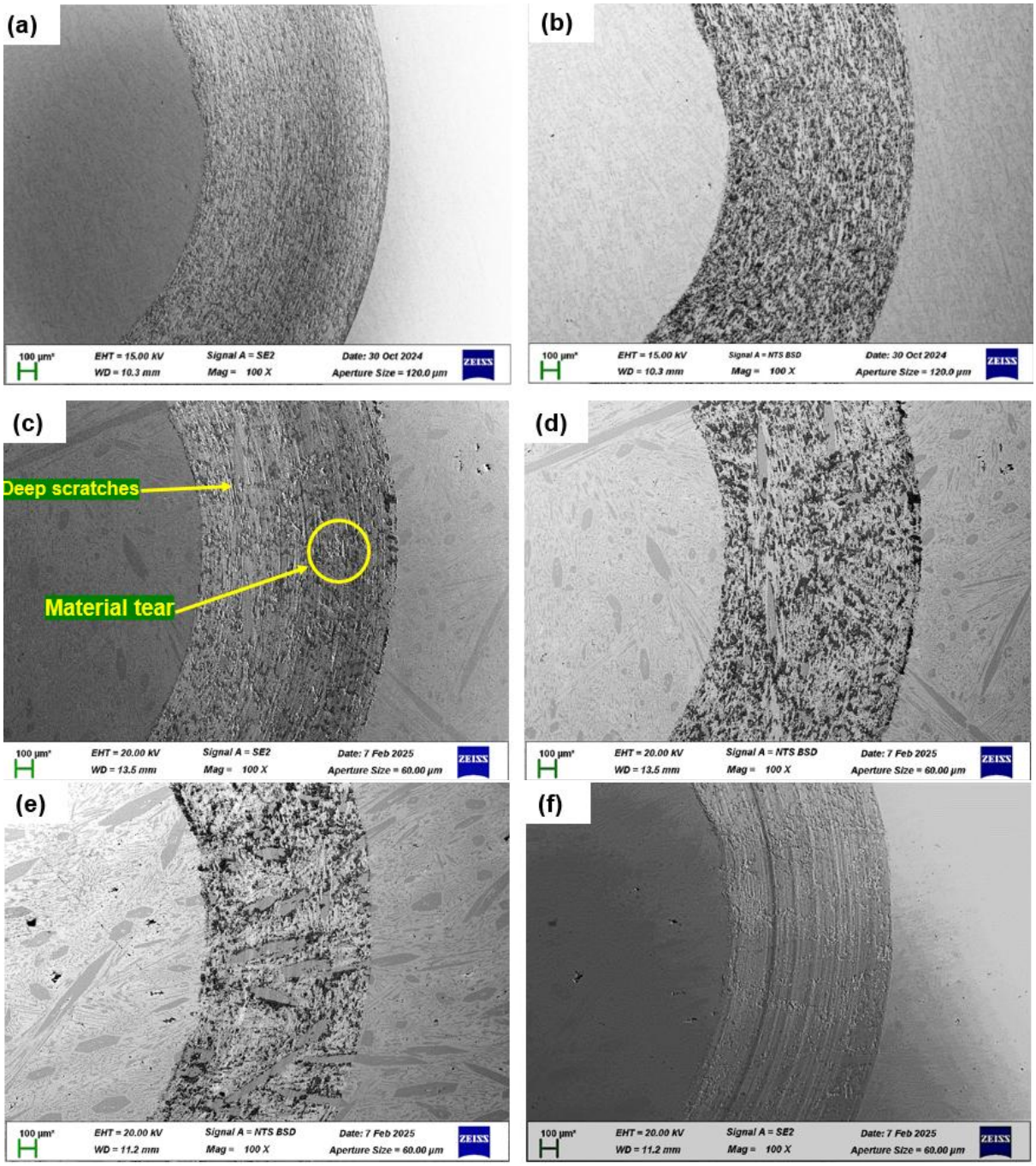

Figure 6.13: SEM images of wear track for P1ht(a), P2ht(c) and P3ht(e) at 100x magnification in BSE imaging and P1ht(b), P2ht(d) and P3ht(f) at 100x magnification in SE imaging.

Figure 6.14 shows the scars for the heat-treated samples P1 to P3 at higher magnification (500x) in BSE and SE imaging. The wear observed in Figures 6.14a and b primarily indicates a combination of mild abrasive wear and adhesive wear for P1ht. The presence of fine grooves and a continuous wear track suggests micro-abrasion, where small abrasive particles or asperities gradually wear down the surface without causing deep cutting or ploughing. The even wear pattern and smooth surface features suggest adhesive wear, where material is

transferred between surfaces due to the adhesion of the surfaces of the alumina ball and the alloy surface and then removed over time. Figures 6.14c and d show images of P2ht with scratches and grooves over the surface, indicating abrasive wear. The depth of the grooves varies, with some being scratched and some showing signs of tearing. The images also show some primary carbides cracked during wear. In certain locations, the debris appears smeared over the surface, which could indicate slight adhesive wear. The surface is uneven, with certain portions wearing faster than others, particularly where there are fewer carbides. The higher magnification images in Figure 6.14e and f show fine and shallow grooves on the wear surface, with a more uniform wear pattern compared to P1ht and P2ht. The surface has small fractured primary carbides, but they appear less frequent than in P2ht. There are regions of material smearing, with some areas showing slight adhesion marks. The grooves are continuous and less deep, with no significant tearing or rough ploughing marks. The wear debris is present but appears more evenly spread, without large, accumulated patches. The overall surface texture appears smoother, with fewer sharp edges and material removal marks.

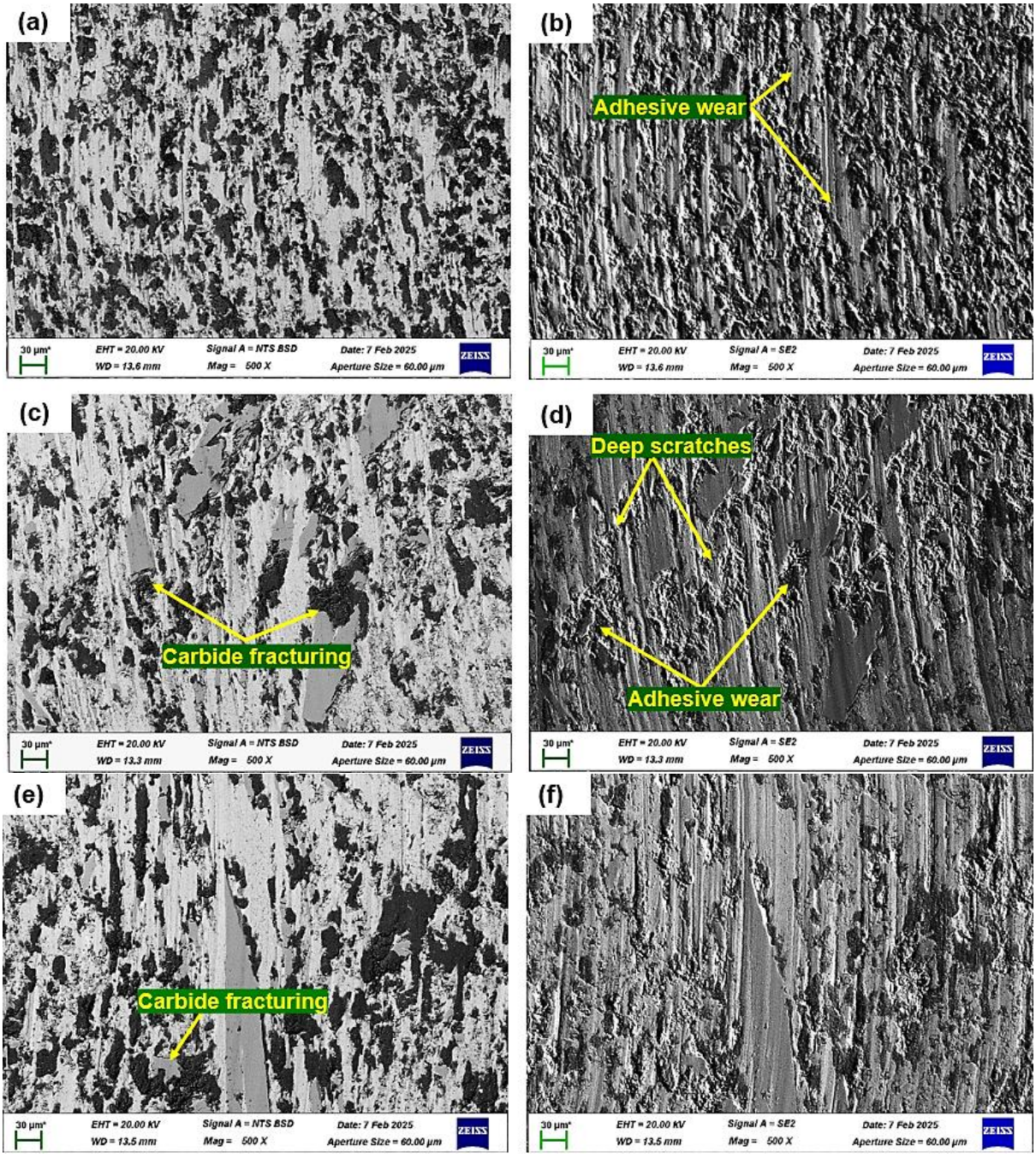

Figure 6.14: SEM images of wear tracks for P1ht(a), P2ht(c) and P3ht at 500x(e) magnification in BSE imaging and P1ht(b), P2ht(d) and P3ht(f) at 500x magnification in SE imaging.

6.3.4 Surface Topography of the Wear Surfaces for As-Cast and Heat-Treated HCCI Samples

When comparing the heat-treated samples (P1ht, P2ht, and P3ht) to their as-cast counterparts (P1, P2, and P3), noticeable differences in surface roughness, wear mechanisms, and material loss can be seen. The topography images in Figure 6.15 help show how heat treatment changed the way each material wears.

In Figure 6.15a, P1 has a very rough and uneven wear surface, with deep grooves and sharp peaks, which suggests severe abrasive wear. The rough texture shows that a lot of material was lost due to plastic deformation and tearing. In contrast, P1ht Figure 6.15b has a smoother and more even surface, with shallower grooves and fewer sharp edges. The wear is more spread out, meaning the material is worn away in a more controlled way. This suggests that heat treatment helped by making the primary carbide structure stronger through homogenisation and better load distribution between the matrix and the primary carbides. This improved how the material handles wear, leading to less material loss overall. In Figure 6.15c, P2 has a moderately rough surface with fine grooves and mild abrasive wear. The wear track looks relatively stable, with less material tearing compared to P1. However, P2ht in Figure 6.15d shows a much rougher and uneven surface than P2. The grooves are deeper, and there is more evidence of primary carbide breaking, leading to three-body abrasion shown by the increased valleys and peaks on the surface. This suggests that after heat treatment, the primary and eutectic carbides in P2 became more brittle, making them more likely to fracture under sliding wear. The broken carbide pieces acted like extra abrasive particles, increasing wear. This explains why P2ht wore down much faster than P2, as the increased brittleness led to more material being lost through three-body abrasion instead of protecting the surface. In Figure 6.15e, P3 shows the most uniformly worn surface amongst the as-cast samples, with shallow grooves and a mix of mild abrasive and adhesive wear. The wear surface looks stable, with consistent material tearing throughout the track. P3ht, Figure 6.15f, however, does not show the same level of surface wear uniformity as P3. The grooves are still fine, but the surface is not as even. There are sections where the track has more peaks and valleys than others, which alludes to the differences in the wear rate between the matrix and the primary carbides. This means that while heat treatment made the material harder, the variance in the carbide size still determined how the wear was experienced on the surface.

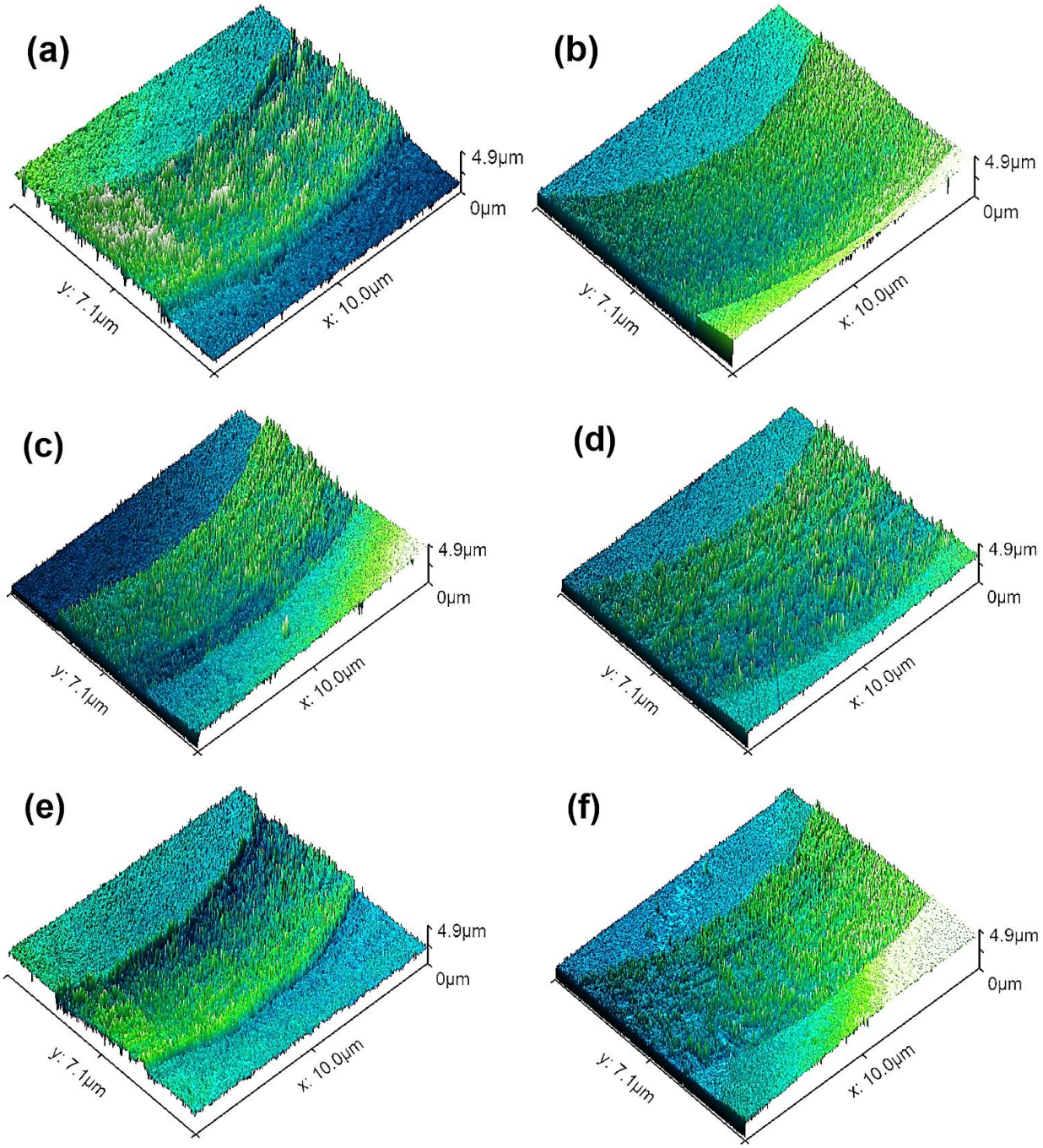

Figure 6.15: Surface topography of the wear surfaces for as-cast samples P1(a), P2(c) and P3(e) and heat-treated samples P1ht(b), P2ht(d), P3ht(f).

The additional hardness of the matrix introduced through heat treatment also made the material more brittle, preventing the same protective tribolayer from forming as in P3 due to the smearing of the adhesive debris over the worn surface areas as there was less matrix tearing in P3ht. This matches with the COF trends, where the COF for P3 suddenly dropped at the end, likely because a protective layer of wear debris had built up, lowering friction. In P3ht, the

COF stayed slightly higher, meaning its surface did not stabilise in the same way. While P3ht still performed well, it did not show the same drastic reduction in friction and wear as P3.

Heat treatment helped improve wear resistance in P1ht, but P2ht wore down much faster due to carbide growth and brittleness. P3ht remained highly wear-resistant, but unlike P3, it did not develop the same protective surface over time. This suggests that while heat treatment strengthened the matrix through secondary carbides precipitation, its effect on long-term wear stability depended on how the primary carbides changed in each material. The effect of secondary carbide precipitation led to a more even distribution of wear on the surface changing the primary mode of corrosion from being adhesive wear mostly experienced by the as-cast to abrasive wear which was more prominent after heat treatment.

6.3.5 Wear Balls After Dry Sliding Wear of As-Cast HCCI Samples

The surface of the alumina balls of the heat-treated samples is shown in Appendix B-1 c and d. The surface of the balls does not show significant damage on the surface of the ball thus the wear on the balls was considered negligible. The balls show significantly less wear debris on the surface as opposed to the as-cast ball surface. This shows that the heat-treated samples underwent lesser severe adhesive wear and a more balanced wear between the abrasive and adhesive wear.

6.3.6 EDS Analysis of Wear Tracks for Heat-Treated HCCI Samples

The EDS spectrum in Figure 6.16b presents the elemental composition of the wear debris from the analysed area shown in Figure 6.13a for sample P1ht. The spectrum reveals Fe as the dominant element, followed by Cr, and some C content. In this spectrum Mo was detected as well. Based on these results, it is reasonable to assume that most of the debris originates from the matrix, with some contribution from the carbides. However, as in P1ht, relying solely on EDS for this conclusion is only indicative, the same factors affecting the bias in EDS results for P1 would influence the results for P1ht.

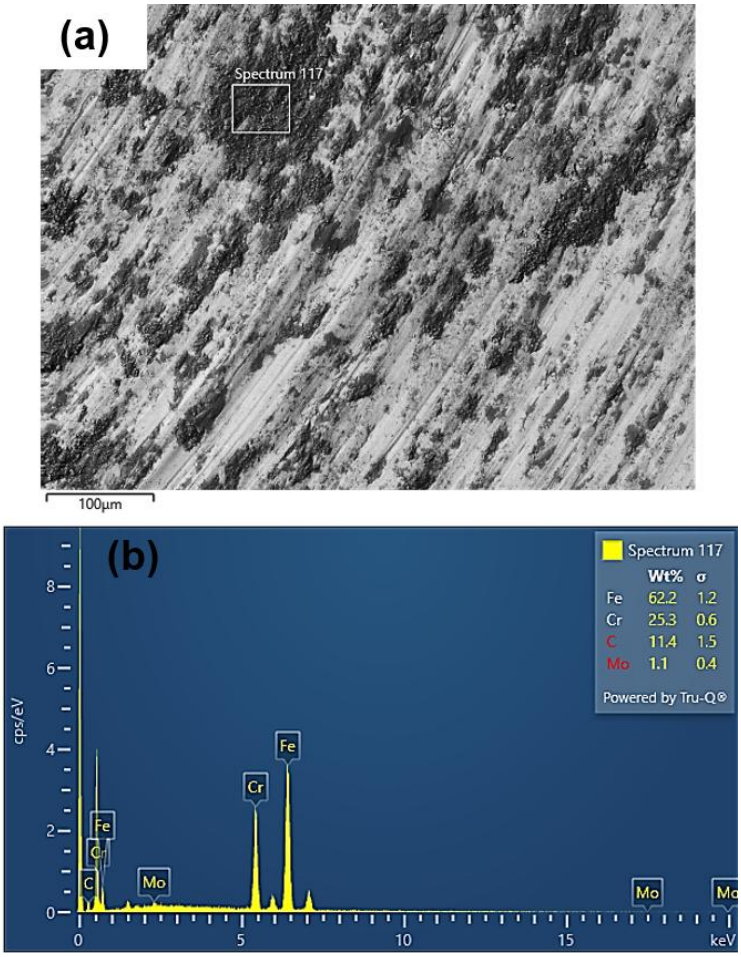

Figure 6.16: EDS a) image of area analysis done of wear debris and b) spectrum of the area analysis for sample P1ht.

The EDS spectra for P2ht and P3ht are shown in Figures 6.17 c and d, with Figures 6.17 a and b displaying the areas where the analysis was conducted. Both spectra reveal Fe as the dominant element, followed by Cr and some C content. P3ht in Figure 6.17d spectrum also reveals some Mo content. Similar to the observations made for P1ht, the results suggest that the matrix was the primary material worn away during testing, with some fractured primary carbides contributing to the debris. However, these findings remain inconclusive due to the beam penetration depth and interaction area probably analysing deeper and wider than the debris smeared on the surface.

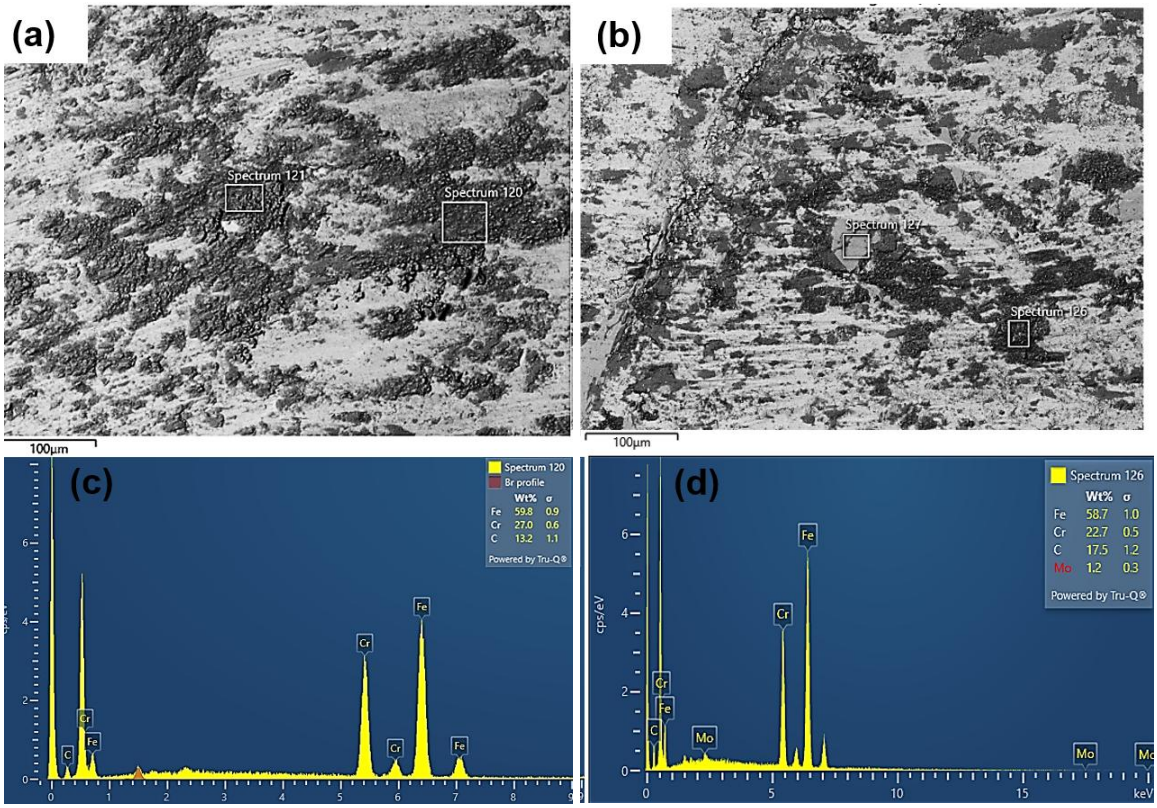

Figure 6.17: SEM images a) and b) showing the selected areas for EDS analysis in P2ht and P3ht, respectively. The corresponding EDS spectra c) and d) present the elemental composition of the analysed regions.

6.4 Discussion

6.4.1 Coefficient of Friction of As-Cast and Heat-Treated HCCIs

During the running-in phase observed at the beginning of the wear process in Figure 6.1, friction increases as the rough surface features of the material come into contact and start to wear down leading to higher resistance. Over time, as wear continues, the contact surfaces become smoother, causing the friction to stabilise. The final stable friction values represent the steady-state behaviour of each sample under wear conditions. Sample P1 has fewer primary and eutectic M_7C_3 carbides and a softer matrix, resulting in slightly lower friction as observed in Figure 6.1 (Kaba et al., 2024). However, because it is softer, it deforms more when under pressure, which leads to more material sticking to the surface. This adhesion effect increases friction despite the lower hardness. Sample P2 has the lowest friction because it has a more balanced microstructure with smaller, evenly distributed primary and eutectic carbides. This structure helps to spread the load more evenly, reducing stress and friction. Additionally, the finer primary and eutectic carbide network creates a smoother surface, lowering resistance to sliding (Liu et al., 2014). Sample P3 has the highest friction due to its hard and carbide-rich microstructure. The presence of large, plate-like primary M_7C_3 carbides and continuous carbide

networks makes the surface rougher and increases resistance to sliding. Additionally, the primary carbides are brittle, meaning they can crack and break apart, producing debris that further raises friction. The COF of P3 in Figure 6.1 decreased towards the end of the test because the wear surface may have become smoother through reduced carbide fracturing, wear debris settling or the matrix becoming more stable in load-bearing. These results indicate that while P3 has the highest hardness, it also causes more friction. On the other hand, P2 provides a better balance between friction, hardness, and wear resistance, making it the most optimised in terms of performance.

The changes in the microstructure for P1ht as seen in Figure 4.11a, explain the changes in its COF. The alloys show marginal differences in the COF before and after heat-treatment with P1 exhibiting more aggressive fluctuations during the test. The finer, more homogenised primary M_7C_3 carbides in P1ht are more closely packed than in P1.This made the surface smoother, which helped reduce friction between the ball and the different phases. Compared to the as-cast state in Figure 4.7a where primary carbides were a bit further apart, the refined microstructure in P1ht allowed for slightly better load distribution, preventing sudden friction spikes (Kaba et al., 2024). Additionally, the precipitation of secondary carbides strengthened the matrix and provided slightly more support to the matrix. This led to a more stable COF. However, as wear continued, the overall COF of the two alloys do not portray any significant differences.

The difference in the fluctuation behaviour of P2ht and P2 with P2 showing more aggressive fluctuations than P2ht can also be explained by the difference in the homogenisation effect of the heat treatment. After heat treatment, P2ht in Figure 4.11b showed some effects of carbide coarsening. However, the interconnectedness of the primary and eutectic carbides as well as the homogeneity was maintained. The precipitation of secondary M_7C_3 carbides during the heat treatment, further decreases interaction of the rough asperities and the matrix to help reduce friction . The smaller primary carbides, with smaller eutectic and secondary carbide precipitates in between help create a smoother and more uniform wear surface (Kaba et al., 2024). This reduces direct contact between rough asperities, minimising sudden friction spikes and preventing excessive resistance to sliding. Additionally, the secondary carbides strengthen the matrix, making it stronger and enabling better load distribution throughout the worn surface areas. In P2ht the primary and eutectic carbides are more evenly spread due to the homogenisation effect of heat-treatment, they provide better load distribution across the wear surface. This means that during sliding, the applied load is shared more efficiently between the

hard carbides and the matrix, reducing stress concentration in specific areas. Secondary carbides further enhance this effect by filling gaps in the microstructure, making the surface more homogeneous and stable. As a result, there is less severe ploughing or material tearing, which would otherwise increase friction. The combination of smaller, well-distributed primary and eutectic carbides, secondary carbide strengthening, improved load-bearing support, and reduced surface roughness (Stojanovic et al., 2013)explains why P2ht maintains a lower friction throughout the test compared to the as-cast state. This means P2ht maintains consistent wear behaviour throughout the test and may in the long run be better for wear resistance than P2.

There are slight differences shown in the COF of P3 and P3ht with P3ht showing a slightly lower COF than P3 from around 200m until around 700m where the COF of P3 dropped to below that of P3ht. This suggests that P3ht exhibited better protection from the carbides and less contact of the ball with the softer matrix. This may also be explained by the further homogenisation of the carbides after heat treatment which saw better interconnection of the primary and eutectic carbides. The additional recrystallisation of the primary carbides to smaller, more blocky primary carbides reduced the variability between the larger primary carbides and the eutectic carbides ultimately promoting more uniform covering of the matrix than in P3. The additional precipitation of secondary carbides further strengthened the matrix to withstand better load distribution of the load during the test. The further homogenisation of the microstructure of P3ht led to less of the softer matrix being exposed to contact with the ball, decreasing the amount of material loss sustained by the matrix. The refinement of the matrix and increased primary and eutectic carbide connectivity created a more uniform wear surface, minimising fluctuations in COF. These microstructural changes resulted in a smoother COF trend in P3ht, despite maintaining high friction levels, as carbide dominance in wear became more pronounced after heat treatment.

The COF results in Figure 6.9 match the microstructural changes caused by heat treatment. The observed results from the COF trends align with work reported by Stojanovic et al. (2013), Liu et al. (2014), Ding et al. (2024), and Kaba et al. (2024) on the effects of the carbide size and volume on the COF behaviour in metallic alloys. P3ht due to further homogenisation and carbide refinement showed significant improvement in the COF with less aggressive fluctuations than P3 making it more resistant to sliding. P2ht, despite some primary carbide growth, has the lowest COF among the heat-treated samples because its primary and eutectic carbides are more evenly distributed, helping reduce friction. P1ht starts off with a COF closer

to P2ht, but gradually increases to match P3ht, as secondary carbide precipitation and progressive carbide exposure make it harder and rougher over time. The steady COF values over the 1000 m test suggest that after the running-in phase, all samples reached a stable friction state. These differences between the COF of the three heat-treated alloys are, however, marginally different and thus indicate the samples had similar wear behaviour after heat-treatment. Compared to the as-cast samples, the changes in COF after heat treatment were mainly due to increased carbide volume as seen in Figure 6.11, maintained homogeneity in P2ht and the further homogenisation of P3ht. In addition, secondary carbide precipitation, and a harder, less ductile matrix all played a role in how friction changed over time.

However, P3 still maintained the highest COF amongst all the samples as observed in Figure 6.11 until about 700 m, where it drastically dropped to well below all the others. The drastic drop in COF for P3 might have occurred because the wear surface became smoother over time, lowering friction and causing the COF to drop. The rough surface of P3 and large plate-like primary carbides, with smaller eutectic carbides in between, led to increased resistance to sliding in the beginning, which resulted in its initially high COF. As wear proceeded, the rough areas gradually wore down, reducing surface roughness. A thin layer of compacted wear debris formed a tribolayer on the wear track surface, acting as a protective layer that lowered direct contact and friction with the matrix (Galetz et al., 2010; Wang et al., 2018). This also means that, despite their size, the primary and eutectic carbides in P3 remained more stable than in P2, where they broke and produced more abrasive debris, which further accelerated wear. As a result, the wear mechanism shifted from predominantly abrasive wear to more adhesive wear, which generally lowers friction over time by forming a thin protective film over the sliding surface (Galetz et al., 2010; Wang et al., 2018). Together, these elements contributed to the gradual reduction in COF, causing P3 to drop below all other samples towards the end of the test. In the long run, the drastic drop in COF for P3 suggests that its wear process became more controlled and less aggressive, leading to better long-term wear resistance. The formation of a smooth, compacted wear surface means that material loss slowed down, reducing the risk of rapid deterioration (Bedolla-Jacuinde & Rainforth, 2005; Yen et al., 2014). The solid carbide network in P3 performed an important role because it prevented excessive carbide fracturing and debris accumulation, resulting in a more equal wear surface. The primary and eutectic carbides in P3 remained more stable, minimising the amount of free debris that might further damage the material, unlike P2 where broken carbides produced loose abrasive particles increasing wear. The change from abrasive to adhesive wear also shows that the surface of P3

changed with time to accommodate the sliding conditions, hence lowering friction and stabilising wear behaviour. Given its wear mechanism changes to a less damaging process with prolonged usage, P3 would thus probably survive longer in practical settings. By functioning as a natural lubricant and therefore reducing direct contact between the matrix and the alumina ball, helping to protect the material and slow down additional wear advancement. The interconnectedness of the primary and eutectic carbides assisted to ensure that the matrix was less exposed to direct wear, therefore promoting a more homogeneous and consistent wear process.Overall, the COF drop in P3 reflects a more efficient wear process, with a balanced interaction between the carbides, matrix, and wear debris, ensuring that P3 remains the most wear-resistant sample in the long term. The combination of a strong carbide network, tribolayer formation, and a shift to adhesive wear all contributed to the significant reduction in COF, reinforcing the superior wear resistance of P3 compared to the other samples.

6.4.2 Wear Performance of As-Cast and Heat-Treated HCCIs

The wear behaviour of the samples follows well-established trends observed in high chrome cast irons, where wear resistance is closely linked to microstructural features such as carbide distribution, hardness, and matrix properties. The presence of hard carbides generally improves wear resistance by acting as load-bearing structures, reducing direct contact between the softer matrix and the sliding surface (Abdel-Aziz et al., 2017; Ping et al., 2021; Xu et al., 2023). However, the effectiveness of carbides depends on their size, volume fraction, and distribution, as excessive coarsening or poor connectivity can lead to increased material loss (Yang et al., 2009; Guo et al., 2021; Liu et al., 2023). Wear mechanisms observed include a combination of two-body and three-body abrasion, adhesive wear, and varying levels of plastic deformation, depending on the microstructure of the sample. Surface topography analyses reveal differences in track roughness, with smoother tracks indicating more stable wear and rougher tracks associated with severe material removal. The coefficient of friction trends further supports these findings, showing how wear transitions from an initial running-in phase to more stable steady-state wear.

P1 has the highest wear rate among the as-cast samples, meaning it loses the most material during sliding wear. This happens because it has the softest matrix, underdeveloped carbides, and the lowest carbide volume, making it less resistant to wear (Kaba et al., 2024). Without a strong carbide network, the soft matrix is in direct contact with the sliding surface, making it easy to wear away. The matrix deforms under stress, leading to deep penetration and high material loss. The worn surface, as shown in Figure 6.4a and b, has deep grooves and rough

edges, showing that abrasive wear is the main wear mechanism. Two-body abrasive wear dominates in P1, where hard asperities from the alumina ball and detached debris plough through the soft matrix, creating deep grooves. As wear continues, small carbide fragments detach and mix with the wear debris, forming a third body between the sliding surfaces, causing three-body abrasive wear (Su et al., 2021). Since there are not enough carbides to reinforce the matrix, adhesive wear also occurs, where the soft matrix sticks to the sliding counter surface and tears away, worsening wear (Guo et al., 2018). The unstable sliding behaviour of P1 is reflected in Figure 6.1, where the COF fluctuates significantly. The surface topography in Figure 6.6a confirms severe wear, with high peaks and valleys that indicate heavy material removal. The absence of well-distributed carbides leads to more direct contact with the counter surface, making wear worse overtime (Rodenburg & Rainforth, 2007).

P2 performs significantly better than P1, with a much lower wear rate. This is because it has finer and more evenly spread primary M_7C_3 carbides, along with smaller eutectic carbides, which protect the matrix from wear (Cui et al., 2016). The wear track in Figure 6.4c and d is smoother than P1, with fewer deep grooves and more uniform wear. Unlike P1, where severe two-body abrasion dominates, three-body abrasive wear becomes more significant in P2. Some primary carbides fracture under stress, creating sharp debris that gets trapped between the ball and the material surface. These broken carbide fragments act as hard abrasives, cutting into the surface and causing three-body abrasion, further increasing material loss (Guo et al., 2018; Liu et al., 2023). The penetration depth is lower, meaning P2 resists deep wear better than P1. While abrasive wear is the dominant wear mechanism, adhesive wear is also present in P2, especially where wear debris gets compacted and causes localised bonding between the surface and alumina ball. This explains why Figure 6.5c and d show fractured carbides within the wear track, confirming that carbide breakage contributes to the overall wear process. The COF of P2 in Figure 6.1 is lower than P1, showing that the more balanced carbide distribution helps to reduce friction spikes (Liu et al., 2014). The surface topography in Figure 6.6b confirms a smoother wear surface with fewer sharp peaks and valleys, indicating a more controlled wear process. The worn surface area for P2 is the largest, meaning that instead of deep wear, the material loss is spread out over a wider region. This helps distribute stress evenly and reduces severe material removal (Yang et al., 2009; Kaba et al., 2024).

P3 has the lowest wear rate among the as-cast samples, but its difference compared to P2 is very small. Despite their almost identical wear rates, P3 is expected to show better wear resistance in the long run due to its stronger carbide network. The wear track in Figure 6.4e

and f appears smoother than both P1 and P2, with fine, continuous grooves and minimal material tearing. P3 experiences mainly mild three-body abrasion and adhesive wear, rather than the severe abrasive wear seen in P1 and P2. The primary and eutectic M_7C_3 carbides in P3 are well-connected and cover a larger portion of the surface, meaning less of the softer matrix is exposed to wear. These well-distributed carbides help reduce direct contact between the matrix and the alumina ball, preventing deep material removal. The strong carbide network also prevents large-scale carbide breakage, meaning that less abrasive debris is generated, reducing three-body abrasion (Fortini et al., 2022; Khamroev et al., 2024). While some primary carbide fracturing occurs, as seen in Figure 6.5e and f, it is much less severe than in P2, meaning the carbides remain more stable during sliding wear (Guo et al., 2018). The COF in Figure 6.1 shows a stable trend for most of the test, but towards the end, there is a drastic drop. This suggests that as wear continued, a tribolayer of compacted wear debris formed, reducing friction and shifting the wear mechanism from abrasive wear to adhesive wear. The transition to adhesive wear meant that instead of the alumina ball directly cutting into the surface, material transfer occurred more smoothly, reducing material loss. The topography in Figure 6.6c confirms this, showing a more uniform wear pattern, with a smoother surface and less material deformation.

The wear behaviour of the as-cast samples is influenced by carbide volume, carbide distribution, and matrix strength. P1 experiences the most severe wear due to its weak matrix and lack of strong carbide reinforcement, leading to both severe two-body abrasive and adhesive wear. The deep grooves and rough surface confirm that severe two-body abrasion dominates, where hard asperities cut into the soft matrix. P2 has a much lower wear rate than P1 due to its finer, well-distributed carbides, which reduce deep penetration and spread wear over a larger area. Three-body abrasion occurs in P2 as fractured carbides act as loose abrasives, contributing to further wear. P3 has the lowest wear rate, but its difference from P2 is very small. However, in the long run, P3 is expected to have the best wear resistance due to its strong carbide network, lower matrix exposure, and better stability. Mild three-body abrasion and adhesive wear dominate in P3, leading to a more controlled wear process and less material removal. The COF trends, wear tracks, and surface topography all suggest that while P2 and P3 have nearly identical wear rates, the structure of P3 gives it an advantage in long-term wear resistance.

Microstructure, carbide shape, and matrix characteristics affected the wear behaviour of the heat-treated samples (P1ht, P2ht, and P3) relative to their as-cast counterparts (P1, P2, and P3).

Heat treatment changed the hardness, carbide distribution, and wear mechanisms, therefore producing slight modifications in wear resistance. However, the variations in wear performance were not significant, as the general wear processes remained similar, with only minor modifications in material loss and wear track features. A smoother and more consistent track suggests that P1ht showed a modest increase in wear resistance over P1. This can be ascribed to the improved refinement of the microstructure during heat treatment, which produced a more uniformly distributed carbide network and secondary carbide precipitation (Kaba et al., 2024). The homogenisation of the microstructure through the redistribution of the primary carbides distribution and the further precipitation of secondary carbides reinforced the matrix, improving load distribution and minimising plastic deformation (Liu et al., 2023). For P1ht (Figure 6.13a and b), the wear track revealed less severe material tearing and less deep grooves than in P1 (Figure 6.13a and b), implying a change towards a more regulated wear process. Although the degree was less, the principal wear mechanisms stayed a mix of abrasive and adhesive wear, however. Fine grooves showing modest two-body abrasion were visible (Figure 6.13a and b), suggesting that the tougher matrix resisted deep material removal more effectively than P1. While in P1ht the softer matrix allowed for more steady material loss, the smoother wear surface reflects a reduction in plastic deformation, implying that the softer matrix in P1 was more prone to severe deformation. P1ht retained the highest wear rate among the heat-treated samples because of its rather low carbide volume. Though more equally distributed, the primary carbides in P1ht were still few, consequently the matrix stayed the main phase resisting wear. Having fewer carbides means the matrix is still subjected to sliding stress (Ding et al., 2024), since carbides offer the main resistance to wear. Secondary carbide precipitation in P1ht improved wear resistance by strengthening the matrix, making it more resistant to plastic deformation (Liu et al., 2023). P1ht remained the least wear-resistant heat-treated sample since P1ht still lacked a strong carbide network, so matrix deformation rather than carbide reinforcement controlled wear primarily. Despite these improvements, P1ht still had significant material loss. The increase in hardness from heat treatment reduced plastic deformation but did not completely prevent wear. The worn surface area increased compared to P1 (Figure 6.4), indicating that instead of deep penetration, the material loss was spread over a larger region. This is likely because the refined microstructure allowed for more even stress distribution during sliding, preventing highly localised wear but increasing the overall worn surface area.

P2ht displayed a small increase in wear rate when compared to P2, suggesting that heat treatment did not enhance wear resistance but rather made it somewhat more vulnerable to

wear. This increase in wear was due to primary carbide coarsening, increased carbide size variation, and increased brittleness after heat treatment (Pokusová et al., 2016). The primary carbides in P2 were finer and more uniformly dispersed, which increased load-bearing and wear resistance. However, following heat treatment, these carbides coarsened thereby changing the size difference between the main and eutectic carbides. This unequal carbide distribution produced areas where the matrix was more susceptible to wear, thereby causing localised material loss. With deeper grooves and more indication of material breaking, the wear track for P2ht (Figure 6.15d) is rougher and more uneven than for P2 (Figure 6.13c and d). However, the retained homogeneity kept the amount of damage sustained during wear. This is consistent with the COF of P2 in Figure 6.9 which showed less aggressive fluctuations compared to the as-cast. P2ht shows three-body abrasion at higher magnification (Figures 6.14c and d), wherein broken carbide particles function as extra abrasives, increasing the rate of material removal. The fractured carbide debris contributed to additional wear, causing further scratches and deep grooves, as seen in the wear track (Su et al., 2021). The secondary carbide precipitation in P2ht did contribute to some strengthening of the matrix, helping to slow down wear to some extent. However, the negative effects of primary carbide coarsening were more dominant, as the larger carbides created stress points that led to fracture and increased material loss (Liu et al., 2023). Furthermore, the change in hardness brought about by heat treatment changed the matrix deformation during wear. In P2, the matrix was tougher and more able to absorb stress, but in P2ht, the hardened matrix became more brittle. This led to increased localised cracking, which worsened the wear process (Yang et al., 2009). The carbide-matrix bonding was also affected, as some primary carbides detached more easily after fracturing, leaving the surrounding matrix unprotected (Ruangchai et al., 2023).

P3ht also had good wear resistance like P2ht, with a marginal increase in wear rate compared to P3. This was due to slightly increased carbide volume, secondary carbide precipitation, and recrystallisation of primary carbides into blocky hexagonal shapes. P3ht retained its high wear resistance because of a slight increase in its primary and eutectic carbide volume, which provided slightly more wear-resistant phases covering the wearing area. Additionally, the matrix was further strengthened by the precipitation of secondary carbides, improving hardness and load-bearing capacity (Guo et al., 2016). Another factor that contributed to its good wear resistance was the restructuring of primary carbides, which changed from a dominant long plate-like structure to more defined blocky hexagonal shapes due to recrystallisation (Kaba et al., 2024). This transformation helped improve load-bearing capacity and reduced stress

concentration points that could lead to fracture (Ruangchai et al., 2023) This is also consistent with the COF of P3ht which showed less aggressive fluctuations than its as-cast counterpart while also resembling P2ht closely. The wear track of P3ht (Figure 6.13e and f) appears smoother and more uniform than P1ht and P2ht, with fine, continuous grooves and minimal material tearing. Compared to P3 (Figure 6.4e and f), the surface of P3ht was slightly rougher, indicating a minor increase in wear rate. However, it still maintained a stable wear mechanism, with predominantly mild abrasive wear and some adhesive wear. Figures 6.13e and f show that the grooves in P3ht are fine and shallow, meaning that wear occurred gradually and in a controlled manner. Unlike P2ht, which had extensive carbide fracture, P3ht maintained its carbide network, reducing excessive material loss. While some small carbides fractured, the majority remained intact, allowing the surface to resist severe wear.

With superior carbide dispersion, secondary carbide precipitation, and matrix hardening lowering deep wear penetration, P1ht showed a minor increase in wear resistance compared to P1. However, because of its low carbide volume, it remained the least wear-resistant. P2ht showed a marginal increase in wear rate due to primary carbide coarsening, increased carbide size variation, and brittle carbide fracture, leading to more carbide fragmentation and three-body abrasion. With higher carbide volume, matrix strengthening from secondary carbide precipitation, and primary carbide recrystallisation enhancing its wear resistance, P3ht kept the best wear resistance.

The increase in hardness in the heat-treated samples had a significant impact on their wear behaviour. While harder materials are generally expected to have better wear resistance, in this case, the heat-treated samples showed marginally more wear than the as-cast sample, which was softer. This suggests that the increase in hardness may have made the material more brittle, leading to the wear in the heat-treated samples occurring through micro-cracking and primary carbide fracturing instead of significant matrix wear like in the as-cast (Chotěborský, 2013; Zhou et al., 2015; Mariani et al., 2016). In the as-cast sample, the softer matrix likely provided better support to the carbides by absorbing and distributing stress more effectively during wear. However, this meant that the matrix was more prone to plastic deformation during the wear which is how the surface lost material (Matsuo et al., 2005; Camurri et al., 2021). Since the matrix was more ductile, it could deform plastically under load, reducing the chances of stress concentrating at the carbide-matrix interface. This helped to prevent excessive strain on the carbides, allowing them to remain intact and resist fracture. In contrast, in the heat-treated

samples, the increased hardness made the matrix more brittle. While this improved resistance to plastic deformation, it also reduced the ability of the material to absorb impact and stress (Zhou et al., 2015). As a result, the carbides fractured under wear conditions. The higher hardness likely led to an increase in internal stresses, making the carbides more susceptible to cracking when subjected to repeated loading or abrasive forces (Li et al., 2008; Zhou et al., 2015; Chen et al., 2022). Once fractured, the carbides lost their effectiveness in resisting wear, leading to an overall wear rate occurring in this manner due to the increased hardness. This suggests that while hardness is an important factor in wear resistance, excessive hardness can lead to carbide embrittlement and increased material loss through fracture. Thus, it is important to strike a balance between adequate hardness increases and retained toughness in the microstructure. In the as-cast sample, the softer matrix likely provided better support to the carbides, allowing them to remain intact during wear. However, in the heat-treated samples, the harder matrix might have been less able to absorb impact and stress, causing the carbides to break or detach more easily. This would have led to material loss despite the higher hardness in the heat-treated samples.

Although heat treatment improved the microstructure rather than significantly altering the wear resistance, in some cases (P1ht) it resulted in little improvement and in others (P2ht) it resulted in marginal declines. While the differences may be marginal, they indicate how small changes in the primary carbide size, carbide homogeneity and how secondary carbide precipitates may influence the manner in which wear occurs. P3ht stayed the most wear-resistant, which emphasises the need of striking the ideal balance between matrix strength, carbide size, and volume to maximise wear resistance. While P3ht had the best resistance to material loss, the COF drop in P3 suggests that tribolayer formation played a critical role in extending wear life in the as-cast state. This means P3, despite a slightly higher wear rate initially, may have stabilised better in long-term wear conditions, while P3ht exhibited greater overall resistance but without the same COF reduction effect.

The wear trends in this work show how the carbide size, types of carbides and their arrangement in the matrix and the carbide volume can produce mixed effects on how the material responds to wear. A balance of the appropriate ratios of carbide volume, carbide size and arrangement needs to be struck in order to find the optimum microstructure capable of efficiently resisting wear. This is consistent with the findings of previous authors Chung et al. (2013), Filipovic et al. (2013), Filipovic et al. (2013), and Kaba et al. (2024) who discussed how the effects of the microstructure such as the carbide volume, the types of carbides and the arrangement of

carbides in the microstructure affect the type of wear experienced and the severity of resulting wear resistance. Chung et al. (2013) examined the impact of titanium additions on the microstructure and wear resistance of hypereutectic high chromium cast iron (Fe-25 wt.%Cr - 4 wt.%). Their work found that adding titanium produced TiC carbides, which improved the microstructure by decreasing the size of primary M_7C_3 carbides. Owing to the higher hardness and better carbide distribution throughout the matrix, this refinement produced better wear resistance. Filipovic, Kamberovic, Korac, and Gavralovski (2013) looked at how microstructure and wear resistance correlated in white cast iron alloys. Wear resistance and fracture toughness were shown to be much impacted by carbide volume fraction, size, and distribution. Higher volume percentages of well-distributed carbides specifically enhanced wear resistance however, if the carbides were too coarse, they could lower fracture toughness. Their findings underlined the need of balancing carbide qualities in order to maximise mechanical properties and wear resistance in white cast irons. In another work, Filipovic, Kamberovic, Korac, & Jordovic (2013) investigated Fe-Cr-C-V alloys wear resistance and fracture toughness under varying vanadium content and heat treatment levels. Increasing vanadium concentration, they found, produced hard vanadium carbides (VC), which improved wear resistance, but too high vanadium caused carbide coarsening, which reduced fracture toughness. By optimising carbides, appropriate heat treatment was found to maximise the microstructure and hence provide a desired balance between wear resistance and toughness. The microstructure and wear behaviour of Fe-Cr-C-Nb white cast irons were examined in Kaba et al., (2024) by niobium (Nb) additions. They discovered that Nb additions produced NbC carbides, which improved microstructural refinement and hardness. This refinement enhanced the alloys wear resistance. They also observed, nonetheless, that a too high volume proportion of the carbide phase could lower wear resistance because of more brittleness. Their research underlined how careful regulation of Nb content is necessary for best wear performance. Collectively, these studies underscore the critical role of microstructural control particularly carbide formation, distribution, and refinement, in determining the wear resistance and mechanical properties of white cast iron alloys.

The wear behaviour observed in these experiments falls under the Equal Pressure (EP) mode of wear as discussed by (Axen & Jacobson, 1994), where the applied load is evenly distributed between the matrix and the reinforcing carbides, rather than being preferentially carried by the harder phase. This is because for samples P1 to P3 the dominating phases exposed to wear is the matrix taking up to 70% of the surface area. This produces a wear process whereby,

particularly at reduced carbide percentages, the softer matrix phase dominates in material removal. Low volume fraction of reinforcing carbides limits their capacity to improve wear resistance since they cannot take on an excessive percentage of the load. As evident in the link between carbide content and wear rates, the results from the tests confirm that the wear performance of the samples fits this mode.

In EP mode, the load is evenly distributed over the matrix and the reinforcing phase, so every phase experiences the same surface pressure independent of its hardness or wear resistance. This load distribution produces an inverse rule of mixture, whereby the weaker phase, usually the matrix, especially at low carbide fractions significantly influences the total wear resistance of the alloy. Therefore, even if the reinforcing phase, such as M_7C_3 carbides in high chrome cast irons, carries just a proportionate share of the load compared to its area fraction, it does not appreciably increase wear resistance when present in tiny numbers. Though the carbides themselves are quite wear-resistant, the matrix, which is more prone to wear, rules the wear behaviour and causes faster material removal and greater wear rates. The findings in this work clearly show this effect. Lower carbide fractions, such as in P1, showed a higher wear rate since the matrix was the main load-bearing phase, which caused more material loss. On the other hand, P2 and P3 showed some improved wear resistance since the reinforcing phase was more successful in lowering the contact between the softer matrix and the alumina ball, even if their volume proportion of carbides was higher. The notion that wear resistance increases more visibly at higher carbide fractions is reinforced, though, since P2 and P3 have almost comparable worn volumes and the modest increase in carbide fraction in P3 had only minor effect. This validates that in EP conditions, the wear resistance does not scale linearly with carbide content at lower fractions and that meaningful gains only emerge when the carbide volume percent is sufficiently large to affect the general load distribution and wear behaviour. Therefore, P2 and P3 behave similarly since the difference in carbide content is not sufficient to fully transition out of EP mode, implying that further increases in carbide volume fraction or a stronger matrix phase would be required to shift towards EW (Equal Wear) mode, where the carbides can better protect the matrix from direct contact with the alumina ball. This also applies to the samples after heat treatment where there was not much change after heat treatment except marginal increases. This reinforces that the increment in the carbide phase needs to be sufficiently high enough to create a positive difference. This may also imply that if not adequately added, the small increment in the volume of carbides through secondary carbides precipitation may have an inverse effect on the wear rate.

6.5 Conclusion

The wear behaviour of high-chromium cast iron was determined by both carbide characteristics and matrix hardness. In the as-cast condition, P3 (with a low Cr/C ratio) exhibited high initial friction and rapid debris formation because its coarse, interconnected carbides protruded from the surface. Over time a protective tribolayer formed, slowing the wear rate. P2, which featured fine, evenly distributed carbides, achieved the lowest friction and the most uniform wear rate, as its carbides interrupted direct metal-to-metal contact without fracturing. In contrast, P1's sparse carbide network and softer matrix allowed extensive plastic deformation, resulting in the highest wear volume. After heat treatment, primary carbides became finer and secondary carbides precipitated, both of which increased the matrix hardness but also introduced brittleness. P1ht showed only a modest improvement, since its limited carbide content still permitted plastic flow under load. In P2ht and P3ht this brittleness caused frequent carbide fracture and three-body abrasion, raising their wear rates despite the harder matrix. Therefore, this shows that while higher hardness improves resistance to plastic deformation, excessive hardness can lead to increased carbide fracture and higher wear through abrasive mechanisms. The observations also show that while smaller primary carbides help slow down wear, carbide size alone does not determine wear resistance. Optimising both carbide size and volume is essential, as having a sufficient number of carbides is just as important as their size. If either carbide size or volume is too high or too low, the material may not perform well in resisting wear. This highlights the importance of balancing carbide distribution, morphology, and hardness rather than relying solely on any single factor to achieve optimal wear resistance in HCCI materials.

6.6 References

Abdel-Aziz, K., El-Shennawy, M., & Omar, A. A. (2017). Microstructural characteristics and mechanical properties of heat treated high-cr white cast iron alloys. *International Journal of Applied Engineering Research*, *12*(14), p4675–4686.

Axen, N and Jacobson, S. (1994). A model for the abrasive wear resistance of multiphase materials. In *Wear*, *174* (1-2), p (187-199)

Bedolla-Jacuinde, A., & Rainforth, W. M. (2005). Electron microscopy analysis on the worn surface of a high-chromium white iron during dry sliding contact. *Materials Research Society Symposium Proceedings*, *843*, 299–304.

Camurri, C., Maril, J., & Romero, E. (2021). Effect of the morphology, size, distribution and homogeneity of carbides and matrix on wear resistance in high Cr-alloys white cast iron.

Chen, Z., Guo, Q., Fu, H., & Zhi, X. (2022). Effect of heat treatment on microstructure and properties of modified hypereutectic high chromium cast iron. *Materialpruefung/Materials Testing*, *64*(1), p33 – 54.

Chotěborský, R. (2013.). *Effect of heat treatment on the microstructure, hardness and abrasive wear resistance of high chromium hardfacing*.

Chung, R. J., Tang, X., Li, D. Y., Hinckley, B., & Dolman, K. (2013). Microstructure refinement of hypereutectic high Cr cast irons using hard carbide-forming elements for improved wear resistance. *Wear*, *301*(1–2), p695–706.

Cui, J., Guo, H., Li, J. W., Li, D. Y., Parent, L., & Tian, H. (2016). A computational study on the benefit of core-shell structured carbides to the erosion resistance of high-Cr cast irons. *Tribology International*, *103*, p432–439.

D'Amato, R., Calvo, R., Ruggiero, A., & Gómez, E. (2017). Measurement capabilities for ball bearing wear assessment. *Procedia Manufacturing*, *13*, 647–654.

Deng, X. T., Fu, T. L., Wang, Z. D., Misra, R. D. K., & Wang, G. D. (2016). Epsilon carbide precipitation and wear behaviour of low alloy wear resistant steels. *Materials Science and Technology (United Kingdom)*, *32*(4), p320–327.

Deleanu, L., Ionescu, T. F., Cristea, G. C., Suciu, C. C., & Georgescu, C. (2022). 3D texture parameters for wear scars after severe regime. *Industrial Lubrication and Tribology*, *74*(3), 324–334.

Ding, T., Li, C., Jing, W., Di, X., & Hu, W. (2024). Influences of boron on the microstructural characteristics and wear performance of hypereutectic Fe-Cr-C-Mo-xB hardfacing alloy. *Surface and Coatings Technology*, *478*.

Filipovic, M., Kamberovic, Z., Korac, M., & Gavrilovski, M. (2013). Correlation of microstructure with the wear resistance and fracture toughness of white cast iron alloys. *Metals and Materials International*, *19*(3), 473–481.

Filipovic, M., Kamberovic, Z., Korac, M., & Jordovic, B. (2013). Effect of niobium and vanadium additions on the as-cast microstructure and properties of hypoeutectic fe-cr-c alloy. *ISIJ International*, *53*(12), 2160–2166.

Fortini, A., Suman, A., Zanini, N., & Cruciani, G. (2022). Erosive Wear Behaviour of High-Chromium Cast Iron: Combined Effect of Erodent Powders and Destabilization Heat Treatments. *Coatings*, *12*(8).

Galetz, M. C., Seiferth, S. H., Theile, B., & Glatzel, U. (2010). Potential for adhesive wear in friction couples of UHMWPE running against oxidized zirconium, titanium nitride coatings, and cobalt-chromium alloys. *Journal of Biomedical Materials Research - Part B Applied Biomaterials*, *93*(2), 468–475.

Guo, Q., Fu, H., Guo, X., Xing, Z., & Lin, J. (2021). Effect of carbon content on microstructure evolution and properties of hypereutectic high chromium cast iron. *Surface Review and Letters*, *28*(10).

Guo, Z.-H., Xiao, F.-R., Lu, S.-L., Liu, R.-L., & Liao, B. (2018). Effects of heat treatment and counterface on the wear behaviour of Cr21 cast iron. *Ironmaking and Steelmaking*, *45*(3), 257–263.

Hu, Z. D., Yan, H., Qiu, H. Z., Zhang, P., & Liu, Q. (2012). Friction and wear of magnetorheological fluid under magnetic field. *Wear*, *278–279*, 48–52.

Kaba, M., Filiz, H. I., Cui, Z., Baydogan, M., Cimenoglu, H., & Alpas, A. T. (2024). Microstructural effects on impact-sliding wear mechanisms in D2 steels: The roles of matrix hardness and carbide characteristics. *Wear*, *538–539*.

Khamroev, N., Egamberdiev, I., Ashurov, K., Asatov, S., & Khamidov, B. (2024). Exploring the Influence of the Casting Process, Structural Components and Heat Treatment on the Mechanical Properties of High-Chromium Cast Irons: A Review. *AIP Conference Proceedings*, *3244*(1).

Li, H., Xie, H., Zhang, M.-X., & He, F.-S. (2008). Effects of heat treatment on properties of low carbon-high chromium cast iron. *Jinshu Rechuli/Heat Treatment of Metals*, *33*(11), 87–90.

Liu, Y.-H., Deng, Y.-Z., & Deng, X.-S. (2014). Effect of chemical composition and microstructure on abrasion resistance of surfacing materials. *Advanced Materials Research*, *912–914*, 111–114.

Liu, Z., Wang, Z.-J., Jiang, Y.-H., & Zhou, M.-J. (2023). Microstructure and Properties of High Chromium Cast Iron Under Vibration Condition. *Zhuzao/Foundry*, *72*(5), 523–528.

Mariani, F. E., Rêgo, G. C., Neto, A. L., Totten, G. E., & Casteletti, L. C. (2016). Wear behaviour of a borided nickel-based self-fluxing thermal spray coating. *Materials Performance and Characterization*, *5*(4).

Matsuo, T. T., Kiminami, C. S., Fo, W. J. B., & Bolfarini, C. (2005). Sliding wear of spray-formed high-chromium white cast iron alloys. *Wear*, *259*(1–6), 445–452.

Ogunlana, M. O., & Akinlabi, E. T. (2016). Wear behaviour characterization of Ti6A14V-B4C composites. *Lecture Notes in Engineering and Computer Science*, *2226*, 915–919.

Ortega-Cubillos, P., Nannetti-Bernardini, P. A., Celso-Fredel, M., & Campos, R. A. (2015). Wear resistance of high chromium white cast iron for coal grinding rolls. *Revista Facultad de Ingenieria*, *2015*(76), 134–142.

Pelleg, J. (2016). Diffusion in alumina single crystals. *Solid Mechanics and Its Applications*, *221*, 113–177.

Ping, Z.-F., Zheng, B.-C., Tu, X.-H., & Li, W. (2021). Application of Directional Solidification Technology to High Chromium Cast Iron. *Zhuzao/Foundry*, *70*(8), 899–905.

Rodenburg, C., & Rainforth, W. M. (2007). A quantitative analysis of the influence of carbides size distributions on wear behaviour of high-speed steel in dry rolling/sliding contact. *Acta Materialia*, *55*(7), 2443–2454.

Ruangchai, K., Tongsri, R., Pearce, J. T. H., Chairuangsri, T., & Wiengmoon, A. (2023). Effect of Heat treatment on Dry-Sliding Wear and Corrosion Behaviour of High Chromium Cast Irons. *28th IFHTSE 2023 Congress*.

Saikko, V. (2014). In vitro wear simulation on the RandomPOD wear testing system as a screening method for bearing materials intended for total knee arthroplasty. *Journal of Biomechanics*, *47*(11), 2774–2778.

Stojanovic, B., Babic, M., Mitrovic, S., Vencl, A., Miloradovic, N., & Pantic, M. (2013). Tribological characteristics of aluminium hybrid composites reinforced with silicon carbide and graphite. A review. *Journal of the Balkan Tribological Association*, *19*(1), 83–96.

Su, C., Sang, X., Niu, S., & Ren, R. (2021). A Comparison of the Abrasive Wear Behaviours of Cast Iron and Cast Steel Materials. *Journal of Materials Engineering and Performance*, *30*(6), 4572–4582.

Shaha, K. P., Pei, Y. T., Martinez-Martinez, D., & De Hosson, J. T. M. (2011). Influence of surface roughness on the transfer film formation and frictional behaviour of TiC/a-C nanocomposite coatings. *Tribology Letters*, *41*(1), 97–101.]

Wang, W., Salvatore, F., Rech, J., & Li, J. (2018a). Effects of belt's adhesive wear on surface integrity in dry belt finishing. *Procedia CIRP*, *71*, 31–34.

Wang, W., Salvatore, F., Rech, J., & Li, J. (2018b). Effects of belt's adhesive wear on surface integrity in dry belt finishing. *Procedia CIRP*, *71*, 31–34.

Xu, L., Wang, F., Li, M., Li, F., Wang, X., Jiang, T., Deng, X., & Wei, S. (2023). Fabrication and abrasive wear property of high chromium cast iron with high vanadium and high nitrogen content (HCCI-VN). *Wear*, *523*.

Yang, J., Wang, B., Yang, M., Ding, W.-C., Wang, P., & Luo, D.-J. (2009). Effect of instant modification on microstructure and properties of high chromium cast iron. *Zhuzao/Foundry*, *58*(2), 166–168.

Yen, C.L., Chen, F.-J., & Pan, Y.-N. (2014). Research on the wear resistance of high-chromium white cast iron and multi-component white cast iron. *Advanced Materials Research*, *859*, 64–69.

Zhou, S., Shen, Y., Zhang, H., & Chen, D. (2015a). Heat treatment effect on microstructure, hardness and wear resistance of Cr26 white cast iron. *Chinese Journal of Mechanical Engineering (English Edition)*, *28*(1), 140–147.

Zhou, S., Shen, Y., Zhang, H., & Chen, D. (2015b). Heat treatment effect on microstructure, hardness and wear resistance of Cr26 white cast iron. *Chinese Journal of Mechanical Engineering (English Edition)*, *28*(1), 140–147.

Zumelzu, E., Goyos, I., Cabezas, C., Opitz, O., & Parada, A. (2002). Wear and corrosion behaviour of high-chromium (14-30% Cr) cast iron alloys. *Journal of Materials Processing Technology*, *128*(1–3), 250–255.

Chapter 7: The Influence of Microstructural Constituents on Corrosion Properties of High Chrome Cast Irons

7.1 Introduction

This chapter investigates the influence of microstructural constituents as influenced by the Cr/C ratio, on the corrosion behaviour of high chromium cast irons (HCCIs) in chloride, acidic, and sodium hydroxide environments. To achieve this objective, open circuit potential (OCP) measurements were conducted to observe passivation behaviour over time, while potentiodynamic polarisation tests evaluated passivation behaviour, corrosion potential (Ecorr), corrosion current density (Icorr) and corrosion rate (CR) of the HCCIs. Scanning electron microscopy was used to examine surface morphology after corrosion, revealing the mode of attack and material degradation. This chapter provides valuable insights into optimising the microstructure of HCCIs for enhanced corrosion resistance, guiding material selection and heat treatment processes for industrial applications.

7.2 Corrosion Behaviour of As-Cast HCCIs in 3.5 wt.% NaCl Solution

7.2.1 OCP Behaviour of As-Cast HCCIs in 3.5 wt.% NaCl Solution

The OCP curve of as-cast HCCI alloys exposed in 3.5 wt.% NaCl solution for 3600 seconds is shown in Figure 7.1. The as-cast HCCI alloys exhibited the same OCP trend that comprises of an initial rapid rise followed by a downward trend before stabilising in the 3.5 wt.% NaCl solution (Figure 7.1). P1 has the highest open circuit potential and gradually decreases until it stabilises at approximately -0.43 V. P2 started with high potential up to 300 s followed by a decrease in potential, eventually stabilising at around -0.44 V. In contrast, P3 begins at the lowest potential around -0.475 V, with an initial increase, then continues to decrease, reaching approximately -0.49 V by the end of the test. Slight fluctuations were observed in the OCP curve of P2 at 2270 s, 2460 s, 3150 s and 3570 s. Similarly, fluctuation was observed in the OCP curve of P3 at 2330 s. Fluctuations can be attributed to instability caused by the chloride ions in the solution or dissolution and re-passivation of the oxide film on the material's surface (Parkhutik, 2006; Shen et al., 2020)

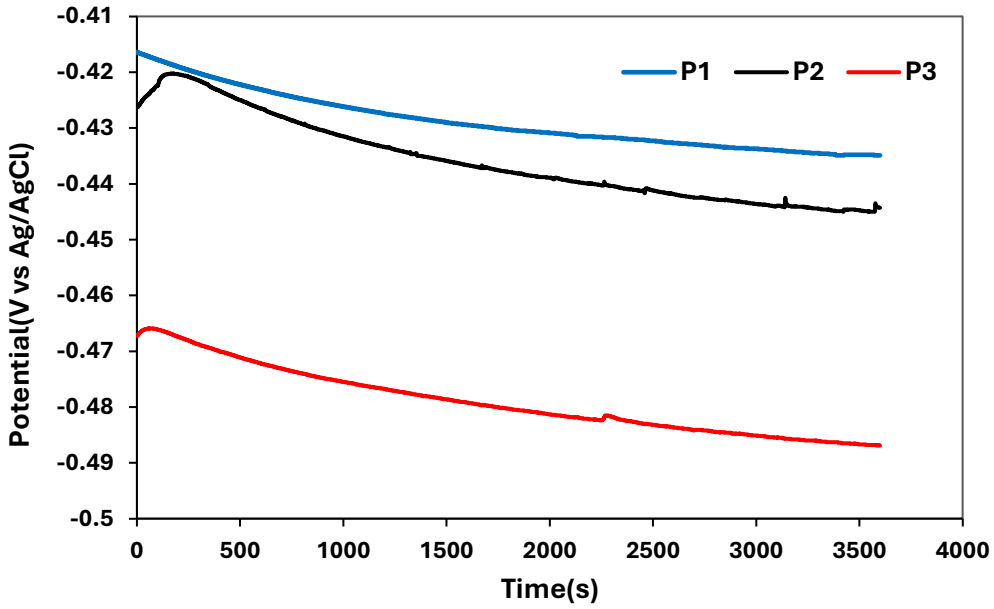

Figure 7.1: OCP curve of as-cast HCCI alloys in 3.5 wt.% NaCl solution.

7.2.2 Potentiodynamic Polarisation Behaviour of As-Cast HCCIs in 3.5 wt.% NaCl Solution

The potentiodynamic polarisation curves of the as-cast HCCI alloys in 3.5 wt.% NaCl solution is shown in Figure 7.2. All three curves exhibited very similar characteristics of active dissolution after reaching the corrosion potential. All samples exhibited identical behaviour with both having about the same corrosion potential with increased current density as anodic potential increased. Table 7.1 shows the electrochemical parameters of the as-cast HCCIs in 3.5 wt.% NaCl solution. In 3.5 wt.% NaCl solution, the three samples show very similar corrosion potential values which align with the OCP curves (Figure 7.1). The Icorr of samples (P1 and P2) are similar and have slightly lower Icorr than P3. The corrosion rates of P1 and P2 are similar and are slightly lower than the corrosion rate of P3. This indicated that the samples have identical corrosion susceptibility when exposed to 3.5 wt.% NaCl solution.

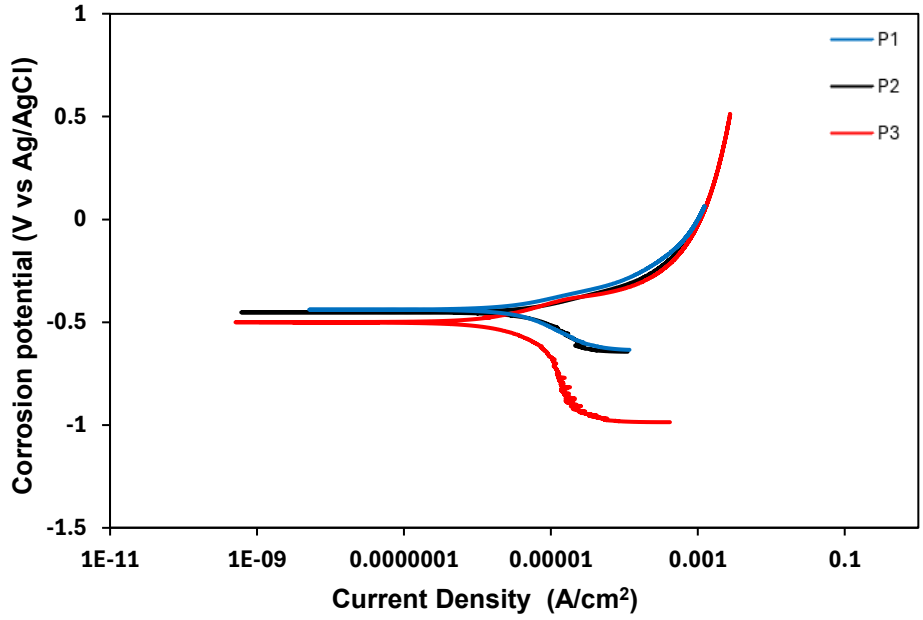

Figure 7.2: Potentiodynamic polarisation curves of the as-cast HCCIs alloys in 3.5 wt.% NaCl solution.

Table 7.1: The electrochemical parameters of the as-cast HCCIs in 3.5wt% NaCl solution.

As-cast			
3.5 wt. % NaCl solution			
HCCIs	**Icorr (A/cm^2)**	**Ecorr (V)**	**CR (mm/yr)**
P1	0.0000067±0.08	-0.437±0.19	0.075±0.10
P2	0.0000069±0.06	-0.452±0.20	0.074±0.49
P3	0.000027±0.08	-0.504±0.22	0.279±0.43

7.2.3 Surface Morphology of As-Cast HCCIs After Exposure in 3.5 wt.% NaCl Solution.

The BSE SEM images of surface morphology after corrosion in 3.5 wt.% NaCl solution are shown in Figure 7.3.The SE images of the images are presented in Appendix C-1. Relatively intact surface with minimal pitting and dissolution at the carbide-matrix interface was observed for P1 (Figure 7.3a) and P2 (Figure 7.3b). This observation is consistent with the similar corrosion rate in Table 7.1. The fine M_7C_3 carbides remain embedded in the matrix and there are no large voids or deep grooves. The fine and evenly distributed M_7C_3 carbides provide better passivation, reducing the extent of corrosion. The corrosion attack is uneven, with different areas showing varying degrees of material loss. In P3, there is more matrix dissolution, especially in areas surrounding the large primary carbides (Figure 7.3c). This observation aligns with the slightly higher corrosion rate among the three samples. The matrix

appears partially eroded, with slightly deeper grooves and voids forming where the material has been removed. Some areas show early signs of carbide detachment, as the surrounding matrix has corroded away. The remaining structure is primarily carbide-rich, suggesting that the matrix was the main site of corrosion attack in P3. In general, all three samples experienced corrosion, with P1 and P2 showing slightly lesser damage with minimal pitting and dissolution, and P3 losing some sections of its metallic matrix. This is in agreement with the similar behaviour observed in the potentiodynamic polarisation curves in Figure 7.2 which all show the similar potential to corrode, active dissolution and similar corrosion susceptibility.

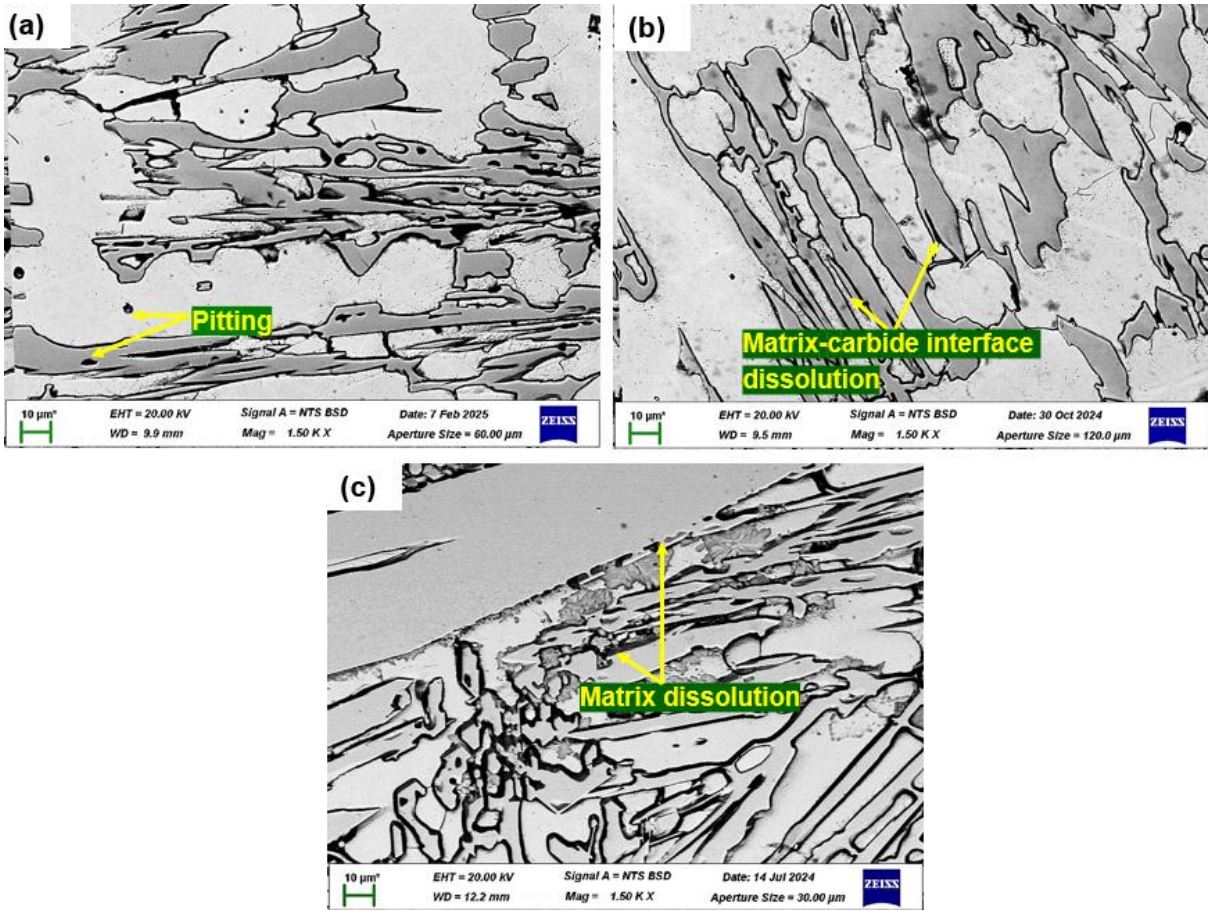

Figure 7.3: BSE-SEM images of as-cast P1 (a) P2 (b) and P3 (c) after electrochemical testing in 3.5 wt.% NaCl solution.

7.3 Corrosion Behaviour of As-Cast HCCIs in 0.5M NaOH Solution

7.3.1 OCP Behaviour of As-Cast HCCIs in 0.5M NaOH Solution

The OCP curve of as-cast HCCI alloys exposed in in 0.5 M NaOH solution for 3600 s is shown in Figure 7.4. P1 exhibited the highest potential, beginning at a slightly low corrosion potential of about -0.31 V, then a shallow increase ultimately stabilising at approximately -0.30 V, remaining constant till the end. P2 followed the same trend, starting at a lower corrosion

potential of about -0.55V however, it continually and steadily increased till it reached -0.42 V at the end of the 3600 s. P3 started at the lowest corrosion potential starting slightly lower than P2 at about –0.62 V and gradually increases, stabilising near -0.45 V. All three alloys initially show a shift in corrosion potential before reaching a more stable state, with P1 maintaining the highest potential value throughout the test duration and the most stable corrosion potential. The OCP curves are all very smooth with no visible fluctuations. Stable OCP has been attributed to the building of compact and protective oxide films on alloy surfaces (Leshetla et al., 2022; Murmey et al., 2023).

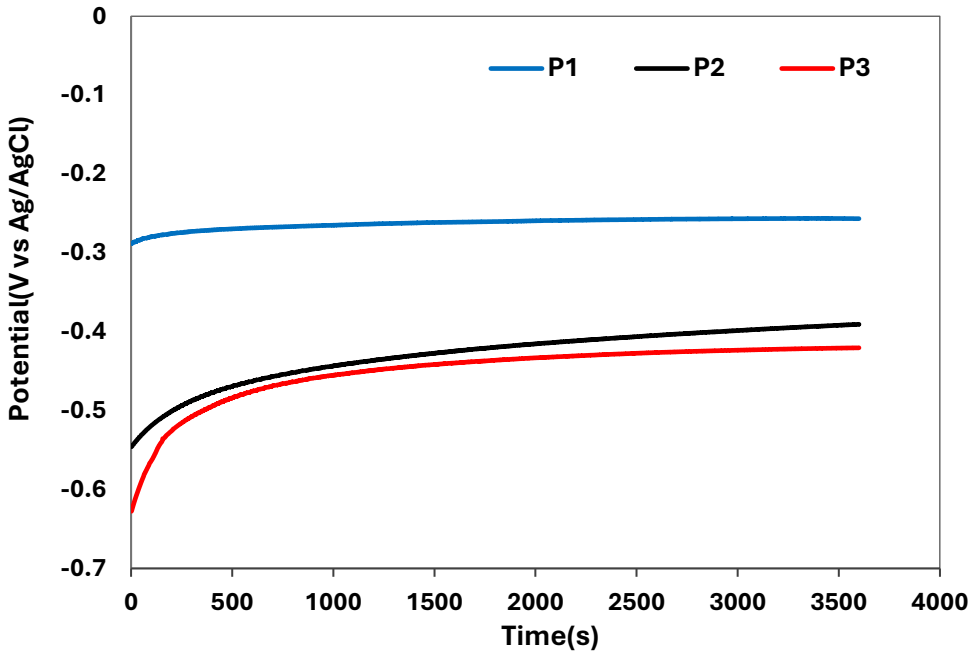

Figure 7.4: OCP curves of as-cast HCCI alloys in 0.5 M NaOH solution.

7.3.2 Potentiodynamic Polarisation Behaviour of As-Cast HCCIs in 0.5M NaOH Solution

The potentiodynamic polarisation curves of the as-cast HCCI alloys in 0.5 M NaOH solution is shown in Figure 7.5. All three curves exhibited very similar characteristics of active dissolution, then followed by short passivation and transpassivation. P1 exhibited the highest potential, indicating better stability and resistance to corrosion compared to the other samples. P1 also shows the highest shift towards high current density and the best passivation with fewer minor fluctuations (green arrow) in passive film stability. This suggests a strong protective layer formation. The extent of passive film instability is moderate, as the fluctuations (green arrow) are present but do not severely disrupt the overall passivation. The curve of P2 exhibited

the lowest corrosion potential, indicating higher reactivity and less stability. It also shows the greatest shift towards lower current density which means it experienced the lowest rate of corrosion. P2 also shows the largest fluctuations in the passive layer. The passive region exhibits passive film instability to a greater extent, showing more pronounced fluctuations in the passive film, suggesting a less stable protective layer. P3 curve showed a moderate passivation, with a protective layer forming but not as effectively as in P1. The passive region shows passive film instability, but the fluctuations (green arrow) are less pronounced than in P2, indicating better passive film stability than P2, but not as stable as P1. Table 7.2 shows the electrochemical parameters of the as-cast HCCIs in 0.5 M NaOH solution. In 0.5 M NaOH solution, P1 exhibited the highest corrosion potential (-0.189 V), followed by P3 (-0.343 V) and P2 (-0.444 V), matching the OCP curves (Figure 7.4), where P1 displayed the most stable corrosion potential. The Icorr values of the samples are significantly lower in NaOH, indicating very slow corrosion rates. The corrosion rates confirm this trend, with P1 having the highest, followed by P3 and P2. These values are supported by the potentiodynamic polarisation curves (Figure 7.5), where all samples showed strong passivation, where P1 showed the greatest shift towards high current density indicating higher corrosion activity and P2 had the greatest shift towards lower current density indicating lower corrosion activity.

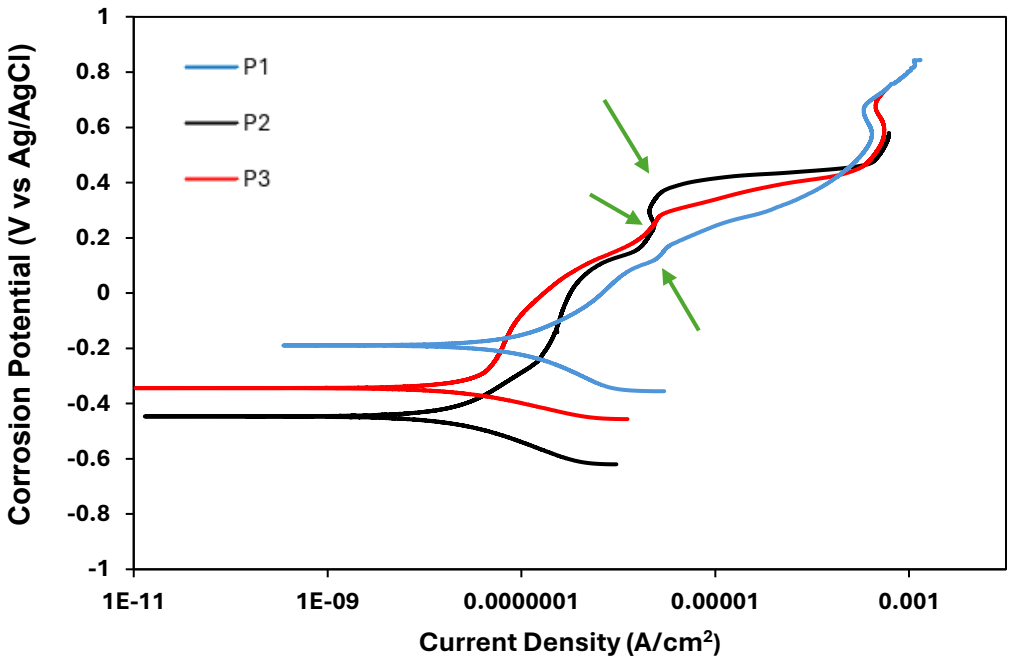

Figure 7.5: Potentiodynamic polarisation curves of the as-cast HCCI alloys in 0.5M NaOH solution. Green arrows showing fluctuations.

Table 7.2: The electrochemical parameters of the as-cast HCCI alloys in 0.5M NaOH solution.

As-cast			
0.5 M NaOH solution			
HCCIs	**Icorr (A/cm^2)**	**Ecorr (V)**	**CR (mm/yr)**
P1	0.000000174±0.00015	-0.189±0.08	0.00196±0.002
P2	0.0000000446±0.0013	-0.444±0.19	0.00048±0.03176
P3	0.0000000557±0.0005	-0.343±0.15	0.00058±0.03958

7.3.3 Surface Morphology of As-Cast HCCIs After Exposure in 0.5M NaOH Solution

The BSE SEM images of surface morphology after corrosion in 0.5M NaOH solution are shown in Figure 7.6. The SE images of the images presented are presented in Appendix C-2. The microstructure of P1 remains well-defined with minimal signs of matrix dissolution (Figure 7.6a). The localised dissolution occurred along primary carbide boundaries, with narrow corrosion channels forming in the carbides. The microstructure appears largely intact with shallow pits where the carbides are positioned. The middle of the carbides remains largely intact in some areas while there is more noticeable carbide dissolution. This shows that the carbides in some regions of the microstructure were dissolved in NaOH. The corrosion attack in P2 is in the carbides, with clear dissolution of carbides (Figure 7.6b). The dissolution of the carbides generated deeper cavities, while the surface remains well-defined with no signs of dissolution. Larger carbides show higher degree of corrosion compared to the smaller carbides which stayed largely intact. The dissolution of the carbides on the surface leaves the matrix protruding above the hollowed carbides. The P3 sample matrix remains intact without dissolution like in P2 (Figure 7.6c). However, carbide dissolution occurred along different regions of P3 with the larger primary carbides experiencing more corrosion than the smaller carbides. This validates the corrosion behaviour observed in Figure 7.5 which shows the growth of a strong passive layer with the dissolution of the carbides which continued to protect the matrix from attack. The inconsistent dissolution of the carbides presented by the fluctuations can also be observed on the microstructure where the corrosion is occurring more in the larger carbides than the smaller carbides thus causing an inconsistency in the building of the passive layer. However, the continuous growth of the passive layer is consistent with the carbide dissolution as opposed to the matrix.

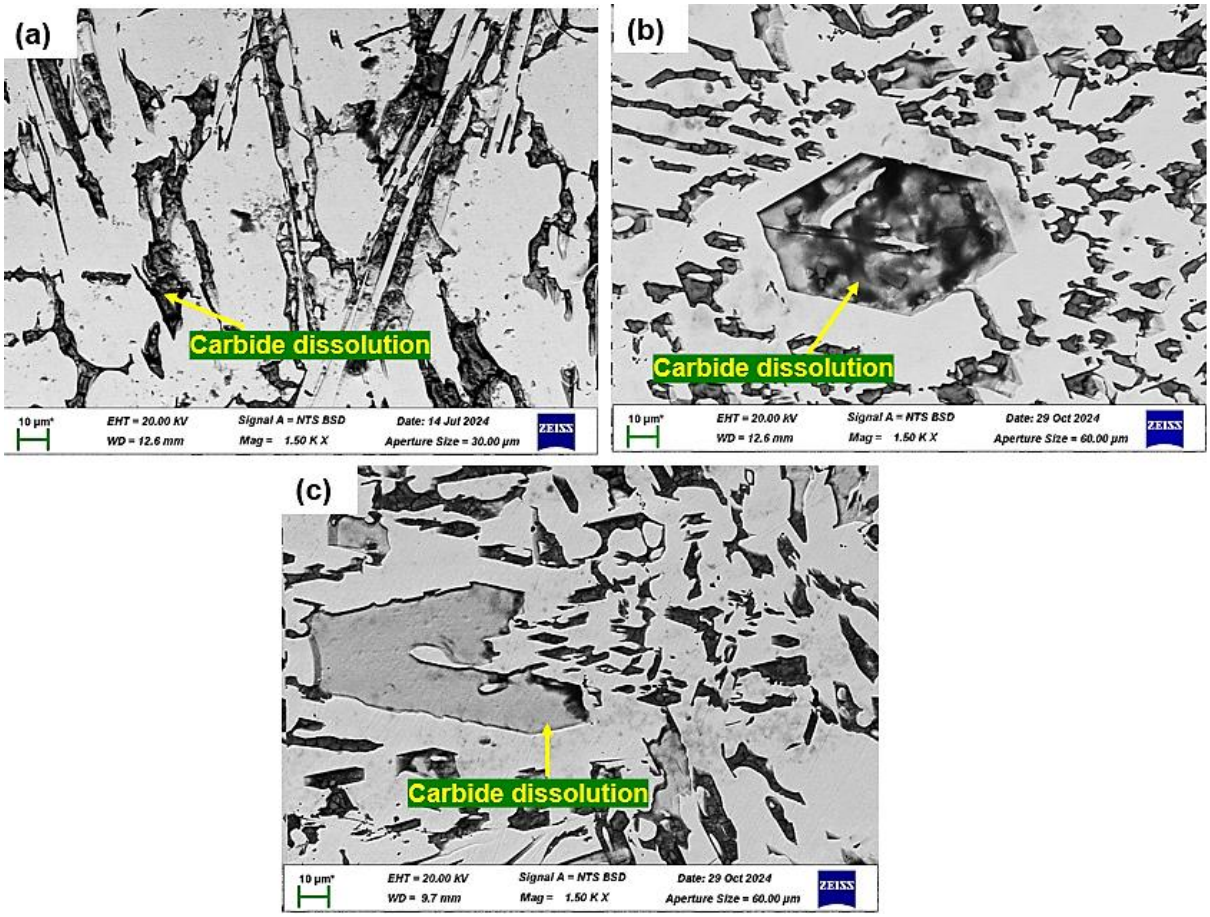

Figure 7.6: BSE-SEM images of surface morphology of as-cast P1 (a) P2 (b) and P3 (c) after electrochemical testing in 0.5 M NaOH solution.

7.4 Corrosion Behaviour of As-Cast HCCIs in 0.5M H_2SO_4 Solution

7.4.1 OCP Behaviour of As-Cast HCCIs in 0.5M H_2SO_4 Solution

The OCP curves of as-cast HCCIs in 0.5 M H_2SO_4 solution for 3600 s is shown in Figure 7.7. The OCP results reveal distinct trends for each sample when exposed to 0.5 M H_2SO_4 solution for 3600 s. P1 started at approximately -0.44 V and initially shows a steady increase in corrosion potential, reaching around -0.425 V. It then stabilises with minor fluctuations but remains relatively constant for the remainder of the scan showing a decreasing trend towards the end. P2 started at approximately -0.46 V, experienced an initial increase, and then gradually stabilised around -0.455 V, showing slight fluctuations throughout the test. P3 starts at around -0.455 V, however its corrosion potential is highly unstable, with frequent dips, kinks, and sudden spikes observed at multiple points. The corrosion potential continues fluctuating throughout the test, with noticeable sharp peaks around ~2400s and ~3600s, indicating instability in the passive film.

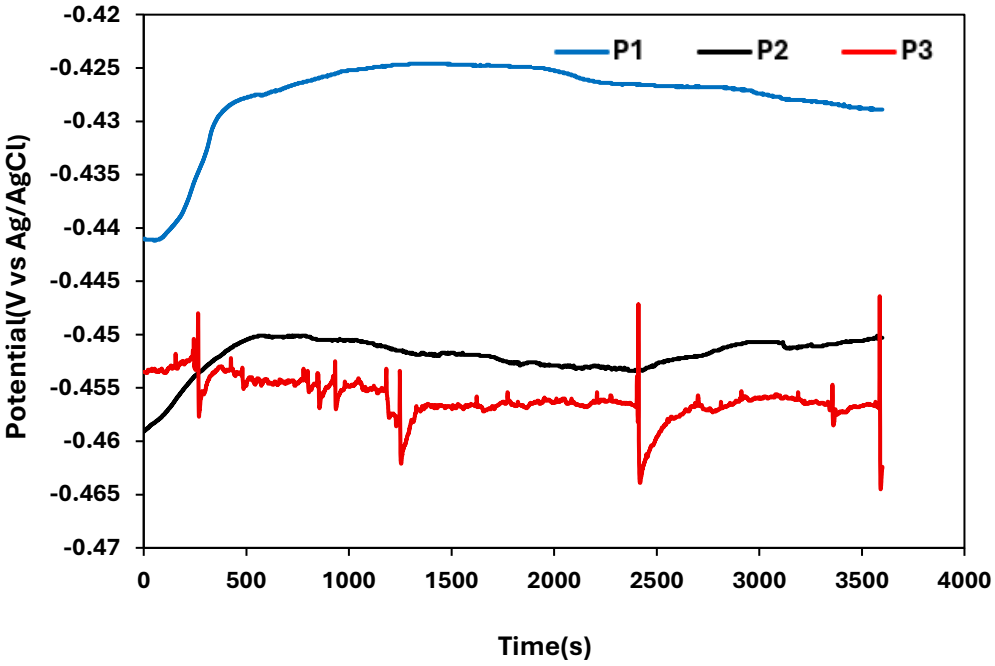

Figure 7.7: OCP curves of as-cast HCCIs in 0.5 M H_2SO_4 solution.

7.4.2 Potentiodynamic Polarisation Behaviour of As-Cast HCCIs in 0.5M H_2SO_4 Solution

The potentiodynamic polarisation curves of the as-cast HCCIs in 0.5 M H_2SO_4 solution is shown in Figure 7.8. All three curves exhibited very similar characteristics of active dissolution region, however, instability region indicative of pitting (green arrows) in P1 and P3. The sample P1 has the highest Ecorr, with its curve shifting towards more positive potential. P1 also shows a fluctuating passive region at anodic potential. P2 and P3 have lower corrosion potential than P1 showing similar corrosion characteristics. P2 and P3 show more stable passive region at anodic potentials although P3 experiences a large increase in current density in the passivation region whereas P2 shows no fluctuations. The fluctuations observed in the passive region of P1 and at about -0.02 V in P3 showed they might be prone to pitting corrosion. This aligns with the OCP behaviours observed in Figure 7.7 where the OCP of P1 and P2 show more stable passive films with P2 having the most stable film. This compared to P3ht which is highly unstable and experiences periods of rapid dissolution and stable film instability. Table 7.3 shows the electrochemical parameters of the as-cast HCCIs in 0.5 M H_2SO_4 solution. In 0.5 M H_2SO_4 solution, the Ecorr is highest for P1, while P2 and P3 have more negative values. The Icorr values indicate more severe corrosion, with P3 having the highest confirming the potentiodynamic polarisation behaviour where P3 exhibited the most rapid dissolution. The

corrosion rate follows the same order, with P3 having the highest, followed by P2 and P1, indicating that all samples experience rapid material loss in acidic conditions.

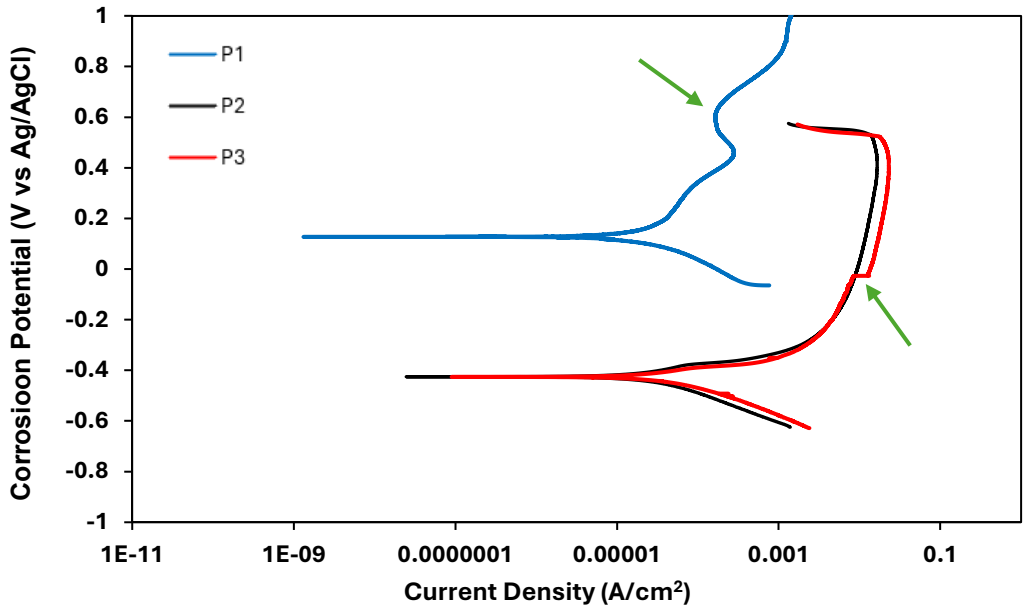

Figure 7.8: Potentiodynamic polarisation curves of the as-cast HCCI alloys in 0.5M H2SO4 solution. Green arrows showing fluctuations.

Table 7.3: The electrochemical parameters of the as-cast HCCI alloys in 0.5M H_2SO_4 solution.

As-cast			
0.5M H_2SO_4 solution			
HCCIs	**Icorr (A/cm^2)**	**Ecorr (V)**	**CR (mm/yr)**
P1	0.00000416±0.01	0.127± 0.05	0.0469±0.04
P2	0.00000575±0.015	-0.425±0.19	0.0614±0.12
P3	0.0000458±0.01	-0.426 ±0.19	0.0871 ±0.37

7.4.3 Surface Morphology of As-Cast HCCIs in 0.5 M H_2SO_4 Solution

The BSE SEM images of as-cast HCCIs after electrochemical testing in 0.5 M H_2SO_4 solution are shown in Figure 7.9. The SE images of the images presented are presented in Appendix C-3. P1 showed surface roughening and mild matrix dissolution with some places showing shallow grooves and etching along carbide boundaries (Figure 7.9a). There are some deep grooves, and shallow pits observed around the fine carbides. However, the carbides remain whole, implying some heterogeneous material loss has occurred, however at a shallow level.

This is evidence of the localised corrosion attacks. This agrees with the corrosion behaviour observed in the potentiodynamic polarisation curve where the curve for P1 shows a significant increase in the potential showing significantly less corrosion. The passive region shows the fluctuations in the passive film showing the active dissolution of the matrix. P2 exhibited localised corrosion at carbide-matrix interfaces, with extensive dissolution in some areas while other areas remain essentially intact (Figure 7.9b). The attack is not completely homogeneous since some regions show more material loss than others, possibly due to different microstructures and microgalvanic interactions between the matrix and carbides. The images also show matrix undercutting; wherein partially exposed or projecting carbides are left behind since the surrounding metallic matrix is corroding quicker than the carbides. This implies that the main mode of corrosion in P2 is selective matrix dissolution with localised attack, which helps to produce the uneven corrosion depth over the surface.

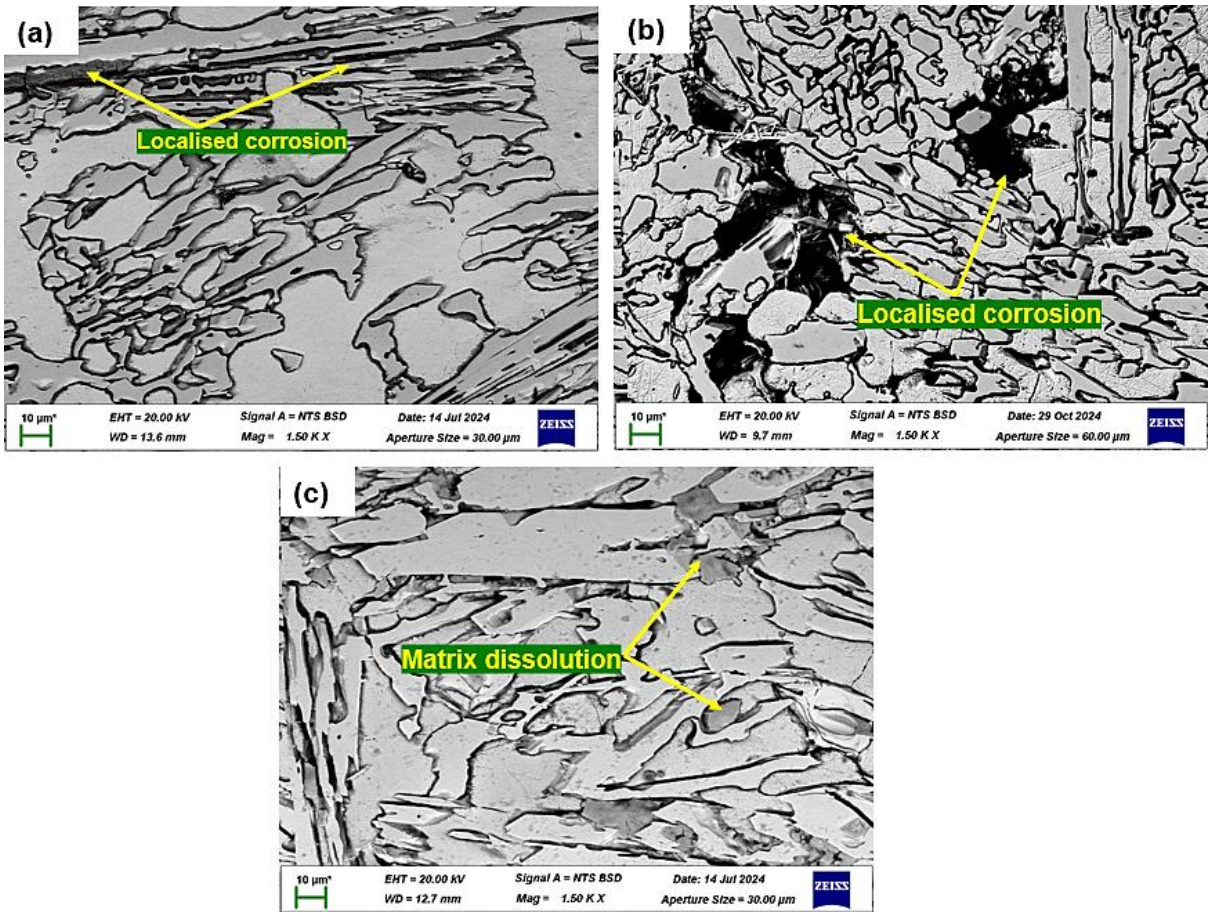

Figure 7.9: BSE-SEM images of surface morphology of as-cast P1 (a) P2 (b) and P3 (c) after electrochemical testing in 0.5 M H_2SO_4 solution.

P3 exhibited extensive matrix dissolution which results in the creation of deep grooves around the carbide-matrix interface (Figure 7.9c). P3 shows more widespread material loss over the surface than P2, in addition to the dissolution on the carbide-matrix interface producing a more obvious network-like structure of carbides. While the surrounding matrix has been considerably eroded, the large and continuous carbides, however in some regions the carbides show early signs of carbide detachment. The damage appears widespread, suggesting continuous matrix dissolution, where the exposed carbides remain intact, while the matrix continues to corrode away. The corrosion mode in P3 appears to be severe homogenised matrix dissolution and carbide-matrix dissolution, in which the metallic matrix is gradually destroyed, leaving behind a densely interconnected carbide. This agrees with the observed potentiodynamic behaviour observed in Figure 7.8 which shows significantly higher potential compared to P1 showing less severe corrosion. The passive film for P3 shows a fluctuation showing that the passive film forms and breaks which shows the simultaneous corrosion of the matrix and the carbide-matrix interface leading to ultimate carbide pullout whereas P2 shows more corrosion at the carbide-matrix interface leading to carbide pullout and a more stable passive film compared to P3. However, P2 and P3 show very similar corrosion behaviour.

7.5 Corrosion Behaviour of Heat-Treated HCCIs in 3.5 wt.% NaCl Solution

7.5.1 OCP Behaviour of Heat-treated HCCIs in 3.5 wt.% NaCl Solution

The OCP curves of the heat-treated HCCIs in 3.5 wt.% NaCl solution over 3600 seconds are shown in Figure 7.10. P1ht started at -0.15 V and gradually decreases, reaching approximately -0.40 V, where it has fluctuating downward trend before fluctuating at a more levelled range towards the end. The curve for P1ht is not smooth, showing minor fluctuations in OCP potential over time. P2ht began at approximately -0.60 V, following a more stable trend with minor fluctuations, gradually decreasing and stabilising near -0.68 V. The potential for P3ht started at around -0.61 V, closely following P2ht, but continued to slightly decline and settled around -0.70 V. Like P2ht, the curve for P3ht is not entirely smooth and has slight fluctuations throughout the scan. The curves of P2ht and P3ht remain close in potential, with small variations and occasional peaks observed in the later stages.

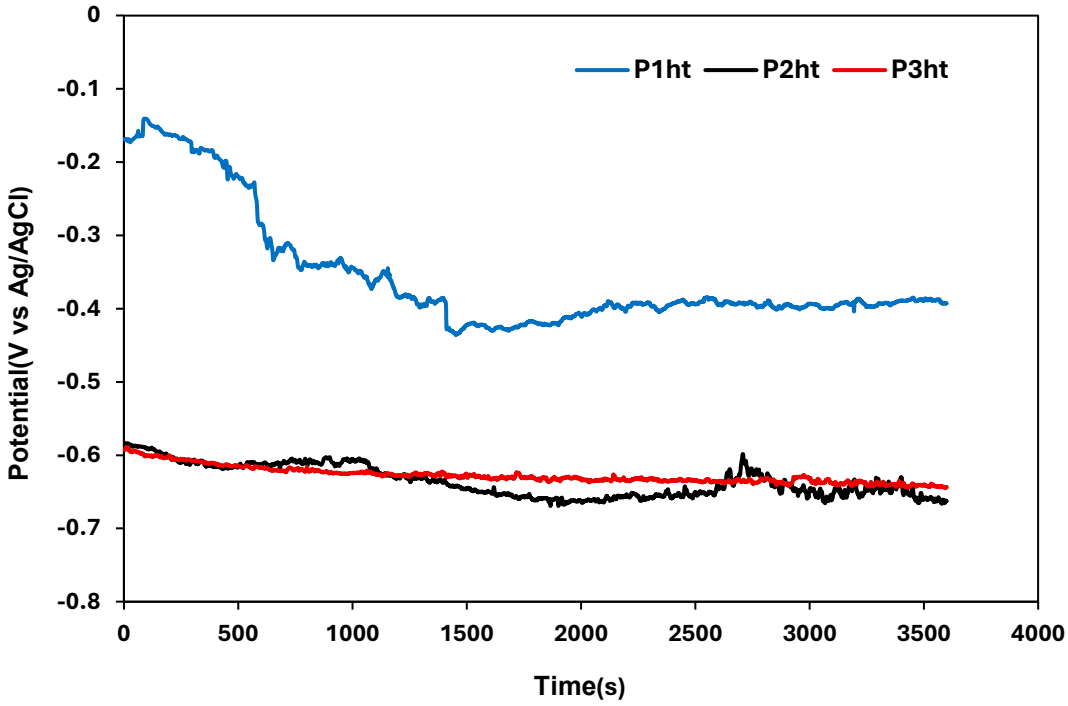

Figure 7.10: OCP curves of heat-treated HCCIs in 3.5 wt.% NaCl solution..

7.5.2 Potentiodynamic Polarisation Behaviour of Heat-Treated HCCIs in 3.5 wt.% NaCl Solution

The potentiodynamic polarisation curves of the heat-treated HCCIs in 3.5 wt.% NaCl solution are shown in Figure 7.11. All three curves exhibited very similar characteristics of active dissolution as indicated by increased current density with increasing potential. For all three samples, there is a slight decrease with increasing applied potential above -0.4V.

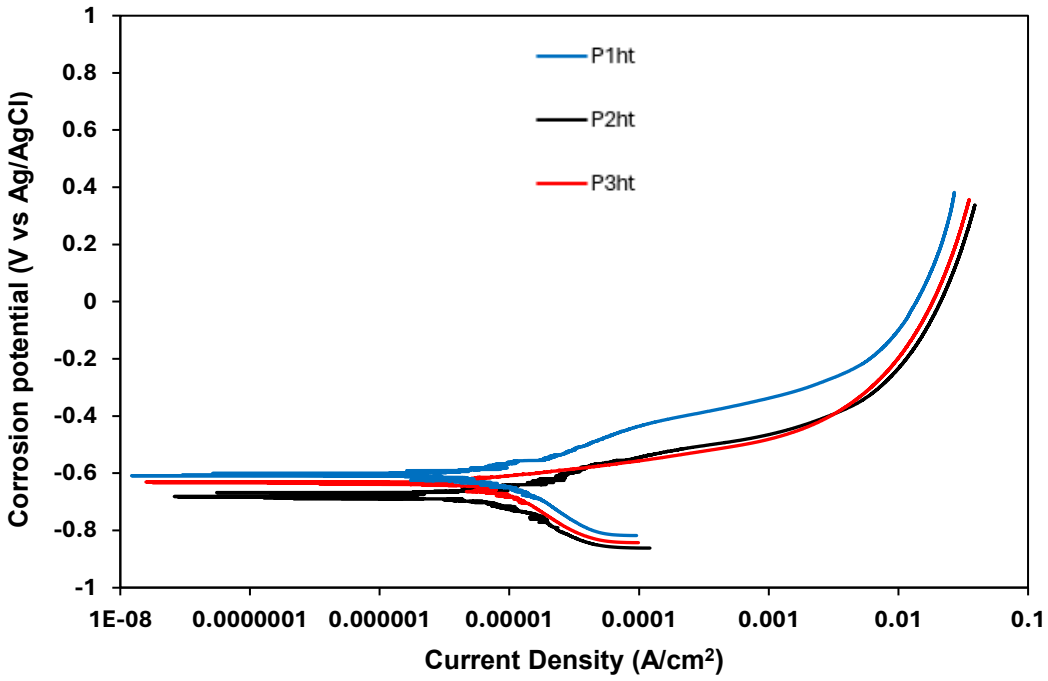

Figure 7.11: Potentiodynamic polarisation curves of the heat-treated HCCIs in 3.5wt% NaCl solution.

Table 7.4 shows the electrochemical parameters of the heat-treated HCCI alloys in 3.5 wt.% NaCl solution. In 3.5 wt.% NaCl solution, the Ecorr for the heat-treated samples shows that all samples P1ht to P3ht show very similar susceptibility to corrosion. This is reflected in their very similar Ecorr values and corrosion behaviour. The Icorr values are close for all three samples, with P3ht having a marginally higher Icorr, to P1ht and P2ht. The corrosion rate follows a similar pattern showing they all have the same tendency to corrode as well as similar corrosion rates in this solution. This alludes to the changes that heat treatment might have made to the microstructure of the samples in favour of improved corrosion behaviour. Overall, the heat-treated samples demonstrate improved corrosion resistance in 3.5 wt.% NaCl.

Table 7.4: Electrochemical parameters of the heat-treated HCCI alloys in 3.5 wt.% NaCl solution.

Heat-Treated			
3.5wt % NaCl solution			
HCCIs	Icorr (A/cm^2)	Ecorr (V)	CR (mm/yr)
P1ht	0.00000126±0.001	-0.608 ±0.27	0.01423 ±0.001
P2ht	0.00000113±0.0002	-0.6815±0.30	0.01227±0.042
P3ht	0.00000157±0.001	-0.634±0.28	0.01496 ±0.044

7.5.3 Surface Morphology of Heat-Treated HCCIs After Exposure in 3.5 wt.% NaCl Solution

BSE SEM images of P1ht, P2ht, and P3ht after electrochemical testing in a 3.5 wt.% NaCl solution are shown in Figure 7.12. The SE images of the images presented are presented in Appendix C-4. The surface exhibited localised pitting and material loss, with some areas appearing slightly roughened (Figure 7.12a). Pits and cavities are visible, particularly at carbide-matrix interfaces. The primary and eutectic carbides remain intact, while the surrounding matrix shows evidence of selective dissolution. The passive layer appears to have partially broken down in certain locations, leaving the surface vulnerable to continuous corrosion attack. For P2ht, corrosion appears more apparent, with wider pits and deeper material loss across the surface (Figure 7.12b). The carbide interfaces show apparent signs of corrosion, with the phase selectively dissolving around the carbides. Some sections have interconnected corrosion pathways, indicating that chloride ions infiltrated weak spots, causing widespread damage. The surface is uneven, with many pits merging into bigger corroded sections. The corrosion behaviour of P3ht is similar to P2ht, but with slight differences in pit distribution and depth. Both samples exhibit deep grooves and corrosion pathways along carbide-rich regions, P3ht also shows some extensive matrix dissolution in some areas (Figure 7.12c). The remaining structure in both samples is mostly carbide-dominated, indicating that the P3ht was highly vulnerable to chloride attack. Selective matrix dissolution occurs because the metallic matrix is more reactive compared to the carbide phases. These images show that corrosion in 3.5 wt.% NaCl solution largely affects other phases, with selective dissolution happening around carbides. All samples experienced the same corrosion behaviour. The mechanism of corrosion is also the same which is selective dissolution of the matrix with some pitting around the carbide-matrix interface. This is agreement with the corrosion behaviour of all three samples as observed in the potentiodynamic curves in Figure 7.11 showing similar corrosion behaviour of increase in active dissolution with an increase in current density.

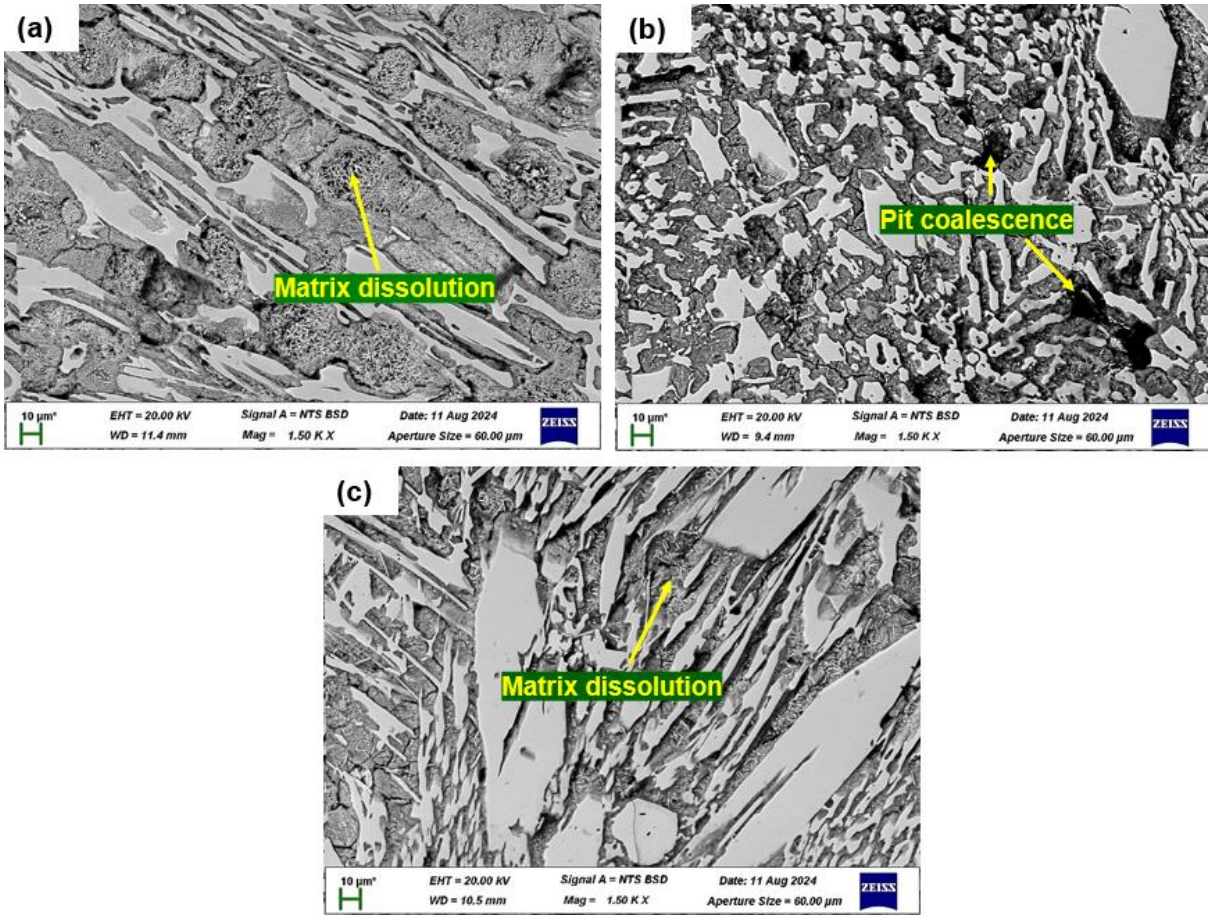

Figure 7.12: BSE-SEM images of heat-treated a) P1ht, b) P2ht and c) P3ht after electrochemical testing in 3.5wt% NaCl solution.

7.6 Corrosion Behaviour of Heat-Treated HCCIs in 0.5M NaOH Solution

7.6.1 OCP Behaviour of Heat-Treated HCCIs in 0.5M NaOH Solution

The OCP curves of heat-treated HCCIs in 0.5 M NaOH solution for 3600 s is shown in Figure 7.13. P1ht started at the highest potential around -0.455 V, then increased to around -4.50V, then translated to an unsteady downward trend and fluctuating till the end where there is a slight increase in corrosion potential. P1ht is a lot more stable compared to P2ht and P3ht. P2ht started at a potential of approximately -0.475 V and gradually increased. The OCP curve is relatively smooth with minor fluctuations, showing a consistent upward progression. The OCP curve eventually surpasses P1ht around 1500s, reaching around -0.438 V towards the end of the scan. P3ht started at the lowest potential, around -0.485 V, and gradually increases over time to the end. Fluctuations are more visible in the OCP curve of P3ht sample, with sharp dips occurring between 1800 s and 2000 s before continuing along a general increasing path. By the end of the OCP scan, P2ht and P3ht increased with increasing exposure time while exceeding the OCP of P1ht at around 1500 and 3500 s respectively. The implication of the OCP observed

is that the passive films formed on the alloys are expected to be thicker in the order of P2ht where P2ht is expected to have a thicker more protective oxide layer, followed by P1ht and finally P3ht. However, with longer exposure time, P3ht may have thicker protective oxide layer than P1ht.

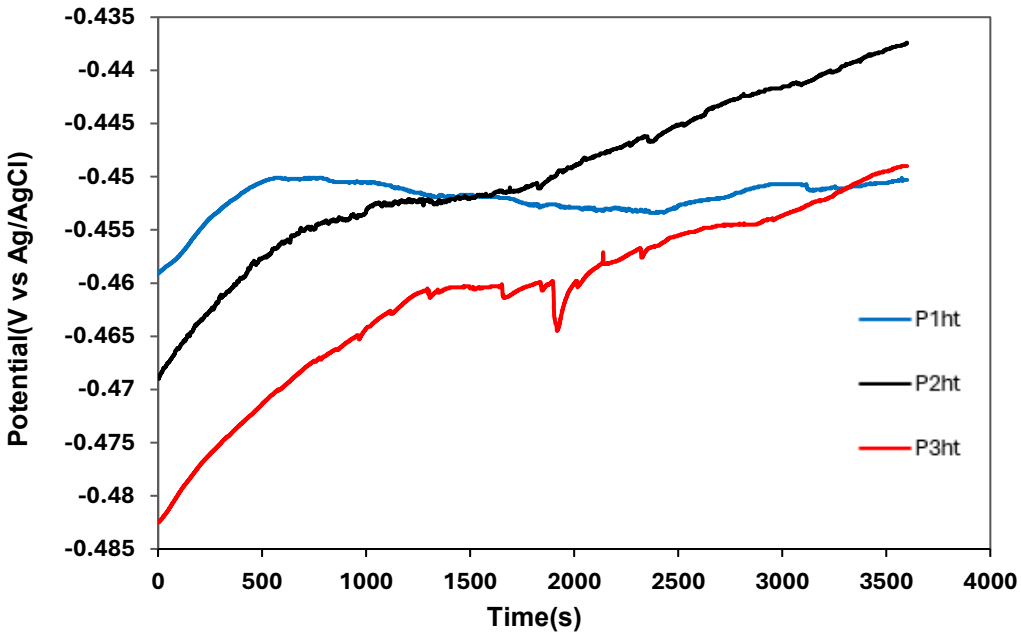

Figure 7.13: OCP curves of heat-treated HCCIs in 0.5M NaOH solution.

7.6.2 Potentiodynamic Polarisation Behaviour of HCCIs in 0.5M NaOH Solution

The potentiodynamic polarisation curves of the heat-treated HCCIs in 0.5 M NaOH solution are shown in Figure 7.14. Fluctuations were observed in the anodic curve of P1ht and later undergoes transpassivation. The polarisation curves had a lower corrosion potential for P1ht and P3ht. This shift suggests a more negative potential and reduced electrochemical activity for P1ht and P3ht. The polarisation curves for P1ht exhibited a minor fluctuation in the passive region while P2ht showed a drastic shift towards higher potentials. This means that P2ht exhibited the best corrosion behaviour compared to P1ht and P3ht. Despite showing the best corrosion behaviour, P2ht also showed fluctuations in the passive region indicating instability in the passive film formation and suggested pitting corrosion. In NaOH solution, the OCP is not fully reproducible due to several factors related to the passive film formation, and variations in electrochemical conditions. If surface preparation differs slightly, such as inconsistencies in polishing or cleaning, the initial OCP values may vary (Ahmadian et al., 2014; Lynch et al.,

2020; Ma et al., 2020). Electrolyte conditions also impact OCP reproducibility. Slight differences in temperature, or dissolved oxygen levels can influence the passivation process. If the electrolyte conditions changes slightly between tests, the rate of film formation and stabilisation can differ. The reference electrode stability in NaOH can also introduce small potential shifts, leading to minor variations in OCP readings (Moslemi et al., 2011). NaOH promotes gradual passivation, making time-dependent variations more noticeable in OCP measurements. The time required for full stabilisation may vary between samples, especially if secondary carbide precipitation from heat treatment affects the availability of chromium in the matrix. By contrast, potentiodynamic polarisation is more reproducible because it applies an external voltage, actively controlling the electrochemical process rather than relying on passive equilibrium. This reduces variability in measurements compared to OCP, which is highly dependent on time and surface conditions. Overall, the OCP in NaOH is not fully reproducible due to potential passive film growth differences due to time exposure difference, electrolyte variability, surface preparation inconsistencies, and reference electrode fluctuations. These factors contribute to variations in the stabilisation process, making OCP trends differ between separate tests. However, the OCP trends still show the general trend observed in the samples of the growth of the passive film with the corrosion of carbides and thereby the release of chromium increasing the growth of the passive film.

The electrochemical parameters of the heat-treated HCCI alloys after exposure in 0.5 M NaOH solution are shown in Table 7.5. In 0.5 M NaOH solution, P2ht has the highest Ecorr, followed by P1ht and P3ht where P1ht and P3ht show marginal differences. The Icorr is lowest for P2ht followed by P1ht. This indicates significantly higher electrochemical activity in P3ht compared to the P2ht and P1ht samples. The corrosion rate reflects the same pattern, with P3ht showing the highest rate, followed by P1ht and P2ht also showing marginally different corrosion rates compared to P2ht. The potentiodynamic polarisation curves and OCP confirmed that P2ht developed a more protective passive film, while P1ht and P3ht exhibited weaker passivation, leading to higher corrosion rates. Additionally, P3ht and P1ht show very similar corrosion susceptibility compared to P2ht as observed in the potentiodynamic curves in Figure 7.14. The difference between the corrosion rates of P1ht and P3ht are not significantly different compared to P2ht. P2ht has far superior corrosion resistance than P1ht and P3ht.

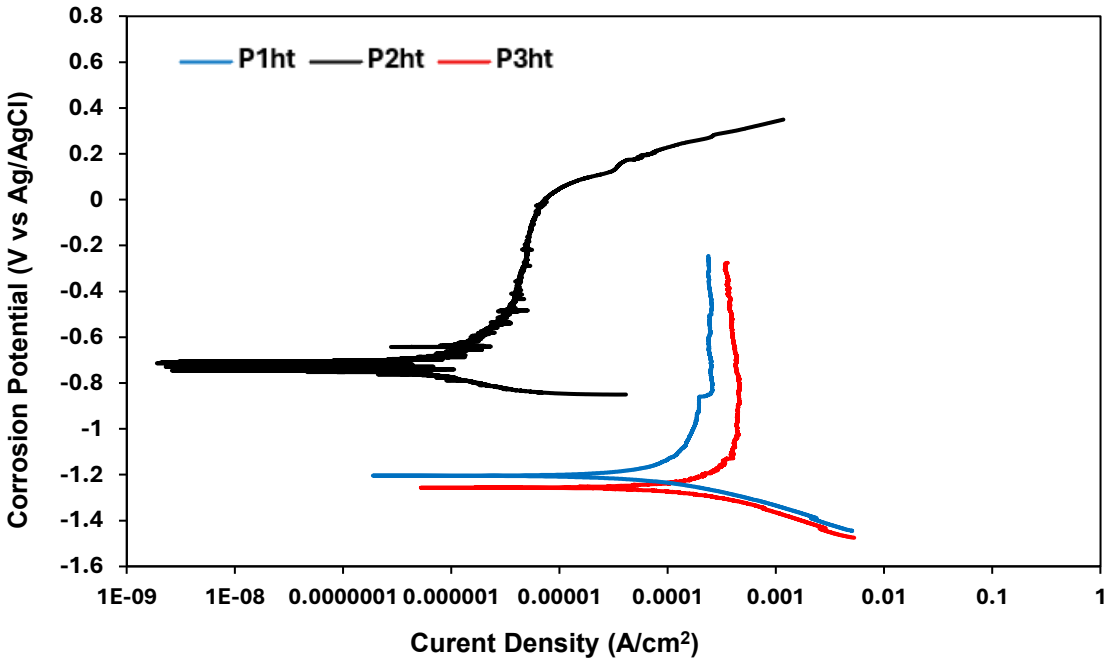

Figure 7.14: Potentiodynamic polarisation curves of the heat-treated HCCIs in 0.5M NaOH solution.

Table 7.5: Electrochemical parameters of the heat-treated HCCI alloys in 0.5M NaOH solution.

Heat-Treated			
0.5 M NaOH solution			
HCCIs	Icorr (A/cm^2)	Ecorr (V)	CR (mm/yr)
P1ht	0.0000101±3.49	-1.203±0.53	0.1139 ± 0.08
P2ht	0.000000128±0.31	-0.743±0.33	0.0014±0.38
P3ht	0.0000280±2.73	-1.254±0.56	0.2937±1.03

7.6.3 Surface Morphology of HCCIs After Exposure in 0.5 M NaOH Solution

The BSE SEM images of the heat-treated HCCIs in 0.5 M NaOH solution are shown in Figure 7.15. The SE images of the images presented are presented in Appendix C-5. In P1ht, the carbides show grooves around the edges, showing that corrosion started at the primary carbide-matrix boundaries (Figure 7.15a). The grooves are deep and uneven, suggesting that the edges of the primary carbides dissolve faster than the centres and that corrosion did not occur uniformly with more corrosion happening at the larger primary carbides. The centres of the carbides are mostly intact, while the matrix remains uncorroded. This is in agreement with how P1ht also showed some fluctuations in the passive region in Figure 7.14 which would be explained by the way P1ht corroded with uneven corrosion occurring across the primary

carbides where the larger primary carbides corroded more uniformly than the smaller primary carbides leading to the fluctuation observed. In P2ht sample, the primary carbides are etched more evenly across their surfaces (Figure 7.15b). The cavities are shallower, and more uniformly corroded compared to P1ht. Some minipores can also be observed in the secondary carbides which might later coalesce to form larger pits. This agrees with the polarisation curve in Figure 7.14 of P2ht which shows the highest potential on the potentiodynamic polarisation curve with fluctuations in the passive region which amount to the corrosion of the primary carbides however still exhibiting the best corrosion resistance compared to P1ht and P3ht. The carbide-matrix boundaries are smoother, with less aggressive corrosion. This suggests that the primary carbides dissolve slowly and consistently.

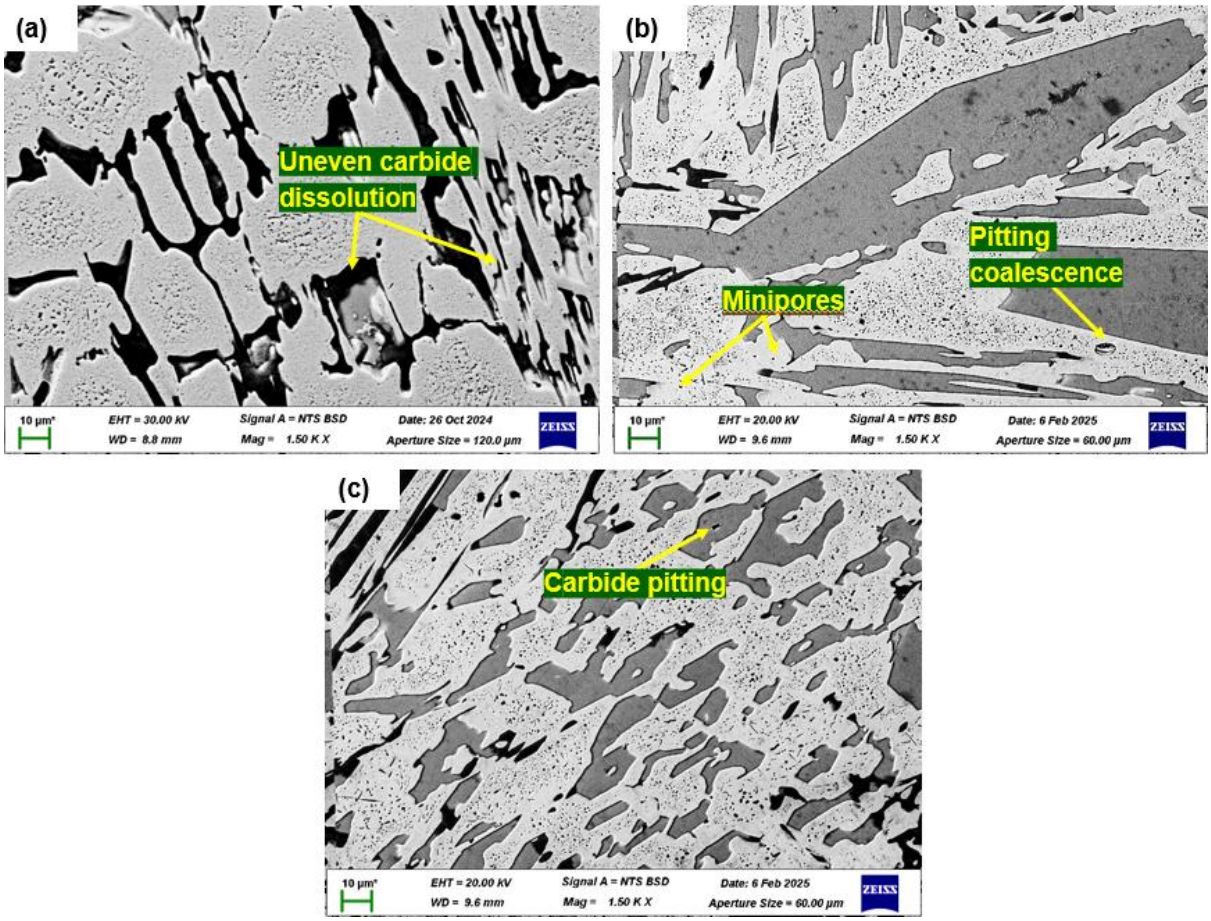

Figure 7.15: SEM images of heat-treated P1ht (a), P2ht (b) and P3ht (c) after electrochemical testing in 0.5 M NaOH solution.

P3ht in Figure 7.15c shows a similar corrosion surface to P2ht with even dissolution of the primary carbide surface. Complete surface dissolution of primary and eutectic carbides has occurred in P3ht compared to P1ht. Some primary carbides also have pits in the centres, showing that corrosion penetrates deeper. The surrounding matrix is smooth, but the grooves

and uneven surfaces show that the primary and eutectic carbides are the main sites of corrosion. P3ht in Figure 7.14 showed a smoother passive film region as it experienced complete carbide dissolution at a more uniform rate.

7.7 Corrosion Behaviour of Heat-Treated HCCIs in 0.5 M H_2SO_4 Solution

7.7.1 OCP Behaviour of Heat-Treated HCCIs in 0.5 M H_2SO_4 Solution

The OCP curves of heat-treated HCCIs in 0.5 M H_2SO_4 solution conducted for 3600 s are shown in Figure 7.16. The HCCIs almost had similar OCP behaviours with very noticeable fluctuations before stabilising. For P1ht, the OCP curve started at approximately -1.225 V, then gradually decreases with fluctuations till the final 3600 s. For P2ht OCP curve started at around -1.265 V, fluctuating throughout the test and following a slightly increasing trend, continuing till the final 3600 s. P3ht started at about -1.265 V, but instead of increasing like P2ht it gradually decreases and stabilises near -1.28 V. Unlike P1ht and P3ht samples, P2ht does not show a clear downward trend but rather fluctuates with small increases over time. The curve for P3ht also shows more aggressive irregular fluctuations but follows a steady downward trend till the end.

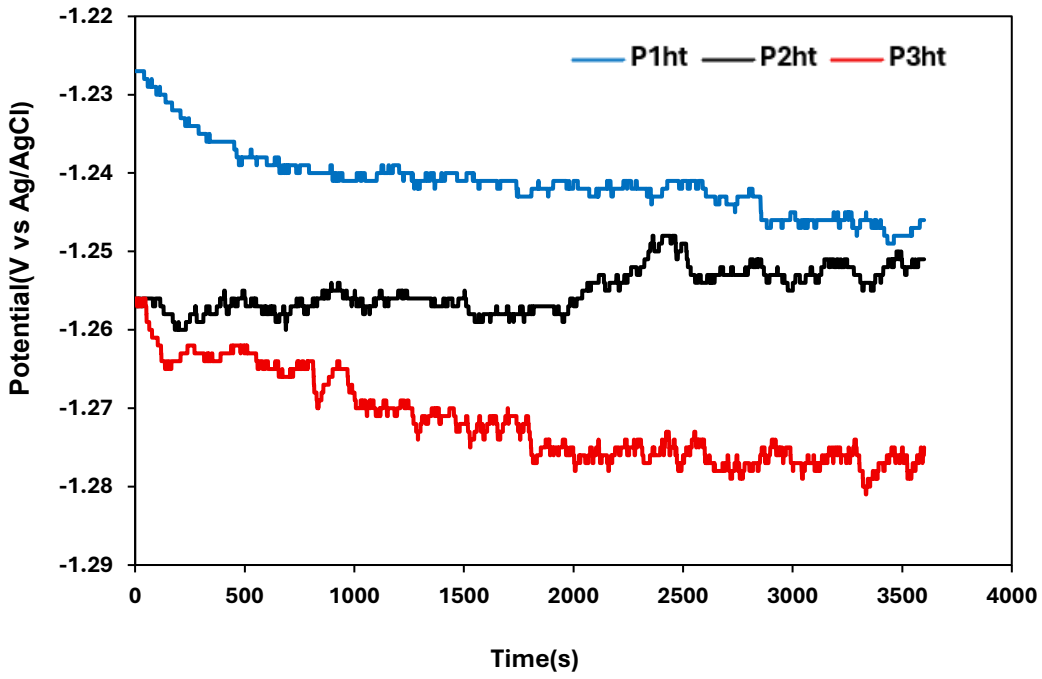

Figure 7.16:OCP of heat-treated HCCIs in 0.5 M H_2SO_4 solution.

7.7.2 Potentiodynamic Polarisation Behaviour of Heat-Treated HCCIs in 0.5M H_2SO_4 Solution

The potentiodynamic polarisation curves of heat-treated HCCIs in 0.5 M H_2SO_4 solution are shown in Figure 7.17. The curves highlight differences in corrosion potential and passivation behaviour, indicating varying electrochemical responses of the alloys in acidic conditions. The HCCIs had similar Ecorr values. All samples show similar anodic region behaviour with fluctuations in the passive region indicating instability in the passive film. The curves show noticeable fluctuations, suggesting frequent breakdowns and repassivation events. P3ht also shows a similar pattern to P2ht and P1ht however with an earlier onset passivation compared to the other curves. The fluctuations are sharp and irregular like in P1ht and P2ht, indicating instability in the passive film and rapid dissolution occurring once the film breaks down. Again here, the OCP results are not reproducible due to the experiments being conducted in different instances. In H_2SO_4 solution, the OCP is not fully reproducible due to the highly aggressive nature of the acid and its effects on the passive film, matrix dissolution, and electrochemical reactions. The passive film in sulphuric acid experiences the continuous breakdown and reformation due to the attack by sulphate ions, leading to fluctuations in the passive film formation. Unlike in chloride or alkaline environments, H_2SO_4 promotes active dissolution of the metal matrix, meaning small differences in material exposure or surface condition can lead to variations in OCP trends (Yue et al., 2018). Additionally, hydrogen evolution occurs as part of the cathodic reaction, and variations in hydrogen gas formation can temporarily block active sites, affecting the local pH and further destabilising the passive film (Deng et al., 2018; Feng et al., 2021). Even minor differences in sample preparation, such as surface polishing, oxidation, or contamination, can influence how the material interacts with the acid and affect the time required for OCP to stabilise (Yue et al., 2018). Variations in temperature, dissolved oxygen levels, and stirring rate may have also impacted the corrosion process, making it difficult to reproduce identical OCP readings (Su et al., 2019; Atiyah & Albusalih, 2023). The Ag/AgCl reference electrode may experience slight potential drift in strong acids, further contributing to discrepancies, especially when paired with the temperature difference produced during acid preparation (Shen et al., 2020; Farquhar et al., 2021). Since OCP reflects the natural equilibrium of the system, any variation in reaction kinetics over time can affect the trend. In contrast, potentiodynamic polarisation is more reproducible because it applies an external voltage, forcing the material into a controlled electrochemical state rather than relying on passive stabilisation.

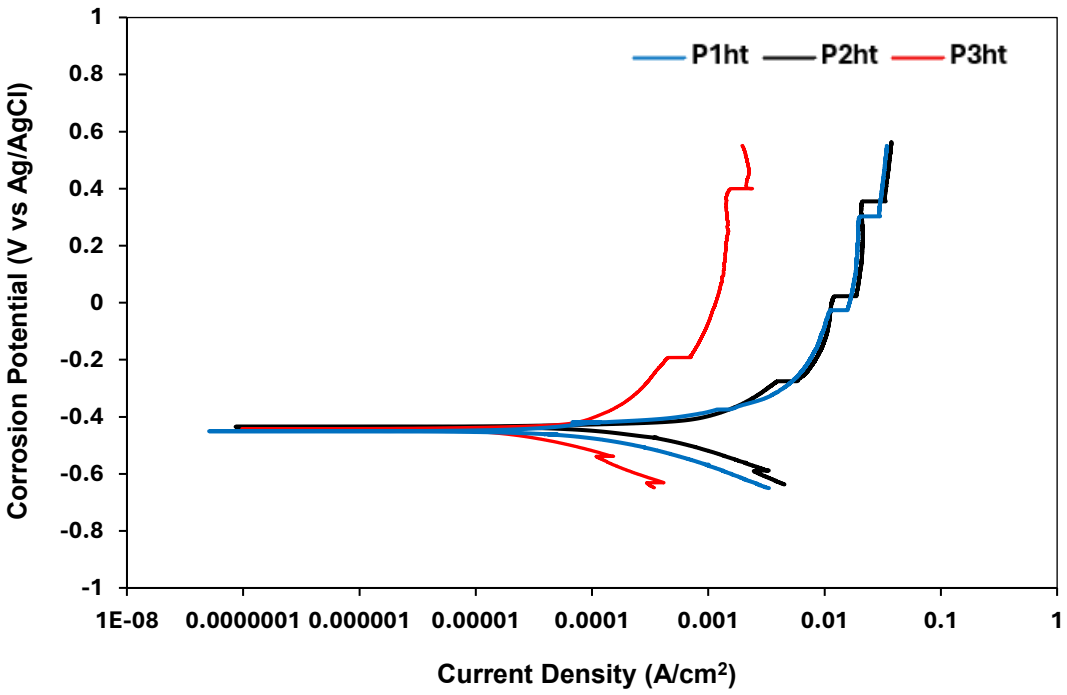

Figure 7.17: Potentiodynamic polarisation curves of the heat-treated HCCIs in 0.5 M H_2SO_4 solution.

Overall, the lack of reproducibility in OCP for H_2SO_4 is mainly due to passive film instability, active-matrix dissolution, hydrogen evolution, electrolyte variability, and surface condition differences, all of which influence the response of the system over time. However, the OCP trends still reflect the highly unstable nature of the passive films in H_2SO_4 which is also evident in the passivation behaviour of the samples shown in Figure 7.17 showing frequent passive layer breakdown and reformation.

The electrochemical parameters of the heat-treated HCCI alloys after exposure in 0.5 M H_2SO_4 solution are shown in Table 7.6. In 0.5M H_2SO_4 solution, all samples show a similar potential to corrode. P1ht has the lowest Icorr among HCCIs. Consequently, P1ht has the lowest corrosion rate, followed by P2ht and P3ht. These results are supported by the potentiodynamic polarisation curves, where P3ht exhibits more rapid dissolution, while P1ht retains slightly better passivation than the others. Corrosion was the most severe in this environment.

Table 7.6: Electrochemical parameters of the heat-treated HCCI alloys in 0.5 M H_2SO_4 solution.

	Heat-Treated		
	0.5M H_2SO_4 solution		
HCCIs	**Icorr (A/cm^2)**	**Ecorr (V)**	**CR (mm/yr)**
P1ht	0.0000161±0.06	-0.450 ± 0.20	0.1809 ±0.19
P2ht	0.0000336±0.31	-0.435± 0.19	0.3515±2.87
P3ht	0.0000481±0.08	-0.447± 0.20	0.5039±2.04

7.7.3 Surface Morphology of HCCIs After Exposure in 0.5 M H_2SO_4 Solution

The BSE SEM images of the heat-treated HCCIs in 0.5 M H_2SO_4 solution are shown in Figure 7.18. The SE images of the images presented are presented in Appendix C-6. Pitting corrosion is obvious in P1ht, with deep cavities emerging in specific locations of the metallic matrix (Figure 7.18a). The carbides are still securely embedded, but in certain areas, the matrix has begun to remove, exposing carbide edges. In the P2ht, the corrosion appeared to be more aggressive than that in P1ht (Figure 7.18b). The matrix displays disintegration, with a significant amount of metallic matrix dissolution. The carbides are substantially intact, however there is indication of weakening where the matrix has corroded beneath them. As the matrix weakened, some regions exhibited signs of carbide separation. P3ht exhibited the most severe corrosion, with P3ht demonstrating substantial matrix disintegration (Figure 7.18c). The structure consisted primarily of exposed and interconnected carbides, with vast holes and deep grooves indicating significant metallic matrix dissolution. The significant deterioration of the matrix causes some carbides to appear unattached. The surface is extremely porous, indicating that corrosion has spread extensively within P3ht. The heat-treated samples in 0.5M H_2SO_4 solution exhibit progressive matrix dissolution, with P3ht incurring the most severe corrosion, followed by P2ht and subsequently P1ht. This is in agreement with the dissolution behaviour observed in all the curves for P1ht to P3ht, which show the severe fluctuating and active dissolution in the passive region, which meant the passive film was being attacked heavily, after which active dissolution was occurring. This would then be followed by the rebuilding of the film and again active dissolution.

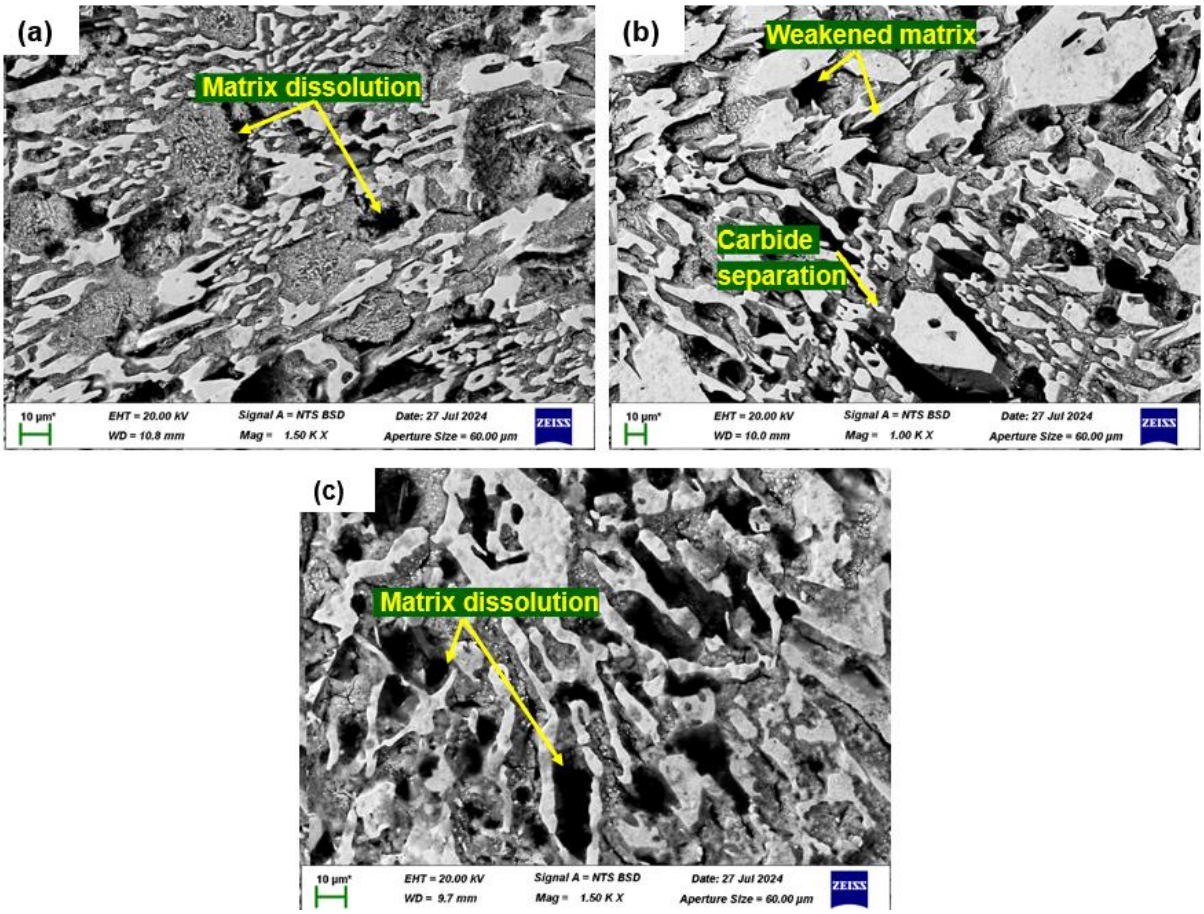

Figure 7.18: BSE-SEM images of heat-treated P1ht (a), P2ht (b) and P3ht (c) after electrochemical testing in 0.5 M H_2SO_4 solution.

7.8 Discussion

7.8.1 Comparison Between the Corrosion Behaviour of As-Cast and Heat-Treated HCCIs in Chloride Solution

Increasing the chromium content in the HCCI alloys improves corrosion resistance by forming a more stable passive layer, which protects the material from further corrosion (Tang et al., 2009). The lower carbon content leads to the formation of smaller primary carbides, which refine the microstructure as well as produce fewer carbides, thereby reducing the number of active corrosion sites (Salasi et al., 2011; Tang et al., 2011; Gong et al., 2023).

The uniform distribution of carbides enhances passivation and reduces localised corrosion, leading to a higher and more stable OCP over time (Yang et al., 2009). The carbides are hard, stable compounds made of chromium and carbon, spread throughout the material, creating a more uniform and refined structure. A finer microstructure reduces weak points where corrosion can begin, improving overall resistance to degradation (Zhou et al., 2018; Wang et al., 2024). Localised attacks, such as pitting or crevice corrosion, often start in weak areas of

the material, but the evenly distributed carbides reinforce the structure, limiting exposure to corrosion. This improves the durability of the material and stability in aggressive environments such as the 3.5 wt.% NaCl.

In 3.5 wt.% NaCl solution, the primary modes of corrosion observed for the as-cast HCCI samples (P1, P2, and P3) were pitting corrosion and localised microgalvanic corrosion as observed in P1, Figure 7.3. The fine primary carbide dispersion can help to preserve passivation by lowering weak areas where chloride ions could enter and initiate localised corrosion attacks (Zhou et al., 2018). It is more difficult for chloride ions to break down the more homogeneous and stable passive layer from fine and evenly distributed M_7C_3 carbides (Zhang et al., 2020). P1 has fine and evenly distributed primary M_7C_3 carbides within the metallic matrix. These primary carbides are smaller and homogeneously dispersed than in the other samples, contributing to better passivation in several ways (Li et al., 2019; Zhang et al., 2020). This reduces the number of weak points where chloride ions can initiate localised attacks. Pitting occurred due to the aggressive attack by chloride ions, which led to localised breakdowns of the passive film, exposing the underlying metal to further corrosion. Additionally, localised microgalvanic corrosion was observed at the carbide-matrix interfaces due to the electrochemical corrosion potential differences between the chromium-rich carbides and the surrounding phases. The corrosion behaviour in NaCl solution is primarily influenced by the distribution of chromium-rich carbides and the availability of chromium to form a protective passive film. P1 exhibited a lower corrosion rate due to its high chromium content and well-distributed primary carbides, which form a stable and continuous passive film.

P2 has a higher carbide volume than P1, forming a network of hexagonal-shaped primary carbides and finer eutectic carbides. The increased primary and eutectic carbide content and decreased chromium provide more cathodic sites, leading to slightly higher corrosion than P1, as there is less chromium readily available to form a strong passive film (Chang et al., 2010). Despite the large volume of primary and eutectic carbides in P2, the smaller, homogeneous, and more densely dispersed carbides compared to P3 significantly decrease the number of carbide-matrix interfaces exposed to the solution, which led to microgalvanic corrosion. This decreased the severity of the corrosion that occurs at the carbide matrix interface, thereby decreasing the corrosion rate of the sample when compared with P3.

P3, like P2, due to the large volume of carbides forming part of the microstructure, has a significantly decreased amount of chromium readily available for a stable and strong passive

film formation. The segregation of chromium and carbon at grain boundaries plays a crucial role, with more chromium segregating to the middle of the carbides as opposed to the carbide-matrix interfaces (Heo & Kim, 2012). During solidification, elements like Cr and C separate unevenly, which leads to areas with less Cr. These areas are more likely to corrode because they cannot form a strong protective layer (Tang et al., 2009). This leads to a weaker protective layer forming in the carbide matrix interfaces. Thus, the passive film becomes weaker and more likely to break down, and corrosion is more prone to occur on this side first (Tang et al., 2009). The large variability in P3 with the large primary carbides and smaller eutectic carbides leads to more matrix being exposed in some parts than others. The additional larger surface of primary carbides increases the amount of exposed surface area, making the galvanic reactions stronger, causing P3 to corrode faster. This then causes more corrosion to occur in some sites than others, causing uneven corrosion throughout the microstructure. Additionally, the larger size of the primary carbide in P3 increased the number of microgalvanic sites for active corrosion compared to P2. This is because in these areas the matrix acts as cathodic sites, while the carbides become anodes, creating small galvanic cells that speed up corrosion in the material (Chang et al., 2010).

The precipitation of secondary carbides can lead to further Cr depletion in the surrounding matrix, which reduces the corrosion resistance (Yan et al., 2020). This is because Cr is a key element that forms a passive film on the surface, protecting against corrosion. The redistribution of elements to a more uniform distribution through the matrix homogenisation limits the areas of extreme segregation of chromium and carbon, thereby causing more uniform corrosion of the matrix. Secondary carbides can play a significant role in the initiation of corrosion. They can act as sites for localised corrosion due to differences in electrochemical corrosion potential between the carbides and the matrix. While secondary carbides influence the initial phases of corrosion, the primary carbide content and its sizes and shapes are more dominant in the progression and orientation of corrosion within the structure (Sarac & Dikici, 2019). However, secondary carbides, when they are homogeneously distributed in the matrix, can act to strengthen the matrix and reduce the corrosion in the matrix (Wiengmoon et al., 2011). In 3.5 wt.% NaCl solution, the primary modes of corrosion observed for the heat-treated HCCI samples (P1ht, P2ht, and P3ht) were pitting corrosion and localised microgalvanic corrosion. The presence of chloride ions led to localised breakdowns of the passive film, resulting in pitting corrosion. Additionally, microgalvanic corrosion occurred at the carbide-matrix interfaces due to the electrochemical corrosion potential differences between the refined

M_7C_3 carbides and the surrounding matrix. The corrosion behaviour in NaCl was mainly influenced by the refinement and redistribution of carbides during heat treatment. P1ht has good corrosion resistance due to its more uniform and finely dispersed carbides, which promoted a consistent and continuous passive film. The finer and more evenly distributed M_7C_3 carbides acted as barriers, reducing the rate of chloride ion penetration, leading to a significantly lower corrosion rate. Consequently, more of the corrosion occurred on the surface of the matrix for P1ht as opposed to the deep eroding of the matrix that occurred in P1, which ultimately led to the removal of carbides, thereby significantly increasing the corrosion rate. The additional redistribution of chromium in the matrix led to the attack happening more uniformly across the matrix surface rather than the dominant localised corrosion at the carbide-matrix interface observed for sample P1. Due to the strengthening of the matrix from secondary carbides, the amount of dissolved matrix significantly decreased. For P2ht, heat treatment caused more coarsening of the primary carbides than in P2; however, homogeneity was maintained. The dense dispersion of the carbides in the matrix with the additional strengthening from the secondary carbides precipitates decreased the amount of readily available matrix to corrode, slowing down the dissolution of the matrix, which caused significantly lower corrosion to occur than P2. P3ht experienced recrystallisation of the primary carbides into more blocky carbides as opposed to the dominating plate-like morphology observed in P3. This significantly decreases the amount of available surface prone to microgalvanic corrosion introduced by larger plate-like carbide morphology. The more highly interconnected carbide network formed during heat treatment and the increased strengthening from the secondary carbides decreased the amount of corrosion compared to P3.

Overall, in NaCl, the main forms of corrosion observed in as-cast samples, localised corrosion and micro-galvanic corrosion, were mitigated by the redistribution of elements in the microstructure, resulting in a more uniform dispersion of elements and phases. This uniformity reduced the number of areas that were more susceptible to corrosion. In the as-cast samples, chromium segregation at the carbide-matrix interfaces caused the NaCl solution to attack these chromium-depleted sites preferentially. After heat treatment, the carbides were more homogeneously distributed, which significantly reduced these vulnerable sites and led to corrosion occurring mainly in the matrix instead. These carbides, which were the preferential sites for corrosion due to chromium depletion, led to deeper corrosion attacks at these interfaces. This advanced corrosion, as the deep corroding of the carbide-matrix interface, led to the pulling out of a significant amount of the carbides. This, as opposed to the corrosion of

a more homogeneously dispersed chromium-rich matrix, which is where the corrosion shifted to after heat treatment, meant that the matrix was less prone to the localised corrosion attack by the chloride ions, leading to the pulling of carbides. This is observed in the corrosion rate in the as-cast samples (Table 7.1), which was modestly higher than the heat-treated samples (Table 7.4) by an average factor of ~10±0.14. Furthermore, the precipitation of secondary carbides decreased the amount of exposed matrix available for corrosion, thereby spreading the matrix corrosion more evenly over the surface. Thus, in NaCl, the main form of protection against corrosion is the reduction of the available sites for microgalvanic corrosion by the homogenisation of the phases and element distribution throughout the microstructure.

7.8.2 Comparison Between the Corrosion Behaviour of As-Cast and Heat-Treated HCCIs in 0.5M Sodium Hydroxide Solution

In NaOH environment, carbides corrode first because they have a lower self-corrosion potential than the matrix (Liu et al., 2023). In NaOH solutions, the primary corrosion mechanism involves the degradation of the carbides. Clegg & McLeod (2013) and Liu et al. (2023) reported that at lower temperatures, significant corrosion occurs at the carbide component, while at higher temperatures, the matrix corrodes preferentially, exposing carbide particles to mechanical damage. As the carbides dissolve, they leave behind more matrix and more chromium gets released to form a stronger passive film, which helps form a stronger protective passive film. The equation governing the cathodic reaction at the matrix is Equation 7.1 (Abd El-Aziz et al., 2015)

$$O_2 + H_2O + 4e^- \rightarrow 4OH^- \qquad \text{Equation 7.1}$$

This is the same behaviour observed in the strong passive region of the sample corroded in NaOH in Figure 7.5 potentiodynamic polarisation curves and the highly stable OCP behaviour in Figure 7.4. This behaviour can be attributed to the fact that in highly alkaline environments, the carbides corrode preferentially over the metal matrix due to their lower self-corrosion potential (Clegg & McLeod, 2013; Liu et al., 2023).

In 0.5 M NaOH solution the primary type of corrosion for the as-cast HCCI samples (P1, P2, and P3) were selective carbide dissolution. Owed to their lower self-corrosion potential than the matrix, the carbides corroded preferentially in the strongly alkaline environment, leaving a matrix rich in chromium that progressively developed a passive layer. The corrosion behaviour in NaOH solution is primarily influenced by the volume and distribution of carbides as well as the progressive release of Cr as the primary and eutectic carbides dissolve. In the alkaline

NaOH solution, the carbides tend to corrode preferentially, leaving behind more of the matrix. As the carbides dissolve, additional chromium is gradually released, which slowly strengthens the passive film. Corrosion resistance in the as-cast samples is mainly controlled by the formation of a passive film, and this is strongly affected by the carbide volume, distribution, and size. In P1, there is more chromium available to build a strong passive film, but very few primary carbides were formed. This means that when the NaOH solution attacks, it preferentially dissolves the few carbides available. Because these carbides are small, they tend to dissolve deeper rather than spreading out, and the large volume of the solution quickly overwhelms them. In addition, the wider dendrite spacing in P1 creates more active sites for corrosion, thus, even though chromium is released to form a passive film, the overall corrosion rate remains high. In P2, the volume of carbides is much higher than in P1, which initially uses up some of the chromium required for a passive film formation. However, the carbides in P2 are more homogeneous and densely packed, with a smaller, more hexagonal shape. This reduces the interactions between the carbides and the matrix that lead to microgalvanic corrosion. The more even distribution helps the passive film to develop steadily as the carbides dissolve deeper rather than wider, eventually strengthening the film and lowering the corrosion rate over time. In contrast, P3 has carbides that are slightly more dispersed and a bit more numerous than in P2. Their larger size gives them a greater surface area for dissolution, so they corrode faster on the surface, and the corrosion occurs wider rather than deeper. This initially makes the passive film less effective and increases the corrosion rate compared to P2, though over time the extra chromium released helps to improve the film and reduce corrosion.

After heat treatment, the formation of secondary carbides further depletes the chromium available for building the passive film. In P1ht, this means that the already few carbides are even less effective at releasing chromium, so the passive film becomes weaker, leading to deeper carbide corrosion and a higher overall corrosion rate. In P2ht, although the carbides remain homogeneous after heat treatment, carbide coarsening slightly increases the surface area exposed to the solution, causing a bit more surface dissolution. For P3ht, the larger volume and size of carbides mean that even more chromium is tied up in secondary carbides, while the increased surface area leads to wider, more aggressive corrosion. The as-cast samples had far superior corrosion resistance in the NaOH environment compared to the heat-treated samples by a factor of 135±35. This is mostly due to the strong and stable passive film formed in the as-cast from the onset, because more chromium was readily available to form the passive film. Additionally, the precipitation of secondary carbides tied up more of the chromium which

would have slowed down the corrosion rate in the samples. The slower release of the tied-up chromium led to a slower building of the passive layer. This is evident in Figure 7.4 where all the sample begin with a very strong and stable passive layer which stabilises in a shorter period, whereas in the OCP in Figure 7.13 of the heat-treated samples show a gradual increase in the building of passive film overtime. This is also evident in the lower potential to corrosion exhibited by the heat-treated samples in the potentiodynamic curves in Figure 7.14 as opposed to the higher potential observed for the as-cast samples. Overall, the main mode of corrosion resistance in NaOH is the formation of a stable passive film, and a homogeneous, densely packed carbide network helps to reduce the surface area exposed to the solution, thereby limiting corrosion.

7.8.3 Comparison Between the Corrosion Behaviour of As-Cast and Heat-Treated HCCIs in Acidic Solution

As the passive film degrades, weak areas may experience localised breakdown, allowing the acid to penetrate and cause pitting or crevice corrosion starting at the grain boundaries, which disrupts the electrochemical balance and leads to a gradual decrease in corrosion potential (Lee et al., 2021, Lee et al., 2024). The presence of sulphate ions may also interfere with film stability, preventing complete repassivation and leading to a slow but steady decline in corrosion potential (Abdel-Aziz et al., 2017). The equation governing the anodic reaction of the matrix is Equation 7.2(Abd El-Aziz et al., 2015)

$$Fe \rightarrow Fe_2^+ + 2e^- \qquad \text{Equation 7.2}$$

This behaviour is exhibited in the OCP curves of H_2SO_4 in Figure 7.7 and the potentiodynamic polarisation curves in Figure 7.8. In the acidic environment, the matrix is more anodic relative to carbides, leading to selective dissolution at the carbide-matrix boundaries (Wiengmoon et al., 2011).The primary and eutectic M_7C_3 carbides, which are effective at stabilising the passive film in neutral and alkaline environments, are less effective in H_2SO_4 because the high acidity disrupts the chromium-rich oxide layer. This leads to the exposure and dissolution of the carbide-matrix boundaries, resulting in more pronounced grooves and microstructural damage. Localised material removal can occur in some regions, where corrosion is quite severe, other parts remain intact. This non-uniform corrosion behaviour implies that the alloy is prone to localised attack where the carbide-matrix interface serves as locations for accelerated corrosion (Zhang et al., 2020). Thus, in an acidic environment, the decrease of chromium available for passive film formation due to the production of more carbides increased the rate of corrosion.

In 0.5 M H_2SO_4 solution, the as-cast HCCI samples (P1, P2, and P3) exhibited active dissolution and localised galvanic corrosion. The highly acidic environment favoured constant matrix dissolution due to aggressive sulphate ion attack, which prevented the formation of a stable passive film. The electrochemical corrosion potential differences between the chromium-rich carbides and the surrounding metal matrix resulted in localised galvanic corrosion at the carbide-matrix interfaces. Corrosion in H_2SO_4 solution is primarily influenced by carbide volume and distribution, as well as the availability of chromium to create a protective passive coating. P1 had the highest corrosion resistance due to the lower carbide volume and higher chromium concentration. The lower carbide volume means less chromium was used up to form the carbides and more chromium is readily available to form a stronger passive film. However, the P1 passive film was still prone to frequent breakdowns due to the extremely aggressive sulphate ions. Due to the acid aggressively attacking the passive film, the reduced volume of carbides in P1 decreased the number of sites where the acid can attack and cause active dissolution of the matrix. P2 exhibited intermediate corrosion resistance due to its larger carbide volume and lower Cr concentration available for passive film formation. The significant reduction in chromium available to readily form the passive film caused the increase in corrosion rate. Additionally, the increase in primary and eutectic carbide volume increased the number of galvanic interactions at the carbide-matrix contacts, which resulted in more localised corrosion. Together, the decrease in chromium and the aggressive attacks on the carbide-matrix interfaces led to more frequent breaks and repassivation occurrences. P3 has the lowest corrosion resistance because of the high volume of interconnected primary and eutectic carbides and the limited amount of chromium readily accessible for passivation film formation. Additionally, the larger continuous carbide network resulted in a significantly increased galvanic corrosion rate on the carbide matrix interface, promoting quick localised corrosion and more frequent passive film breakdowns. This indicated ineffective passive film and significant active dissolving in H_2SO_4 solution.

In 0.5 M H_2SO_4 solution, the primary modes of corrosion observed for the heat-treated HCCI samples (P1ht, P2ht, and P3ht) were active dissolution and localised galvanic corrosion. The same principle as in the as-cast state applied to the heat-treated samples. The highly aggressive sulphate ions in the acidic solution hindered the formation of a stable passive film, leading to continuous metal matrix dissolution. Thus, the further lowering of available chromium to form the passive film increased the corrosion rate experienced. The corrosion rate progressed with the progressive increase in carbide volume. P1ht shows the best corrosion resistance among

the heat-treated samples due to its finely dispersed and uniformly distributed primary M_7C_3 carbides, which promoted more uniform dissolution and reduced localised attack. The increased amount of chromium readily available to form the film led to a decrease in the corrosion rate while the lower volume of carbides led to fewer sites available for active galvanic corrosion which decreased the rate at which the corrosion occurred. However, compared to P1ht, the corrosion resistance in P1 decreased. This is due to the further decreased available chromium for passive film formation and the increased carbides due to secondary carbide precipitation as a result which increased the number of active sites for galvanic corrosion. The same trends were observed for P2ht and P3ht where P2ht shows moderate corrosion resistance because the increased volume of carbides depletes the available chromium for passive film formation. The increased number of carbides due to secondary carbide precipitation increased the number of active sites for galvanic corrosion than in P2. The coarsening of the primary carbides after heat treatment may have also increased the corrosion rate through the increase in the area of carbide-matrix interactions, promoting microgalvanic corrosion. However, the maintained homogeneity still ensured the amount of surface area exposed to the attack of acid was reduced, consequently leading to a lesser corrosion rate than P3ht. The coarser carbides created more active sites for localised attack, leading to more frequent passive film breakdowns and a more fluctuating passive region, resulting in a higher corrosion rate than P1ht. P3ht shows the highest corrosion resistance compared to the other heat-treated samples due to the decreased availability of chromium available for film formation. Additionally, the extensive galvanic sites at the carbide-matrix interfaces caused by the larger carbide size led to an increase in the corrosion rate. This promoted rapid localised corrosion and more frequent passive film breakdowns, leading to the highest corrosion rate among the heat-treated samples. The increased volume of carbides restricted the formation of a continuous passive film, leading to the more severe active dissolution and the least effective passivation in H_2SO_4 solution. Consequently, this also increased the corrosion rate in P3ht as opposed to P3. Due to depleted chromium for stable passive film formation used to precipitate the secondary carbides and the secondary carbides become sites for microgalvanic corrosion, this further facilitated the corroding of the P3ht than P3.

Overall, the as-cast samples showed marginally better corrosion resistance compared to the heat-treated samples by a factor of 0.188±0.13. The above observations show the secondary carbides actively caused an increase in corrosion rate by decreasing the amount of chromium available for passive film formation. It is observed that an increase in corrosion resistance from

P1ht to P3ht is due to the increase in carbide size, availability of chromium content, and homogenisation of the microstructure. The further depletion of chromium available for passive film formation also caused an increase in the severity of corrosion in the heat-treated samples than the as-cast. Additionally, the secondary carbides also acted as micorgalvanic sites for active corrosion thereby increasing the rate of corrosion in the heat-treated samples. This emphasised the importance of the balance in the Cr/C ratio in order to produce the best microstructure for corrosion resistance. Overall, the highest corrosion rates were observed in H_2SO_4 solution, followed by 3.5wt.% NaCl solution, while in NaOH it was the lowest due to NaOH promoting the formation of the passive layer instead of attacking it.

The above observations are in agreement with work done by Tang et al. (2009); Abd El-Aziz et al. (2015), Marimuthu & Kannoorpatti, (2016); Liu et al. (2023), and Dos Santos et al. (2024). All four studies show how important the microstructure is, especially the carbides, when it comes to corrosion in NaOH, H_2SO_4, and NaCl solutions. Abd El-Aziz et al. (2015) investigated the wear and corrosion behaviour of high-chromium white cast iron alloys in various corrosive media. The authors show that the performance of the alloy is strongly linked to its microstructure specifically the volume, size, and distribution of primary and eutectic carbides, as well as the chromium content in the matrix. In corrosive environments like NaCl, NaOH, and H_2SO_4, the alloys form a passive film that helps protect against corrosion; however, the effectiveness of the film depends on how evenly and densely the carbides are distributed. The study also indicated that while the hard carbides provide excellent wear resistance, they can serve as initiation sites for localised corrosion under aggressive conditions such as H_2SO_4. Furthermore, heat treatment alters the microstructure by creating secondary carbides, which may either enhance or reduce corrosion resistance by affecting the availability of chromium for passive film formation and the main mode of attack by the solution. Overall, the paper highlights that balancing carbide characteristics and chromium content is key to optimising both wear and corrosion resistance in high-chromium white cast iron alloys. Marimuthu & Kannoorpatti (2016) argued that the corrosion rate varies with the environment and carbon content, attributed to the varying free chromium concentration in the matrix as carbon increases, affecting the passivation capability of the alloys. Liu et al. (2023) in the study with Nb alloying to HCCIs suggest that in NaOH the corrosion rate increases with increasing carbide content due to microgalvanic couples forming between the carbides and the matrix due to differences in self-corrosion potential. As the Fe-Nb content increased, the proportion of

primary NbC phase also increased, leading to a decrease in corrosion resistance due to the lack of iron to form a stable passivation layer in the NbC structure.

7.9 Conclusion

Acidic environments such as H_2SO_4 cause the most corrosion because they attack both the carbides and the metal matrix. This study shows that corrosion of high chromium white cast iron depends on carbide volume, distribution and chromium content. Each medium attacks the alloy in its own way. In 3.5 wt % NaCl, small, evenly spread carbides help form a stable passive film that stops localised corrosion at the carbide and matrix boundaries. Sample P1, with higher chromium, resists corrosion best, while P3, with more carbides and less chromium, corrodes fastest. In 0.5 M NaOH, carbides dissolve first since they have a lower corrosion potential. This releases chromium into the film, and P2, with dense carbides, slows corrosion more than P1 or P3. In 0.5 M H_2SO_4, aggressive sulphate ions continuously break down the passive film and expose fresh metal. P1 shows the shallowest matrix attack because its higher chromium content allows the film to reform more quickly between breakdown events. P3 suffers the worst damage where the large carbides create extensive galvanic sites that accelerate film breakdown, and its lower chromium content inhibits the film from repairing itself effectively. Heat treatment causes secondary carbides to form around existing carbides and along grain boundaries. These secondary carbides use up chromium that would otherwise help build the passive film. In NaCl this shift of corrosion from the film to the metal can reduce overall matrix attack. In acid it makes corrosion worse by creating more galvanic sites and by weakening the film. Overall, balancing the Cr / C ratio and maintaining a uniform carbide distribution before and after heat treatment is key to good corrosion resistance. Rates are highest in acid, lower in chloride and lowest in alkaline solutions. Overall, achieving an optimal Cr/C ratio and a homogeneous microstructure is crucial for enhancing corrosion resistance, with the highest corrosion rates observed in acid, followed by chloride, and the lowest in alkaline solutions.

7.10 References

Abd El-Aziz, K., Zohdy, K., Saber, D., & Sallam, H. E. M. (2015a). Wear and Corrosion Behaviour of High-Cr White Cast Iron Alloys in Different Corrosive Media. *Journal of Bio- and Tribo-Corrosion*, *1*(4).

Abdel-Aziz, K., El-Shennawy, M., & Omar, A. A. (2017). Microstructural characteristics and mechanical properties of heat treated high-cr white cast iron alloys. *International Journal of Applied Engineering Research*, *12*(14), 4675–4686.

Ahmadian, Z., Danaee, I., & Golozar, M. A. (2014). Effect of surface treatment on corrosion resistance of 304 stainless steel implants in Tyrode solution. *Archives of Metallurgy and Materials*, *59*(1), 25–30.

Atiyah, A. A., & Albusalih, D. (2023). Corrosion Behaviour of Steel 37 under Dynamic Conditions in 0.1 N H2SO4. *Journal of Engineering and Technological Sciences*, *55*(6), 639–646.

Chang, C. M., Hsieh, C. C., Lin, C. M., Chen, J. H., Fan, C. M., & Wu, W. (2010). Effect of carbon content on microstructure and corrosion behaviour of hypereutectic Fe-Cr-C claddings. *Materials Chemistry and Physics*, *123*(1), 241–246.

Clegg, R. E., & McLeod, A. J. (2013). Corrosion behaviour of high chromium white cast irons in high tempearture caustic solutions. *Annual Conference of the Australasian Corrosion Association 2013: Corrosion and Prevention 2013*, 580–587.

Deng, Y., Zhang, J., & Jiao, K. (2018). Viscosity measurement and prediction model of molten iron. *Ironmaking and Steelmaking*, *45*(8), 773–777.

Dos Santos, R. S. G., Cabral, T. S., Rodrigues, L. A. S., Loayza, C. R. L., Silva, R. N. J. F., & Braga, E. M. (2024). Study of the corrosion resistance of high chromium white cast iron welds in the presence of NaOH (30% w/w). *Journal of Materials Research and Technology*, *30*, 7563–7574.

Sarac, M. and Dikici, B. (2019) Effect of heat treatment on wear and corrosion behaviour of high chromium white cast iron. *Materials Testing*, 61 (7), 659-666.

Farquhar, A. K., Henshaw, G. S., & Williams, D. E. (2021). Understanding and Correcting Unwanted Influences on the Signal from Electrochemical Gas Sensors. *ACS Sensors*, *6*(3), 1295–1304.

Feng, G., Jiao, K., Zhang, J., & Gao, S. (2021). High-temperature viscosity of iron-carbon melts based on liquid structure:The effect of carbon content and temperature. *Journal of Molecular Liquids*, *330*.

Fu, N., Tang, X., Li, D. Y., Parent, L., & Tian, H. (2015). In situ investigation of local corrosion at interphase boundary under an electrochemical-atomic force microscope. *Journal of Solid State Electrochemistry*, *19*(2), 337–344

Gong, L., Fu, H., & Zhi, X. (2023). Corrosion Wear of Hypereutectic High Chromium Cast Iron: A Review. In *Metals* (Vol. 13, Issue 2). MDPI.

Guo, E., Wang, L., Wang, L., & Huang, Y. (2009). Effects of RE, V, Ti and B composite modification on the microstructure and properties of high chromium cast iron containing 3% molybdenum. *Rare Metals*, *28*(6), 606–611.

Heo, N. H., & Kim, S.-J. (2012). Anomalies in segregation kinetics of solutes under tensile stress in heat resistant steel. *Materials Science and Engineering: A*, *556*, 533–539.

Lee, J.-S., Baasanjav, O., Oh, J.-S., & Lee, J.-H. (2024). Time-Dependent Corrosion Behaviour of High Chromium White Cast Iron in an Acidic Solution. *Corrosion Science and Technology*, *23*(4), 310–314.

Lee, J.-S., Lee, J.-H., Oh, J.-S., & Lee, J.-H. (2021). General Corrosion Behaviour of High Chromium Cast Iron in an Acid Solution. *Corrosion Science and Technology*, *20*(6), 367–372.

Leshetla, M., Klenam, D. E., van der Merwe, J., Potgieter, H., Whitefield, D., & Bodunrin, M. O. (2022). Corrosion resistance of iron-containing experimental titanium alloys exposed to simulated body fluids. *Materials and Corrosion*, *73*(8), 1298–1307.

Li, Y., Li, P., Gong, M., & Tong, W. (2019). Diffusion behaviour in high-chromium cast iron/low-carbon steel bimetals. *Philosophical Magazine Letters*, *99*(11), 397–403.

Liu, D., Long, W., Lednev, V. N., Wei, P., & Wang, R. (2023). Influence of Nb Additive on Alkaline Corrosion Behaviour of Slag-Free Self-shielded Metal-Cord Welding Overlay. *Journal of Materials Engineering and Performance*, *32*(22), 10064–10076.

Lv, H., Zhou, R., Li, L., Ni, H., Zhu, J., & Feng, T. (2018). Effect of electric current pulse on microstructure and corrosion resistance of hypereutectic high chromium cast iron. *Materials*, *11*(11).

Lynch, B., Wang, Z., Ma, L., Paschalidou, E.-M., Wiame, F., Maurice, V., & Marcus, P. (2020). Passivation-Induced Cr and Mo Enrichments of 316L Stainless Steel Surfaces and Effects of Controlled Pre-Oxidation. *Journal of The Electrochemical Society*, *167*(14), 141509.

Ma, L., Pascalidou, E. M., Wiame, F., Zanna, S., Maurice, V., & Marcus, P. (2020). Passivation mechanisms and pre-oxidation effects on model surfaces of FeCrNi austenitic stainless steel. *Corrosion Science*, *167*.

Marimuthu, V., & Kannoorpatti, K. (2016). Corrosion Behaviour of High Chromium White Iron Hardfacing Alloys in Acidic and Neutral Solutions. *Journal of Bio- and Tribo-Corrosion*, *2*(4).

Moslemi, H., Shamsi, P., & Habashi, F. (2011). Pyrite and pyrrhotite open circuit potentials study: Effects on flotation. *Minerals Engineering*, *24*(10), 1038–1045.

Murmey, P., Nichul, U., Chikode, M., & Hiwarkar, V. (2023). Effect of Post-processing on Corrosion Behaviour of LPBF Built Inconel 718 Alloy. *JOM*, *75*(1), 32–44.

Parkhutik, V. P. (2006). Oscillations of open-circuit potential during immersion plating of silicon in CuSO4/HF solutions. *Russian Journal of Electrochemistry*, *42*(5), 512–522.

Salasi, M., Stachowiak, G. B., & Stachowiak, G. W. (2011). Chloride effect on corrosion & corrosive wear of high-Cr cast irons in different pH solutions. *18th International Corrosion Congress 2011*, *2*, 1335–1346.

Shen, X., Sinclair, N., Wainright, J., Akolkar, R., & Savinell, R. F. (2020). Evaluating and Developing a Reliable Reference Electrode for Choline Chloride Based Deep Eutectic Solvents. *Journal of The Electrochemical Society*, *167*(8), 086509.

Su, H., Liang, Y., Wang, Y., Wang, B., Tong, H., Yuan, Y., & Wei, S. (2019). Effect of dissolved oxygen on pitting corrosion behaviour of low-alloy steel under hydrostatic pressure. *International Journal of Electrochemical Science*, *14*(5), 4812–4827.

Tang, X. H., Chung, R., Li, D. Y., Hinckley, B., & Dolman, K. (2009). Variations in microstructure of high chromium cast irons and resultant changes in resistance to wear, corrosion and corrosive wear. *Wear*, *267*(1–4), 116–121.

Tang, X. H., Chung, R., Pang, C. J., Li, D. Y., Hinckley, B., & Dolman, K. (2011). Microstructure of high (45wt.%) chromium cast irons and their resistances to wear and corrosion. *Wear*, *271*(9–10), 1426–1431.

Wang, Y., Li, G., Qi, H., Zhang, W., Chen, R., Su, R., Yu, B., & Qu, Y. (2024). Effect of non-metallic carbon content on the microstructure and corrosion behaviour of AlCoCrFeNi high-entropy alloys. *Intermetallics*, *166*.

Wiengmoon, A., Pearce, J. T. H., & Chairuangsri, T. (2011). Relationship between microstructure, hardness and corrosion resistance in 20 wt.%Cr, 27 wt.%Cr and 36 wt.%Cr high chromium cast irons. *Materials Chemistry and Physics*, *125*(3), 739–748.

Yan, H., He, Z., Nan, L. ü., Wei, C., Xu, T., & Liu, J. (2020). Effects of cooling rate on the precipitation behaviour of grain boundary carbide and corrosion resistance of 5Cr15MoV stainless steel. *Materials and Corrosion*, *71*(8), 1257–1265.

Yang, J., Wang, B., Yang, M., Ding, W.-C., Wang, P., & Luo, D.-J. (2009). Effect of instant modification on microstructure and properties of high chromium cast iron. *Zhuzao/Foundry*, *58*(2), 166–168.

Yue, Y., Liu, C., Shi, P., & Jiang, M. (2018). Passivity of stainless steel in sulphuric acid under chemical oxidation. *Corrosion Engineering Science and Technology*, *53*(3), 173–182.

Zhang, Y., Song, R., Pei, Y., Wen, E., & Zhao, Z. (2020). The formation of TiC–NbC core-shell structure in hypereutectic high chromium cast iron leads to significant refinement of primary M_7C_3. *Journal of Alloys and Compounds*, *824*.

Chapter 8: Conclusions and Recommendations

8.1 Conclusions

This study comprehensively examined microstructural evolution, mechanical properties, wear behaviour, and corrosion resistance of HCCI alloys, highlighting the critical influence of the Cr/C ratio, carbide volume, morphology and distribution on performance in different environments.

The objectives of the study were to:

1. Investigate how the Cr/C ratio affects the alloy's solidification and microstructure.
2. Examine the influence of the Cr/C ratio on hardness and toughness.
3. Assess how Cr/C ratio-induced microstructural variations impact wear performance.
4. Evaluate the effect of Cr/C ratio on corrosion resistance under industrial conditions.

The conclusions drawn are based on the objectives set out to be achieved. The findings confirm that the Cr/C ratio significantly impacts both the microstructure and the performance of HCCIs. Optimizing the Cr/C ratio and carbide distribution is crucial for balancing mechanical properties, wear resistance, and corrosion performance for industrial applications

The Effects of Cr/C ratio on the Microstructure of High Chrome Cast Iron.

The microstructural analysis showed that the Cr/C ratio plays a major role in determining carbide formation, type, morphology, size, and distribution. A higher Cr/C ratio led to a lower volume of fine and evenly distributed carbide network in an austenitic matrix, while a lower Cr/C ratio resulted in higher volume of coarser, more interconnected carbides in an austenitic matrix. Heat treatment further refined the microstructure, promoting secondary carbide precipitation, which influenced both mechanical and corrosion properties.

The Influence of Cr/C ratio on the Hardness and Fracture Toughness of High Chrome Cast Iron.

The hardness and toughness results confirmed that carbide volume and morphology as a result of Cr/C ratio directly impact mechanical performance. Higher carbide volume as a result of lower Cr/C ratio increased hardness by impeding deformation through the increase in hard carbide phases, but excessive carbide connectivity led to a more brittle matrix and lower fracture toughness. Heat treatment enhanced hardness but also increased brittleness, making

fracture behaviour more cleavage-dominated, especially in low Cr/C ratio samples. This demonstrates the need for an optimal balance between hardness and toughness to ensure good mechanical integrity.

The Influence of Microstructural Constituents on Wear Performance of High Chrome Cast Iron.

The wear behaviour analysis showed that carbide distribution is more important than hardness alone in determining wear resistance. A strong, interconnected carbide network effectively protected the matrix from direct contact with the counter surface, reducing material loss. However, excessive carbide coarsening led to increased three-body abrasion, causing higher wear rates in some heat-treated samples. The lowest wear resistance was observed in samples with fewer carbides and a softer matrix, as they experienced plastic deformation and adhesive wear. While heat treatment increased hardness, it had a limited effect on improving wear resistance, as excessive hardness led to more carbide fracture and abrasive wear debris.

The Influence of Microstructural Constituents on Corrosion Properties of High Chrome Cast Irons.

The corrosion behaviour of the HCCI alloys was heavily influenced by the microstructure, with different environments attacking the material in distinct ways. In acidic solutions, corrosion was most severe, as sulphate ions continuously broke down the passive film, exposing the matrix to rapid dissolution. A larger, interconnected carbide network worsened corrosion by limiting the availability of chromium in the matrix, preventing strong film formation. In chloride environments, corrosion mainly occurred at the carbide-matrix interfaces, where chromium segregation created weak points, leading to pitting and microgalvanic attack. A fine, well-dispersed carbide network helped stabilise the passive film and reduce corrosion rates. In alkaline environments, selective carbide dissolution was dominant, as carbides corroded first, releasing chromium to gradually build a protective film. Here, a more homogenous and closely packed carbide structure slowed down the corrosion process, while larger carbides led to faster surface degradation.

Heat treatment further modified corrosion resistance by introducing secondary carbides, which had different effects depending on the environment. In chloride solutions, secondary carbides helped stabilise the passive film by shifting corrosion towards the matrix. However, in acidic conditions, secondary carbides acted as galvanic sites, accelerating corrosion due to the lack of

chromium available for film formation. Overall, corrosion resistance was lowest in acidic environments, moderate in chloride solutions, and highest in alkaline solutions, reinforcing the importance of optimising microstructural features to improve material durability in specific service conditions.

General Conclusion

The heat treatment process applied in this study was designed to enhance fracture toughness while maintaining good wear and corrosion resistance, as intended by the patent owners. However, the expected improvements in wear and corrosion resistance were not fully achieved, and the fracture toughness increased in all samples, suggesting that the heat treatment did not optimise the microstructure for all properties simultaneously. One key reason for this underperformance could be that the heat treatment procedure was originally developed for a Cr28 alloy composition, whereas the alloys in this study had a lower chromium content (Cr24). Cr28 alloys contain more chromium, which significantly influences phase transformations, carbide precipitation, and passive film formation. Since the heat treatment was optimised for Cr28, its effectiveness in Cr24 alloys was reduced, leading to underperformance in wear and corrosion resistance while still increasing toughness.

In summary, this study highlights the necessity of optimising the Cr/C ratio, carbide distribution, and heat treatment conditions to achieve the best balance of mechanical properties, wear resistance, and corrosion performance. While a higher carbide volume improves wear resistance, it can also increase brittleness and corrosion susceptibility if the matrix lacks sufficient chromium for passive film formation. The best-performing alloys achieved a balance between carbide size, volume, and uniform distribution, ensuring both durability and resistance to material loss in wear and corrosive environments. These findings provide valuable insights for designing HCCI alloys for industrial applications, where tailored microstructural control is key to enhancing performance and longevity.

8.2 Recommendations

- **Optimisation of the Cr/C Ratio for Targeted Applications**: Future studies should prioritise the optimisation of the Cr/C ratio for specific industrial applications. Although this work established the influence of Cr/C ratios on microstructure and performance, further research can explore a finer range of compositions to determine the exact ratios that yield optimal combinations of hardness, toughness, corrosion resistance, and wear performance. This can be achieved by designing a controlled

experimental matrix with smaller incremental variations in Cr/C ratio and analysing the corresponding effects on mechanical and chemical behaviour. Incorporating statistical regression analysis and machine learning models to correlate composition with performance metrics can enable predictive alloy design tailored to particular service conditions.

- **Heat Treatment Optimisation for Targeted Microstructures**: A deeper investigation into the interaction between Cr/C ratio and post-casting heat treatments (such as austempering and quenching and partitioning) is essential. These treatments should be optimised not only for general property enhancement but for property-specific performance such as improving fracture toughness in impact-prone environments or refining carbide networks to enhance wear resistance. The use of EBSD accompanying XRD will be valuable in characterising the resulting microstructures, especially in analysing crystallographic orientation, strain fields, and carbide-matrix interface behaviour, allowing for microstructure tailoring that directly supports property targets.
- **Application-Specific Performance Testing**: A major recommendation is the implementation of application-specific performance testing. Although simulated laboratory conditions were used in this work, future studies should involve testing that aligns more closely with industrial service conditions. For example, wear testing under slurry or high-load abrasion, and corrosion testing in acidic or high-chloride environments would better mimic real-world exposure. These tests should follow ASTM internationally recognised standards for wear and for corrosion. Results can then be benchmarked against currently used industrial alloys to determine the competitiveness and suitability of HCCIs developed in this research.
- **Fracture Toughness and Crack Propagation Mechanisms:** There is a need to further investigate the mechanisms of fracture toughness and crack propagation in HCCIs, particularly since literature in this domain is limited. This could be achieved by subjecting specimens to controlled fracture testing such as instrumented Charpy impact or compact tension tests, followed by high-resolution fractography using SEM and electron backscatter diffraction (EBSD). Crack path analysis, in combination with finite element modelling, could be used to understand how carbide morphology, volume fraction, and matrix phase influence fracture resistance.
- **Detailed Classification of Wear Mechanisms**: The classification of wear mechanisms as a function of both Cr/C ratio and thermal history should be explored in more depth.

This would involve characterising worn surfaces using SEM, energy-dispersive spectroscopy (EDS), and 3D profilometry to identify whether abrasive, adhesive, oxidative, or delamination wear predominates under different conditions. Such work could be enhanced by conducting long-duration tests with intermediate inspections to capture microstructural evolution during wear, enabling time-resolved insight into degradation.

Appendix A: ImageJ Analysis of Carbide Volume Determination of As-Cast HCCI Samples

The following images are representative of multiple sample areas taken to calculate the carbide volume of the samples.

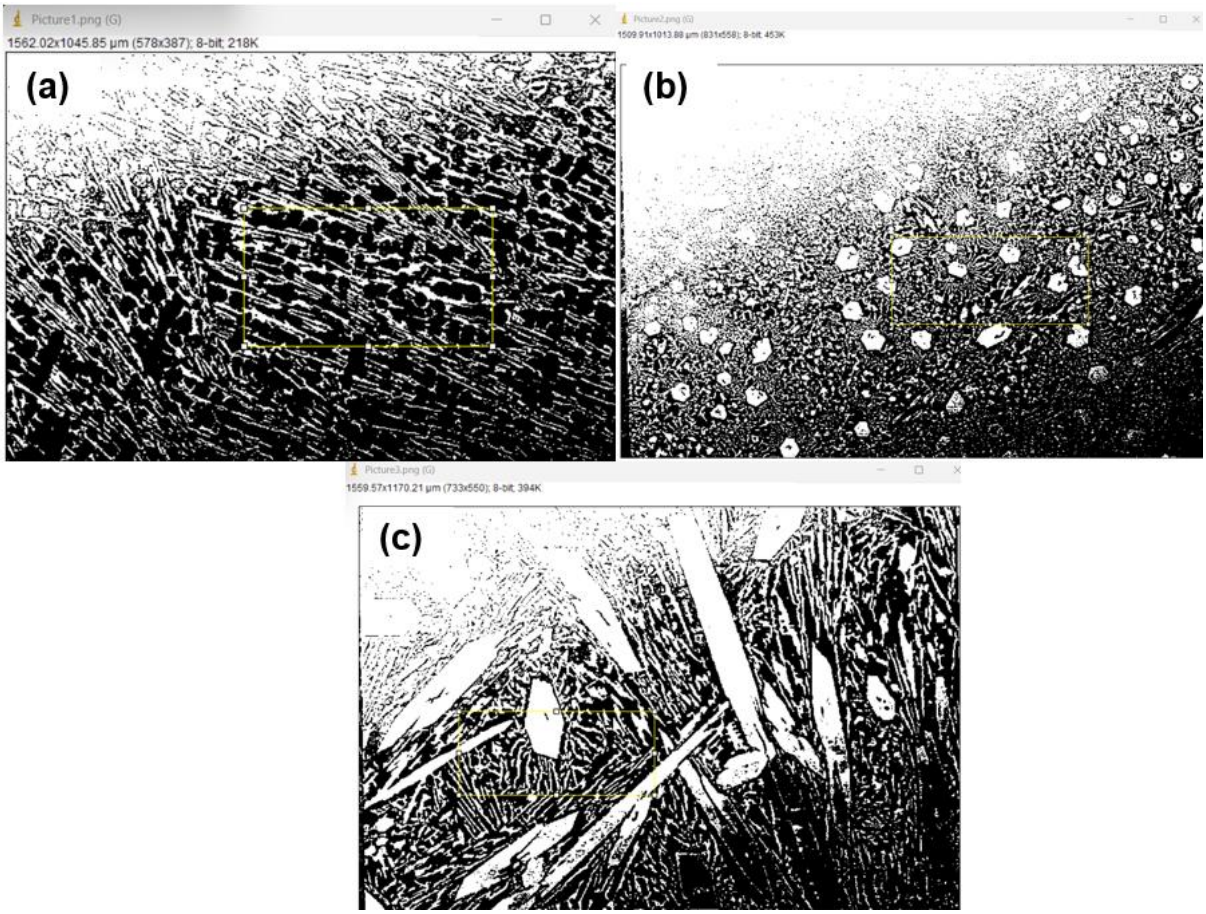

A-1: Representative area of ImageJ area analysis for carbide volume determination for samples P1(a), P2(b) and P3(c).

Appendix B: Wear Balls After Dry Sliding Wear

The following figures represent the wear surface of the alumina wear balls after dry sliding wear of as-cast and heat-treated samples.

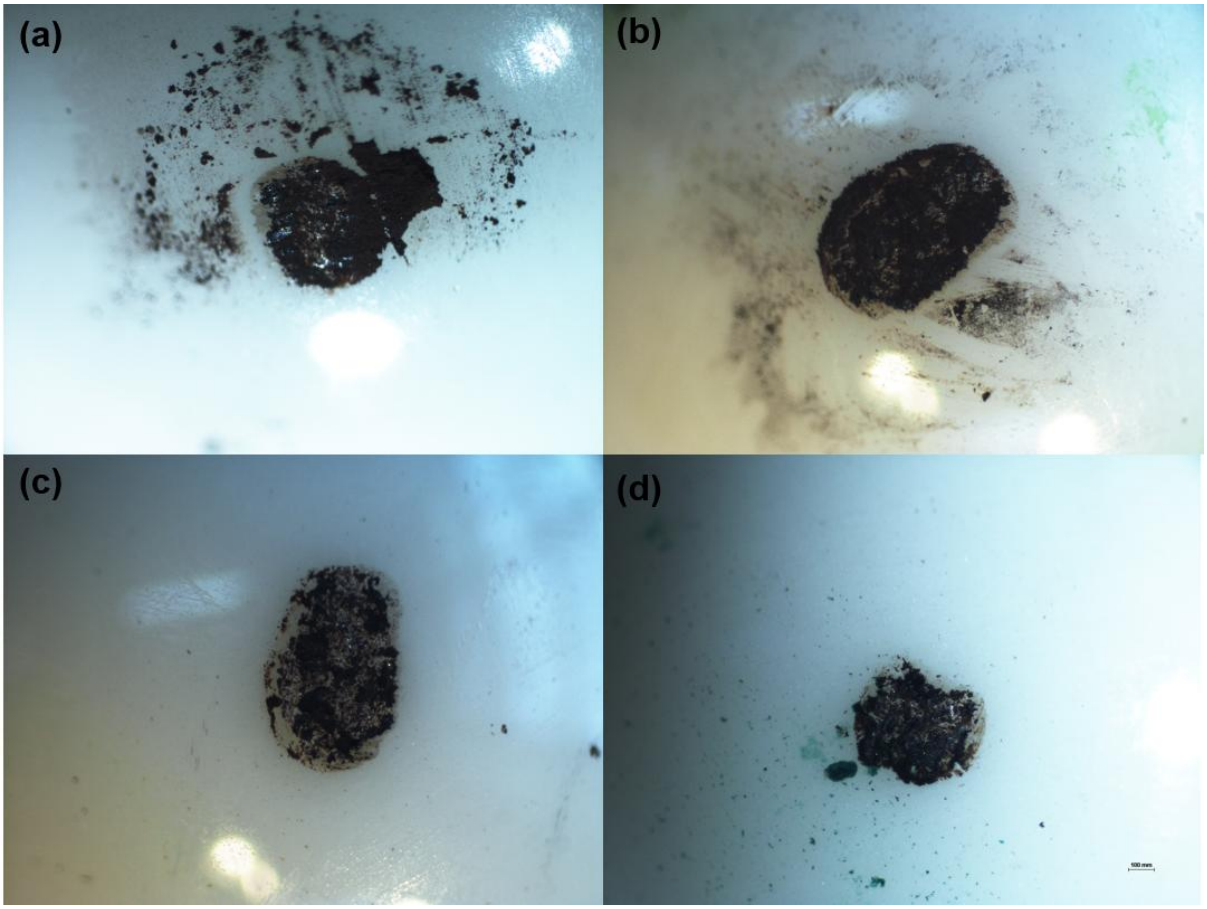

B-1: The above figures are representative of the surfaces of the alumina balls after dry sliding wear where the surfaces show the wear surface after sliding against as-cast samples P1(a), P2 and P3 alike(b) and the heat-treated samples P1ht(c) and P2ht and P3ht alike(d).

Appendix C: Microstructure of HCCI Samples After Corrosion in SE Imaging

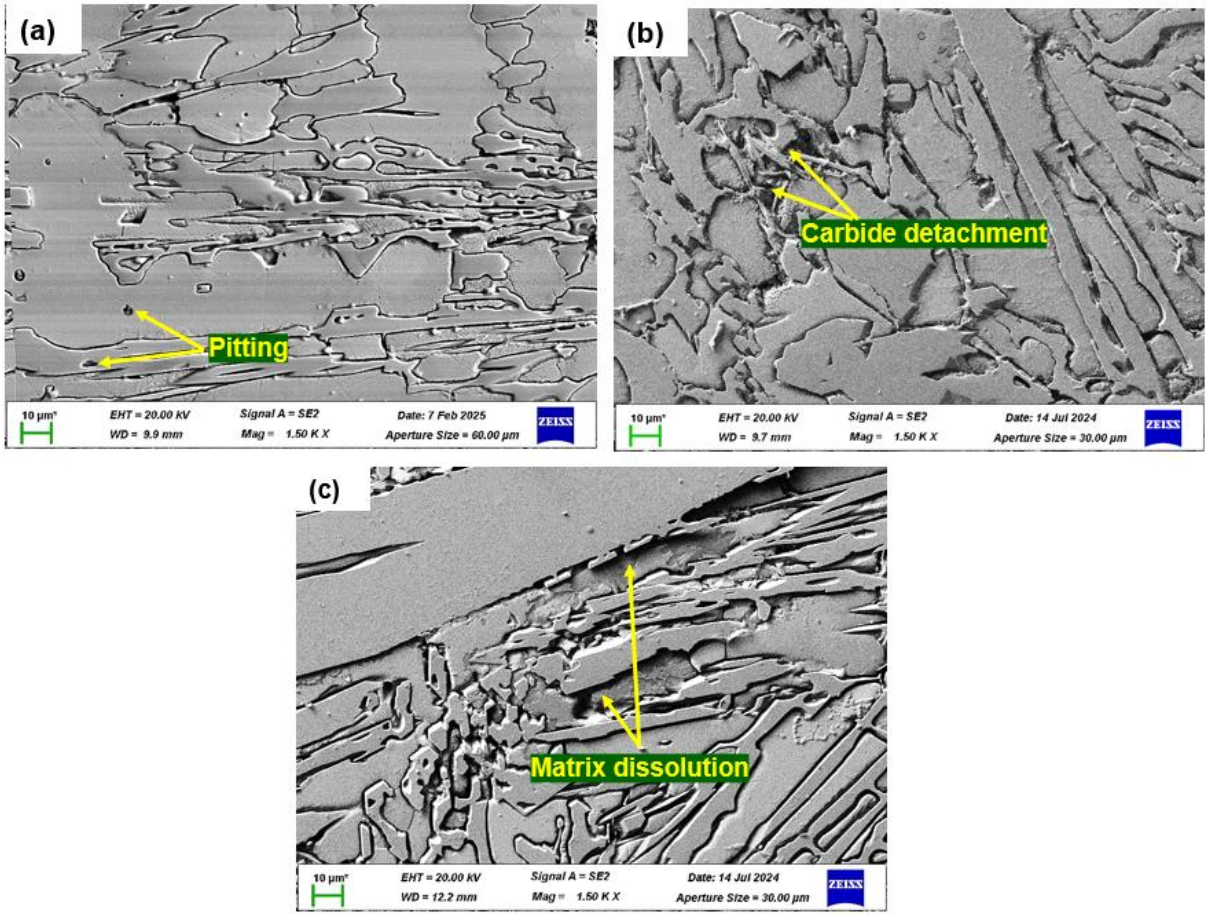

C-1: SE SEM images of as-cast samples P1 (a), P2 (b) and P3 (c) after electrochemical testing in 3.5wt.% NaCl solution.

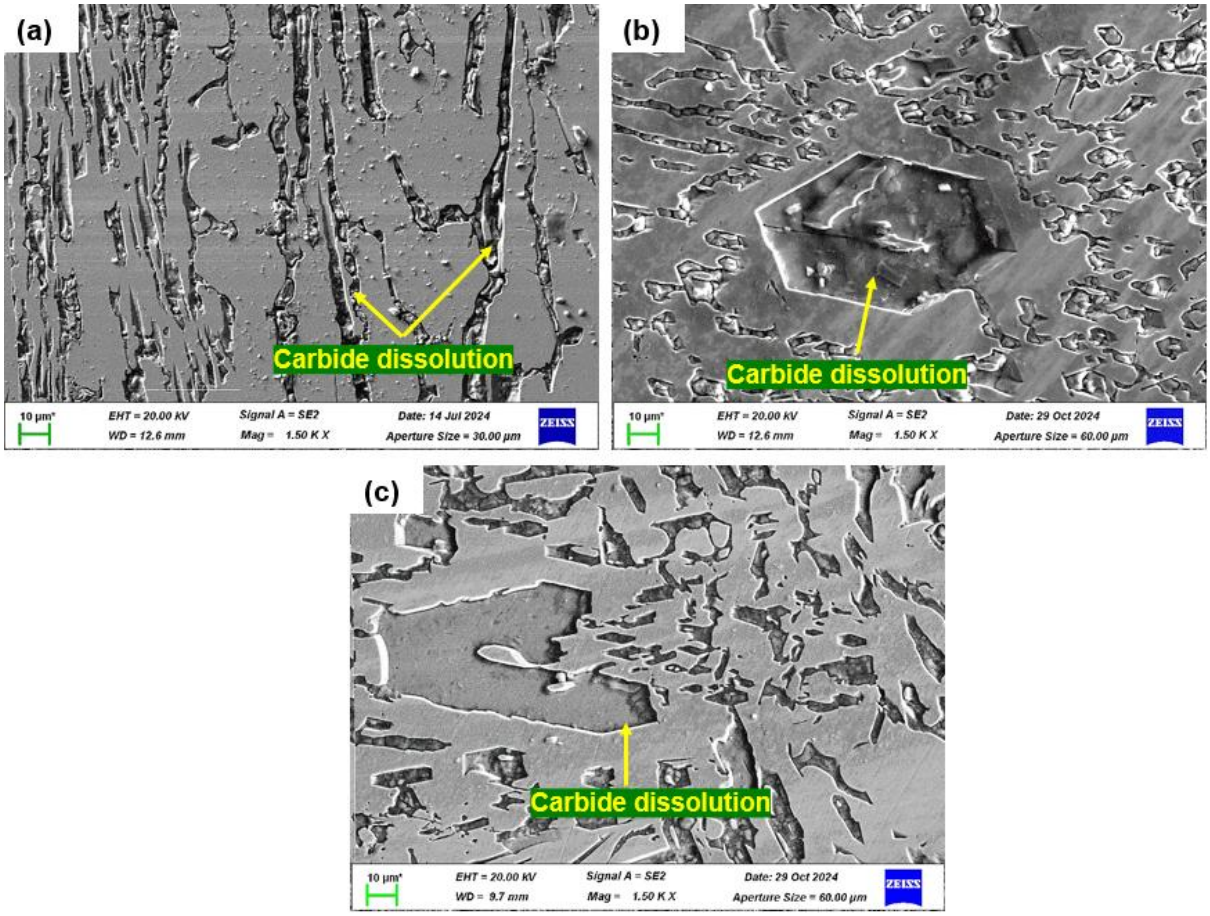

C-2: SE SEM images of as-cast samples P1 (a), P2 (b) and P3 (c) after electrochemical testing in 0.5M NaOH solution.

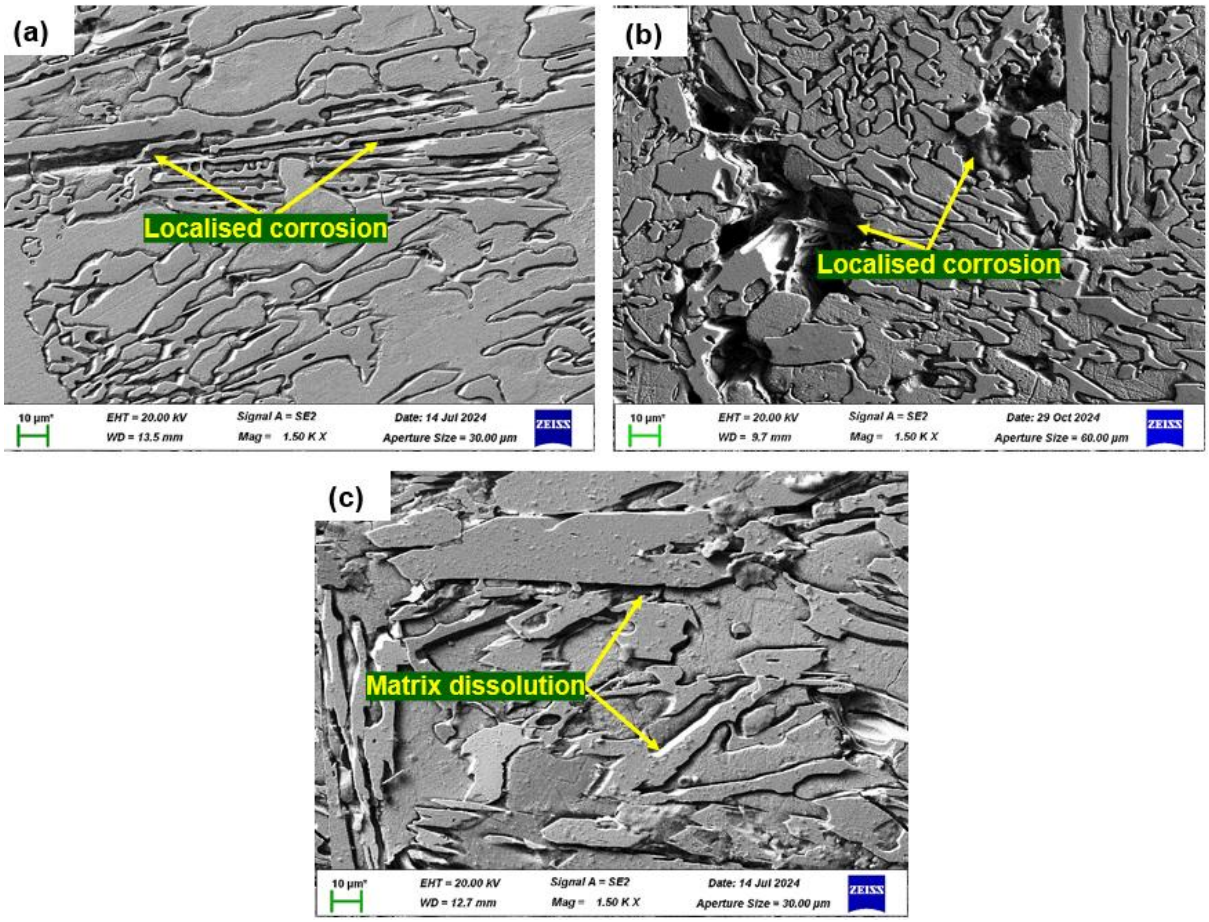

C-3: SE SEM images of as-cast samples P1 (a), P2 (b) and P3 (c) after electrochemical testing in 0.5M H_2SO_4 solution.

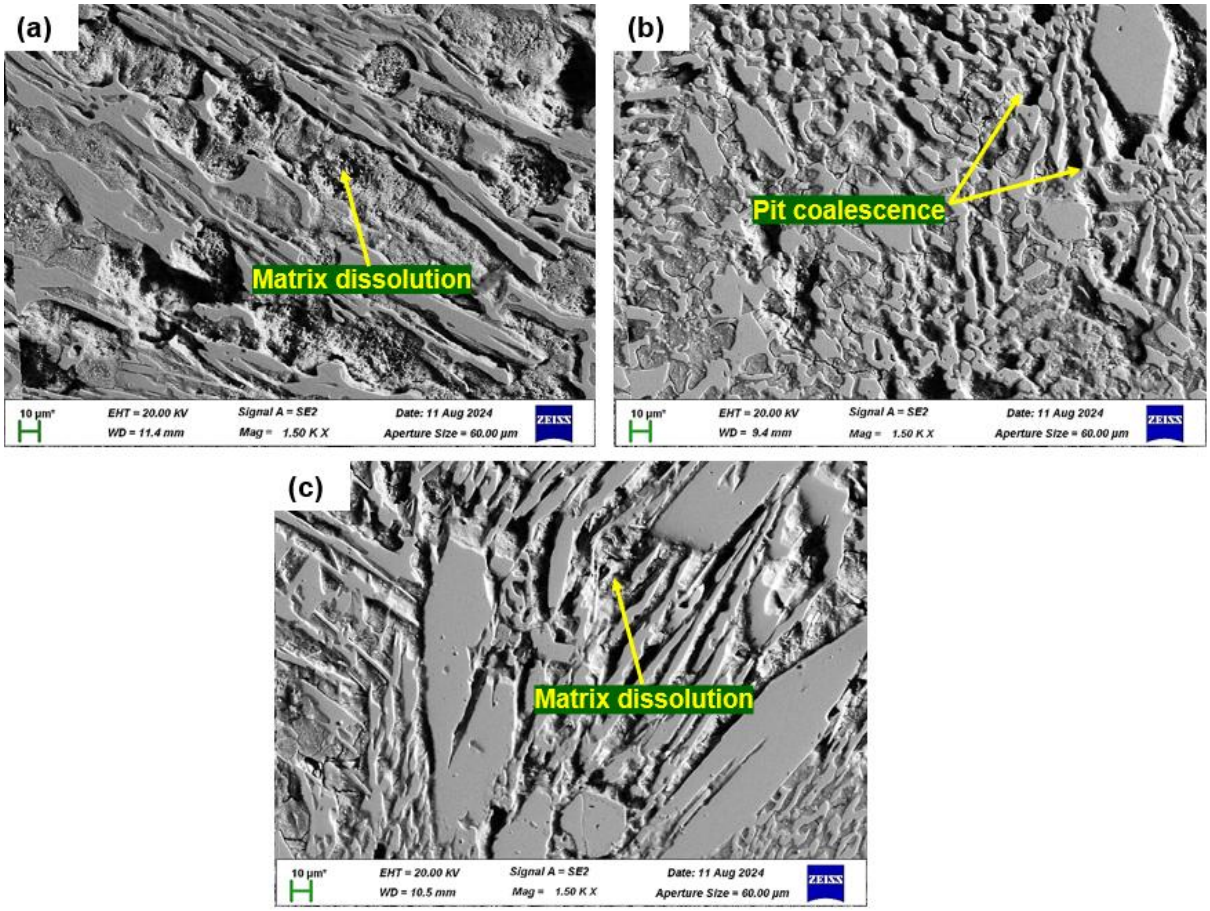

C-4: SE SEM images of heat-treated samples P1ht(a), P2ht(b) and P3ht(c) after electrochemical testing in 3.5wt.% NaCl solution.

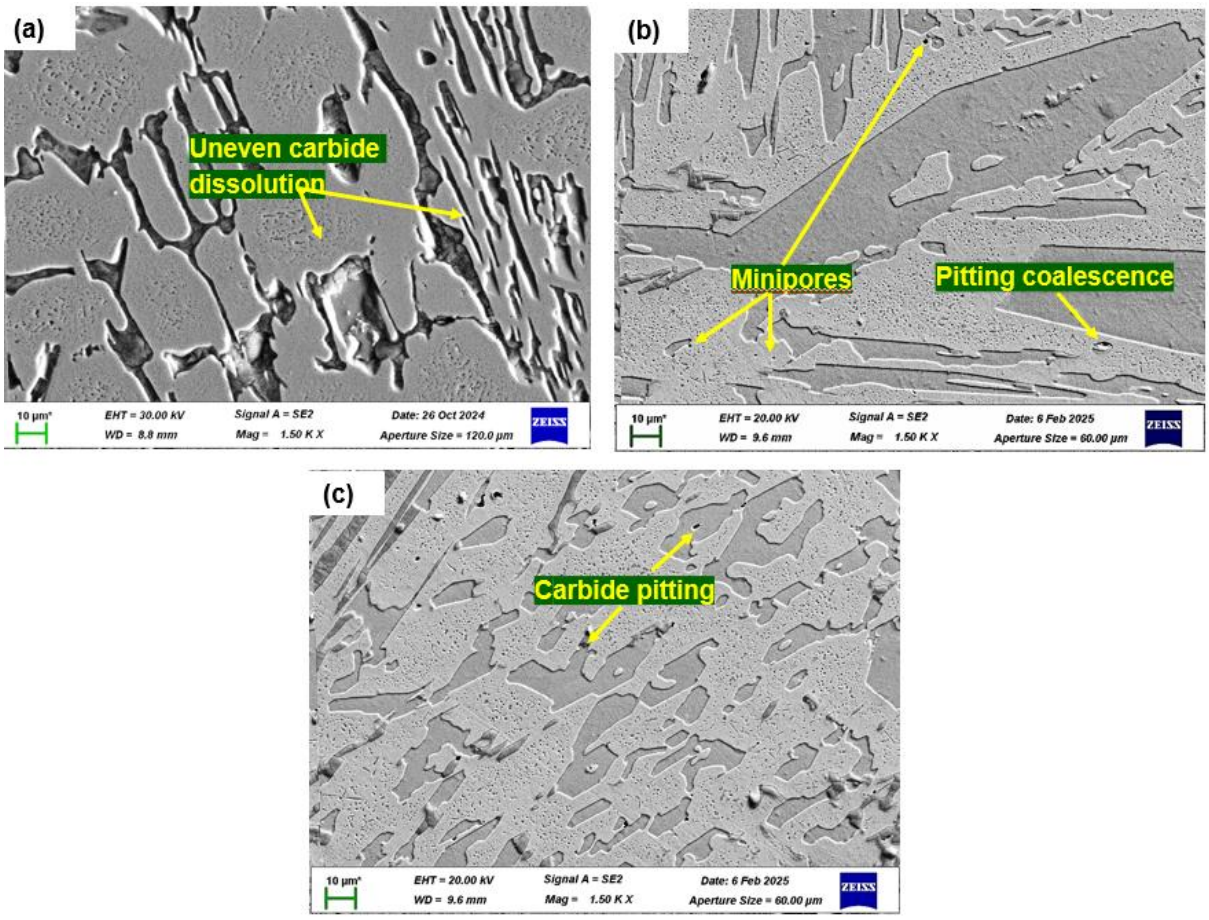

C-5: SE SEM images of heat-treated samples P1ht (a), P2ht (b) and P3ht (c) after electrochemical testing in 0.5M NaOH solution.

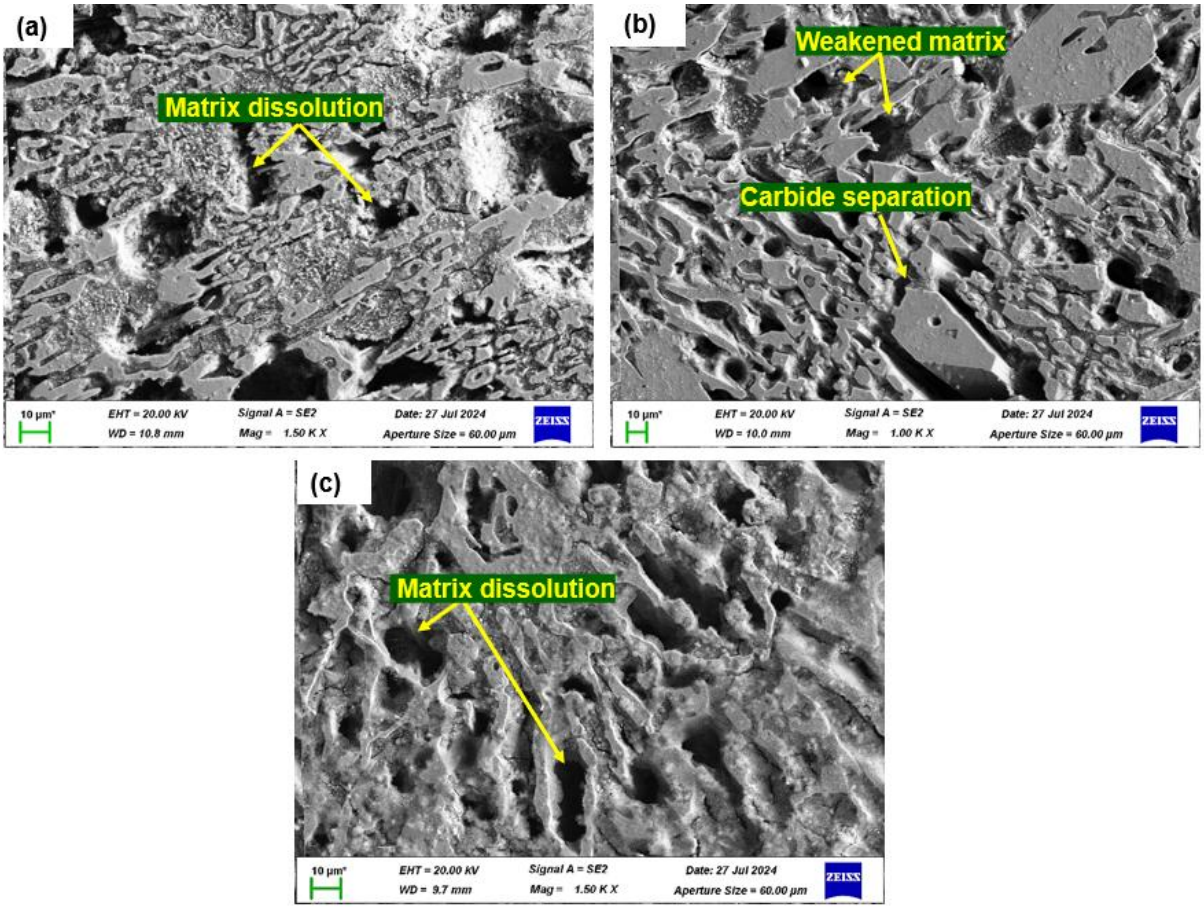

C-6: SE SEM images of heat-treated samples P1ht(a), P2ht(b) and P3ht(c) after electrochemical testing in 0.5M H_2SO_4 solution.